

**TRULY SUSTAINABLE IMIDAZOLIUM IONICS
TOWARDS EXPANDING APPLICABILITY IN NEXT-GENERATION
BATTERIES**

Steffen Tröger-Müller

Univ.-Diss.

zur Erlangung des akademischen Grades

"doctor rerum naturalium"

(Dr. rer. nat.)

in der Wissenschaftsdisziplin "Kolloid- und Grenzflächenwissenschaften"

eingereicht an der

Mathematisch-Naturwissenschaftlichen Fakultät

Institut für Chemie

der Universität Potsdam

und

Max-Planck-Institut für Kolloid- und Grenzflächenforschung

Hauptbetreuer/in: Prof. Dr. Markus Antonietti

weitere Gutachter: Prof. Dr. Andreas Taubert

Prof. Dr. Andrea Balducci

Contents

| | |
|---------------------------------------------------------------------------------|----|
| Contents..... | I |
| 1. Introduction | 3 |
| 1.1 Broader context and motivation | 3 |
| 1.2 Outline of this work..... | 5 |
| 1.3 Basic concepts | 6 |
| 1.3.1 Why green chemistry?..... | 6 |
| 1.3.2 Ionic liquids as agents of green chemistry | 9 |
| 1.3.3 Energy storage <i>beyond lithium</i> | 16 |
| 2 Ionic liquids and solids <i>via</i> modified Debus-Radziszewski reaction..... | 21 |
| 2.1 General considerations | 21 |
| 2.2 Direct anion tuning..... | 23 |
| 2.3 Cation design..... | 32 |
| 2.4 Polymer synthesis <i>via</i> modified Debus-Radziszewski reaction..... | 37 |
| 2.5 Summary | 44 |
| 3 Green polyelectrolyte networks for energy storage | 45 |
| 3.1 Relevance | 45 |
| 3.2 Mechanical properties | 47 |
| 3.3 Membranes from PENs | 52 |
| 3.4 Summary | 62 |
| 4 Magnesium electrochemistry – a <i>zwitterionic</i> solution?..... | 63 |
| 4.1 Protection of the C2-position | 64 |
| 4.2 Magnesium electrochemistry in zwitterionic liquid electrolytes | 78 |
| 4.3 Summary | 92 |
| 5 Conclusion and outlook..... | 93 |

| | | |
|-----|-------------------------------------------------------|-----|
| 6 | Appendix | 96 |
| 6.1 | Methods | 96 |
| 6.2 | Synthesis of compounds by chapter of occurrence | 122 |
| 6.3 | Abbreviations and units used | 144 |
| 6.4 | Materials..... | 145 |
| 6.5 | Declaration | 147 |
| 7 | Acknowledgements | 148 |
| 8 | References | 149 |

1. Introduction

1.1 Broader context and motivation

Over the geologically short time that we as a species have spent on earth, we constantly adapted to face and master new challenges. We did so quite successfully to come to the state that our civilizations have reached today. This process is often pictured to have started from a state where humans have been in harmony with nature, in other words from a romantic state of sustainability. Quite the contrary, more recent research indicates that even early human beings were not only able to *adapt to* their environment but also *adapted their environment* on unprecedented and potentially devastating scale through predation and the use of fire.^[1]

Since then, technological advancement and population growth have expanded our radius of influence to the point that we impact the whole planet.^[1,2] As a result the consequences of our manipulations are becoming harder to ignore in this day and age, manifesting in numerous fields from the aggravation of weather phenomena^[3] and the change of oceanic currents^[4] to pushing whole sets of species to the brink of extinction (and beyond).^[5]

While we do face great challenges in a complex network of interactions and agendas today, we have also reached a state of technological advancement and understanding that gives us the opportunity to work towards and even achieve a sustainable lifestyle *for the first time*. Consequently, sustainability is one of the great topics of our time – indeed it may be the one grand challenge of this age.

Chemistry is the foundation of the high standard of life that our society has achieved. Its products have high impact on all levels of society, and many fields relevant to the improvement of sustainability are dependent on chemical products, among them batteries and other energy storage technologies.^[6] Therefore, the key to reconcile the needs of a sustainable society with the standard of life of our society is in the hands of the chemist. In order to advance energy storage technologies in conjunction with the sustainable synthesis of their components it will be necessary to improve existing approaches, implement new strategies and sometimes to rediscover reactions that were used before the advent of oil-based chemistry.



Figure 1: Sustainability must be a unifying principle of both synthesis and application. Figure inspired by bikablo-publications (www.bikablo.com).

This work is dedicated to a special class of substances that shows promise in many sustainable applications: ionic liquids (ILs). Especially in the field of battery research, ionic liquids have been praised for their unique characteristics (cf. chapter 1.3.2). In order to unfold the full potential of ionic liquids, however, sustainable synthesis is equally important. Unfortunately synthesis of ILs is not usually carried out in a sustainable way. Imidazolium ionic liquids (ImILs) are a special class of ionic liquids in this regard, because to this day their commercial synthesis is based on the *modified Debus-Radziszewski reaction* (mDRr), which allows the formation of the imidazolium ring in its already quaternized form. This sustainable approach to ImIL synthesis predates petro-chemistry and supersedes the need for alkylation reactions or use of halogenated chemicals.

In order to change the way society impacts ecology, sustainability must become a unifying concept of the way we address the challenges of modern life. This work combines the use and improvement of known approaches for the sustainable synthesis of imidazolium compounds with the implementation of new strategies to explore and expand their application in energy storage. The rare opportunity to bring together a sustainable approach in synthesis of ionic liquids with applications in green chemistry is the concern of the following thesis.

1.2 Outline of this work

This work deals with the sustainable synthesis of imidazolium based molecules by the modified Debus-Radziszewski reaction, their modification and their application in next-generation batteries.

The capabilities of the mDRr for the synthesis of imidazolium based molecules will be explored in chapter 2. It allows the design of cations with different functionalities to produce both ionic liquids and zwitterionic molecules. Using different acids in synthesis also allows the incorporation of different anions without metathesis reactions. Finally, using linear diamines in conjunction with molecules with more than two amino groups, the modified Debus-Radziszewski reaction will be used for the synthesis of polyelectrolyte networks.

The so obtained crosslinked polyelectrolytes incorporate the imidazolium moiety into the backbone of their structure. Chapter 3 will focus on the investigation of the applicability of these novel materials for the fabrication of anion conducting membranes. The high charge density of the cationic network obtained allows said membranes to block the transition of cations while permitting the transition of anions. Consequently charge sensitive membranes could be fabricated from renewable resources.

Finally, chapter 4 will focus on the electrochemical applications of imidazolium based systems. Electrochemical properties of imidazolium based ILs will be discussed. A crucial limitation of imidazolium cations in this regard is the reactivity of the C2-position. Unfortunately the modified Debus-Radziszewski reaction does not allow the facile protection of said position. This chapter will show how protection of the C2-position by formation of a liquid zwitterionic species after ring formation results in improved properties. After suppressing the reactivity of the C2-position, the imidazolium based compound demonstrates promising applicability in magnesium electrochemistry.

1.3 Basic concepts

1.3.1 Why green chemistry?

Over the 20th century fossil feedstocks have become the major driving force of our technological advancement. They offered cheap and abundant fuel for transportation and allowed the everyday use of electricity. This was accompanied by the optimism that alternatives to the use of fossil (and other finite) feedstocks would be found and that any limitation would be overcome by virtue of science. New energy sources would be found and the prosperity that follows would eventually spread to all parts of the world.^[7]

While science and especially chemistry along with the use of fossil feedstocks have not only tremendously increased our quality of life but have even transformed the way our society works with the development of modern computers, transportation and medical breakthroughs^[7], we know today that not all of those dreams did come true. We did not overcome our addiction to depleting and non-renewable resources, and prosperity did not spread over the whole world. Instead we also face the negative effects of the extensive use of fossil feedstocks, in the shape of climate change: rising temperature, the increase in frequency and severity of droughts, heat waves and hurricanes.^[3]

So, why green chemistry?

Chemistry needed a new mindset to face the problems of a society that wants to prosper without destroying its environment. Since the use of fossil and other non-renewable feedstocks negatively affects the environment, a straight forward approach to improve the situation is the use of renewable resources. In fact, this gives rise to the possibility of a *sustainable chemistry*, which is one of the first concepts related to *green chemistry*:

"Sustainable chemistry is a scientific concept that seeks to improve the efficiency with which natural resources are used to meet human needs for chemical products and services. Sustainable chemistry encompasses the design, manufacture and use of efficient, effective, safe and more environmentally benign chemical products and processes."^[8]

This is the official definition as given by the European Organization for Cooperation and Development (OECD). The use of non-depleting resources is one important step for a chemical industry that serves a society that wants to both satisfy its everyday desires and keep its environment healthy. However, due to the special requirements of chemistry, the use of renewable resources alone is not enough.

In the 1989 textbook *Green chemistry. Theory and practice*, Paul Anastas and John Warner describe the concept of *sustainability* as “[...] the ability to maintain the development of the quality of life while not compromising the ability of our progeny to do the same.”^[9] This aspect is important because it stresses the responsibility (of chemistry, in this case) beyond the use of resources. The authors further elaborate that the prevention of waste is central to the protection of the environment and define *green chemistry* as “[...] the utilization of a set of principles that reduces or eliminates the use or generation of hazardous substances in the design, manufacture and application of chemical products” while mindfully acknowledging that “[...] all of the advances and innovations towards this goal will contain some discrete risk.”^[9] This definition captures the mindset needed for a chemistry that serves both society and the environment. The *set of principles* the authors refer to are the famous *12 Principles of Green Chemistry* (cf. Table 1). The principles give practical advice on how to do green chemistry and will be held as the canon of rules to determine the *greenness* of synthetic approaches in this work.^[9]

Table 1: The Principles of Green Chemistry, as given in the Book by Anastas and Warner^[9] and their shortened names as depicted in the green chemistry pocket guide^[10].

12 Principles of Green Chemistry

| | |
|-----------------------------------------------------------------|--------------------------------------------------------------------------------------------------------------------------------------------------------------------------------------|
| 1 – waste prevention | It is better to prevent waste than to treat or clean up waste after it is formed. |
| 2 – atom economy | Synthetic methods should be designed to maximize the incorporation of all materials used in the process into the final product. |
| 3 – less hazardous synthesis | Wherever practicable, synthetic methodologies should be designed to use and generate substances that possess little or no toxicity to human health and the environment. |
| 4 – design benign chemicals | Chemical products should be designed to preserve efficacy of function while reducing toxicity. |
| 5 – benign solvents & auxiliaries | The use of auxiliary substances (e.g. solvents, separation agents) should be made unnecessary wherever possible and innocuous when used. |
| 6 – design for efficiency | Energy requirements should be recognized for their environmental and economic impacts and should be minimized. |
| 7 – use of renewable feedstocks | A raw material or feedstock should be renewable rather than depleting, wherever technically and economically practicable. |
| 8 – reduce derivatives | Unnecessary derivatization (blocking group, protection/deprotection, temporary modification of physical/chemical processes) should be avoided whenever possible. |
| 9 – catalysis (vs. stoichiometric) | Catalytic reagents (as selective as possible) are superior to stoichiometric reagents. |
| 10 – design for degradation | Chemical products should be designed so that at the end of their function they do not persist in the environment and break down into innocuous degradation products. |
| 11 – real-time analysis for pollution prevention | Analytical methodologies need to be further developed to allow for real-time, in-process monitoring and control prior to the formation of hazardous substances. |
| 12 – inherently benign chemistry for accident prevention | Substances and the form of a substance used in a chemical process should be chosen so as to minimize the potential for chemical accidents, including releases, explosions and fires. |

comprise a very large and diverse class of substances with different characteristics. One thing ionic liquids do have in common is their negligible vapor pressure, which is a consequence of their ionic nature. Most ILs also share a characteristic derived from their low vapor pressure: While volatile molecular solvents lead to air contamination, the low vapor pressure of ionic liquids cancels this and, since no flammable vapors can be formed, also decreases the flammability of most ionic liquids even at relatively elevated temperatures^[14]. Beyond this, however, the characteristics of ILs can be virtually anything from edible^[15] to toxic.^[16] A second characteristic that is attributed to the whole of ILs is the ability to tune them to their application. This is usually done by mindful choice of the respective anions and cations.^[14] Figure 2 gives an overview about relevant cations and anions. The cations depicted in Figure 2 can be further diversified by different substitution patterns. Together with the large number of available anions, myriad combinations are possible. Indeed the number of possible ionic liquids is estimated to be at least a million (counting binary combinations only).^[17] In order to tune the characteristics of an IL, as a general rule of thumb, the anion is often seen responsible for tuning the physics and the cation for the chemistry.^[17,18] Following this rule, it is possible to transform an ionic liquid from hydrophilic to hydrophobic by exchanging the anion from an acetate to the bis(trifluoromethylsulfonyl)imide anion.^[19] Fine tuning of ILs can be achieved by variation of the cation type (e.g. ammonium, pyrrolidinium, imidazolium) or the length and type (alkane, alkene, ether) of pendant chains, e.g. to optimize dissolution power, mass transport related characteristics or range of liquidity.^[20–22]

The chemistry of an IL is usually influenced by introduction of functional groups into the cation such as ethers for complexation purposes^[23], redox active groups^[24] or reactive groups for the synthesis of poly(ionic liquids) (PILs)^[25]. Modification of the anions is usually limited to the exchange of existing ions through anion metathesis^[19,26], although functionalized anions are known, such as ethersulfates^[27] and -carboxylates^[28], or amino acids^[29].

1.3.2.2 Promise and pitfalls of ionic liquids as agents of green chemistry

The great promise of ionic liquids as agents of green chemistry lies in their characteristics and consequently their applications. Generally ILs are applied in various fields, such as synthesis and catalysis^[30–32], biomass treatment^[20,33], as well as energy storage and conversion^[34]. ILs are also used in large scale industrial processes, such as the BASIL™ process (where they act as separation agents)^[17,35], the production of ϵ -caprolactam^[36], or in general to aid catalysis or catalyze organic reactions themselves, even allowing stereocontrol^[30,37]. Due to the IL's inherent low vapor pressure, this can take place without the typical atmospheric contamination or the dangers incurred by pressure build up in closed systems at elevated temperatures. Figure 3 illustrates their use in different fields of chemistry. As such, ILs comply with the principles of green chemistry, such as *Less Hazardous Synthesis* (3), *Benign Solvents and Auxiliaries* (5), *Reduce Derivatives* (8), *Catalysis (vs. Stoichiometry)* (9), *Inherently Benign Chemistry for Accident Prevention* (12).

However, ILs are very diverse and not every single one can keep up with the above. Consequently, the great number of possible combinations and the degree of tunability of ILs has led to the concept of *task-specific* ionic liquids (TSILs) or *designer ILs*, which elevate ionic liquids beyond specialized solvents by grafting task-crucial moieties onto the ionic liquid. It has also been pointed out that the greenness of ILs is not a given fact, but must be evaluated critically. This should include life cycle analysis (from synthesis to disposal) as

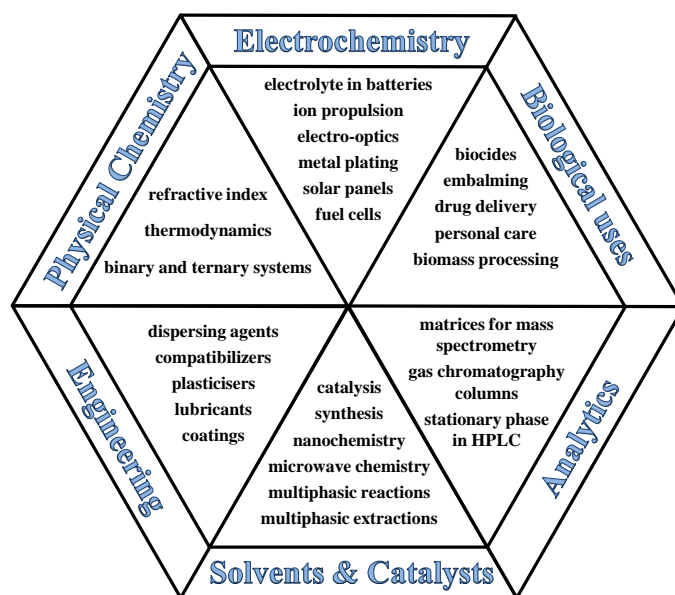


Figure 3: Applications of ILs in different fields of Chemistry based on their characteristics. Reproduced from reference^[17] with permission of The Royal Society of Chemistry.



Figure 4: Schematic representation of traditional ionic liquid synthesis by quaternization and subsequent metathesis. Please note that the starting material may already be the result of longer synthetic routes.

well as a sound analysis of toxicity, risk evaluation, bioaccumulation and the like. The main pitfall of ILs as green chemical agents lies in their synthesis, which is usually carried out as a multistep reaction as illustrated in Figure 4.

From a suitable starting material (neutral species) the cation is obtained via alkylation.^[38] This step also releases the anion of the IL intermediate to satisfy charge balance. The so obtained IL intermediate is usually a halide (or sometimes a methanesulfonate or p-toluenesulfonate) salt, industrially often a chloride.^[39,40] This is unsuitable for many applications (due to the corrosivity, the usually high viscosity, etc.). Consequently, tuning of the physical characteristics needs an additional step and often proceeds through anion metathesis followed by dialysis.^[38,40,41] Anion metathesis is realized by adding a suitable salt of the desired anion to the IL intermediate. In some cases the change of anion introduces the formation of a second phase, if a hydrophilic anion is exchanged by a hydrophobic one. In those cases the ionic liquid product can be obtained more elegantly without extensive dialysis, but must still be thoroughly washed to remove the residual salt that is formed as the by-product of metathesis.^[19,30,32,42]

The use of this multi-step approach is problematic since alkylation and metathesis suffer from bad atom economy and the use of usually non-green solvents. Another disadvantage of multistep reactions is the necessity to purify the products after each step. Furthermore the starting material is mostly obtained from fossil feedstocks, which is a general problem of organic chemistry. Together, this violates basically every *Principle of Green Chemistry*. In order to classify as true agents of green chemistry, ionic liquids must be produced by green chemistry and then applied for green chemistry.

1.3.2.3 Benign cation synthesis

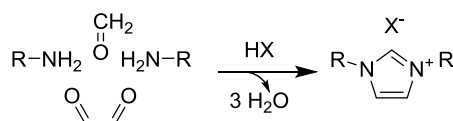


Figure 5: Simplified reaction scheme of the modified Debus-Radziszewski Reaction.

In response to the lack of green chemistry in ionic liquid synthesis, several approaches have been developed. One such approach is to derive ILs from naturally occurring molecules such as choline^[43], nicotine^[44] and amino acids^[29]. This is appealing because the starting material is at least theoretically obtainable from natural resources. Another benefit is the possibility to make use of existing molecular complexity, as opposed to building it up. Unfortunately, even in this case alkylation and metathesis reactions usually play their part. In addition the use of existing structures can limit the chemical tunability of the resulting molecules. On the other hand, there are approaches to build up cations from smaller molecules without the use of alkylation reactions by utilization of ring formation reactions.^[19,26,45]

This work will make use of the modified Debus-Radziszewski reaction¹ (mDRr), as discussed below. The simplified reaction scheme of the mDRr is depicted in Figure 5. It releases three equivalents of water and thus classifies as a condensation reaction. It has been shown that the conversion can be driven forward by tuning the stoichiometry, which makes it an attractive candidate for polymerization reactions.^[46,47] It is noteworthy that to this day, industrial synthesis of imidazole and alkylimidazoles^[48,49] is still based on the work of Debus^[50] and Radziszewski^[51] dating back over 130 years and several approaches to produce imidazole and imidazolium compounds with various substitution patterns and tolerance to manifold organic functionalities have been developed using this elegant procedure or similar ring-forming reactions.^[26,45,52,53,54]

Although Figure 5 may imply a concerted reaction, the Debus-Radziszewski reaction is assumed to be a multi-step reaction^[48] as depicted in Figure 6. Different mechanisms have

¹ There are several synthetic approaches that qualify as modified Debus-Radziszewski reactions. However, in this work, only the direct synthesis of imidazolium cations from two equivalents of an amine, one equivalent of a carbonyl and a 1,2-dicarbonyl compound in the presence of weak acid will be referred to as mDRr.

been proposed for the modified Debus-Radziszewski reactions (v.i.), starting from nucleophilic attack of the nitrogen at either the carbonyl^[47] or the dicarbonyl compound^[49,55].

Figure 7 illustrates the appeal of the mDRr. The upper part of the figure shows a simplified route from the basic chemicals available for industrial production of methyl-butyl imidazolium acetate by use of a variation of the original Debus-Radziszewski reaction to form methyl imidazole and subsequent alkylation followed by anion metathesis. The lower part of the figure shows the direct synthesis of the comparable butyl-butyl imidazolium acetate by modified Debus-Radziszewski reaction without the use of alkylation or metathesis.^[56] By simply exchanging primary amine and ammonia used in the alkyimidazole synthesis of the standard procedure to the use of two primary amines and adding a weak acid such as acetic acid, the synthesis can be reduced from 29 steps to 17 steps. Also the multi-step imidazolium formation approach can be replaced by a one-pot procedure, reducing the number of work-up steps. It is immediately obvious that direct synthesis of the quaternized product without need for alkylation is far more efficient and thus greener. Figure 7 assumes that the educts are derived from fossil feedstocks, which is not necessarily the case. Acetic acid is also produced industrially by fermentation^[57]. Formaldehyde is derived from oxidation of methanol, which is in turn available from biomass^[58] or waste products^[59] (even though the industrial process

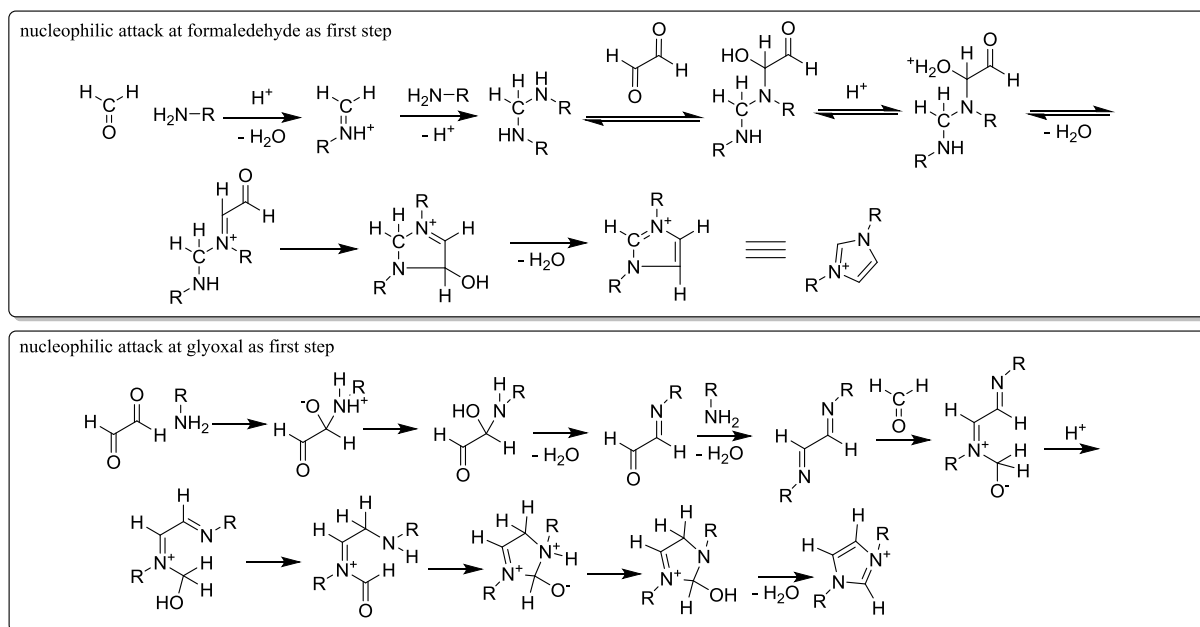


Figure 6: Proposed reaction mechanisms of the modified Debus-Radziszewski reaction. Upper part: nucleophilic attack of the amine at the formaldehyde as the first step (adapted from Dani et al.^[47] with permission of the Royal Society of Chemistry). Lower part: nucleophilic attack of the amine at the glyoxal as the first step (adapted with permission from Krannig et al.^[55], copyright 2014, American Chemical Society and adapted from Wang^[49] with permission of John Wiley and Sons).

relies on synthetic gas^[60]). Glyoxal can be obtained from acetic aldehyde industrially^[61] which may be obtained from ethanol in turn.^[62] Additionally, substitution of glyoxal with other dicarbonyl compounds, such as pyruvaldehyde has been reported.^[45,47] Pyruvaldehyde is obtainable from glycerol^[63] or as a byproduct of lactic acid production from fructose^[64]. Amines, carrying manifold chemical functionalities, are usually produced industrially from the corresponding alcohols^[65], but may also be obtained from aldehydes^[66] which opens the door for many naturally occurring molecules, as well as alcohols from other sustainable sources such as food waste^[67] in addition to substrates that innately carry amino groups, such as amino acids.

This highlights the great potential of the modified Debus-Radziszewski reaction to produce task-specific ionic liquids *from* green chemistry, even if industrialized pathways to chemicals are not always innately green. Concerning the use in research, the mDRr has also been shown to be realizable with a flow-reactor setup and easily upscalable if conducted in batch, which makes it a robust and convenient reaction on the lab-scale.^[26,54]

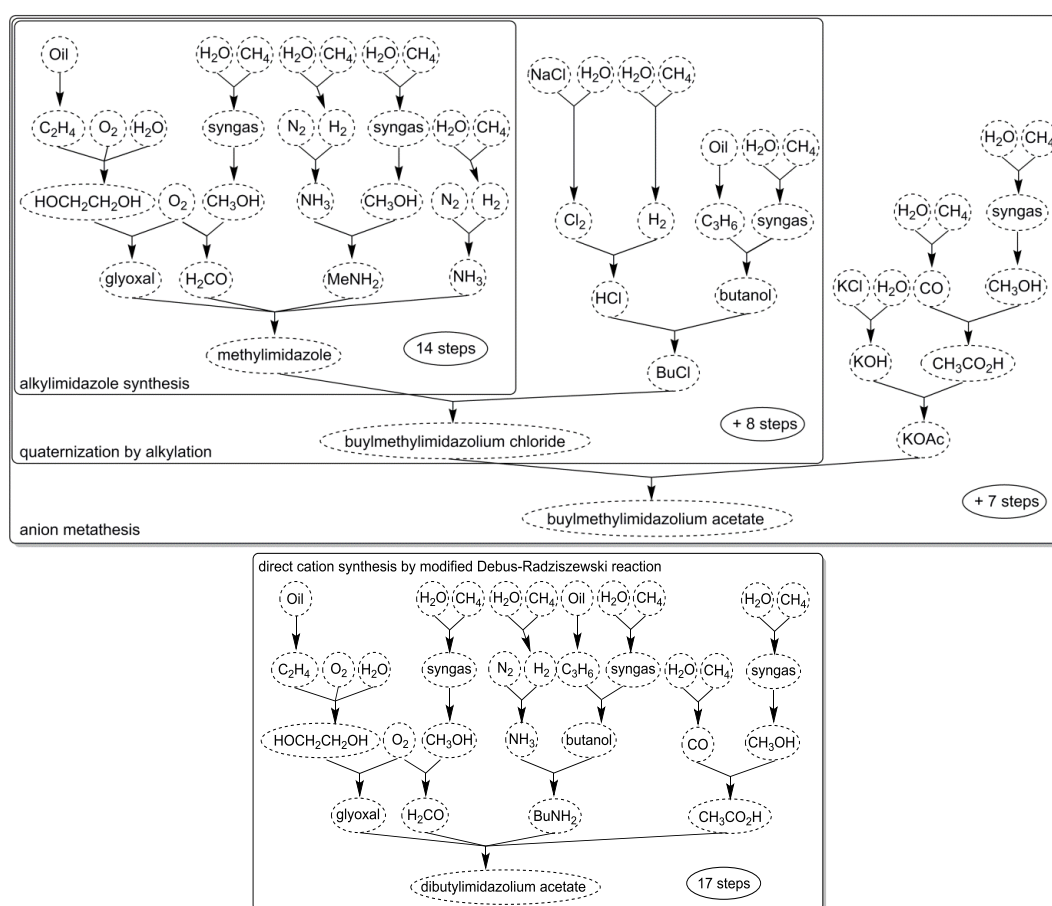


Figure 7: Upper part: Synthetic steps to the ionic liquid butyl-methyl imidazolium acetate: Synthesis of methylimidazole followed by alkylation and anion metathesis. Lower part: Synthesis of the similar ionic liquids butyl-butyl imidazolium acetate by modified Debus-Radziszewski reaction to directly yield the product IL. Adapted and from Jessop^[56] with permission of the Royal Society of Chemistry.

1.3.3 Energy storage *beyond lithium*

The development of laptops, smartphones and related gear is founded on the lithium-ion technology for power supply.^[68] State of the art lithium-ion batteries (LIBs) allow for fast charge, high capacity and long cycling ability, which even makes them viable for mobile transportation.^[68,69]

However, the lithium-ion technology faces major challenges related to safety, capacity and the resources used to produce it. In order to overcome those challenges and improve the sustainability of mobile energy supply in times of an increasing demand of both the number of batteries and their capacity, technologies beyond the lithium-ion battery are needed. One of those post-lithium approaches is the development of magnesium based batteries. The following subchapters are aimed to show why we need post-lithium technologies, the promise of magnesium in post-lithium applications and the beneficial role of ionic liquids in magnesium battery research.

Lithium in itself is a very reactive metal. It reacts with oxygen, water and even nitrogen at room temperature. When burning or molten, lithium will even be reactive towards carbon dioxide and silicates (such as concrete),^[70] which will have to be considered if lithium should be used in electric cars on a large scale. When it comes to lithium-ion batteries, safety concerns relate to the fact that they can be subject to battery fires. The low reduction potential (ca. -3.0 V vs. normal hydrogen electrode, NHE) and high capacity (3862 mAhg^{-1} or 2061 mAhcm^{-3}) of lithium metal^[71] make it an excellent material for battery applications. Unfortunately its tendency to form dendrites upon cycling which can cause a short circuit in the battery^[72] severely limits its applicability. Consequently rechargeable lithium-ion batteries do not use lithium metal and instead are based on lithium-ions cycled between two intercalation electrodes. This severely limits the realizable capacity (e.g. 372 mAhg^{-1} or 837 mAhcm^{-3} for a carbon intercalation electrode LiC_6),^[71] which is further limited by non-active material such as casing. Even in Li-ion based systems, battery fires are still a concern and can be caused by dendritic growth, as shown by the battery fires in Samsung Galaxy S7 smartphones^[73], or by thermal runaway as brought to attention by the support battery of a Boeing 757 catching fire in flight^[73]. The use of flammable carbonates as solvents further adds to this problem.^[73] Electrolyte systems may be developed to mitigate this through additives or the use of non-flammable and non-volatile solvents, but due to the generally advanced state of development of the Li-ion technology, the increase of capacity in said

batteries is reaching its limits^[68] and the gap between the energy needed for more powerful devices and the state-of-the-art technology widens.^[71]

The last concern about lithium batteries relates to their raw materials. Lithium itself makes up about 0.006% of the earth's crust by weight and is as such not among the more abundant elements. Furthermore, lithium is not found in dedicated lithium minerals, but as a side product in magmatic minerals and, more importantly, continental brines.^[70] Next to lithium as the critical raw material for the fabrication of a lithium-ion battery, other elements are needed, such as nickel, cobalt and manganese.^[74] Among them especially cobalt has roused public interest recently, due to the involvement of precarious working conditions and child labor into its supply chain.^[75]

1.3.3.1 Magnesium batteries

One way to tackle the challenges related to lithium-ion batteries is the use of other active materials. In this regard, magnesium has received significant interest.

The first advantage of magnesium is its high abundance. It is by three orders of magnitude more abundant in the earth's crust than lithium (2.1 % magnesium vs. 0.006 % lithium by weight).^[70,76] This means that both the cost of magnesium batteries and their impact on society and ecology possibly undercut lithium based systems. Since magnesium batteries are still in the process of development, a direct comparison to commercial lithium-ion battery cathodes is not possible. However, the cathode materials subject to research are mostly based on chevrel phases and other molybdenum based systems, as well as vanadium oxides and sulfur compounds. The mentioned cathodes are usually cobalt-free.^[77]

In terms of capacity, magnesium possesses lower specific capacity than lithium (2205 mAhg⁻¹ vs. 3862 mAhg⁻¹, respectively) but almost double the volumetric capacity of lithium (3832 mAhcm⁻³ vs. 2061 mAhcm⁻³).^[71] Also it should be kept in mind that lithium metal anodes are not used in rechargeable batteries due to formation of dendrites, which cancels the advantages of their theoretically high specific capacity. In contrast to this, the current scientific opinion is that magnesium does not form dendrites, which allows the use of magnesium metal anodes and taking advantage of their high capacity.^[78] The redox potential of magnesium, albeit higher than that of lithium, is still low enough to fabricate high voltage batteries (-2.3 V for magnesium vs. -3.0 V for lithium both vs. NHE).^[71] The high volumetric capacity in conjunction with the low redox potential make magnesium a good pick for battery

applications where smaller size trumps lower weight, such as in mobile devices like smartphones.

When it comes to safety, magnesium is much more benign than lithium. First of all, while magnesium can be very reactive, such as in the case of Grignard reagents, it quickly passivates in contact with reducible species, such as water, due to the formation of protective magnesium hydroxide films. It is also able to form stable films based on oxides and fluorides which renders it resistant to fluorine compounds including hydrofluoric acid.^[76,79,80] As such, magnesium is much safer to handle than lithium.

Due to the advantages of magnesium in terms of abundance, safety and capacity, it has received attention as a post-lithium alternative for energy storage. The first successful attempt at plating and stripping magnesium was published 1927, using Grignard reagents. The key problems related to those electrolytes were low electrochemical stability and low conductivity.^[81] After this, the field received little interest until the development of organoborate based electrolytes for magnesium in 1990 by Gregory et al.^[82] and the use of organohaloaluminate based electrolytes. The latter finally led to the first prototype of a rechargeable magnesium battery in 2000.^[83] State of the art research includes the use of organic and inorganic magnesium salts based on chloride^[84], bis(trifluoromethylsulfonyl)imide^[85] and hexamethyldisilazane^[86]. In addition to this, the use of borohydrides and magnesium carboranes has recently been shown to be highly promising.^[71,87-89]

The multitude of research in the field of magnesium batteries has shown that the main obstacles for the development of magnesium batteries are the absence of suitable cathodes and electrolytes.^[71,77,79,88] In terms of suitable cathodes, the bivalency of the magnesium ion and rather slow kinetics of its insertion into intercalation materials are seen as major problems.^[80] When it comes to the electrolytes, it has been shown that many anions known to produce good results in electrochemical applications, such as perchlorate, tetrafluoroborate and bis(trifluoromethylsulfonyl)imide, are insufficiently stable towards magnesium metal and similar problems have been reported for standard solvents such as carbonates.^[88] In this regard the ability of magnesium to form protective films on its surface becomes problematic, since those films are usually non-conducting for magnesium ions^[77,80] and trace impurities such as water can be detrimental for a magnesium battery^[85]. Due to those limitations, solvents in magnesium electrochemistry are often ethers such as tetrahydrofuran (THF) or dimethylethers of ethyleneglycols of varying molecular weight (glymes). While they are

electrochemically stable and able to solve most of the magnesium salts subject to research, they are also problematic due their toxicity and/or volatility.^[79,85,87–90]

1.3.3.2 Ionic liquid based electrolytes

On a general level, an electrolyte system consists of the electroactive species and a solvent. Additives are often mixed into the electrolyte system to improve its characteristics.^[73] This system should be (electro)chemically and thermally stable within a large operating window. It must be compatible to other parts of the battery (i.e. non-corrosive towards casing, current collectors, etc.) and should possess no or low volatility, flammability and toxicity. All the while, of course, facilitating transport and reaction of the electroactive species, which should possess decent solubility in the medium.^[80,88] Keeping in mind the principles of green chemistry, it should also be available from renewable resources. In the case of magnesium, special notice must be paid to the formation of passivating layers on the surface of the metal in the presence of common salts or solvents.^[88] In order to satisfy the prerequisites above, state of the art magnesium battery research uses electrolyte systems based on ethers (see chapter 1.3.3.1).

Taking the capabilities of ionic liquids into account, they have the potential to be a splendid match to the requirement profile of battery electrolytes due to their tunability and low volatility/flammability. Different ionic liquids have been tested for magnesium related applications with varying results. Magnesium could be deposited successfully from a methoxyethyl-substituted quaternary ammonium TFSI ionic liquid using magnesium TFSI in the presence of lithium TFSI^[91]. Even reversible plating and stripping was achieved using an ionic liquid mixture based on an ether substituted quaternary ammonium cations with a mixture of TFSI and bis(fluorosulfonyl)imide (FSI) anions after removal of trace water with magnesium borohydride.^[92]

Using a pyrrolidinium TFSI ionic liquid with polyethyleneglycol monomethylether sidechains of varying lengths and magnesium borohydride as the electrolyte, magnesium was successfully cycled.^[23] The appeal of ionic liquids in this case is the combination of their non-volatility and tunability. In this given examples, ether chains were grafted to the ionic liquids to allow chelation of magnesium and facilitate stable cycling.

When it comes to imidazolium ionic liquids, literature has seen conflicting publications about their use in magnesium electrochemistry.² Imidazolium ionic liquids with an unprotected C2-position (c.f. Figure 8), do not possess sufficient electrochemical stability to allow magnesium cycling. The stability of imidazolium cations to reduction can be assumed to be around -1.9 V vs. SHE. However, protection with a methyl group or similar alkyl chain has been shown to increase the electrochemical stability by up to 0.5 V to up to -2.4 V vs. the standard hydrogen electrode (SHE).^[96] This would theoretically allow magnesium cycling at low overpotentials. However, the viscosity of imidazolium ionic liquids usually increases upon C2-protection with alkyl chains^[21,97], which has negative impact upon the electrochemical performance due to the (fractional) Walden rule.^[98,99]

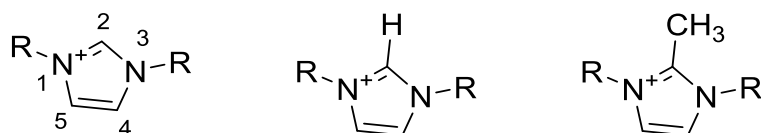


Figure 8: L.t.r: Numbering scheme for imidazolium cations; unprotected imidazolium cation (C2-position carries a proton); imidazolium cation protected by a methyl group at the C2-position.

² Several publications^[93,94] have claimed the successful application of imidazolium ionic liquids, but the results were not reproducible by other groups^[95].

2 Ionic liquids and solids *via* modified Debus-Radziszewski reaction

2.1 General considerations

The modified Debus-Radziszewski reaction (mDRr) is an efficient way to synthesize imidazolium based molecules. It is easy to handle, realizable with a flow-reactor setup and can be conducted below, at and close to room temperature. Even better, the mDRr can make use of simple and sustainable starting materials for the synthesis of task-specific ionic liquids and other molecules. The aim of the following chapters is to show how different design strategies can be used to tune the characteristics of ionic liquids and solids obtainable from this approach. By doing so, the variability of the mDRr and its tolerance towards a wide array of different functionalities and reaction conditions will be demonstrated.

In this work, three design strategies for imidazolium synthesis will be discussed. As shown in the introduction (cf. Figure 5, p. 13; Figure 6 p. 14), the mDRr must be conducted in the presence of an acid to provide protonation and maintain charge balance. The acid present will be transformed into the counterion of the synthesized imidazolium moiety. The first design strategy (*direct anion tuning*) utilizes this to tune the characteristics of the ionic liquid by mindful choice of the acid (and as such the resulting counterion). This approach allows to skip or simplify further metathesis steps that are often part of traditional tuning schemes (cf. chapter 2.2).

The other two approaches focus on cation-design. On one hand, the *N*-substitution pattern can be controlled by use of different amines in the mDRr. On the other hand, the carbonyl compounds can theoretically be used to influence the *C*-substitution pattern of the imidazolium ring. Both strategies will be discussed in this work. However, controlling the *N*-substitution pattern is much more straight-forward and will be the focus of this work. Using different starting material with one amino group, it is possible to produce various imidazolium compounds, with various functionalities and in doing so to tune the physical characteristics over a wide range (cf. chapter 2.3).

Making use of starting material with more than one amino group, it is possible to use the same synthetic approach to produce polyelectrolytes and polyelectrolyte networks. In contrast to most poly(ionic liquids) (PILs), the resulting products are main chain imidazolium polymers.

The synthesis of polyelectrolyte networks (PENs) will be discussed in chapter 2.4. The different design strategies used in this work are illustrated in Figure 9.

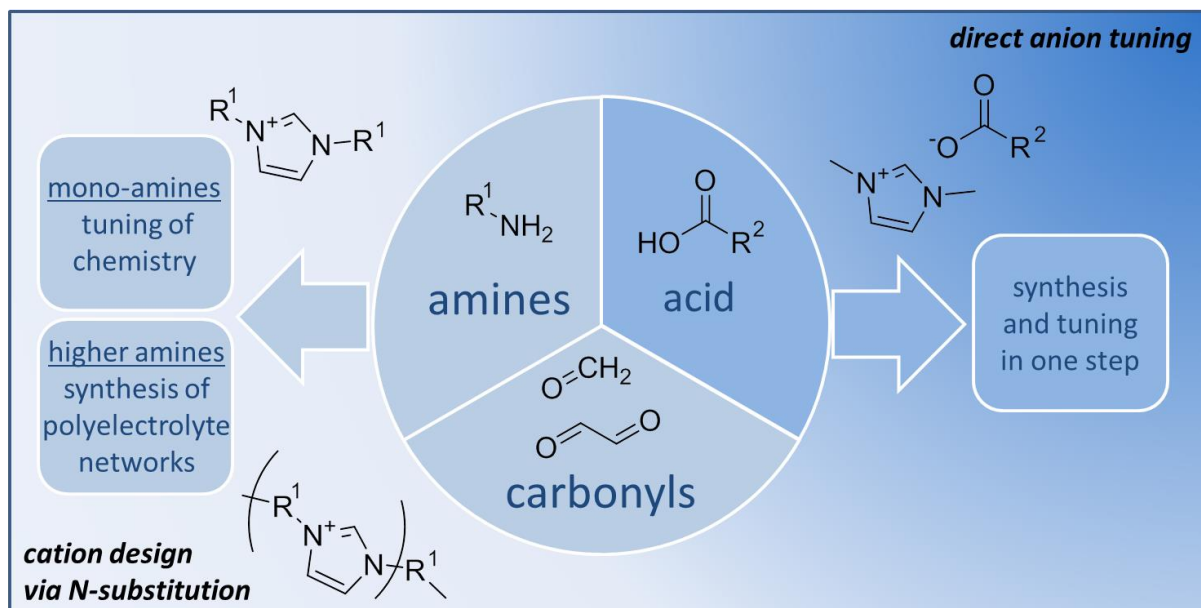


Figure 9: Overview of the synthetic approaches chosen in this work.

2.2 Direct anion tuning³

Standard ionic liquid synthesis follows the multi-step approach that is illustrated in Figure 4 (p. 12). In typical quaternization reactions that proceed *via* alkylation, the leaving group of the alkylating agent will become the counterion of the ionic liquid intermediate. This limits the products to halides and in some cases sulfonates (such as methanesulfonate).^[38] Synthesis *via* mDRr on the other hand follows a different route and directly yields the fully formed imidazolium ring in the presence of an acid. This acid is transformed into the anion of the resulting ionic liquid during the reaction. Since the number of available acids is much larger than the number of typical leaving groups in alkylating agents, this increases the number of directly available cation/anion combinations. Making use of this allows tuning the characteristics of the resulting ionic liquid *via* direct synthesis. With this, the mDRr becomes an all-in-one approach that shortcuts towards the IL product as illustrated in Figure 10.

In line with the general concern of this work, the chosen starting material represents a combination of functionality and sustainability. Tetrahydrofurfurylamine is an interesting molecule in this regard, as it is usually obtained from furfural *via* reductive amination e.g. over nickel catalysts. Furfural is obtained from agricultural wastes such as sugar cane bagasse or corncobs^[101]. This molecule was chosen because tetrahydrofuran (THF) is used in a wide array of applications from biomass treatment to electrochemistry.^[88,89,102] The incorporation of a THF-moiety into an ionic liquid has the potential to combine the non-volatility of ILs with the solvent/ligand qualities of THF. In conjunction with the renewable character of the resources used, this can produce safer, tunable green molecules to substitute THF. Glyoxal and formaldehyde, used in the synthesis, have been discussed already (cf. chapter 1.3.2.3). In order to test the capabilities of the mDRr to combine synthesis and tuning in one pot, a small

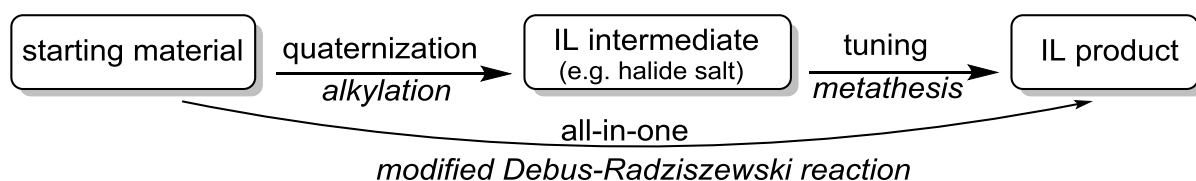


Figure 10: Schematic of traditional ionic liquid synthesis and the short-cut available through use of the modified Debus-Radziszewski reaction. Please note that the starting material may already be the product of longer synthetic routes.

³ Parts of this chapter have been published^[100]. Data and figures presented in this chapter are therefore taken from this reference.

library of ionic liquids was synthesized by variation of the acids present during reaction (synthesis see chapter 6.2). The reaction follows the simplified scheme shown in Figure 11. Several acids were chosen based on their pK_A , the relevance of the resulting counterion and their availability from green sources. Yields and general information about the synthesis are given in Table 2.

The synthesis was always carried out under the same conditions and as such the influence of the acid (and its pK_A) on yield and success of the reaction can be evaluated. Figure 12 summarizes the yield as a function of the acid constant. The acids used differ in their molecular structure, the number of acid groups and their pK_A value. In absence of functional groups that react with any of the other reactants (apart from acid-base reactions), it will be assumed that the main influence of the acid results from the pK_A value. The reaction generally gives good to excellent yields. The highest yield is obtained using acetic acid with a pK_A value of 4.756. Generally, lower values of the acid constant seem to negatively affect the yield. As seen in the case of tartaric and succinic acid it may also be possible that the presence of several acid groups per molecule negatively effects the yield. The negative effect of strong acids on the mDRr has been documented in literature.^[26] Depuydt et al. attributed the negative effect of e.g. hydrochloric and sulfuric acid on the yields of the mDRr to the formation of ammonium based side products due to the protonation of the amine used for the reaction.^[26] However, it is also known that glyoxal and formaldehyde are not stable in the presence of strong acids such as hydrochloric acid.^[103] Side reactions and degradation of the carbonyl compounds must consequently be considered to explain the lower yield at decreasing pK_A value. Overall, however, the reaction is robust towards acids since even at a pK_A value of -7 a yield of 73.6 % is obtained, although the pure product cannot be isolated. As illustrated in Figure 5 (p. 13), the reaction requires the presence of an acidic compound to provide one free proton per turnover. This explains the incompatibility of boric acid with the mDRr: the pK_A value is too high – the acid too weak to protonate the molecule at the necessary steps.

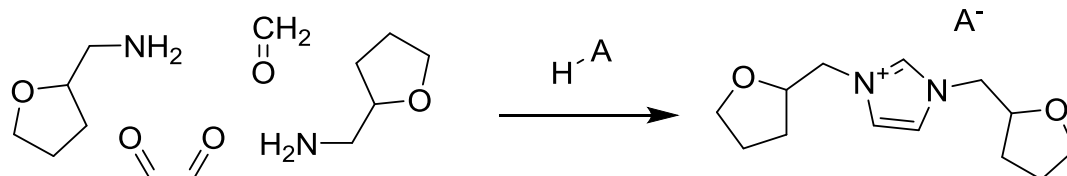
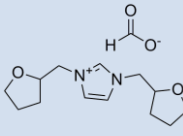
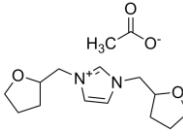
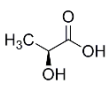
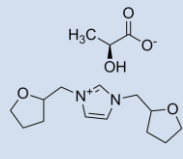
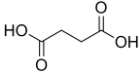
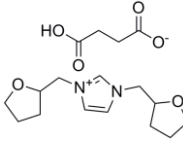
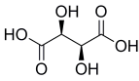
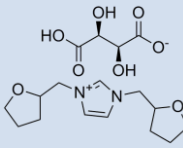
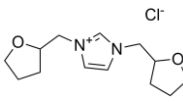


Figure 11: Reaction scheme for the modified Debus-Radziszewski reaction as used in this chapter.

Table 2: Overview of the anion/cation pairs obtained from direct synthesis. Notes: a) yields obtained by NMR-analysis; b) taken from reference^[104]; c) taken from reference^[105]; d) no pure product could be isolated.

| acid used | pK _A of acid group(s) | yield ^a | code | ionic liquid structure |
|---------------------------------------------------------------------------------------------------------|-----------------------------------------------------|--------------------|--------------|---------------------------------------------------------------------------------------|
| formic acid  | 3.75 ^b | 86.3 | THF-1 |  |
| acetic acid  | 4.756 ^b | 96.7 | THF-2 |  |
| L-lactic acid  | 3.86 ^b | 93.6 | THF-3 |  |
| succinic acid  | 4.21 ^b /5.64 ^b | 87.7 | THF-4 |  |
| DL-tartaric acid  | 3.03 ^b /4.31 ^b | 80.7 | THF-5 |  |
| hydrochloric acid HCl | -7 ^c | 73.6 ^d | THF-6 |  |
| boric acid | 9.27 ^b / ^{>} 14 ^b | no reaction | THF-7 | no reaction |

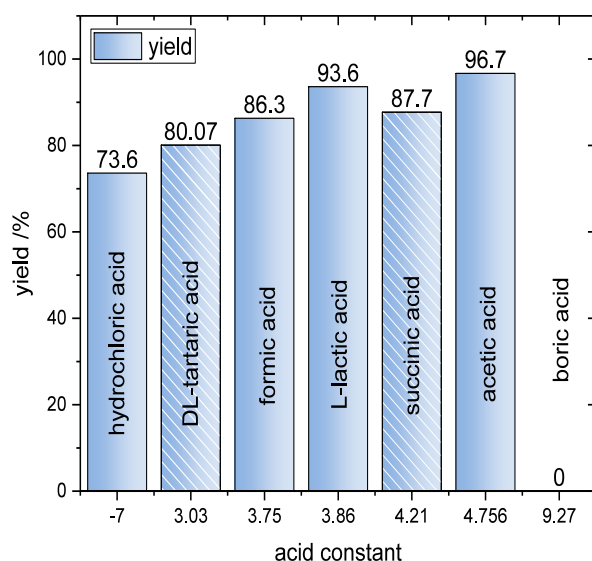


Figure 12: Yield of the mDRr as a function of the pK_A values. Acids with more than one acid function are marked with the diagonal pattern and indexed with their lower pK_A value. Please note that the x-axis is not scaled.

The use of weak acids also allows to facilitate purification and, in the case of anions not available from weak acids, metathesis.^[26] In this regard especially acetic acid shows great potential. On the one hand, excess acid can be removed at reduced pressure due to the relatively high volatility of acetic acid. On the other hand, the acetate counterion can be protonated by strong acids to form acetic acid again, facilitating purification and removing the need for dialysis or similar extensive work-up of metathesis reactions.^[26]

Making use of the latter, the library of ionic liquids synthesized was extended by the hexafluorophosphate and the tetrafluoroborate anion.⁴ These ions are commonly used in

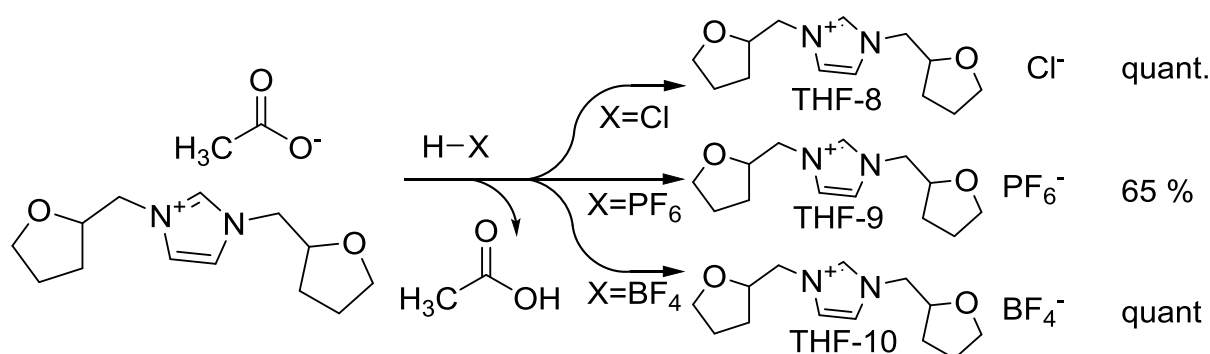


Figure 13: Metathesis reactions starting from the acetate based ionic liquid THF-2 yielding the chloride (THF-8), hexafluorophosphate (THF-9) and tetrafluoroborate (THF-10) ionic liquids.

⁴ cf. chapter 6.2

electrochemical applications, which makes the capacity of the synthetic approach to include those anions a relevant consideration. Since the product of direct synthesis with hydrochloric acid was impure, this scheme was also used to produce a pure version of anionic liquid with the chloride counterion. Figure 13 gives an overview about the metathesis reactions conducted.

In order to evaluate the influence of the anion on thermal stability of the resulting ionic liquid and also the capability of the direct synthesis approach of the mDRr to tune physical characteristics, the synthesized ion pairs were subjected to thermogravimetric analysis (TGA). Ionic liquids tend to form pronounced intermolecular interactions including hydrogen bonds^[106] and are often hygroscopic. In TGA, the first step of mass decrease may therefore be attributed to the evaporation of water. Indeed, thermogravimetric analysis coupled with mass spectroscopy (TGA-MS) reveals, that the only notable ion current below 200 °C is related to water in the case of THF-2 (Figure 14, left side⁵). The fact that water is released up to this very high temperature can be seen as a consequence and further verification of said bonding behavior that traps the water in the IL. Taking into account that mass loss below 200 °C is the result of water evaporation, the following order of stability is obtained for the different anions

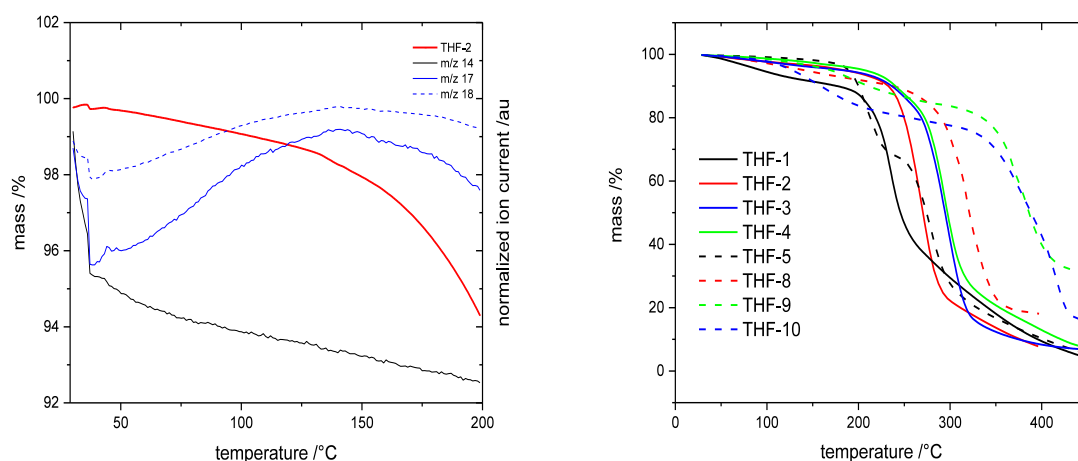


Figure 14: Left: TGA-MS measurement of THF-2 (heating rate: 2.5 Kmin⁻¹). The red line shows the mass trace upon heating. The blue curves represent the normalized ion currents registered at m/z 17 and 18, which refer to the hydroxyl and water radicals, respectively. The black line represents m/z 14, which can refer to the presence of CH₂⁺, CO²⁺, or a variety of other fragments and shows a curve typical for the other m/z measured. For brevity, only one curve is shown (cf. chapter 6.1 for all curves). Right: TGA curves of ionic liquids THF-1 through THF-10 (with the exceptions of THF-6 and THF-7); measurements conducted at 10 Kmin⁻¹. Different decomposition temperatures of compound THF-2 in both figures are a result of the different heating rates.

⁵ For brevity only relevant curves are displayed, cf. chapter 6.1 for more detailed graphs.

(cf. Table 4): tartrate (THF-5) < formate (THF-1) < acetate (THF-2) < lactate (THF-3) < succinate (THF-4) < chloride (THF-8) < tetrafluoroborate (THF-10) < hexafluorophosphate (THF-9).

Table 3: Thermal analysis: Number and temperatures of steps in TGA measurements (steps were determined using the maxima of the first derivative of the TGA-curve) and glass transition temperatures (derived from the inflection points of the glass transition) of the ILs THF-1 through THF-10.

| ionic liquid | TGA-steps | temperature [°C] (mass loss [%]) | glass transition temperature [°C] |
|--------------------------------|-----------|-------------------------------------|--------------------------------------|
| THF-1 – formate | 2 | 86.4 (8.71) | - 46.04 |
| | | 236.2 (88.43) | |
| THF-2 – acetate | 1 | 265.5 (88.4) | - 45.76 |
| THF-3 – lactate | 1 | 290.6 (94.38) | - 30.05 |
| THF-4 – succinate | 1 | 293.7 (93.93) | - 18.72 |
| THF-5 – tartrate | 2 | 207.9 (31.95) | + 18.78 |
| | | 280.1 (63.58) | |
| THF-8 – chloride | 2 | 133.9 (8.07) | - 12.38 |
| | | 318.9 (73.73) | |
| THF-9 – hexafluorophosphate | 3 | 161.6 (18.42) | - 47.24 |
| | | 374.6 (29.12) | |
| | | 418.1 (37.63) | |
| THF-10 – tetrafluoroborate | 3 | 196.4 (15.45) | - 26.24 |
| | | 368.2 (23.30) | |
| | | 383.5 (30.73) | |

Thermal decomposition of imidazolium based ionic liquids is dependent on the nature of the counterion. Ohtani et al. have shown that in the case of more nucleophilic counterions, such as halides, decomposition mainly happens through nucleophilic attack of the counterion at the sidechain of the imidazolium ring and resulting C-N bond cleavage. If there are different side chains, the sterically less demanding seems to be attacked first. In the case of less nucleophilic anions, such as hexafluorophosphate or tetrafluoroborate, thermal decomposition mainly occurs *via* thermal dissociation of the C-N bond: In this case, decomposition seems to favor the thermodynamically more stable product. In addition to this, decomposition of the anion may occur for more complex anions. In the case of hexafluorophosphate and tetrafluoroborate, this will release fluorine and result in the formation of fluorinated decomposition products. No significant products indicating the decomposition of the imidazolium ring itself could be detected by Ohtani et al. at temperatures up to 500 °C.^[107]

Table 4: Decomposition temperatures of the imidazolium ionic liquids based on organic acid anions (determined using the maxima of the first derivative of the TGA-curve) and of alkali salts with the same anions. Notes: a) taken from reference^[108] b) taken from reference^[109] c) taken from reference^[110] d) taken from reference^[111].

| ionic liquid | reference salt | | |
|-------------------|---------------------------------------------|---------------------------|-----------------------------------|
| | decomposition (first step after water loss) | | thermal decomposition temperature |
| THF-1 – formate | 236.2 (88.43) | sodium formate | 261 ^a |
| THF-2 – acetate | 265.5 (88.40) | sodium acetate | 324 ^b |
| THF-3 – lactate | 290.6 (94.38) | none found | - |
| THF-4 – succinate | 293.7 (93.93) | disodium succinate | 425 ^c |
| THF-5 – tartrate | 207.9 (31.95) | sodium potassium tartrate | 220 ^d |

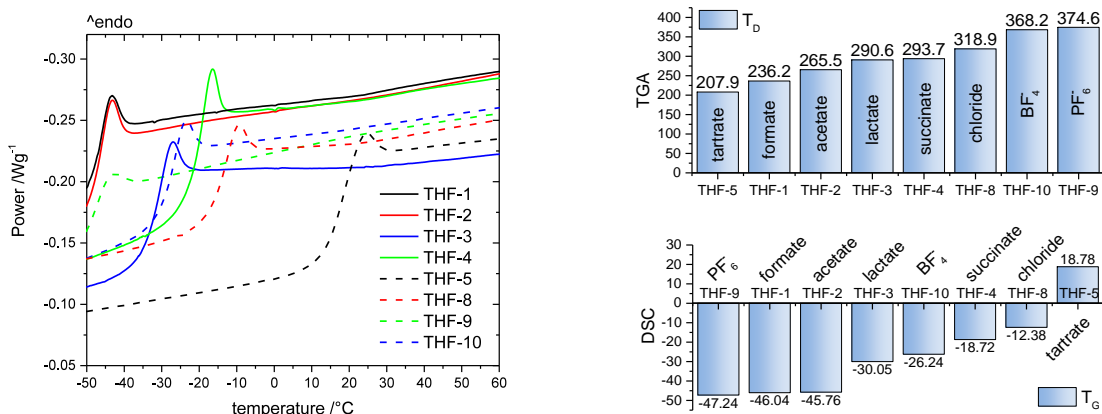


Figure 15: Left: DSC-curves of the ionic liquids THF-1 through THF-10. Top right: decomposition temperatures T_D of the synthesized ionic liquids. Bottom right: Glass transition temperatures T_G of the synthesized ionic liquids.

For the anions used in this work, it can be assumed that all organic anions are more nucleophilic than the halide based anions. Consequently, the ionic liquids THF-8 through THF-10 are thermally more stable than the other ILs. In the case of THF-9 and THF-10 the decomposition temperatures are too similar to deduct reasons for the differences in stability. For the organic anions the order of stability probably results from an overlap between anion stability and nucleophilicity at elevated temperatures. Table 4 compares the decomposition temperatures of THF-1 through THF-5 with the decomposition temperatures of alkali salts based on the same counterion. In the case of the tartrate and formate based molecules, both decomposition temperatures are very similar, which implies that in this case decomposition of the anion may limit the stability of the ionic liquid. The other ionic liquids show degradation temperatures significantly lower than the respective alkali salts and it can be assumed that thermal decomposition is based on the nucleophilicity of the counterion.

The influence of the anions on the thermal behavior was also analyzed using differential scanning calorimetry (DSC). The results are summarized in Figure 15. The glass transition temperatures (T_G) are ascending in the row of hexafluorophosphate (THF-9) \approx formate (THF-1) \approx acetate (THF-2) < lactate (THF-3) < tetrafluoroborate (THF-10) < succinate (THF-4) < chloride (THF-8) < tartrate (THF-5). The order in this case is created by an overlap of anion size and intermolecular interaction. In the row of hexafluorophosphate > tetrafluoroborate > chloride, the inorganic anions become smaller and as such the glass transition temperature rises. In the case of the organic anions, the dominant influence on T_G is the increase of intermolecular interactions. In the row of formate/acetate < lactate <

succinate < tartrate the number of heteroatoms is increasing from two to 6 and the T_G reflect the increased intermolecular interactions.

2.3 Cation design

As outlined in chapter 2.1, the choice of starting material allows control of the cation architecture. The used amines define the *N*-substitution pattern of the imidazolium ring (position 1 and 3, cf. Figure 8, p. 20). The *C*-substitution pattern at positions 2 (aldehyde), as well as 4 and 5 (1,2-dicarbonyl compound) are defined by the carbonyl compounds. Since the C2-position is considered the weakest link of the imidazolium ring, protection *via* different C2-substitution patterns is a relevant concern (c.f. chapter 4). Unfortunately the use of different aldehydes is not straight forward. Depuydt et al. have pointed out that synthesis using enolizable starting materials fails to produce imidazolium compounds and consequently attributed this restriction to the keto-enol tautomerism shown in Figure 16 and the subsequent formation of aldol-type side products.^[26] The failure of the mDRr with enolizable starting materials was also verified in this work using acetic aldehyde. While the equilibrium for most keto-enol tautomerisms actually favors the keto form because it is thermodynamically more stable,^[112] the equilibrium is catalyzed in basic and acidic conditions^[113]. As discussed in the introduction, the mDRr requires the presence of a (weak) acid to both catalyze the reaction and provide the counter ion for the formed imidazolium cation. As such the failure of acetic aldehyde and other enolizable aldehydes to produce imidazolium compounds may be the direct result of the special conditions of the mDRr. This limits the variation of the C2-position by mDRr to non-enolizable starting material. Modification of the C4 and C5 positions seems to be less restricted, which is demonstrated by the use of pyruvaldehyde instead of glyoxal with good yields.^[45,53] In any case, variation of the *C*-substitution pattern is not straight forward and this work will focus on the use of formaldehyde and glyoxal. As a consequence, the use of amines to introduce functionalities seems the most elegant design strategy for cation synthesis. Depuydt et al. have used various linear and branched aliphatic amines to introduce the respective moieties into the imidazolium cation, thus showing the compatibility of the mDRr with alkane chains.^[26]

Most functionalities found in chemicals from renewable resources are based on oxygen^[114] and this work will focus on the use of amines bearing saturated and unsaturated ethers,

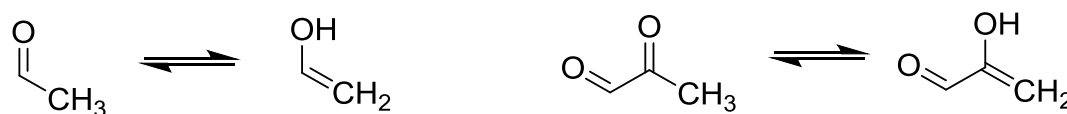
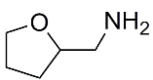
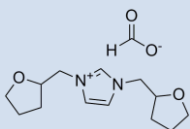
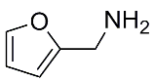
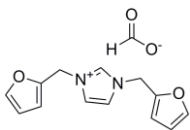
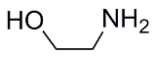
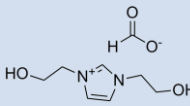
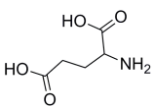
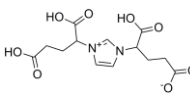
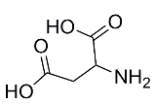
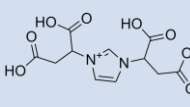


Figure 16: Left: Keto-enol tautomerism of acetic aldehyde. Right: Keto-enol tautomerism of pyruvaldehyde.

alcohols and carboxylic acid functionalities in order to further test the scope of the mDRr in renewable synthesis. The use of amines functionalized with aldehyde and 1,2-dicarbonyl compounds is excluded for the reasons explained above. The amines used are the tetrahydrofurfurylamine from the previous chapter, furfurylamine, ethanolamine, aspartic acid and glutamic acid. Table 5 gives an overview of the conducted reactions (synthesis cf. chapter 6.2).

Table 5: Overview of the different amines used in cation synthesis (TGA steps were determined using the maxima of the first derivative of the TGA-curve) and glass transition temperatures (derived from the inflection points of the glass transition). Notes: a) determined by NMR; b) isolated yield; c) determination of the thermal characteristic not possible due to heavy foaming.

| amine | yield | code | structure | TGA | DSC |
|-------------------------------------------------------------------------------------|----------------------------------------|--------------|-------------------------------------------------------------------------------------|------------------------------------------------|---------------------|
| | | | | T _D [°C] (mass loss [%]) | T _G [°C] |
|  | 95.7 ^a | THF-2 |  | 265.5 (88.4) | - 45.76 |
|  | 53.8 ^a | F-2 |  | 216.2 (69.71) | - 36.71 |
|  | 88.0 ^a | E-2 |  | 177.0 (16.74) 263.1 (67.33) 420.7 (8.57) | - 49.0 |
|  | 74.0 ^a 15.0 ^b | Glu |  | - ^c | - ^c |
|  | 11.3 ^b | Asp |  | - ^c | - ^c |

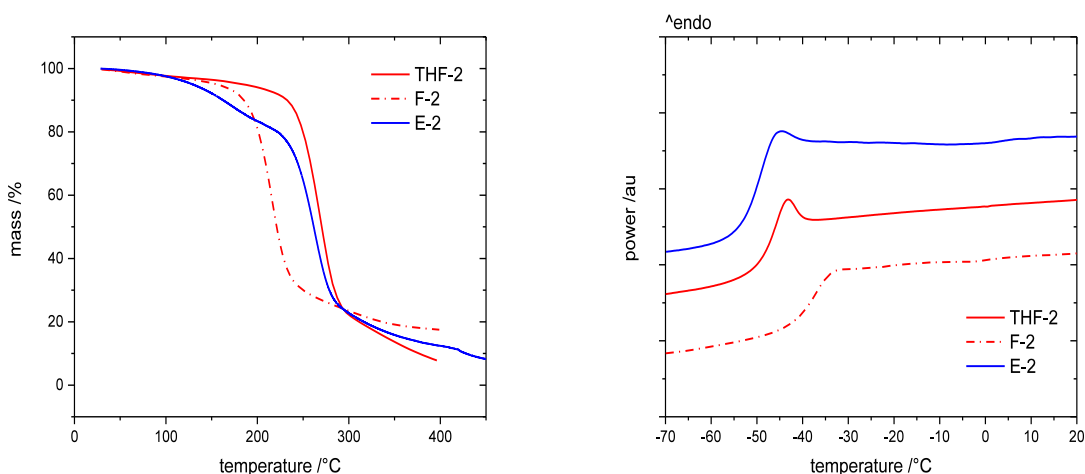


Figure 17: Left: TGA-curves of F-2 and E-2 in comparison to THF-2. Right: DSC-curves of F-2 and E-2 in comparison to THF-2

The yields of the reactions conducted illustrate the compatibility of the mDRr with said functions. The lower yield of **F-2** can be attributed to the increased lipophilicity introduced by the unsaturated sidechain⁶, as also reported in literature.^[26] Since the synthesized ionic liquids differ only in their cationic substitution pattern, they offer the possibility to evaluate the influence of cation architecture on the physical characteristics. In order to do so, they were subjected to thermal analysis. The results are summarized in Table 5 and Figure 17. Following the assumption from chapter 2.2 that decomposition steps below 200 °C are related to the release of water, the decomposition temperature (T_D) increases in the order of $F-2 < THF-2 < E-2$. The different decomposition temperatures can be assumed to be a result of the different stability of the side chains. The glass transition temperature of the ionic liquids increases in the order of $E-2 < THF-2 < F-2$. In contrast to the trend described in the previous chapter, this seems to be the result of the rigidity of the substituents which seems to outweigh the intermolecular interactions. The hydroxyethyl-sidechain can be assumed to be the most flexible substituent and consequently shows the lowest glass transition temperature. Of the two rings the furanyl-substituent is particularly rigid and shows the highest glass transition temperature.

Another group of interesting starting materials are amino acids. As Kirchhecker et al. have shown, the use of amino acids in mDRr forms zwitterionic compounds.^[45,53] Drawing upon

⁶ The work-up includes extraction with diethylether.

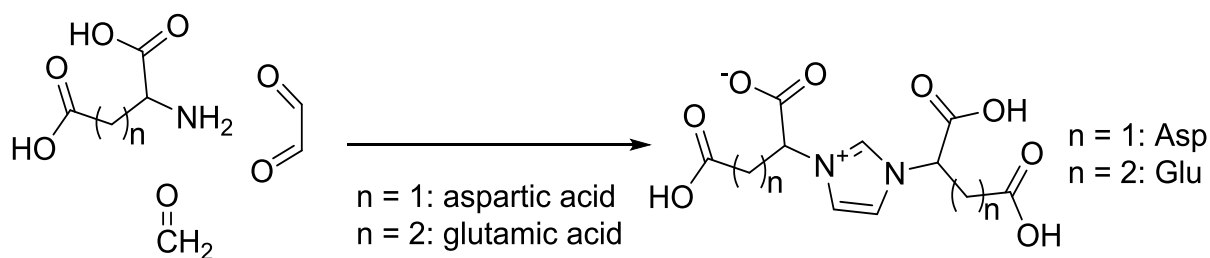


Figure 19: Synthesis of multiacidic imidazolium zwitterions (two equivalents of the amino acid are used).

this scheme, glutamic acid and aspartic acid were used to synthesize zwitterionic structures with multiple acid groups (referred to as Glu and Asp, as obtained from glutamic acid and aspartic acid, respectively). Figure 19 shows the reaction scheme.

The main obstacles of the synthesis are the virtual insolubility of aspartic and glutamic acid in most solvents and the separation of the respective products (synthesis cf. chapter 6.2). The key to both problems is the pH-dependent solubility behavior of the amino acids. In order to conduct the reaction, the amino acid must be transferred to a soluble species. This can be done in the presence of a base, such as sodium hydroxide (almost instantaneous dissolution) or even pyridine (slower dissolution).

Even though the reaction proceeds to a yield of 74 % when mono sodium glutamate is used (calculated by nmr), the product can not be isolated in a pure form by extraction or freeze drying. Instead, the workup proceeds exploiting the pH-dependent solubility which is maintained in both Asp and Glu. In order to do so, the pH of the solution obtained after synthesis must be lowered slowly until precipitation is induced. The proposed mechanism for pH-induced precipitation is shown in Figure 18. Since the monobasic salt of the amino acids is used and two equivalents of it are incorporated into the imidazolium ring, it can be assumed that the product is obtained as the dibasic salt as depicted in Figure 18 on the left side (B^+ denotes the cation formed from the base). As a consequence of charge neutrality, the product must be deprotonated at three carboxylic acid groups. The addition of HCl effects the protonation of carboxylic acid groups of the product to the point where only one carboxylic

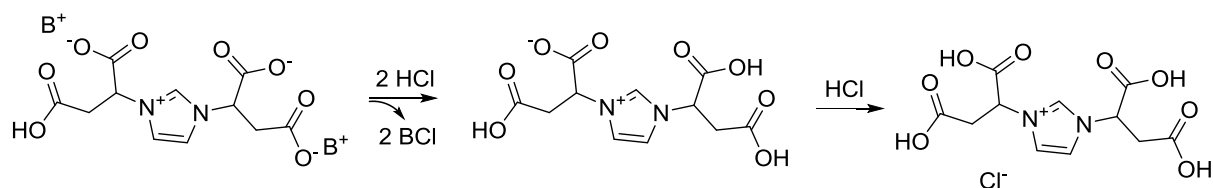


Figure 18: pH-dependent precipitation of the multiacidic compounds. The figure depicts the precipitation of Asp after addition of HCl. Glu behaves in the same manner.

acid is left unprotonated. Asp is now a zwitterionic species. At this point the solution becomes turbid and a yellowish precipitate shows that can be collected, filtered off and washed to obtain the pure product. If further acid is added, the last carboxylic acid group of the molecule is protonated and the hydrochloride of the zwitterion is formed. Following this approach, the pure, isolated products are obtained as zwitterionic species in low yields (22.5 % and 15.0 % for Asp and Glu, respectively). Thermal analysis could not be conducted due to heavy foaming of the compounds. This foaming is related to the decarboxylation of the carboxylic acid group located at the α -position to the nitrogen. This phenomenon has been described by Kirchhecker et al. for both imidazolium and pyridinium based molecules. The vicinity of the acid group to the heteroaromatic ring seems to aid the decarboxylation and thus it can occur at significantly lower temperatures than in free amino acids.^[19,53]

The so obtained zwitterions are, similar to the amino acids, virtually insoluble in most solvents. It is possible, that the zwitterions form chain and network like structures based on the dimer formation mechanism known from acetic acid.^[115] Dissolution of Asp and Glu can, however be achieved easily by using basic (or very strongly acidic) solutions.

As seen in this chapter, the mDRr tolerates a wide range of different substrates and conditions. Moreover, key characteristics of the molecules used as starting materials can be conferred to the ionic compounds synthesized, which is promising for the synthesis of task-specific molecules.

2.4 Polymer synthesis *via* modified Debus-Radziszewski reaction

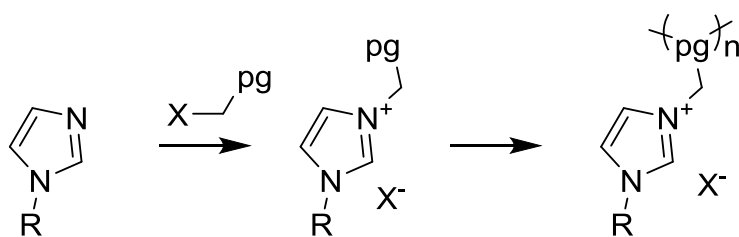


Figure 20: Traditional synthesis of imidazolium based polymers. First the polymerizable group (depicted as pg) must be introduced into the molecule, e.g. by alkylation. The polymerization then proceeds by reaction of the side chain. The result is a polymer chain with dangling imidazolium cations.

The previous chapters have shown that the mDRr allows for cation design and anion control over a range of different starting materials and reaction conditions. This chapter will show its application in polymer synthesis and expand the product space to materials. The synthesis of traditional imidazolium based polyelectrolytes usually proceeds in a two-step process as depicted in Figure 20. First a polymerizable side chain is introduced *via* alkylation. This is then polymerized to yield a polymer with pendant imidazolium moieties.

In order to make use of the mDRr in polymer synthesis, it is necessary to use molecules with more than one amino group, as shown in Figure 21.

The main difference between the two different approaches depicted in Figure 20 and Figure 21 is the position of the imidazolium ring in the resulting polymers. In contrast to the first case, the imidazolium moiety is incorporated into the backbone of the polymer in the case of mDRr⁷.

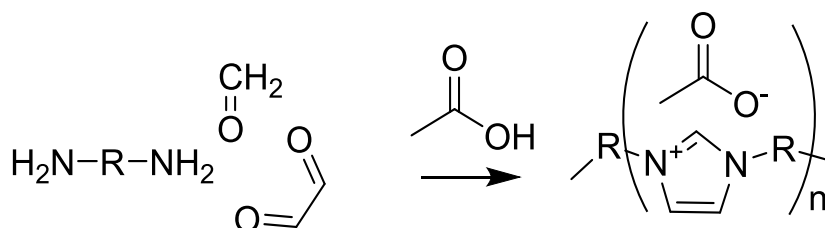


Figure 21: Use of the modified Debus-Radziszewski reaction for polymer synthesis.

⁷ Also, the synthesis depicted in the first case is a polymerization of an ionic liquid, hence the product is a poly(ionic liquid) (PIL). In the latter case, the term polyelectrolyte is more appropriate due to the direct synthesis *via* the multi-component mDRr.

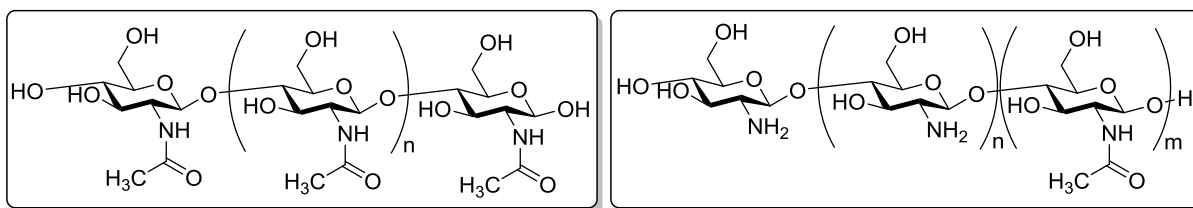


Figure 22: Left: Structure of chitin; Right: chitosan; The degree of deacetylation of the used chitosan is ca. 80 % and consequently the ratio of $n:m$ is ca. 4:1. The molecular weight of one (deacetylated) unit is 161.15 g/mol.

The application of the mDRr in polymer science was explored recently, e.g. for crosslinking reactions^[55,116] of polymer chains with free amino groups and for the synthesis of linear^[46,117] or porous (crosslinked)^[47] polymers. The approach is appealing because of the unusual backbone architecture of the poly(imidazolium) chains. Also, while the reaction releases water and is formally a condensation reaction, it is not dependent on exact stoichiometry and as such can be driven forward by applying stress to the chemical equilibrium.^[46]

The aim of this chapter is to further explore the synthesis of networks based on the mDRr. In order to distinguish this approach from the approach used in the previous chapters, it will be referred to as the poly-Debus-Radzisewski reaction (pDRr). The synthesis of networks requires the use of amines with more than two amino groups in addition to linear diamines. In search of a suitable crosslinker (CL), chitosan was identified as a promising molecule: it is cheap, carries many amino groups, and is available from chitinous waste-biomass such as shrimp-shells by deacetylation (general structures cf. Figure 22). The main obstacle of using chitosan in synthesis is its large molecular weight and thus bad solubility, which is realized using acetic acid/water. For the synthesis of poly-electrolyte networks (PENs) the procedure of Lindner was adapted (synthesis cf. 6.2).^[46] The so obtained networks are usually free-standing.

Different molecular weights of chitosan have been used: low molecular weight chitosan (crosslinker A, ca. 50-190 kDa, median:⁸ 120 kDa) and chitosan oligosaccharide (crosslinker B, ca. 5 kDa). The molecular weight of one (deacetylated) repeating unit of chitosan is 161.15 g mol⁻¹. Neglecting the weight difference between acetylated and deacetylated repeating units, the number of repeating units of chitosan was calculated from its

⁸ The median will be used here for estimations of the molecular weight, since no weight distribution is given by the supplier.

molecular weight to be roughly 310-1179 (median: 745) in the case of crosslinker A and 30 for crosslinker B. The amount of chitosan used in synthesis was calculated so that 3, 5 or 7 % of the total amino groups of the reaction are chitosan based. The remaining 97, 95 or 93 % originate from a linear diamine. Three different amines were used and are displayed in Figure 23. The obtained materials are not soluble in water and no other tested solvent (cf. chapter 3.2) and as such could not be subjected to size exclusion chromatography. Lindner, working exclusively on linear polymers, obtained a maximum molecular weight of 13kDa in the case of the lysine based polymer under similar conditions.^[46] Assuming that the polymer is zwitterionic (no acetic acid), the molecular mass of one repeating unit is 180.2 gmol^{-1} ($\text{C}_9\text{H}_{12}\text{N}_2\text{O}_2$). This means that the number of repeating units is around 72 in the case of the lysine based polymer obtained by Lindner. Using the same assumptions a similar number is obtained for the use of 4,7,10-trioxa-1,13-tridecanediamine (molecular weight of a subunit: 314.38; $\text{C}_{15}\text{H}_{26}\text{N}_2\text{O}_5$, including the acetate; maximum molecular weight of the chain according to Lindner: 23.5 kDa; repeating units: 74). The simplifications chosen for the calculation probably make this an overestimation. It should be assumed that the chains in the case of the PENs are shorter due to the use of crosslinker and not optimized reaction conditions. As such the poly(imidazolium) chains are in the best case of comparable length,

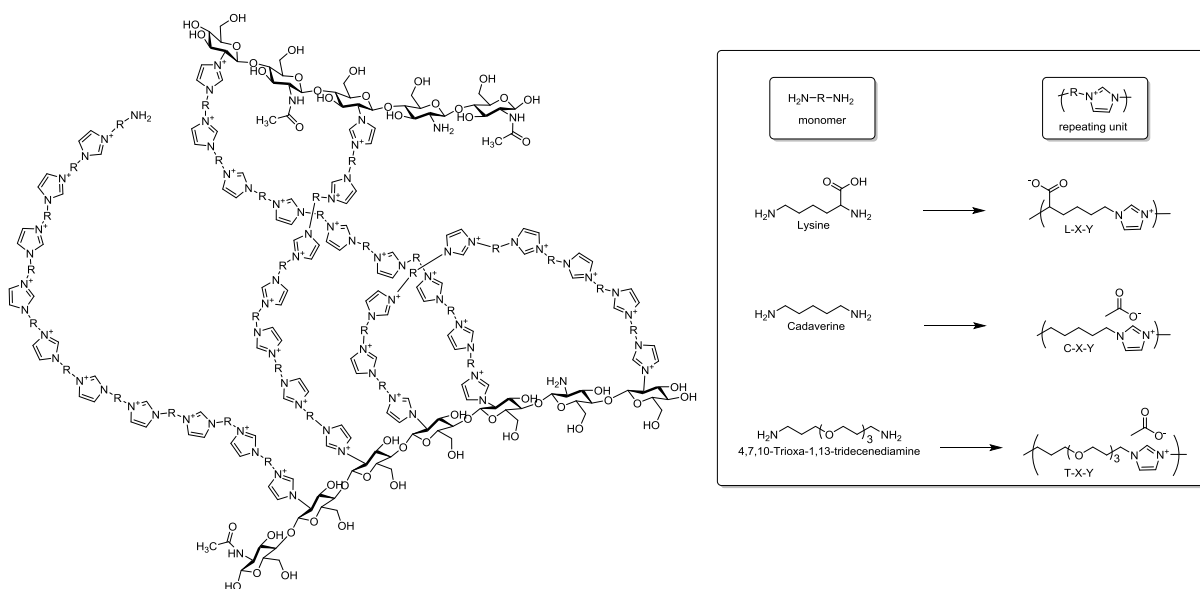


Figure 23: Left: Assumed structure of the polymer network. Right: Overview of the monomers and repeating units (right). The structure is assumed to present open chains, loops and crosslinks. Notes: a) Any tacticity is for convenience of display only. b) The lysine based polymer is displayed as zwitterionic, because $pK_A(\text{lysine}) < pK_A(\text{acetic acid})$. Protonation of some carboxylic groups is probable (resulting in the presence of acetate counterion). This is omitted for brevity. c) Counterions are omitted from the network for image clarity. d) Names of the PENs present the first letter of the monomer used followed by the type of crosslinker used (A or B) and the amount of amino groups originating from the crosslinker.

probably shorter, when compared to the chitosan chain of crosslinker B. In comparison to the chitosan chain of crosslinker A, however, they are short. This brief approximation demonstrates that the crosslinker is not a small molecule with just more than two reactive sites, but a rather long chain polymer with tens to hundreds of reactive sites and a higher length than the synthesized poly(imidazolium) chains.

Table 6: Overview of the networks synthesized. Number and temperatures of steps in TGA measurements were determined using the minima of the first derivative of the TGA-curve. Glass transition temperatures derived from the inflection points of the DSC curve. In some cases mass is lost prior to $T_{D,1}$ with no peak in first derivative: a) 19.6 % b) 15.1 % c) 24.4 %.

| diamine | cross-linker | [%] | sample name | T_D [°C] (mass loss [%]) | T_G [°C] |
|--------------------------------------|--------------|-----|--------------------|-----------------------------------------------------------------------------------------------------------|------------|
| lysine | A | 3 | L-A-3 ^a | $T_{D,1}$: 282.1 (18.6); $T_{D,2}$: 302.4 (38.2) $T_{D,3}$: 425.9 (15.2) | 84.0 |
| | | 5 | L-A-5 ^b | $T_{D,1}$: 303.4 (69.17); $T_{D,2}$: 457.9 (6.7) | 99.8 |
| | | 7 | L-A-7 ^c | $T_{D,1}$: 295.7 (55.8); $T_{D,2}$: 425.3 (12.7) | 76.4 |
| cadaverine | A | 3 | C-A-3 | $T_{D,1}$: 162.4 (30.1); $T_{D,2}$: 281.5 (56.5) $T_{D,3}$: 428.8 (7.8) | -31.4 |
| | | 5 | C-A-5 | $T_{D,1}$: 138.0 (30.3); $T_{D,2}$: 250.2 (13.5) $T_{D,3}$: 280.8 (41.0); $T_{D,4}$: 425.8 (9.7) | -22.5 |
| | | 7 | C-A-7 | $T_{D,1}$: 136.3 (29.0); $T_{D,2}$: 253.9 (15.6) $T_{D,3}$: 283.1 (43.68); $T_{D,4}$: 423.0 (5.4) | -28.9 |
| 4,7,10-trioxa-1,13-tridecane-diamine | A | 3 | T-A-3 | $T_{D,1}$: 135.0 (28.2); $T_{D,2}$: 277.1 (55.6); $T_{D,3}$: 332.2 (8.2); $T_{D,4}$: 400.4 (5.6) | -42.0 |
| | | 5 | T-A-5 | $T_{D,1}$: 172.3 (23.1); $T_{D,2}$: 278.6 (52.8); $T_{D,3}$: 333.2 (11.5); $T_{D,4}$: 397.1 (8.67) | -47.6 |
| | | 7 | T-A-7 | $T_{D,1}$: 131.8 (23.8); $T_{D,2}$: 274.2 (52.3); $T_{D,3}$: 332.2 (10.3); $T_{D,4}$: 397.6 (8.9) | -34.4 |
| | B | 3 | T-B-3 | $T_{D,1}$: 150.3 (23.0); $T_{D,2}$: 277.2 (55.1); $T_{D,3}$: 332.2 (13.3); $T_{D,4}$: 303.0 (5.6) | -39.9 |
| | | 5 | T-B-5 | $T_{D,1}$: 152.9 (23.0); $T_{D,2}$: 277.5 (52.8); $T_{D,3}$: 334.9 (15.0); $T_{D,4}$: 398.6 (6.6) | -35.6 |
| | | 7 | T-B-7 | $T_{D,1}$: 185.9 (20.4); $T_{D,2}$: 277.6 (52.1); $T_{D,3}$: 335.4 (16.5); $T_{D,4}$: 402.2 (5.8) | -34.8 |

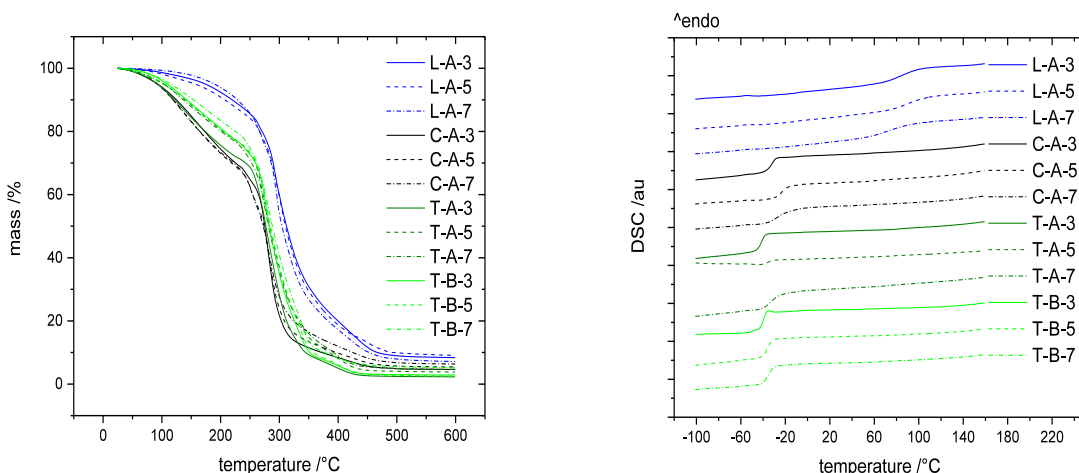


Figure 24: Thermal characterization of the PENs. Left: TGA (heating rate 10 Kmin^{-1}). Right: DSC (intensity not normalized).

In order to see what influence this has on the physical characteristics of the synthesized networks, they were subjected to thermal analysis. Table 6 gives a brief overview over the synthesized samples. The results of thermogravimetric analysis and differential scanning calorimetry are shown also in Figure 24. Notably the mass is reduced more or less continuously from the beginning of the thermogravimetric analysis until the first major decomposition step. While the amount of mass lost and the temperature of this first step is larger than in Figure 14 (cf. p. 27), the shape is similar. This may imply that the first step in mass loss is related to the evaporation of water and probably also acetic acid. In order to investigate this, TGA-MS was conducted on sample T-A-5. The results are shown in Figure 25. For brevity only selected, representative curves are displayed (cf. Figure A - 2, p. 102 for

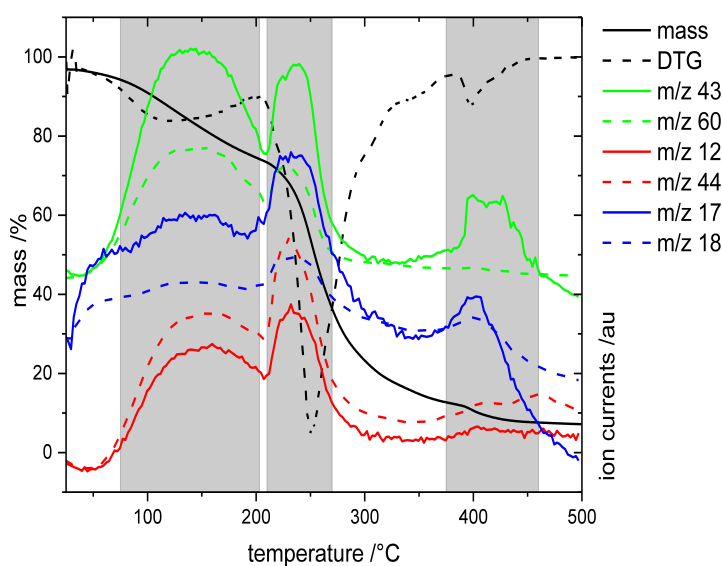


Figure 25: TGA-MS measurement of T-A-5. Three regions of interest are highlighted. The ion currents represent typical currents obtained in the measurement. m/z 43 and 60 indicate acetic acid, m/z 12 and 44 indicate CO_2 , m/z 17 and 18 indicate H_2O . Please note that TGA-MS measurements are carried out at 2.5 Kmin^{-1} (in contrast to ordinary TGA).

more details). Three sets of curves are shown: m/z 17 and 18 are interpreted to originate from the hydroxyl and water radicals, respectively. They indicate the evaporation of water. The detection of m/z 43 and 60 indicate acetic acid and m/z 12 and 44 are characteristic for the evolution of CO_2 , and part of the mass spectrum of acetic acid⁹ (cf. Figure A - 3, p. 103). Three regions of interest are highlighted in Figure 25. They correspond to the three major steps of decomposition with peaks at ca. 120 °C, 250 °C and 400 °C. In the first step water, acetic acid and carbon dioxide can be detected. This can be interpreted as the simple evaporation of residual water and acetic acid from the intact PEN prior to 200 °C. Consequently, it may be assumed that decomposition of the PENs does occur beyond 200 °C, where the onset of the next peak/decomposition step is visible. The next decomposition region (around 250 °C) features the increase of all three sets of ion currents. This may be the result of decomposition of the network. The electrostatically bound acetate is released if C-N bond dissociation removes the charge from the imidazolium ring and consequently acetic acid can be detected in TGA-MS. Obviously water is also released in this step. In the final decomposition step (around 400 °C), again the release of water and acetic acid is indicated. It is assumed that the decomposition happening here is analogue to the decomposition around 250 °C. It should be noted that the decomposition of imidazole rings is not expected below 500 °C (cf. chapter 2.2).^[107] Consequently it must be assumed that different parts of the sample decompose at significantly different temperatures. In summary, TGA-MS reveals three steps of mass loss, all of which detect acetic acid and water related fragments. First, residual water and acetic acid are removed from the PEN by evaporation. The second and third steps relate to the decomposition of the network by imidazolium degradation.

The decomposition steps discussed are visible in all TGA curves (cf. Figure 24 and Table 6, if four decomposition temperatures are given $T_{D,2}$ and $T_{D,3}$ both correspond to the second step). However, the decomposition of the lysine based PENs generally happens at higher temperatures and features lower loss of water and acetic acid in the first decomposition step. This supports the assumption that the lysine based PEN is actually zwitterionic (cf. Figure 23). Apart from this the decomposition curves and temperatures are very similar to each other. The networks seem stable up to ca. 250 °C (300 °C for the lysine based ones) with slight variations. The amount or type of crosslinker has no significant effect on thermal stability.

⁹ If a hard ionization method is used that fragments the molecule, such as electron ionization (EI, cf. chapter 6.1).

The DSC curves reveal that the glass transition temperatures of the lysine based compounds are significantly higher than the glass transition temperatures of the other compounds. The main reason for this is probably the significantly lower amount of residual water and acid present in the lysine based networks (cf. Figure 24). In addition to this, the carboxylic acid group on the side chain provides additional hydrogen bonding sites and electrostatic interaction. Apart from this no clear trend can be observed. The glass transitions of all but the lysine based networks are within a range of 20 °C of each other even though the sidechains introduced vary significantly (5 vs. 13 atoms). It may indicate that the DSC behavior is dominated by the presence and amount of residual solvent molecules and by the influence of the cationic imidazolium moiety which is the same in all repeating units. The presence of charges and consequently electrostatic interactions within the network may also affect the glass transition temperature, as possibly the case in the lysine based polyelectrolytes. Varying the amount and type of crosslinker has insignificant effect on the thermal behavior.

2.5 Summary

In this chapter, the mDRr was used for the direct anion tuning of a small library of ionic liquids. Acids with pK_A -values from -7 to 9.27 were used to design ionic liquids with different decomposition and glass transition temperatures. It has been shown that strong acids still allow for the successful synthesis of ILs, but side reactions occur that cannot be purified easily. The use of compounds with too high pK_A -values fails to produce ionic liquids at all. Pure products can be obtained in the pK_A -range of 3.03 to 4.765. The used synthetic scheme also simplifies metathesis reactions with strong acids. By using different organic acids and by making use of metathesis reactions, the decomposition and glass temperatures could be tuned over a range of 170 °C and 60 °C, respectively.

Furthermore the reaction is suitable for polymer synthesis. Using diamines and molecules with more than two amino groups the synthesis of polymer networks is possible. The so obtained networks incorporate the imidazolium moiety into its backbone and are consequently highly charged polycationic networks.

3 Green polyelectrolyte networks for energy storage¹⁰

3.1 Relevance

The last chapter has dealt with the adaptation of the mDRr to produce polymeric materials instead of small molecules by using starting material with two and/or more amino groups. The result are free standing polyelectrolyte networks (PENs) that can be obtained from cheap and potentially sustainable starting materials using green chemistry. Since the propagation step of the polymerization reaction proceeds through the synthesis of an imidazolium ring, every repeating unit of the green PEN carries a positive charge. The so obtained materials are consequently highly charged cationic networks. In order to maintain charge neutrality, every cationic moiety is accompanied by a counter ion. In case of lysine as diamine species the counter ion is present in the form of a carboxylate group bound to the network, which is in fact a zwitterionic network. In the case of PENs based on cadaverine and 4,7,6,10-trioxa-1,13-tridecanediamine (trioxatridecane for short), this is an acetate anion. Due to the fixed nature of the cations within the network, they could repulse ions of the same charge. This could enable the PENs to permit the transition of anions while blocking cations. The obtained material could be applied as a charge sensitive semi-permeable membrane or, in other words, an anion conductor.

Anion conduction is an important topic in energy materials, for example in the field of anion batteries, such as fluorine or alkaline batteries. As opposed to more prevalent systems such as lithium ion batteries, these systems utilize anions as the charge shuttles in their charge-discharge cycles. Chloride ion batteries (CIBs) are an emerging technology in the field of anion batteries.^[119] In order to develop viable systems electrolytes are necessary that can conduct chloride ions with sufficient electrolytic conductivity at room temperature. The use of polymer based membranes has shown promising results.^[120] It has been pointed out that the use of polymers with cationic groups would be beneficial in this regard.^[119] Another even more relevant application for anion conducting membranes is the use in so called alkaline fuel cells (AFCs). This special class of fuel cells uses a aqueous potassium hydroxide solutions.

¹⁰ Parts of this chapter are part of a publication in progress. Data and figures presented in this chapter are therefore taken from this reference^[118].

Consequently hydroxide ions must be shuttled from the anode to the cathode.^[121] Desired characteristics for membranes applied in AFCs are high ionic/low electronic conductivity, low permeability for neutral molecules to prevent fuel cross-over, mechanical and chemical stability, as well as low cost.^[122] Among the various polymers used in these applications are also poly(ionic liquid) copolymer membranes based on the imidazolium cation.^[123] Their polymer architecture resembles the one depicted in Figure 20 (p. 37). The PENs obtained in this work could present a cost-efficient and far more sustainable alternative to the alkylation based poly(ionic liquid) based membranes.

3.2 Mechanical properties

Since mechanical characteristics are a decisive factor in application, the synthesized PENs were subjected to oscillatory stress-strain measurements to determine their mechanical behavior. The samples were first submitted to a frequency sweep from 0.1 to 100 rads^{-1} at 1 % deformation. They were then subjected to an amplitude sweep measurement at a frequency of 10 rads^{-1} until material rupture. The storage and loss modulus were then obtained by fitting the linear viscoelastic range of the amplitude sweep and calculating the intercept with the y-axis. The storage modulus (G') is a measure for the amount of deformation energy applied to the sample during measurement that is reversibly stored in the sample. It represents elastic behavior. The loss modulus (G'') is a measure of the amount of deformation energy that is dissipated, it represents viscous behavior. The ratio of the loss to the storage modulus is called the loss factor $\tan \delta$:

Equation 1: Calculation of the loss factor $\tan \delta$.

$$\tan \delta = \frac{G''}{G'}$$

If $\tan \delta = 0$ ($G' \gg G''$), the sample behaves ideally elastic. If $\tan \delta = \infty$ ($G' \ll G''$), the sample behaves ideally viscous. Consequently, if both moduli are of equal size, $\tan \delta = 1$. The loss factor calculated from the obtained moduli of the samples is shown in Figure 26 (left). It is generally below 0.25 for all materials, which indicates viscoelastic behavior with a dominant elastic part.^[124] The viscous portion of the behavior may be explained by residual acetic acid and water in a given PEN. Also, since the synthesis was carried out in aqueous medium and the reaction itself releases water, the gels can be supposed to contain water. Also, if their swelling behavior is taken into account (v.i.) they must be considered hydrophilic and hygroscopic. The lysine based PENs are excluded from this analysis since they are too brittle to analyze in the used rheometer setup.

As indicated by the loss factor, the storage modulus is generally larger than the loss modulus for all tested materials. Figure 26 also shows a typical frequency sweep (top right) and amplitude sweep (bottom right) measurement. For brevity only one representative sample is shown here (for further details cf. chapter 6.1). The frequency sweeps show that the storage modulus G' is larger than the loss modulus G'' over the whole test range. The shape of the

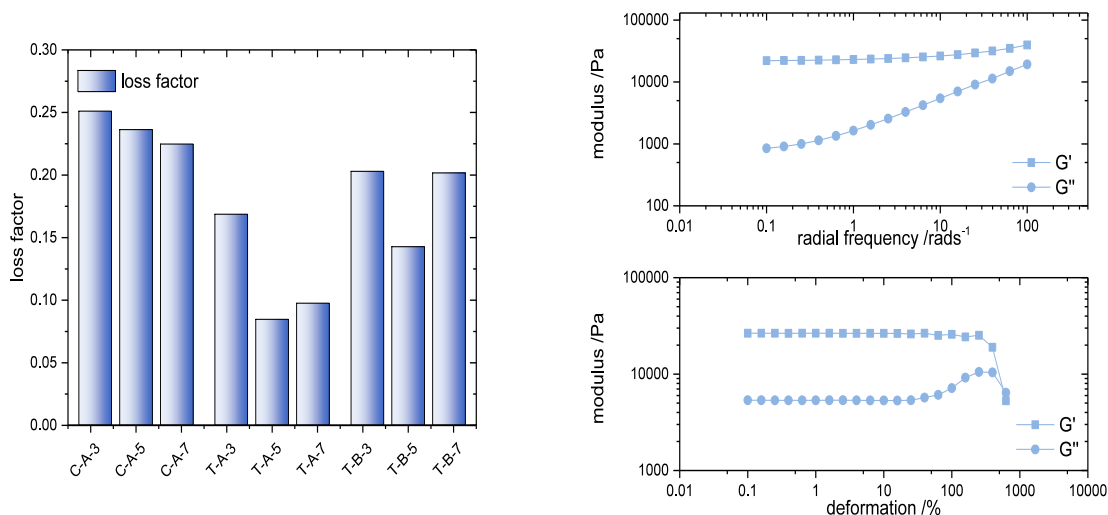


Figure 26: Loss factors (left) and a typical sweep measurement (right). The frequency sweep measurements (top right) were carried out to obtain data about the crosslinking behavior of the materials. The amplitude sweep (bottom right) was carried out to obtain the values of the dynamic modulus. The figures on the right represent typical measurements and have been recorded using T-B-7.

curves is typical for crosslinked polymers.^[124] The amplitude sweep also shows that $G' > G''$. The drop of the curves towards the end are the result of material failure (rupture). The small peak of G'' is a result of the sample slipping between the rheometer plates.

Figure 27 gives an overview of the moduli obtained from the measurements. Comparing the storage modulus among the respective samples, higher values are obtained from samples with higher amounts of crosslinker. The highest values are obtained for the cadaverine based systems. This may be a result of the comparatively short length of the cadaverine molecule (five atoms) in contrast to the longer trioxatridecane molecule (thirteen atoms). The shorter chain could induce less flexibility and as such impose a stronger force to return into the original shape after the end of the application of force. This is the case despite the higher amount of residual water and acetic acid in the cadaverine based PENs (cf. Figure 24, p. 41 and Table 6, p. 40) which contain ca. 30 % of residual solvent in comparison to ca. 20-24 % in the case of the other networks. The trioxatridecane based samples also demonstrate higher moduli for higher amounts of crosslinker, regardless of the type of crosslinker. This trend is more pronounced in the case of crosslinker A based systems than in the case of the crosslinker B (lower molecular weight) based ones. Also a significant increase of the storage modulus can be observed upon increasing the amount of crosslinker from C-A-3 to C-A-5 as well as from T-A-3 to T-A-5. This cannot be observed in the crosslinker B based system. The reason for this may be the different chain length of the used crosslinkers. For crosslinker A (higher molecular weight), there are not enough long chains to allow sufficient entanglement in case

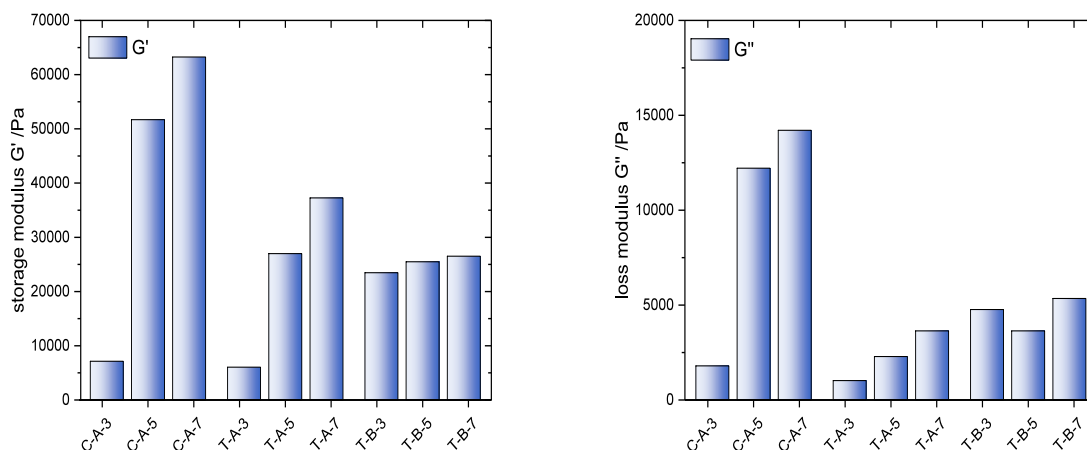


Figure 27: Results for the storage and loss moduli as obtained from rheological testing.

of a low content of crosslinker leading to the drastic increase of the storage modulus at higher contents of crosslinker. In the case of generally smaller chains (crosslinker B), entanglement and the formation of poly(imidazolium) chains crosslinking the chitosan-chains takes place relatively early and no such behavior is observed.

Another important feature of polymer networks is the swelling behavior. To evaluate this, samples have been immersed in de-ionized water and 5 %_m sodium chloride solutions for 24 h. The masses prior to and after swelling were collected and the increase (in %) was calculated according to:

Equation 2: Calculation of the swelling behavior.

$$swelling = \left(\frac{m_1}{m_0} - 1 \right) * 100\%$$

Swelling experiments were conducted in triplicate¹¹. The results of swelling experiments in aqueous media are summarized in Figure 28 (please note the different scales of the ordinates).

Swelling in de-ionized water is generally about three times stronger than in sodium chloride solution, which is a result of the increased ionic strength of the salt solution in comparison to pure water influencing the osmotic pressure and thus reducing the swelling. The lysine based systems represent an exception to this and show almost the same swelling in both media. This is most probably a result of the zwitterionic nature of the lysine based networks. They also

¹¹ Samples were prepared as described in chapter 6.2 and tested swiftly.

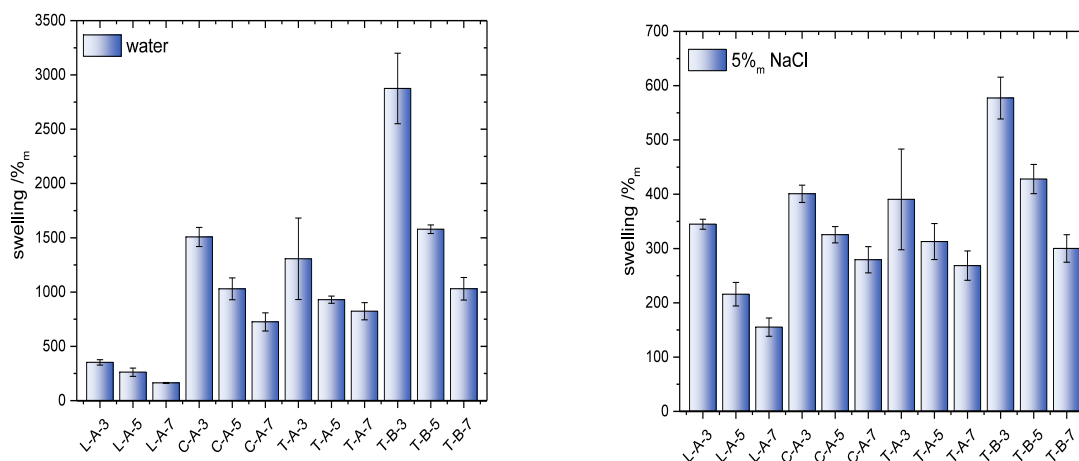


Figure 28: Swelling experiments conducted in de-ionized water (left side) and aqueous sodium chloride solution (5 %_m; right side).

show the weakest swelling behavior of all networks tested, which is probably also an effect of the added electrostatic interactions. Swelling generally decreases with increased crosslinking. This is expected, since increasing crosslinking also increases the rigidity of the network and decreases the ability of the material to accommodate solvent molecules. Comparing the samples based on crosslinker A, both cadaverine and the trioxatridecane based samples exhibit similar swelling behavior in both swelling media. In the trioxatridecane based networks, the swelling is much stronger when the lower molecular weight crosslinker B is used instead of crosslinker A. Over all, the presence of charges in the side chains, followed by the molecular weight of the crosslinker and its amount seem to be most important for the swelling of the tested poly-imidazolium networks.

Swelling also occurs in organic solvents. The results of swelling experiments conducted in organic solvents are summarized in Figure 29. Four networks were tested, all using the same amount of crosslinker, to explore the influence of diamine and crosslinker on the swelling behavior. Generally, swelling is lower in organic solvents than in aqueous media. The strongest swelling is observed in dimethyl sulfoxide (DMSO). The swelling behavior follows the order of DMSO > methanol > ethanol > chloroform > dichloromethane. For toluene, acetone, tetrahydrofuran and diethyl ether, *negative* swelling is observed as depicted in Figure 29 (right side). As outlined above the samples can be expected to contain residual water and acetic acid. The loss of mass upon immersion into organic solvents is most probably a result of residual water leaving the polyelectrolyte network. However, the amount of mass lost in the process indicates that short poly(imidazolium) chains that are not crosslinked into the

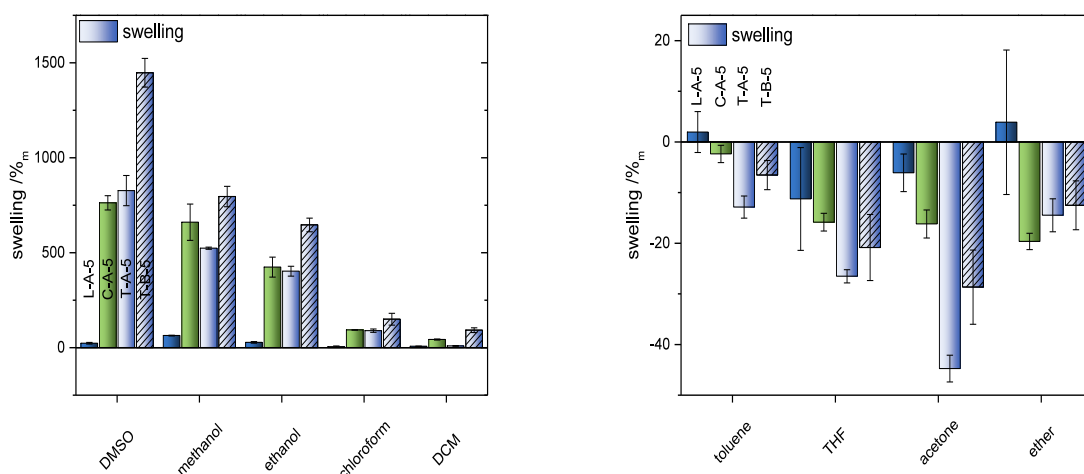


Figure 29: Swelling experiments conducted in organic solvents.

network also leave the PEN in the process. Comparing the positive swelling behavior of the different PENs tested, both cadaverine and trioxatridecane based PENs prepared using crosslinker A show similar swelling behavior. The lysine based PEN on the other hand shows hardly any swelling. This may be a result of the zwitterionic state of lysine within the PEN resulting in a strongly polar network with additional hydrogen bonding sites in the form of carboxylates (i.e. hydrogen bond acceptors) that does not accommodate organic solvent molecules which cannot act as hydrogen bond donors. Change of crosslinker A to crosslinker B results in increased swelling behavior as visible in the case of T-B-5 in comparison to the other PENs tested in organic solvents. Generally the swelling behavior of the four PENs in different solvents does not follow any immediately obvious trend, even though polar solvents seem to work better than nonpolar ones. This is demonstrated in the case of DMSO, methanol and ethanol. The absolute incompatibility with acetone on the other hand seems counter intuitive. The order of swelling intensity does not follow any established polarity scale of solvents. The amount of negative swelling is most probably an overlap of the amount of water and acetic acid residually contained in the PEN (cf. Figure 24, p. 41; Figure 25, p. 41) and the ability of the solvent used in the swelling experiment to take up water and acetic acid. This would explain the strong mass loss in acetone and THF while toluene and ether show less significant behavior.

3.3 Membranes from PENs

As demonstrated in the previous chapter, the PENs show pronounced swelling behavior. Unfortunately this impairs their direct use in any of the fields of energy storage indicated earlier because it negatively affects manageability and mechanical properties. In order to test the ability of the networks to act as semi-permeable membranes and ultimately to apply them, the strong swelling behavior must be mitigated to produce stable membranes.

During the development process two main problems became apparent. First, the strong swelling behavior of the PENs and increased brittleness in the swollen state made handling of the samples, specifically the fixation of the neat PEN into the measurement cell (v.i.) impossible. In order to overcome this, the use of thinner membranes and the addition of cellulose acetate as an internal support were tested, albeit without success.

The use of an external support, such as glass fiber filters or cellulose sheets (paper towels) was identified as a suitable solution. Using an external support uncovered a second problem, this time related to the fabrication process. Since the used crosslinker requires a large amount of solvent for solubilization, the resulting reactive solutions possess a relatively large volume compared to the amount of material obtained or in other words a low concentration of the reactive components. Consequently, simple impregnation and thermal curing of the wet supports did not produce viable membranes. For example, in one of the early stages of using a support, glass-fiber filters (42.5 mm diameter) were impregnated with a reactive solution and thermally cured. The resulting membranes feature an average of 0.12 g PEN per filter, which means ca. 8.3 mgcm^{-2} PEN. Consistently the behavior of the composite membranes is dominated completely by the support material and the composite membranes did not show any activity beyond the behavior of neat glass fiber filters.

Finally, using simple and cheap paper towels based on cellulose as external support, a fabrication method was devised that did produce mechanically stable membranes with a

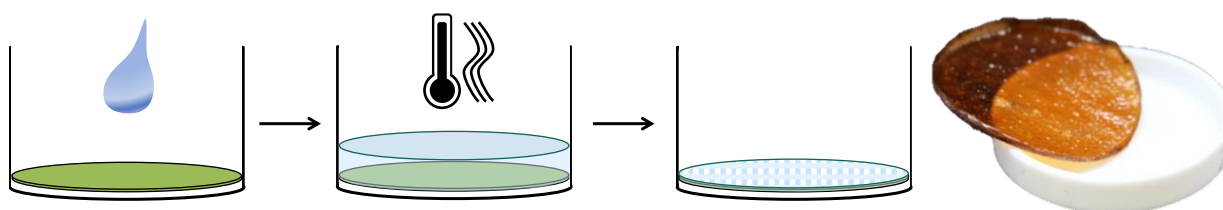


Figure 30: Fabrication of cellulose based membranes (f.l.t.r.): a cellulose sheet is placed on the bottom of a PTFE petri dish and the activated reaction mixture is placed on top. The petri dish is transferred to the oven and the membrane is cured. While most of the PEN has grown inside the cellulose sheet, the resulting membrane is covered by a thin layer of the PEN (depicted as the pattern on the top of the membrane). Finally, a photograph of a membrane as obtained after curing.

sufficiently high amount of PEN incorporated into the support material. The fabrication is depicted in Figure 30. A cellulose sheet (ca. 67 mm diameter) is placed on the bottom of a petri dish. A solution corresponding to the synthesis of T-B-3 (97 % of the amino groups based on trioxatridecane, 3 % based on chitosan crosslinker B) is filled into the petri dish so that it rests on top of the cellulose sheet. The petri dish is then placed in an oven at 60 °C overnight. Cadaverine based membranes were fabricated accordingly.¹² The resulting PEN-based membranes (PENbranes) will be referred to as M-T and M-C (trioxatridecane based and cadaverine based, respectively). This procedure allows the mixture to slowly concentrate during the curing process and consequently allows the product to accumulate in and on top of the cellulose sheet while the reaction proceeds. As a result, the obtained membranes contain more PEN than a membrane obtained from impregnation of a support material with reagent solution, which mitigates the problem of a low amount of PEN in the membrane. For comparison, a membrane produced like described in Figure 30 on average contains 0.81 g PEN per filter, which means ca. 23 mgcm⁻² PEN. This is about three times the amount of active material that the failed glass fiber based membranes featured.

In order to test their capabilities as semi-permeable membranes, they were mounted into a cell that allows the placement of solutions on either side of the membrane (cf. Figure 31). The measurement cell is assembled from two half-cells. The half cells have a circular opening in

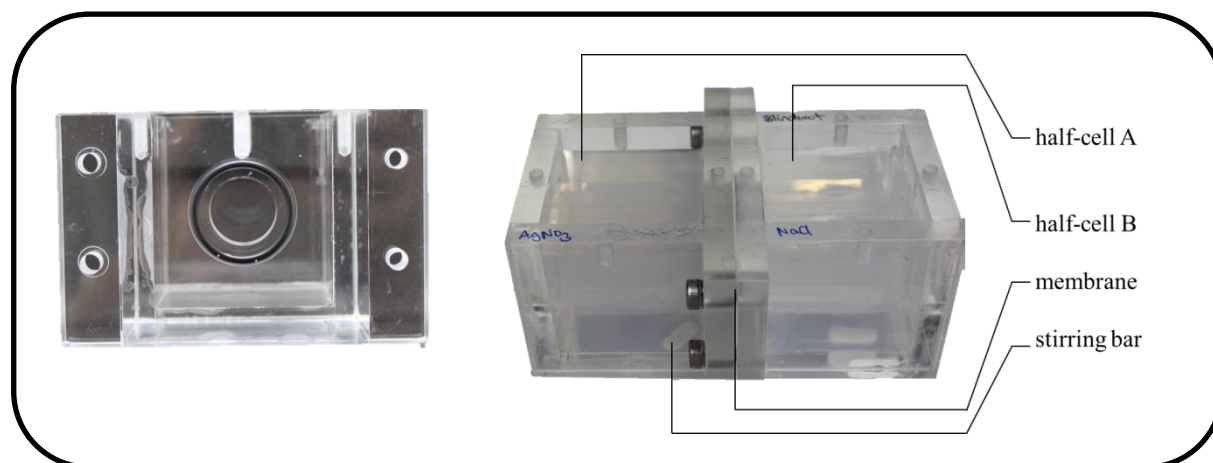


Figure 31: Cell-setup chosen for the permeability testing. Left: the circular opening between the half-cells. Right: The cell has been used to test the system AgNO_3 vs. NaCl in aqueous solution using only a sheet of cellulose paper (blank test). Consequently precipitation/clouding can be observed in both half-cells.

¹² Using an equimolar amount of cadaverine instead of the trioxatridecane and crosslinker B so that 97 % of the amino groups are cadaverine-based (cf. chapter 6.2 for full procedure).

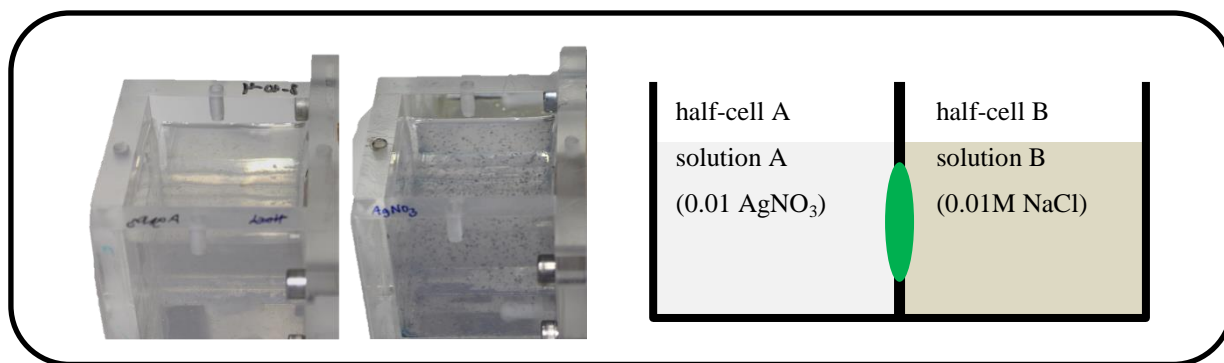


Figure 32: Left: Two half-cells showing the silver chloride test. The first half-cell (left) shows half-cell A several minutes after beginning of the experiment, the second half-cell (middle) after several hours. Right: Testing setup – the left half-cells initially contained a 0.01 M silver nitrate solution (half-cell A) and 0.01 M sodium chloride solution (half-cell B).

one of the walls and no top. The membrane is mounted between the two openings and the half-cells are fixed to each other as depicted in Figure 31 . The resulting measurement cell is then filled with two solutions of different composition in order to test the permeability of the membrane to the ions contained in the solutions (solutions are stirred). Generally, no water leaks out between the half cells, which may be the result of the PENbrane sealing minor gaps due to swelling. Testing was usually carried out over a 24 h period. In order to evaluate the capabilities of the cellulosed based composite membranes, three tests were carried out using different solutions in the half-cells and fresh membranes each time.

In order to test the general applicability of the membrane, the half-cells were filled with 0.01 M silver nitrate and sodium chloride solutions, respectively, as depicted in Figure 32. This approach allows the observation of precipitation behavior in presence of the membranes and to deduce applicability of the membrane from this: If no precipitation is observed, the membrane is not permeable. If precipitate is observed in both half-cells, all ions may pass the membrane. If precipitation occurs on one side only, the membrane is permeable and allows the transition of one ion type only. The half-cell where precipitation occurs allows deduction of the type of ion that can pass the membrane (cf. Table 7). The result of the silver chloride test conducted with M-T is shown in Figure 32. Both half-cells initially contained clear solutions. During the measurement, half-cell A starts to cloud due to silver chloride precipitation. In addition to this, small flakes became visible in the half-cell A, which subsequently took up a deep black color (cf. Figure 32). The reason for this seems to be twofold. First, the fabrication process of the PENbranes effects the formation of a layer of PEN on top of the cellulose sheet (cf. Figure 30). It seems this layer is not stable and detaches from the PENbrane in the form of little flakes when in contact with water. Fortunately this did not seem to impede the function of the rest of the membrane during the 24 h testing period.

Table 7 Possible precipitation behavior and deduction of the permeability of the PENbranes.

| location of precipitation | permeating species | explanation |
|---------------------------|--------------------|--------------------------------------------------------------------------------------------------------------------|
| half-cell A | anions | chloride ions move through the membrane to induce precipitation (nitrate must permeate to maintain charge balance) |
| half-cell B | cations | silver ions move through the membrane to induce precipitation (sodium must permeate to maintain charge balance) |
| both half-cells | both | free transition (observed in the blank experiment, cf. Figure 31) |
| none | none | the membrane is not permeable to any of the tested ions |

Secondly, it can be assumed that silver chloride is adsorbed onto the PEN flakes and will be oxidized to silver oxide over time, resulting in the black color. No precipitation was observed in half-cell B.

Similar results were obtained for M-C. For quantitative analysis, the amount of silver and sodium concentrations were determined using inductively coupled plasma optical emission spectroscopy (ICP-OES). Samples were taken from the solutions before cell assembly (1 in

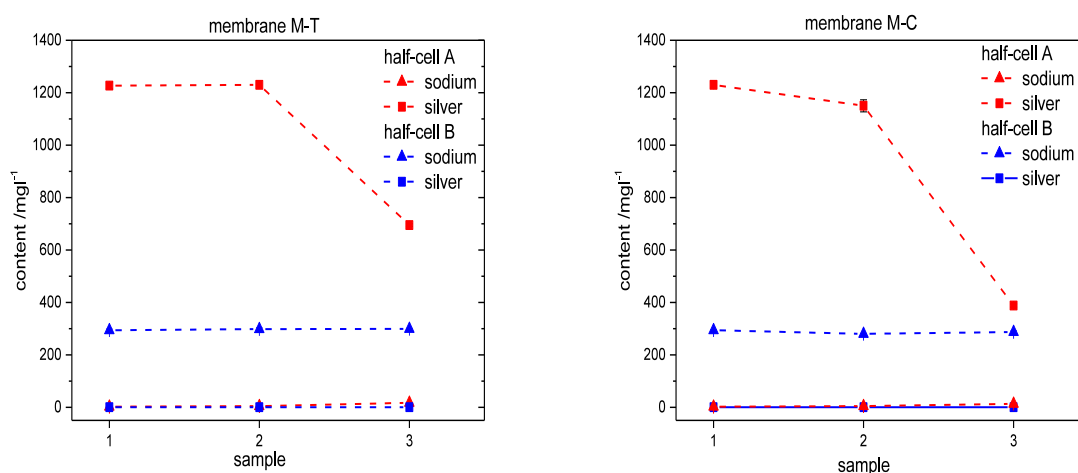


Figure 33: Change of the silver and sodium ion concentrations during the silver chloride test using M-T (left) and M-C (right). Samples taken before assembly of the cell (1), 1 h (2) and 24 h (3) after starting the experiment. The theoretical concentrations (calculated from the concentration of the solutions) of silver and sodium cations are 1078.9 mg l⁻¹ and 229.89 mg l⁻¹, respectively. Also cf. Table A - 1, p. 96 and Table A - 2 p. 97 for further information .

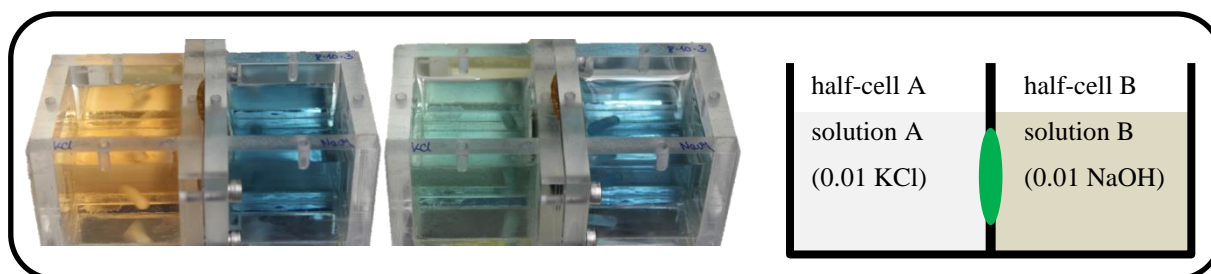


Figure 34: The hydroxide test. Left: Photograph taken of M-C directly after beginning of the test (pH, half-cell A: 5^a half-cell B: 13). Middle: Photograph taken after prolonged testing (pH, half-cell A: 9; half-cell B: 13). Right: schematic of the measurement. Note: a) The low pH in half-cell A at the beginning of the measurement is probably a result of residual acetic acid leaving the membrane. Cf. chapter 2.4.

Figure 33, as reference), one hour after beginning the experiment (2) and after 24 hours (3). The results are shown in Figure 33. Both cells show the same behavior: the concentration of sodium in both half-cells is almost constant, with a minute increase of sodium concentration observable in half-cell A after 24 h (cf. Table A - 1, p. 96 and Table A - 2, p. 97). The silver concentration in half-cell B is negligible, indicating the effective blocking of cations. Silver concentration in half-cell A drops over time. This is a result of silver chloride and silver oxide precipitation which removes the silver ions from the solution. The effect seems stronger in M-C, which may indicate that transition of the anions is easier in M-C compared to M-T. While the silver chloride test revealed that the fabrication method must be further optimized, it also clearly showed that the membranes can act as anion conductors for the chloride and nitrate ions while effectively blocking the silver and sodium cations.

After the general applicability was screened, the ion-conduction behavior of the PENbranes

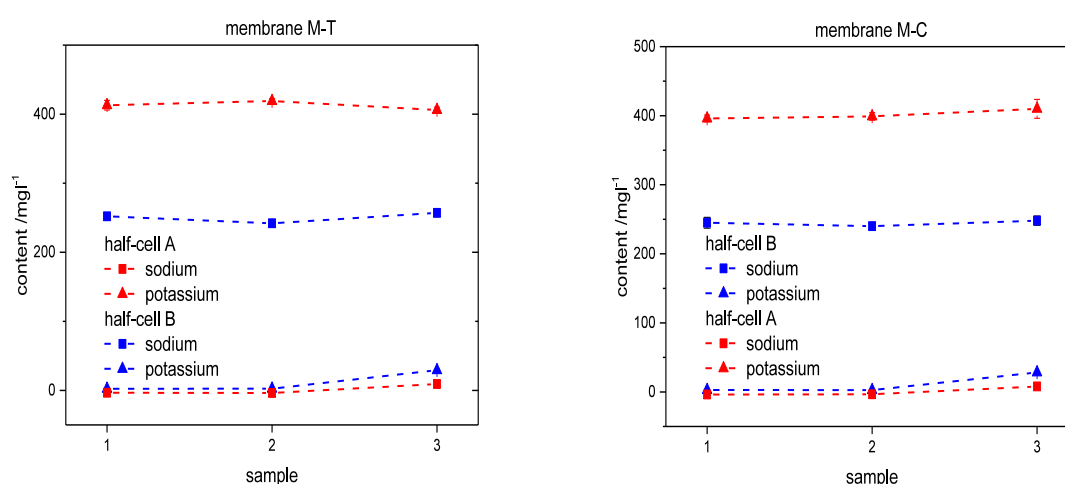


Figure 35: Change of the sodium and potassium ion concentrations during the silver chloride test using M-T (left) and M-C (right). Samples taken before (1) assembly of the cell, 1 h (2) and 24 h (3) after begin of the experiment. The theoretical concentrations (calculated from the concentration of the solutions) of sodium and potassium cations are 229.89 mg l⁻¹ and 390.98 mg l⁻¹, respectively.

under basic conditions was investigated. This time, the cell was filled with 0.01 M potassium chloride solution in one and a 0.01 M sodium hydroxide solution in the other half-cell (hydroxide test). Both solutions contained the same amount of a universal pH-indicator. The test was carried out analogue to the silver chloride test, including submission of samples to ICP-OES. Together this allows monitoring of the cation concentrations and observation of the movement of hydroxide ions. The initial and final state of a typical measurement is depicted in Figure 34. Again, flakes of PEN are detached from the surface of the membrane, albeit without obviously impeding the membrane performance. However, it seems that some of the indicator is adsorbed on the flakes which show a color similar to the solution but of darker shade. Colorimetry reveals that the pH of both half-cells slowly equalizes over the course of the measurement without reaching equilibrium within 24 h. The change of cation concentrations is depicted in Figure 35. The concentrations are almost constant. After 24 h, a small increase in sodium and potassium cation concentration can be observed in the cells that did not initially contain these ions. While this may point to either decomposition in basic media or the slow diffusion of the cations through the membrane, the increase is very small (cf. also Table A - 3 and Table A - 4, p. 97). Generally the hydroxide test reveals that hydroxide ions can shuttle through the membranes. Consequently, this also indicates the transmission of chloride ions to maintain charge balance. Further optimization of the setup is necessary since minute increase of the cation concentrations is also observed. In summary, the membranes also perform well under basic conditions. The results from both the hydroxide and the silver chloride test reveal that anions of various types (chloride, nitrate, hydroxide) can easily permeate the membrane while various cations (sodium, potassium, silver) are blocked or at least severely inhibited from passing through.

In order to observe the behavior of the membranes under acidic conditions, a third test was conducted using 0.01 M sodium chloride and 0.01 M HCl aqueous solutions (half-cell A, and half-cell B, respectively; cf. Figure 36, proton test). In this case ICP-OES can only supply information about the sodium cation. To obtain information about the ion transport, the system was instead monitored by measuring conductivity. Figure 36 compares the change of conductivity during the proton test of both membranes to the change of conductivity if only an unmodified cellulose sheet is used instead of a PENbrane. In the latter case (blank measurement) the conductivity in the sodium chloride half-cell increases by the roughly same amount that the conductivity of the hydrochloric acid half-cell decreases and equilibrium is

reached in less than 24 h. The significant change in conductivity is a result of the large contribution of the proton to conductivity in aqueous systems (Grotthuss mechanism or *proton-hopping*). Similarly, using PENbranes under the same conditions, the conductivity in the sodium chloride half-cell is increasing and the conductivity in the hydrochloric acid half-cell is decreasing. However, the curves do not converge during 48 h.

In order to understand why the average conductivity in presence of a PENbrane seems to be lower than the average (and equilibrated) conductivity without a PENbrane, the following theory is proposed. In the blank measurement the half-cell A initially contains sodium ions and chloride ions and half-cell B contains protons and chloride ions. Dissociation of the hydrochloric acid is complete due to low concentration and high acid strength. Under the assumption that the cellulose sheet does not pose any significant resistance to the transition of any of the ionic species, the ions subsequently mix and the conductivities approach an average value as shown in Figure 36. If a PENbrane is used, the initial composition of the half-cells is the same. Since the previous experiments have shown that the membrane does influence the transition behavior of the different ions, the subsequent changes of conductivity must be interpreted with respect to the membrane.

In order to estimate this possible influence, the composition of the PENbranes, namely the amount of acetate and acetic acid must be approximated. The amount of active material in

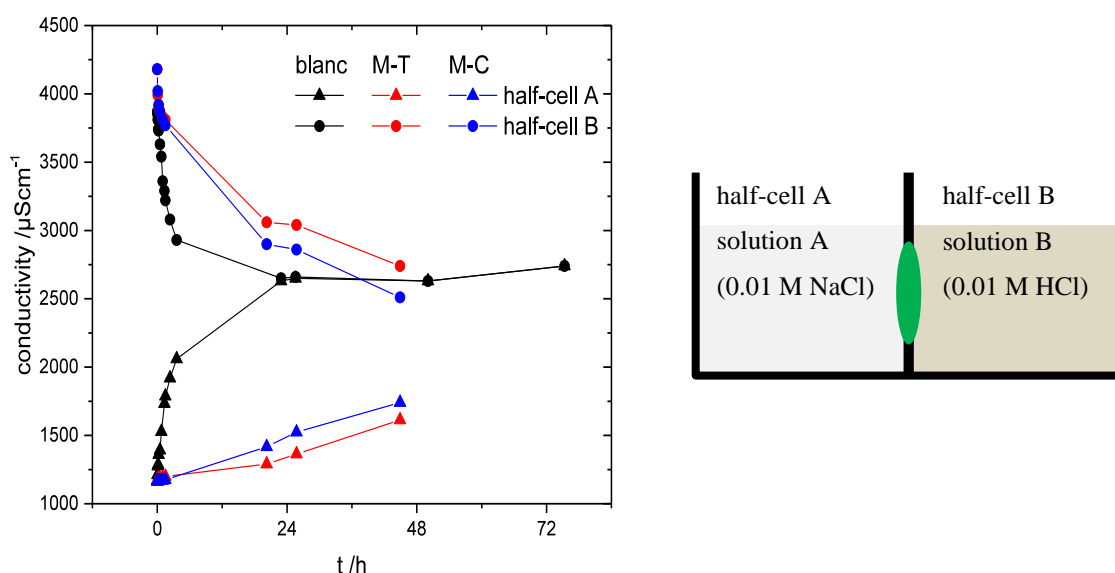
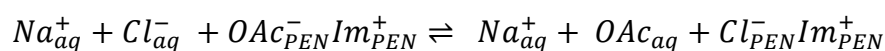


Figure 36: Left: Change of conductivity during the proton test. The graphs show a blank measurement and the measurements of M-T and M-C. Right: Measurement setup and the molar amounts of relevant species in the different half-cells.

each of the membranes is known to be ca. 23 mgcm² and ca. 14 mgcm² or 0.81 g and 0.49 g for M-T and M-C, respectively. From chapter 2.4 it is known that ca. 20 %_m (30 %_m) of the trioxatridecane (cadaverine) based PEN is residual water and acetic acid. If it is assumed that the mass lost completely corresponds to acetic acid (which is probably an overestimation), the amount of free acetic acid per membrane is ca. 0.0027 mol for M-T and 0.0025 mol for M-C. The amount of acetate can be calculated using the weight of one repeating unit based on the trioxatridecane or cadaverine (314.38 gmol⁻¹ and 196.25 gmol⁻¹, respectively cf. Figure 23 for the units). Neglecting the presence of chitosan, the amount of repeating units and consequently the amount of acetate per membrane is 0.002 mol for M-T and 0.0017 mol for M-C. Each half cell is filled with 150 ml of a 0.01 M solution and consequently contains 0.0015 mol of each ion. The numbers are summarized in Figure 37 (right side). The amounts of acetate and acetic acid that can potentially be released from the PENbrane are in the same order of magnitude as the amounts of sodium chloride and hydrochloric acid in solution. Consequently release of acetate ions and acetic acid into the solutions can be expected to influence the conductivity.

As a result of the release of acetic acid (a weak electrolyte) from the PENbrane, the measured conductivity should be higher in both half-cells compared to the blank measurement. This is observed in the case of the half-cell A. The conductivity of half-cell B on the other hand seems to approach a lower value than in the blank measurement. This may be explained by the different acids strength of acetic acid and hydrochloric acid. Previous tests have demonstrated the ability of anions, such as chloride, to traverse the membranes. Consequently, chloride can be expected to diffuse into the membrane and partially replace the residual acetate ions. The now unbound acetate ions can be expected to diffuse out of the membrane to take part in chemical equilibria. The resulting change of conductivity in half-cell A is probably minute since both are strong electrolytes.

Equation 3 Chemical equilibrium of fully dissociated sodium chloride in solution with the PENbrane. The index PEN denotes residency in the PENbrane. Since sodium acetate is a strong electrolyte, dissociation can be assumed.



Comparing hydrochloric acid to acetic acid, however, the dissociation constants are significantly different (cf. Table 2, p. 25). As a consequence of the low dissociation constant of acetic acid and the high dissociation constant of hydrochloric acid, acetate is protonated to form acetic acid.

Equation 4: Assumed chemical equilibrium of fully dissociated hydrochloric acid in solution with the PENbrane. The equilibrium supposedly favors the right side of the equation due to $pK_A(\text{HOAc}) \ll pK_A(\text{HCl})$. The index PEN denotes residency in the PENbrane.



This chemical equilibrium removes protons from contributing to the net conductivity of the hydrochloric acid half-cell by becoming part of acetic acid, which decreases the conductivity.

In order to verify if the superimposition of the above phenomena can be used to explain the behavior observed during the proton test, the solutions in both half cells were replaced with fresh sodium chloride and hydrochloric acid solutions after two days without changing the membrane. The conductivity was measured immediately after the change and after three days. The resulting change of conductivity is depicted in Figure 37. If impurities in the membrane have a significant influence on the change of conductivity, the use of a membrane that was already allowed to equilibrate with chloride containing solutions should result in a different conductivity when the solutions are replaced with fresh ones. The evaluation of this measurement reveals two phenomena. First, the behavior immediately after change of the solutions is indeed different. The two insets in Figure 37 show the behavior of half-cell B directly after first starting the experiment (lower inset) and after exchange of the solutions (upper inset). Both insets display 4 hours time and the region from 3500 to 4500 μScm^{-1} to allow comparison. In the case of the lower inset (first use of the membrane), conductivity

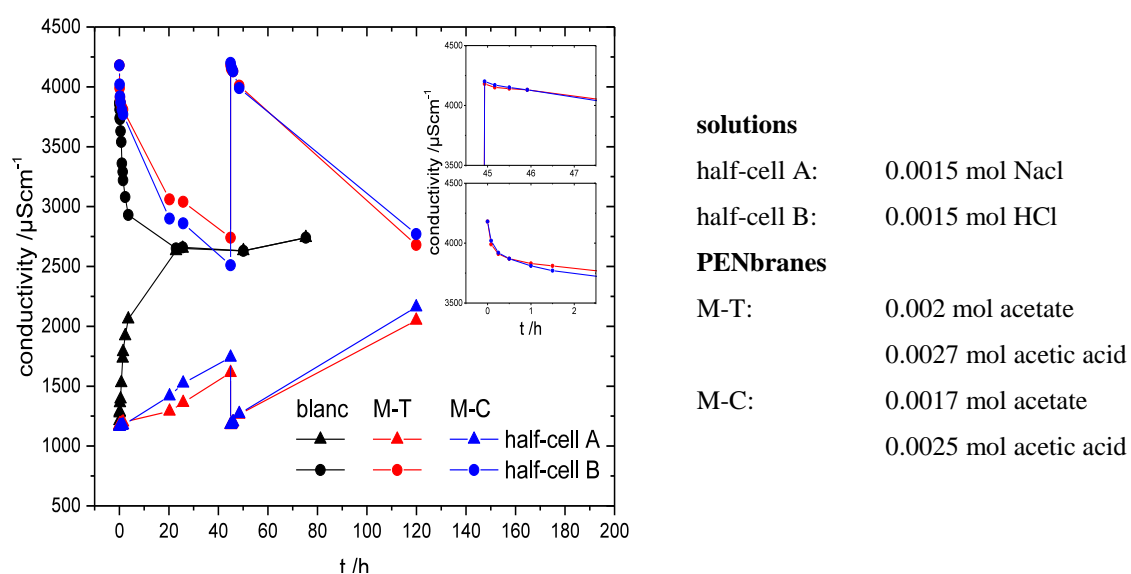


Figure 37: Left: Change of conductivity during the proton test. The graphs show a blank measurement and the measurements of M-T and M-C. After two days the initially used solutions were replaced with fresh ones to observe the effect. The inset displays the change of conductivity in half-cell B immediately after replacing the solutions (upper inset) and after beginning of the experiment (lower inset). Right: Summary of the constitution of the solutions and membranes.

drops by almost $400 \mu\text{Scm}^{-1}$ within one hour. In the case of the upper inset (second use of the membrane), conductivity drops by only $70 \mu\text{Scm}^{-1}$ in the same time.

This indicates that the proposed theory is at least partially justified.

However, the second obvious phenomenon is that in the long term the conductivity approaches roughly the same values in both cases. This indicates that the transition of protons through the PENbranes over long time spans may be possible. While the membrane seems to pose a sufficient barrier to severely inhibit cation transport, the drive of the system to equilibrate concentrations may partially overcome this barrier. It is noteworthy that the membrane still significantly slows down the transport of protons, even though it is swollen with water, which should allow proton-hopping. The conductivity after 48 or 120 h may indicate an equilibrium between the two effects.

3.4 Summary

This chapter has demonstrated the capability of polyelectrolyte networks which were synthesized using the pDRr to act as semi-permeable membranes. By using cellulose based paper towels as a macroscopic support, stable polyelectrolyte network based membranes could be fabricated. The obtained *PENbranes* are able to allow the transmission of anions such as chloride, nitrate, acetate and hydroxide while blocking the transmission of cations such as sodium, potassium and silver. Even protons can be severely repulsed, so they pass through the membrane only partially and significantly slower. As such the *PENbranes* may be applicable as completely sustainable alternatives to conventional membranes in fields such as fuel cells or anion batteries. In order to further optimize the *PENbranes*, various topics should be addressed. The main challenge during fabrication is the use of chitosan as the crosslinker. While the price, abundance and sustainability profile of chitosan are clear advantages, the size and solubility of the polymer complicate fabrication of the membranes. In order to circumvent this, the chitosan may either be depolymerized or replaced by a smaller crosslinker. Both can potentially allow working with lower volumes during fabrication, albeit at a possible loss of sustainability.

4 Magnesium electrochemistry – a *zwitterionic* solution?

The previous chapters have shown both the capabilities and the limitations of the mDRr to modify the cation and anion pattern of sustainable imidazolium ionic liquids and polyelectrolyte networks *during* the ring-formation reaction. One crucial limitation of the mDRr in terms of cation design is the limited possibility to protect of the C2-position of the imidazolium ring (cf. chapters 1.3.3.2 and 2.3).

The following chapter will discuss the relevance of C2-protection in the field of electrochemistry. An alternative route towards a C2-protected imidazolium ring that effects modification *after* the ring-formation reaction will be explored, and the stability of the so obtained molecule as well as its behavior in ^1H , ^{11}B und ^{13}C -NMR-spectroscopy will be discussed. Finally, the scope of its application in magnesium electrochemistry will be investigated with the aim of transferring the sustainable character of imidazolium compounds to post-lithium battery technology.

4.1 Protection of the C2-position¹³

Imidazolium ionic liquids are not considered stable in the presence of reducing agents including magnesium.^[95,96,126] The main reason for concerns about the stability of imidazolium compounds in chemical and electrochemical applications is the special reactivity of the C2-position of the heteroaromatic ring. The carbon atom at this position (cf. Figure 38), located between the two nitrogen atoms, is the most electron deficient position of the whole ring system.^[96,126] As a result, the proton at the C2-position is relatively acidic (pK_A around 22)^[127] and can thus be abstracted using a base. Removal of the proton at the C2-position results in the formation of a carbene (cf. Figure 39). Due to their electron deficiency carbenes are highly unstable and will react even with weak nucleophiles (including bases).^[113] In *N*-heterocyclic carbenes (NHCs), such as those derived from imidazolium cations, the carbene is stabilized by the heterocyclic system which creates comparatively stable molecules that are easier to handle and can even be obtained as stable crystals in some cases^[128]. Due to the special combination of reactivity and stability, NHCs are praised e.g. in catalysis, where they are well known ligands for (transition)metals.^[129]

The C2-position is also prone to electrochemical reduction. Since it is the most electron deficient position of the ring, it is also the site of electrochemical reduction, which occurs at ca. -1.9 V vs. SHE depending on the substitution pattern. The result is a neutral radical species, which rapidly devolves, e.g. into a carbene (cf. Figure 38).^[96,126] Evidently, imidazolium compounds are comparatively easily reduced. In electrochemical applications such as battery electrolytes, the reactivity of the C2-position can be detrimental. Since magnesium readily passivates in the presence of reducible species, this characteristic greatly

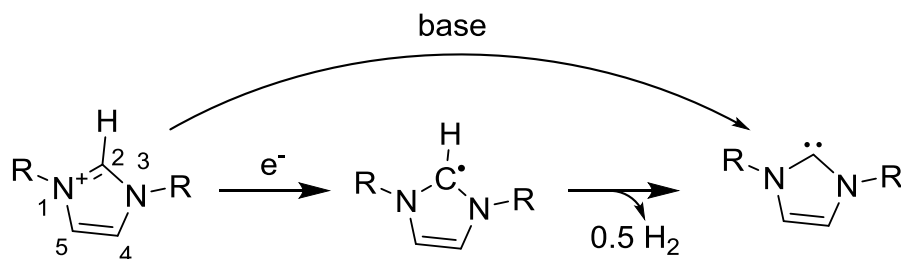


Figure 38: Degradation of unprotected (i.e. C2-protonated) imidazolium molecules. The numbering scheme of the imidazolium ring is displayed on the leftmost compound.

¹³ Parts of this chapter have been published^[125]. Data and figures presented in this chapter are therefore taken from this reference.

hinders the use of imidazolium compounds as electrolytes in batteries based on magnesium and forces the use of compounds based on less sustainable sources. In order to still allow the use of imidazolium compounds and thus transfer their great potential for sustainability to magnesium batteries, the reactivity of the C2-position must be suppressed. A viable approach to do this is the protection of said position. Theoretically the most straight forward way to do this is to substitute the proton at the C2-position with a methyl or benzyl group. Electrochemical reduction of C2-methylated¹⁴ imidazolium compounds takes place at ca. -2.4 V vs. SHE.^[96] C2-methylation also increases the stability towards chemical reduction. Methylated imidazolium compounds are stable in the presence of Grignard reagents and allow electrochemical cycling of them, as opposed to analogous C2-protonated molecules which decompose and show hydrogen evolution.^[21] While C2-protection improves the stability, it usually drastically increases viscosity^[97]. High viscosity incurs decreased conductivity^[98,99] and also complicates the general manageability of chemical compounds, which translates to a big disadvantage, especially in the field of battery research. In the case of weakly interacting counter ions (e.g. I⁻), the reason for the increased viscosity was shown to be related to the mobility of the anion which is hindered by the methyl group at the C2-position.^[97] As a counter measure, bulky anions such as TFSI or FSI can be introduced to decrease viscosity, adding another synthetic step. Also, in these cases, this introduces a fluorinated anion with a very high molecular mass which is a trade-off for electrochemical applications and may generally be considered unsuitable due to its questionable¹⁵ stability in magnesium based systems.^[88]

To use protection of the C2-position to allow the successful applications of imidazolium based systems for magnesium electrochemistry, the concept must be expanded beyond alkyl or aryl groups. A suitable protective group should increase the stability (both chemically and electrochemically) without impeding the viscosity. Due to the limitations of the mDRr in

¹⁴ In the following chapter imidazolium compounds without protected C2-position will be referred to as protonated. Imidazolium compounds with a methyl group at the C2-position will be referred to as methylated. protected may refer to any kind of protection of the C2-position.

¹⁵ Literature lists the successful use of TFSI based systems, if the anion is removed from the immediate coordination sphere of magnesium, e.g. by competing ligands such as glymes^[23].

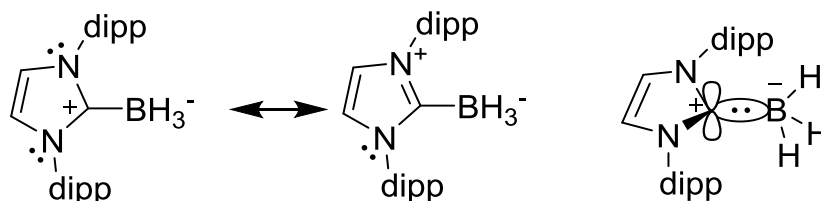


Figure 39: Resonance structures and simplified orbital picture of an imidazolium based NHC-borane. For convenience, the charges are often omitted if the left resonance structure is chosen (adapted from Curran et al.^[130] with permission of John Wiley and Sons).

terms of C2-protection (cf. chapter 2.3), it should be available by a simple synthetic approach, after the formation of the imidazolium ring. Finally, it must be compatible with magnesium.

With the last point in mind, a suitable approach may be found in design strategies used in magnesium battery research. In this regard, the use of borohydride salts as electrolytes seems promising. Among the advantages of those salts are increased reductive stability (they are reducing agents themselves)^[88], compatibility with magnesium and their high reactivity towards water, which allows the removal of trace-water from the system which may otherwise passivate the magnesium surface^[85]. While it seems exotic to protect the C2-position with a boron compound, structures like this are known in chemistry as *N*-heterocyclic carbene boranes (NHC-boranes).^[130] However, a simple and elegant route to introduce a carbon-boron bond to the C2-position of imidazolium molecules was only recently published. Starting from imidazolium iodides, Gardner et al. obtained imidazolium compounds with a BH₃-group at the C2-position by reaction with sodium borohydride.^[131,132] NHC-boranes are reducing agents with applications in various synthetic procedures^[130] and have been suggested as hypergolic ionic liquids for safer rocket fuels (in reaction with strong oxidants).^[133] A NHC-borane derived from imidazolium can be represented using resonance structures, as depicted in Figure 39.^[130]

Similar to NHCs (v.s.), NHC-boranes present a combination of reactivity and stability. As proposed by Gardner et al., the imidazolium is, in fact, first deprotonated at the C2-position and the carbene is formed under hydrogen evolution during synthesis.

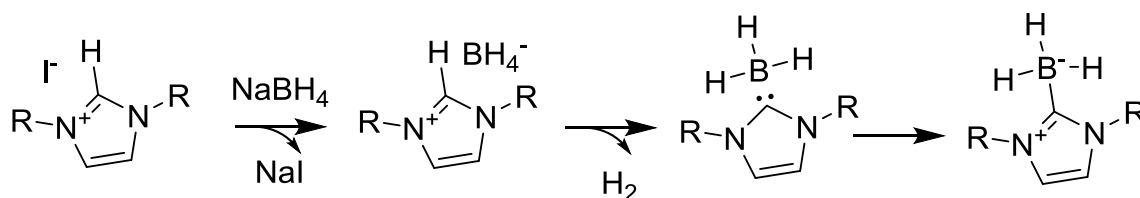
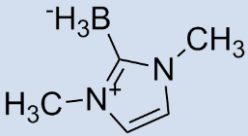
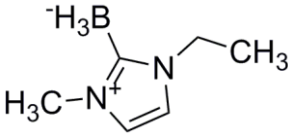
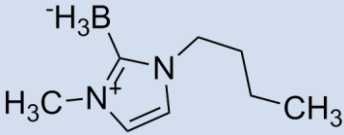
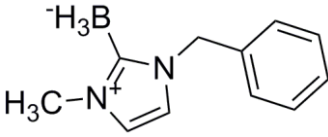


Figure 40: Synthetic scheme proposed by Gardner et al.: The iodide is supposedly exchanged by the borohydride. The carbene is formed from the imidazolium cation under hydrogen evolution and the Lewis-acid Lewis-base pair is formed and consequently collapses to the NHC-borane (adapted with permission from Gardner et al.^[132]; Copyright 2015 American Chemical Society).

Table 8: Overview of the different C2-protected imidazolium derivatives synthesized. Notes: a) yield calculated over both steps of synthesis (cf. chapter 6.2); b) T_G – glass transition; T_M – melting point; c) TGA steps were determined using the maxima of the first derivative of the TGA-curve (heating rate: 10 Kmin⁻¹); d) no melting point observed prior to decomposition. e) product forms crystalline-looking needles; neither DSC nor melting point analysis revealed a melting point prior to decomposition

| name | structure | yield ^a [%] | $T_{G/M}$ ^b [°C] | T_D ^c [°C] (mass loss [%]) |
|-------------------------|-------------------------------------------------------------------------------------|------------------------|---------------------------------------|--------------------------------------------|
| MBH ₃ MIm |  | 30.0 | (solid) ^{d,e} | 243.5 (99.3) |
| EBH ₃ MIm |  | 30.0 | $T_M = 42.2$ (solid) | 241.6 (95.92) |
| BBH ₃ MIm |  | 32.3 | $T_G = -68.3$ (liquid) | 242.6 (82.83) 340.6 (9.56) |
| BenzBH ₃ MIm |  | 7.9 | $T_G = -32.8$ (solid) ^d | 295.2 (88.86) |

It then forms a Lewis-Acid-Lewis-Base pair with the borohydride that consequently collapses into the NHC-borane as shown in Figure 40^[132]. Protection of the C2-position with a borohydride group seems promising for applications in magnesium electrochemistry for various reasons. While the advantage offered by the steric stabilization effect is probably smaller than the one offered by the methyl group, the introduced functionality is a reducing agent and brings a negative charge to a site of the imidazolium ring that is electron deficient and thus prone to reduction. The protective group is also known to be compatible with magnesium. In order to evaluate the effects of this approach towards C2-protection on the relevant physical characteristics, a small library of zwitterionic compounds was synthesized

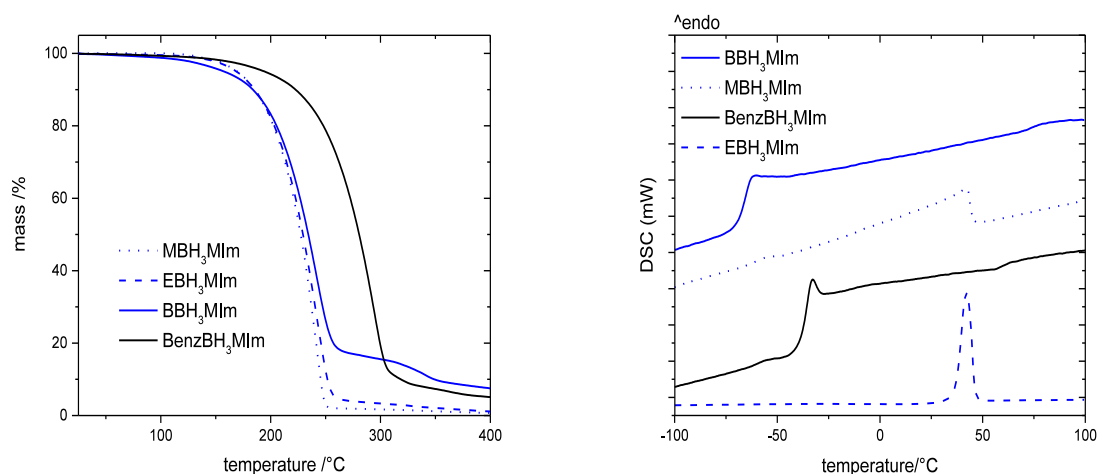


Figure 41: Results of thermal analysis of the four zwitterionic compounds. Left: TGA, right: DSC (intensities are not normalized).

according to an adapted literature procedure^[131,132]. The structures and some general information about the synthesis¹⁶ are given in Table 8.

Thermal analysis reveals that all compounds are stable up to at least ca. 200° C and that out of four compounds only BBH₃MIm is a liquid (cf. Figure 41). The length of the aliphatic side chain seems to have a negligible effect on the decomposition temperature, since the compounds MBH₃MIm, EBH₃MIm and BBH₃MIm possess decomposition temperatures within a range of 6 °C. The slightly different form of the decomposition curve in the case of BBH₃MIm is most probably a result of its liquid state: Even though all compounds are rather hydrophobic, the ability of the liquid to take up water is higher than in the case of the solid compounds MBH₃MIm and EBH₃MIm¹⁷. Overall the decomposition temperatures of all three compounds with aliphatic sidechains show that the thermal stability is sufficient for the application in normal, room temperature based electrochemical systems. Substitution of the aliphatic sidechain to a benzyl group increases the decomposition temperature significantly, which implies that the substitution pattern may be used to further tune and optimize thermal stability. Results of DSC are displayed in Figure 41. With the exception of EBH₃MIm, none of the compounds show a melting point in the measured interval. It can be assumed that

¹⁶ Synthesis cf. chapter 6.2.

¹⁷ Analysis of water content was only carried out by TGA-analysis in the case of NHC-boranes, since they are reducing agents and as such not suited for the standard method for water determination, Karl-Fischer titration, Please also refer to chapter 6.1.

decomposition occurs prior to the melting temperature. The glass transition temperatures are dependent on the substitution pattern (cf. Table 8). MBH₃MIm, a small and symmetric molecule, shows the highest T_G. Substitution of one methyl group by the sterically more demanding benzyl group (BenzBH₃MIm) leads to a lower T_G. BBH₃MIm, which possesses a more flexible and less sterically demanding side chain, presents the lowest T_G and is the only liquid of the set. EBH₃MIm does not show a glass transition. Due to its liquidity, BBH₃MIm was chosen to determine the applicability in magnesium battery electrolytes.

The notion of a zwitterionic liquid is rather counter intuitive, especially after introducing solid imidazolium zwitterions in chapter 2.3. Consequently, the structure of the NHC-Boranes will be discussed here. Huang et al. have conducted X-ray crystallographic analysis to determine the structure of MBH₃MIm and could verify the presence of a carbon-boron bond (1.596 Å). Using electrostatic potential analysis, they could also show that a noteworthy charge separation is present in the molecule whereby the positive charge (0.456 e) is delocalized over the imidazolium ring and the negative charge (-0.456 e) is located at the borohydride group.^[133] To simplify further studies on electrolyte systems and since X-ray crystallographic analysis on liquids is not possible¹⁸, a fast and efficient method for the analysis of the liquid NHC-borane is necessary. A suitable approach for this problem is NMR-spectroscopy: Production of a single crystal is not necessary and the obtained spectral data can be used to easily verify the structures of the obtained molecules, especially in the light of data that can be obtained from literature. Analysis was carried out by combining ¹H, ¹³C and ¹¹B NMR-spectroscopy. The results are shown in Figure 43.

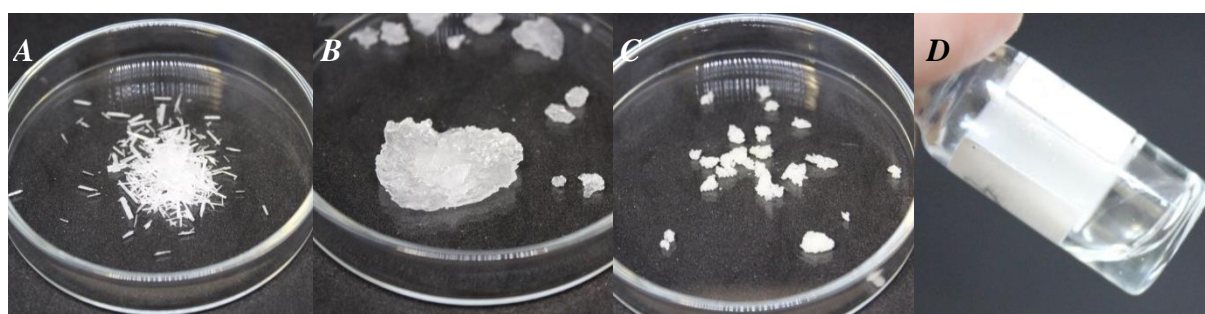


Figure 42: Photographs of the four zwitterionic compounds. A) MBH₃MIm; B) EBH₃MIm; C) BenzBH₃MIm; D) BBH₃MIm. All four are stable to air and water.

¹⁸ It is possible to obtain crystallographic data about low melting ionic liquids using a combination of IR-laser assisted zone melting and low temperature X-ray analysis in specialized equipment.^[134]

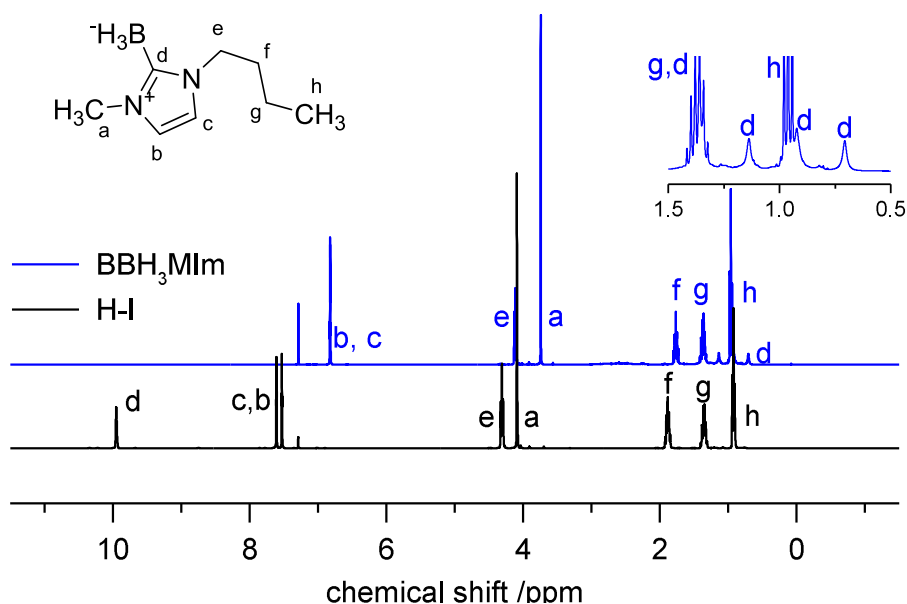


Figure 43: ^1H NMR-spectra of BBH_3MIm and BMImI (cf. Table 9). Peaks are labelled according to the structure given in the top left corner. In the case of BBH_3MIm , the peaks labelled “d” correspond to the protons connected to the boron. The inset shows the region between 0.5 and 1.5 ppm of the spectrum of BBH_3MIm , where those peaks show. The peaks overlap with signals g and h.

Comparing the ^1H -NMR spectra of BBH_3MIm and butyl-methyl imidazolium iodide (H-I, Figure 43; cf. also Table 9), it is obvious that both spectra are very similar. The signals are, apart from minor differences in the chemical shift, mostly the same. The exception is the signal of the C2-proton, which is missing in the spectrum of BBH_3MIm and the presence of additional signals in the spectrum of BBH_3MIm in the range of 0.5 to 1.5 ppm, partly overlapping with the signals of the butyl chain’s protons, which originate from the hydrogens of the borohydride group. There are actually four signals with an intensity of three, as obtained from coupling with one ^{11}B ($J = 3/2$) nucleus according to the multiplicity rule (cf. Equation A - 13, p. 117). ^1H -NMR spectroscopy indicates that the C2-position has been modified but further analysis is needed for verification.

Figure 44 shows the ^{11}B -NMR spectrum of BBH_3MIm and sodium borohydride. Both spectra show only one signal, a quintet and a quadruplet for sodium borohydride and BBH_3MIm , respectively (only the relevant sections of the spectra are displayed). The multiplicity is easily explained by the multiplicity rule: In sodium borohydride the boron nucleus is surrounded by four protons ($J = 1/2$) which means that the obtained signal should be a quintet. In the case of BBH_3MIm , there are three protons and one carbon atom directly bonded to the boron nucleus. However, the natural abundance of carbon ^{13}C is so low that it will not show up in the coupling pattern. The resulting multiplicity of the signal consequently depends on the three

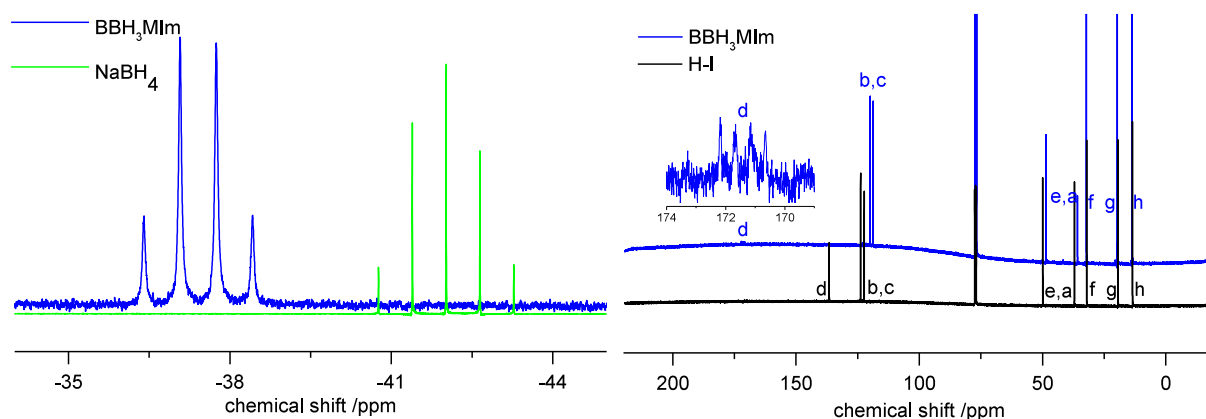
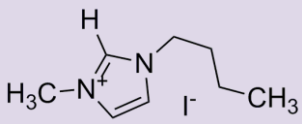
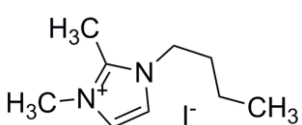
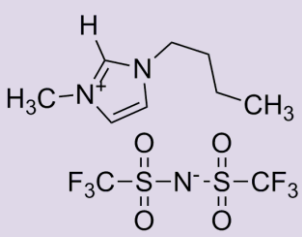
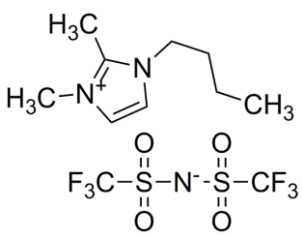
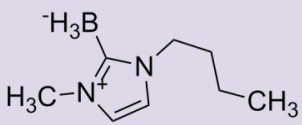


Figure 44: Left ^{11}B -NMR spectrum of BBH_3MIm and NaBH_4 . Spectra were recorded in CDCl_3 and D_2O , respectively, due to solubility requirements. Right: ^{13}C -NMR spectra of BBH_3MIm and H-I , (both in CDCl_3). The peaks are labelled according to Figure 43.

protons ($J = 1/2$) only and is a quadruplet. Information obtained from ^{11}B -NMR spectroscopy allows the fast and simple determination of the purity of the compound (borohydride left over from synthesis). In order to further verify the presence of the carbon-boron bond, ^{13}C -NMR spectroscopy can be used. Similar to the ^1H -NMR spectra, the ^{13}C -NMR spectra of BBH_3MIm and H-I show mostly the same signals (Figure 44, right). In this case, the signal originating from the C2-carbon is seemingly missing on the spectrum of BBH_3MIm . However, as displayed on the inset, the signal is simply transformed into a quadruplet of low intensity (caused by coupling of the carbon nucleus with one ^{11}B , $J = 3/2$). This is a known effect for carbon-boron coupling and relates to the general multiplicity rule and to a relaxation effect.^[135] This shows that NMR-techniques can be used to prove the presence of the carbon-boron bond and verify the structure for the liquid BBH_3MIm (spectra of the other compounds can be found in chapter 6.2).

After verification of the structure of BBH_3MIm by implementing a simple and efficient NMR-screening approach, its characteristics were compared to analogue C2-methylated and protonated imidazolium compounds. In order to do this, a small library of ionic liquids was synthesized and thermal stability, thermal decomposition mechanism, viscosity and electrochemical stability were assessed. In this way, comparison could be carried out despite the fact that literature on imidazolium ionic liquids in the context of magnesium electrochemistry is sparse. Table 9 gives an overview of the synthesized structures.

Table 9: Overview of the ionic liquids and solids used for the conducted study. Notes: i) TGA steps were determined using the onset of decomposition (heating rate: 10 Kmin⁻¹); ii) T_G – glass transition (determined using the inflection of the first derivative); T_M – melting point (peak temperature; T_C – cold crystallization (peak temperature)); iii); electrochemical limits obtained using a stability criterion of 0.15 mA, measured against Li⁺/Li (scan rate 5mVs⁻¹).

| name | structure | T _D [°C] | T _G /T _C /T _M [°C] | red. limit [V vs. Li] | ox. limit [V vs. Li] |
|----------------------|-------------------------------------------------------------------------------------|---------------------|-----------------------------------------------------------------------------------------------------------------|--------------------------|-------------------------|
| H-I |  | 284 | T _G = -68.3 | 0.20 | 3.19 |
| M-I |  | 311 | T _M = 95.0 | - | - |
| H-TFSI |  | 425 | T _G = -85.5 | 0.33 | 5.48 |
| M-TFSI |  | 345 | T _G = -75.4 T _{C,1} = -41.5 °C T _{C,2} = -20.1 °C T _M = 1.3 °C | -0.08 | 5.66 |
| BBH ₃ MIm |  | 202 | T _G = -64.9 | -0.14 | 3.72 |

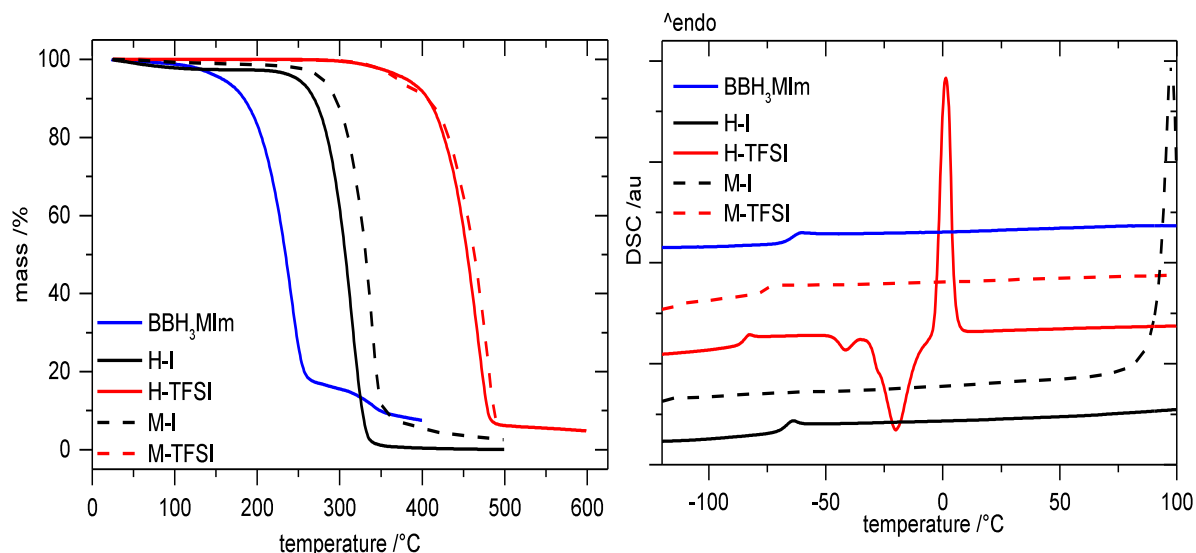


Figure 45: Thermal analysis of the compounds listed in Table 9. Left: TGA; Right: DSC.

The results of thermal analysis are shown in Figure 45. Of the five compounds analyzed, four are liquid at room temperature. Only M-I is a solid¹⁹, showing the onset of a melting peak at 95.0 °C. As for the other compounds, glass transition temperature increases from -85.5 °C to -75.4 °C in the case of H-TFSI compared to M-TFSI. This can be seen as a direct consequence of C2-protection. The effect is even more pronounced in the case of H-I which shows a glass transition at -68.3 °C while the analogue C2-methylated compound M-I is solid at RT and does not qualify as an RTIL (even though it is still an IL). BH₃MIm on the other hand shows a glass transition at -64.9 °C and as such behaves similarly to H-I in terms of DSC. The pronounced peaks in the DSC-curve of H-TFSI are the result of cold crystallization (-41.5 °C, 20.1 °C) and subsequent melting (1.3 °C), which is a known phenomenon for butyl-methyl-imidazolium TFSI.^[136] Interestingly this effect is suppressed by C2-methylation.

Thermogravimetric analysis reveals that the thermal stability of the compounds decreases in the order of M-TFSI \approx H-TFSI > M-I > H-I > BBH₃MIm (cf. Figure 45, left side). The order of stability also illustrates that both cation structure and the anion take an effect onto the thermal stability. In the case of the iodides which are relatively nucleophilic, the protection of the C2-position increases thermal stability, which indicates that decomposition takes place by

¹⁹ Data was obtained promptly after synthesis. After storage for several months, H-I also begins to show signs of crystallization.

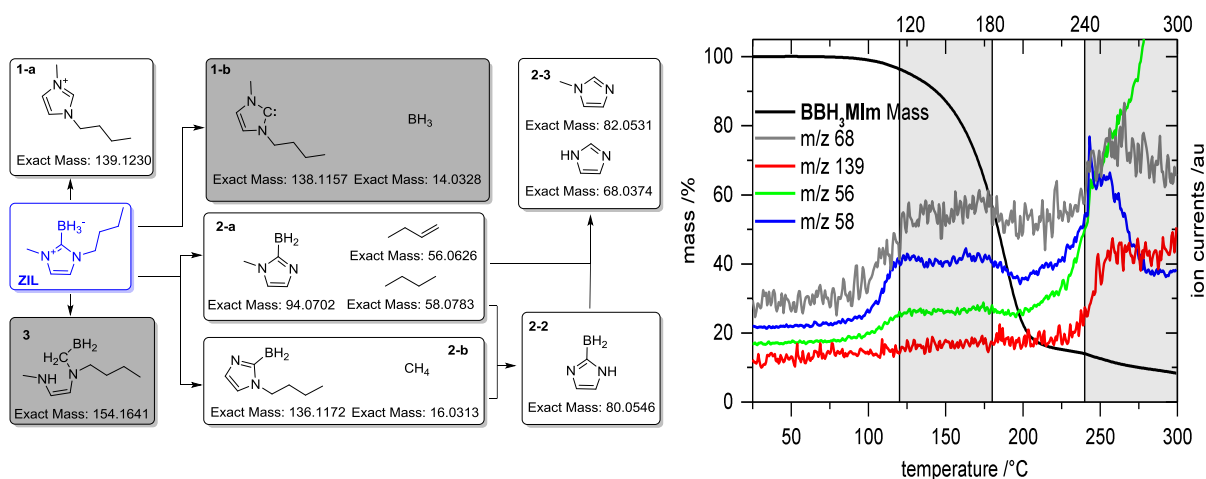


Figure 46: Left: Investigated decomposition pathways. Right: TGA-MS analysis (heating rate 2.5 Kmin^{-1}) revealed that the decomposition seems to take place mainly in two temperature regions. The displayed diagram shows four ion currents that represent the typical shapes of the measurements obtained.

nucleophilic attack of the counter ion. In the case of the TFSI based ionic liquids, the decomposition is more probable to proceed *via* thermal dissociation, and as such the C2-position is less relevant in terms of thermal stability (cf. also chapter 2.2) for the decomposition pathways of imidazolium ionic liquids).^[107]

Comparison with structurally similar ionic liquids highlights the comparatively low thermal stability of BBH₃MIm. While the stability is acceptable for room-temperature applications, the low thermal stability raises the question whether thermal decomposition occurs along the pathways known for ILs. In order to find out, TGA-MS was conducted searching for fragments that would be related to probable decomposition pathways (as depicted in Figure 46). Three main pathways of decomposition were investigated. First, the dissociation of the boron carbon bond, which may lead to the unprotected ionic liquid (1-a in Figure 46) or a carbene (1-b). Secondly the cleavage of the carbon-nitrogen bonds which may cause the butyl chain or the methyl substituent to be lost first (2-a and 2-b, respectively). Dissociation of the boron carbon-bond could be a second step to this (2-3). The decomposition after ring opening due to attack at the C2-position was also investigated (3). As shown in Figure 46, TGA-MS reveals two plateaus or peaks in the ion current graphs. The two plateaus correspond to the main steps of mass loss in the TGA²⁰ curve which take place in between 120 °C to 180 °C and 240 °C to 300 °C. In the first step, mostly fragments related to decomposition pathways 2-a

²⁰ Please note that TGA-MS is measured using a lower heating rate (2.5 Kmin^{-1}) which influences the decomposition temperatures.

are detected in addition to H₂. Also imidazole (m/z = 68) is detected with lower intensity. On the second plateau, both decomposition products related to 2-a and 1-a are detected. No indication of ring-opening (3) or carbene formation (1-b) could be detected. In the latter case, however, this may only be a consequence of the short lifetime of the carbene and not a secure negation of its formation. Together this indicates that the decomposition pathway is not significantly changed, since the main decomposition still takes place by C-N bond cleavage, as is the case in traditional imidazolium cations. It can be assumed that the borohydride group of BBH₃MIm initiates the nucleophilic attack and thus takes the role of the counter ion in traditional imidazolium ILs. The lower decomposition temperature in comparison to the other ILs indicates that the attack by the borohydride group may be favored, possibly due to an intramolecular mechanism. Some things should be noted in addition to this main finding: 1) Recombination of the decomposition products also takes place, as indicated by the detection of dimethyl-2-H-imidazole. 2) From the detected m/z values it is not possible to distinguish the imidazoles of 2-3 in Figure 46 from their isomeric carbenes. Due to the lower thermodynamic stability of the carbenes, it is assumed that the detected species are the imidazoles. 3) No boron compounds could be detected. This may be in analogy to the decomposition of ILs with boron based counter ions, where no boron based compounds could be detected either.^[107] 4) Even though two steps are visible in the TGA-MS analysis, this should not be seen as a proof of a two-step decomposition process. It may simply be the result of the different volatilities of the decomposition compounds.

Viscosity is a major concern when it comes to C2-protection. Handling of BBH₃MIm is conveniently possible using standard pipettes, which indicates a suitable viscosity²¹. In order to compare the ionic liquids, rheological measurements were carried out. The results are depicted in Figure 47 (left side). Measurements were carried out under the driest possible conditions. However, all ILs continually take up water from the ambient atmosphere (cf. Figure A - 10 to Figure A - 17; pp. 109-113). Generally ionic liquids with the TFSI counterion possess lower viscosity, which is within expectation. However, the viscosity of

²¹ It should be noted though that viscosity is too high to determine the density using an oscillating U-tube. Instead, density was estimated by weighing 0.5 ml of the liquid. Measurement was carried out in triplicate and density was determined to be ca. 0.96 gm⁻¹ at 25 °C. Volumes were handled using a positive-displacement pipette.

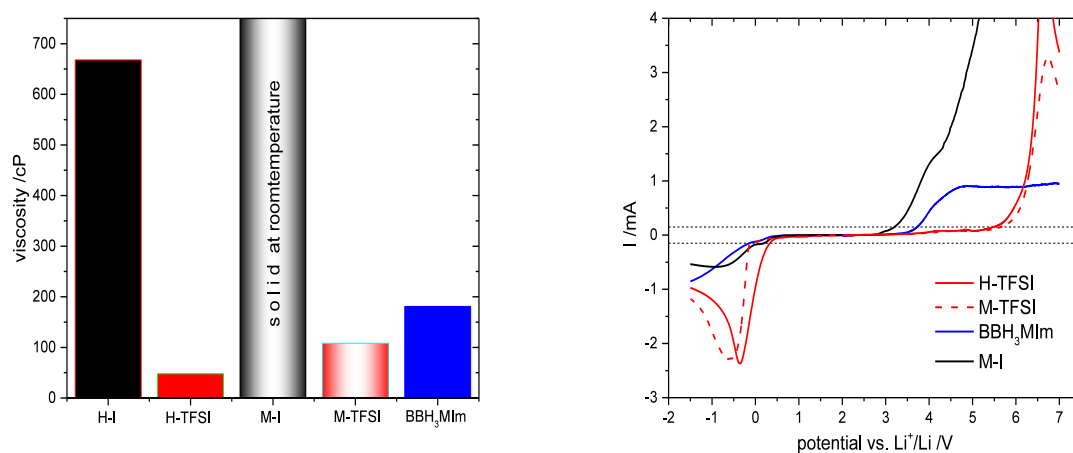


Figure 47: Left: Viscosity of the synthesized ionic liquids. Right: Electrochemical stability vs. Li^+/Li .

C2-methylated M-TFSI is increased by 125 % compared to its C2-protonated analogue (108 cP and 48 cP, respectively). This trend is also visible in the iodides, which generally feature higher viscosity. In this case C2-protection effects the transition from a highly viscous (668 cP) ionic liquid to a solid salt at room temperature. BBH₃MIm demonstrates comparatively low viscosity (181 cP). This low viscosity is achieved without the use of heavy and/or fluorinated counter ions.

With the knowledge that the C2-protection does not negatively affect the viscosity of BBH₃MIm, electrochemical stability was evaluated. As the stability of unprotected imidazolium compounds in the presence of magnesium is questionable, the comparison was carried out using lithium metal as the counter and reference electrode to assure comparability. The results of linear sweep voltammetry measurements are shown in Figure 47 (right side). Electrochemical measurements were carried out on stainless steel working electrodes (316 SS, stainless steel is not corroded by borohydride based electrolytes^[71]) vs. lithium metal electrodes²². Stability was defined to be given below a current threshold of 0.15 mA, the results are summarized in Table 9. Due to its solid nature, M-I was not assessed. Generally the electrochemical stability of the C2-protonated compounds is inferior to the protected compounds. Protection of the C2-position with a methyl group increases the electrochemical

²² Testing was carried out in Swagelok®-type cells. Assembly and description of the cells testing methods cf. chapter 6.1.

stability by ca. 0.5 volts, which is in agreement with literature^[96]. Fortunately, protection with BH_3 has a similar, even slightly better effect on the reductive stability.

Since the synthesized NHC-borane is a reducing agent, it is expected to have low oxidative stability. Still BBH_3MIm outperforms H-I in terms of oxidative stability. H-I starts to decompose at 3.19 V vs. Li^+/Li most probably due to iodide oxidation, while BBH_3MIm is stable up to 3.72 V vs. Li^+/Li . The measurements carried out also illustrate that the oxidative stability is limited by the anion in this case, since the C2-protection does not significantly influence the oxidative stability of the TFSI-based ionic liquids. Both decompose at roughly the same voltage.

Over all BBH_3MIm is a promising candidate for magnesium electrochemistry due to the quite unique combination of excellent reductive stability, low viscosity and possibility of sustainable synthesis. All of this is combined with a low molecular weight in the absence of heavy and/or halide containing counter ions.

4.2 Magnesium electrochemistry in zwitterionic liquid electrolytes²³

After screening several zwitterionic compounds and exploring the promise and limitations of the zwitterionic liquid (ZIL) BBH_3MIm in the previous chapter, this chapter will be focused on the possible application of this zwitterionic liquid in magnesium electrochemistry. In the course of this, electrolyte systems based on BBH_3MIm and H-TFSI will be compared. The TFSI based ionic liquid was chosen as a comparison counterpart due to its prevalence in electrochemistry and to contrast the two compound classes. Also, the available literature data on imidazolium based compounds in magnesium electrochemistry is sparse and partially unreliable²⁴, which encouraged the use of data that was obtained first-hand. After establishing the stability in the presence of lithium in the previous chapter, the first step towards applications in magnesium electrochemistry is the assessment of electrochemical stabilities in the presence of magnesium. To do this, linear sweep voltammetry was conducted using the same stainless steel working electrodes as in the previous chapter and magnesium metal counter electrodes instead of lithium metal. The results are displayed in Figure 48 (left side). Stability was defined to be given below a current threshold of 0.025 mA, and scan rates were chosen to be comparatively slow (5 mVs^{-1}) in order to allow the observation of decomposition. The threshold is lower than in the previous chapter because in contrast to lithium, magnesium is not known to form a constructive solid-electrolyte-interface.^[79] The

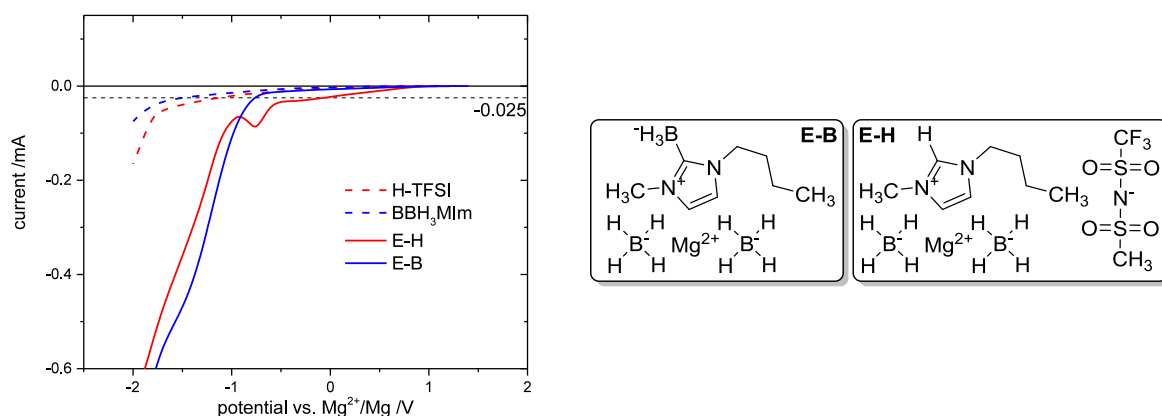


Figure 48: Left: Assessment of stability of the solvents H-TFSI and BBH_3MIm and the electrolyte systems E-H and E-B, based on them, respectively. Right: Schematic of the composition of the electrolyte systems E-B and E-H.

²³ Parts of this chapter are part of a publication in progress. Data and figures presented in this chapter are therefore taken from this reference^[137].

²⁴ Several publications have claimed successful application^[93,94], but could not be reproduced by other groups^[95].

stabilities obtained are -1.49 V and -1.12 V vs. Mg^{2+}/Mg for BBH_3MIm and H-TFSI, respectively (dashed lines in Figure 48, left side). The stabilizing effect of C2-protection with borohydrides also holds true in the presence of magnesium. Also the high stability of the unprotected imidazolium ionic liquid is surprising as several publications describe it as not being stable vs. magnesium.^[21,95] This may indicate that decomposition occurs at lower voltages on stainless steel electrodes than on other electrodes in the case of imidazolium compounds. The type of electrode influences the stability and especially in the case of borohydrides, it is known that e.g. platinum based electrodes facilitate decomposition.^[88] After establishing the general reductive stability vs. magnesium metal, electrolyte systems were prepared by addition of magnesium borohydride to BBH_3MIm and H-TFSI, respectively. Magnesium borohydride was chosen as the electrolyte because it has been shown to be compatible with magnesium^[71,87,89] and because of its structural similarity with BBH_3MIm . The amount of magnesium borohydride was calculated to form a 0.5 mol l^{-1} solution.²⁵ However, upon addition of the magnesium borohydride to the solvents and subsequent stirring, the mixture starts to form bubbles. This is indicative of the formation of hydrogen as a result of the reaction of magnesium borohydride with water. The formed electrolyte systems will consequently have a lower concentration than 0.5 mol l^{-1} and may be regarded as water free within reasonable limits.

The electrolytes display a different behavior in LSV than the pure ionic liquids. Firstly, it is obvious that the magnesium borohydride containing systems show electrochemical activity compared to the neat solvents: both systems show a steep decrease of the curve at roughly the same value of ca. -1 V vs. Mg^{2+}/Mg . This can be attributed to the reduction of magnesium cations at a notable overpotential. Secondly, the electrochemical behavior up to the point of magnesium reduction varies depending on the system. The electrolyte system based on H-TFSI (E-H) shows increased current flow already at positive potentials vs. Mg^{2+}/Mg and also presents a peak prior to the steep decrease attributed to Mg^{2+} reduction. The BBH_3MIm -based electrolyte system (E-B), on the other hand, exhibits unchanged behavior up to the potential attributed to Mg^{2+} reduction. This indicates that E-H is less stable and, since the increased activity starts at a positive voltage vs. Mg^{2+}/Mg , the onset of decomposition begins

²⁵ Concentration chosen in analogy to Mohtadi et al. who used a 0.5 mol l^{-1} solution in THF.^[87]

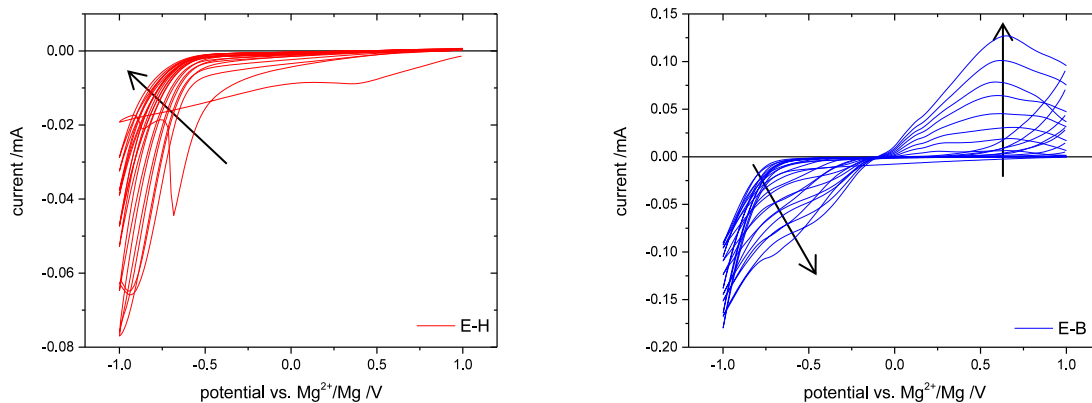


Figure 49: Cyclic voltammetry of the electrolyte systems E-H (left) and E-B (right). Measurements carried out at 5 mVs^{-1} on 316 ss working electrodes vs. magnesium metal counter electrodes. Arrows indicate the evolution of the CV over time. Cycles 1, 5, 10, 20, 30, 40, 50, 60, 70, 80, 90 and 100 are displayed.

fairly early. E-B on the other hand shows excellent stability until the point of magnesium deposition.

To further assess the activity and possible deposition/dissolution capabilities of the electrolyte systems, cyclic voltammetry was conducted in the limits of -1 V to 1 V vs. Mg²⁺/Mg. In the case of E-H, the current at negative potentials vs. Mg²⁺/Mg decreases within 100 cycles until activity is negligible (indicated by the arrow in Figure 49, left). Also, there is no visible activity at positive potentials vs. Mg²⁺/Mg, which indicates the absence of magnesium dissolution. E-B shows more promising behavior. Initially the behavior is similar to E-H. However, over 100 cycles the behavior at negative currents vs. Mg²⁺/Mg gradually changes and activity at positive potentials vs. Mg²⁺/Mg increases, so that after 100 cycles two peaks

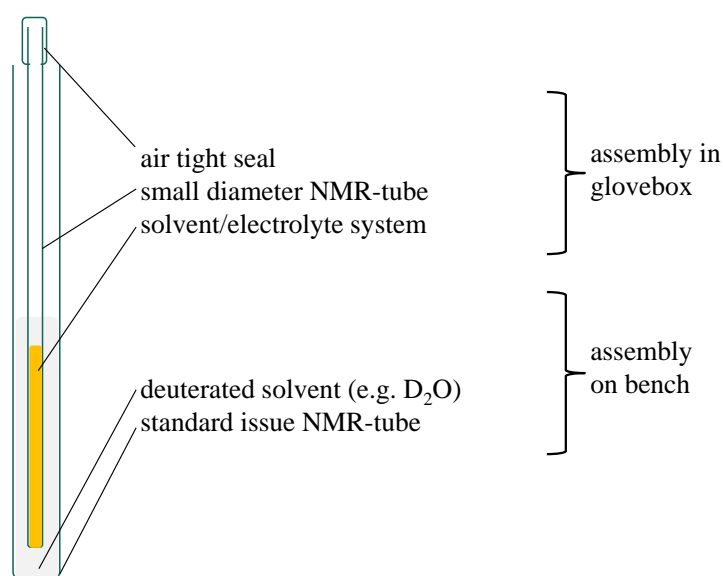


Figure 50: Preparation of samples for bulk NMR-measurements. Since the deuterated solvent is not in contact with the analyte, measurement may be carried out using formally incompatible deuterated solvents.

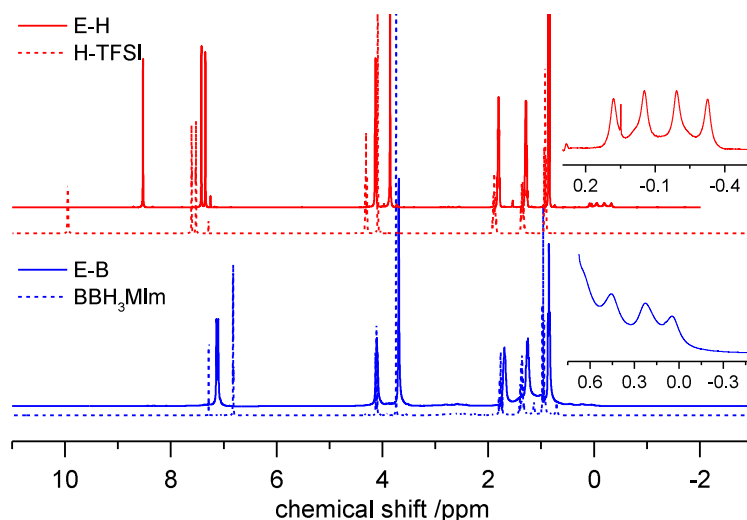


Figure 51: ^1H -NMR spectra of E-H in bulk (red line), H-TFSI in solution (red dashed line), E-B in bulk, (blue line) and BBH_3MIm in solution (dashed blue line). All spectra measured using CDCl_3 .

are visible (indicated by the arrows in Figure 49, right). Assuming that they are corresponding to deposition and dissolution of Mg, the deposition peak is located at ca. $-0.72\text{ V vs. Mg}^{2+}/\text{Mg}$ and the dissolution peak at ca. $0.7\text{ V vs. Mg}^{2+}/\text{Mg}$, which is also a notable overpotential. Still, dissolution as well as deposition start close to $0\text{ V vs. Mg}^{2+}/\text{Mg}$.

Using the approach described in the previous chapter allows the facile determination of any notable decomposition of the solvent, which may occur upon addition of the magnesium borohydride. In order to observe the electrolyte systems under conditions close to reality, the measurements were conducted on bulk samples: The bulk electrolyte system was filled into a small diameter NMR-tube und closed with an air-tight seal inside the glovebox. Since measurement requires the presence of an NMR-solvent for lock and shim procedures, the small diameter tube was inserted into a standard issue NMR-tube with deuterated solvent (cf. Figure 50).

With this setup, ^1H and ^{11}B NMR measurements of the electrolyte systems were recorded (cf. Figure 51 and Figure 52). The ^1H -NMR spectrum of E-H shows the expected peaks corresponding to the butyl-methyl imidazolium (cf. dashed red line in Figure 51) and an additional quadruplet (-0.12 ppm), which arises from the addition of magnesium borohydride to the ionic liquid. No obvious decomposition has taken place. The spectra of E-B and BBH_3MIm , on the other hand, show notable differences. The signals arising from the boron-bound hydrogens seem to be poorly resolved, which in turn negatively affects the peak shape

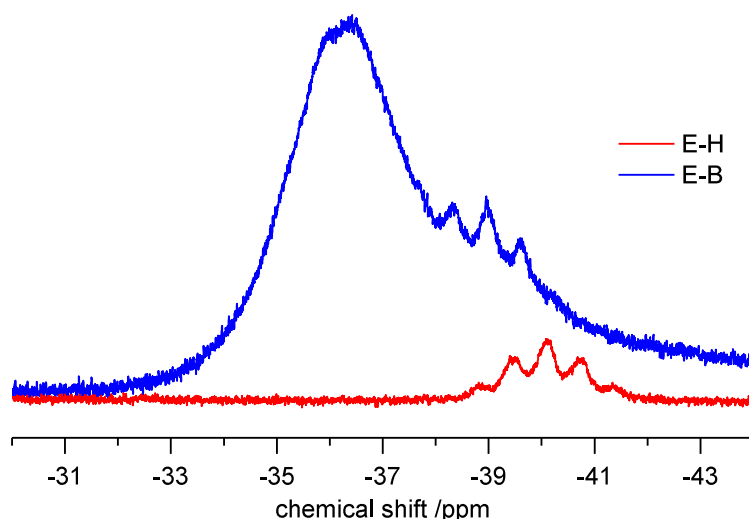


Figure 52: ^{11}B -NMR spectra of the two electrolyte systems.

of the signals they overlap with. The signal that should be arising from the added magnesium borohydride is a barely visible very broad plateau, indicating reduced mobility.

Considering the ^{11}B -NMR spectra, a relatively clear quintet can be observed in the case of E-H and a broad peak with a shoulder peak is visible in the case of E-B. After verifying that the broadened peaks are not a result of instrument failure or the chosen measurement setup²⁶, the reason for the unusual peak-shape was investigated.

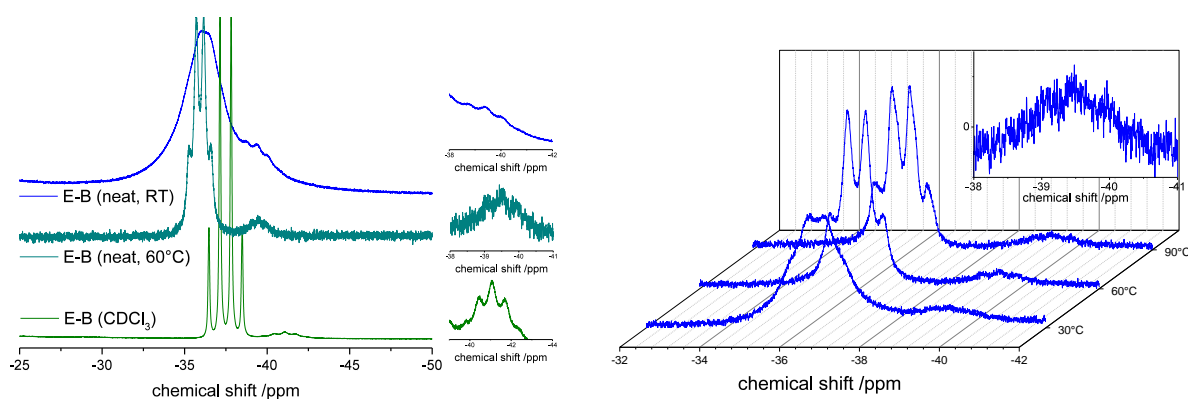


Figure 53: ^{11}B -NMR spectra of E-B. Left: Comparison of bulk E-B at room temperature (dark blue), at 60 °C (teal, middle) and E-B diluted with dry CDCl_3 (inset shows a magnification of the signal corresponding to magnesium borohydride). Right: Comparison of bulk E-B measured at different temperatures. The inset shows a magnification of the signal corresponding to magnesium borohydride (taken from the measurement taken at 90 °C).

²⁶ Measurements conducted on two different machines returned the same result and measurements conducted under different conditions (cf. this chapter) also return results that make instrument failure highly unlikely.

Since similar peaks are usually observed in polymers or other supramolecular assemblies, the peak-shape may indicate decreased mobility resulting from pronounced intermolecular interactions, centering on the hydrogen and boron atoms of the compounds. In the case of weak interactions, heating or dilution with a non-coordinating solvent should disrupt the interaction and result in the detection of defined signals. ^{11}B -NMR spectra recorded under different conditions are displayed in Figure 53. The graph on the left side in Figure 53 compares the ^{11}B -NMR spectrum of the E-B at room temperature (blue line) to a spectrum of E-B taken at 60 °C (teal line) and a spectrum of E-B diluted with dry CDCl_3 (prepared under inert atmosphere, green line). Dilution of the sample effects the formation of two clearly visible signals, a quadruplet and a quintet, which can be attributed to BBH_3MIm and magnesium borohydride, respectively. Increasing temperature has a similar effect but also increases the noise, which makes the identification of the quintet more difficult. The effect of temperature is further visualized on the right side of Figure 53. Increasing the temperature from 30 °C to 60 °C significantly improves the signal resolution. Further increasing the temperature to 90 °C does not further improve the signals. On the contrary, the signal to noise ratio deteriorates and detection of the magnesium borohydride signals is impeded. This process is reversible and upon decreasing the temperature, the signals revert back to the initial state. Both the behavior at elevated temperatures and in dilution implies that the unusual signal shape is indeed the result of pronounced intermolecular interactions. Consequently E-B can be regarded as a highly structured solvent system. This may imply that magnesium electrochemistry could be promoted by entropy based effects similar to the way that dissolution of salts in water is aided by the highly structured nature of water. The interactions can be disrupted by dilution and/or increasing thermal motion within the ensemble. Since only the boron and boron-bonded hydrogen signals are subject to this behavior, the interaction is most probably in place between said boron and hydrogen atoms.

In all spectra of E-B the signal intensity of the magnesium borohydride related peak is suspiciously low. This effect is related to the low molecular weight and density of BBH_3MIm (cf. page 74). At a density of ca. 0.96 gml^{-1} and a molecular weight of 152.05 gmol^{-1} , the content of BBH_3MIm is ca. 6.32 mol^{-1} at 25 °C. In the case of E-H the content of the ionic liquid is ca. 3.41 mol^{-1} at 25 °C ($\rho = 1.43 \text{ gml}^{-1}$; $M = 419.36 \text{ gmol}^{-1}$). Consequently the signal intensities are different due to the different amount of solvent (BBH_3MIm or H-TFSI)

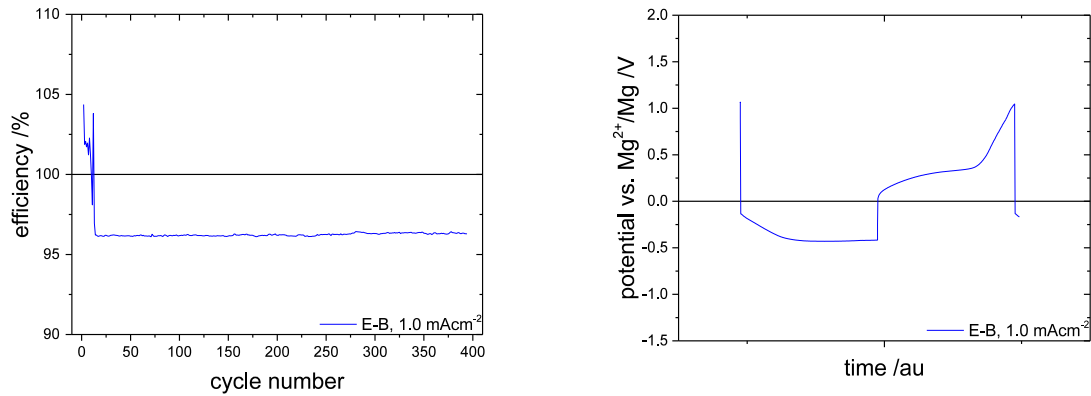


Figure 54: Results of galvanostatic cycling of E-B (SS-WE vs. Mg-CE, 1.0 mAcm⁻²). Left: efficiency vs. cycle number. Right: typical cycle.

compared to the approximately constant amount of electrolyte ($<0.5 \text{ mol l}^{-1}$) in the electrolyte systems.

After investigating the internal conditions of the electrolyte system, the plating and dissolution behavior of both electrolyte systems was investigated using galvanostatic methods and electron microscopy (cf. chapter 6.1 for both).

To summarize the results the efficiency vs. cycle number and a typical cycle²⁷ will be discussed here (also cf. chapter 6.1 for results of cycling). The aim of the study was threefold: i) comparison of E-H and E-B; ii) influence of different current densities (corresponding to

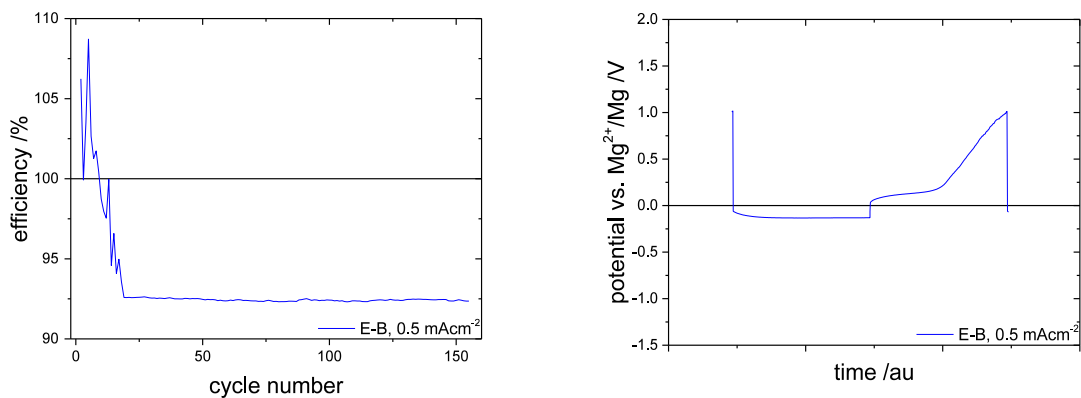


Figure 55: Results of galvanostatic cycling of E-B (SS-WE vs. Mg-CE, 0.5 mAcm⁻²). Left: efficiency vs. cycle number. Right: typical cycle.

²⁷ 1 h negative current and 1 h positive current; no holding or resting times; Current was calculated to fit 0.5, 1.0 or 1.5 mAcm⁻².

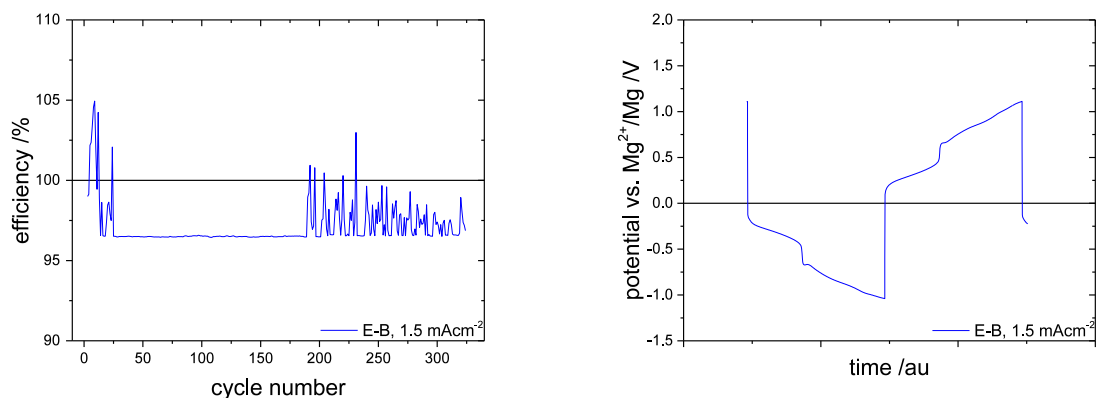


Figure 56: Results of galvanostatic cycling of E-B (SS-WE vs. Mg-CE, 1.5 mAcm^{-2}). Left: efficiency vs. cycle number. Right: typical cycle.

0.5, 1.0 and 1.5 mAcm^{-2}); iii) influence of using different electrode material (Mg vs. stainless steel²⁸).

For the comparison of E-H and E-B, cells were assembled using SS working electrodes and magnesium counter electrodes.

First, the current applied during measurement was adjusted to correspond to a current density of 1 mAcm^{-2} . No reversible cycling was achieved using E-H, which confirms the incompatibility of unprotected imidazolium ionic liquids with magnesium electrochemistry (Figure A - 28, p. 119).

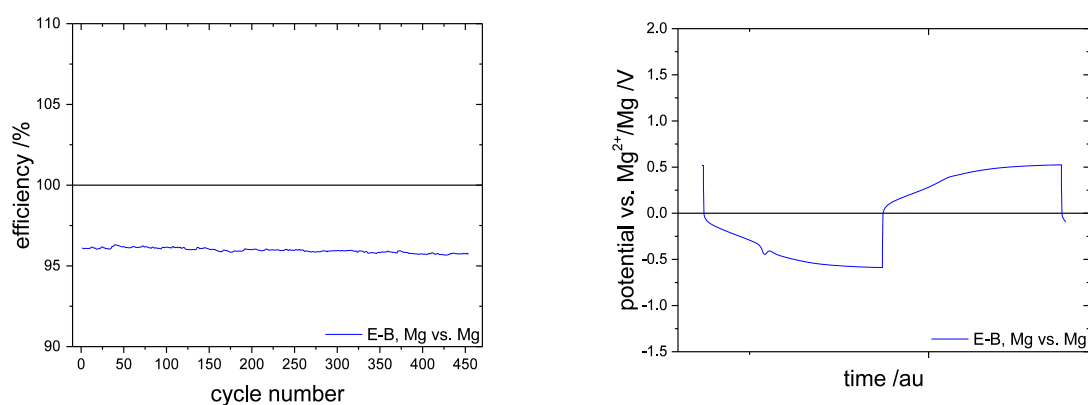


Figure 57: Results of galvanostatic cycling of E-B (Mg-WE vs. Mg-CE, 1.0 mAcm^{-2}). Left: efficiency vs. cycle number. Right: typical cycle.

²⁸ Stainless steel (SS) electrodes used in this work are always fabricated from stainless steel 316. Electrodes are abbreviated as WE (working electrode) or CE (counter electrode), giving the material first (e.g. SS-WE).

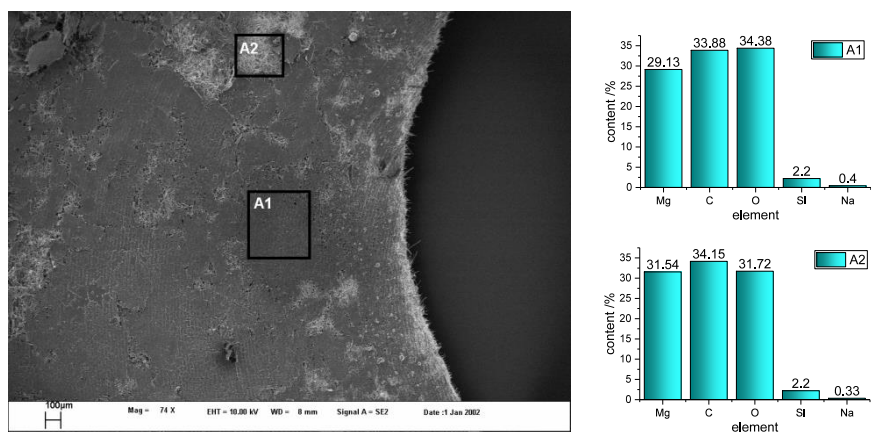


Figure 58: Deposit obtained from galvanostatic deposition of E-B (SS-WE vs. Mg-CE; at 1 mAcm^{-2}). Left: SEM micrograph. Black rectangles indicate the areas of EDX-measurement. Right: Results of EDX-measurements, corresponding to the marked areas.

Using E-B, however, stable cycling was achieved for >245 cycles at an efficiency of $>96\%$ (Figure 54)²⁹. To further investigate the behavior of E-B, the experiment was repeated at different current densities. At a current density corresponding to 0.5 mAcm^{-2} , stable cycling was obtained for >120 cycles at an efficiency of $>92\%$ (cf. Figure 55)³⁰.

Increasing the current density to 1.5 mAcm^{-2} , stable cycling was achieved for up to the 189th cycles at an efficiency $>96\%$, after which the reversibility breaks down (cf. Figure 56). No further optimization of the cells was carried out. Finally, a symmetric cell was assembled using magnesium metal as both the working and counter electrodes (Figure 57). Interestingly,

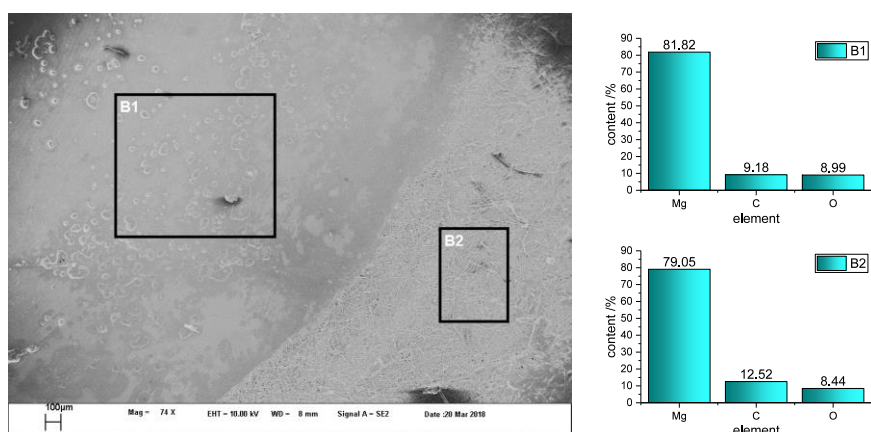


Figure 59: Deposit obtained from galvanostatic cycling of E-B (SS-WE vs. Mg-CE; at 1 mAcm^{-2}). Left: SEM micrograph. Black rectangles indicate the areas of EDX-measurement. Right: Results of EDX-measurements, corresponding to the marked areas.

²⁹ cycling efficiency beyond the 245th cycle stays stable (cf. Figure A - 29, p. 115).

³⁰ cycling efficiency beyond the 120th cycle stays stable (cf. Figure A - 30, p. 116).

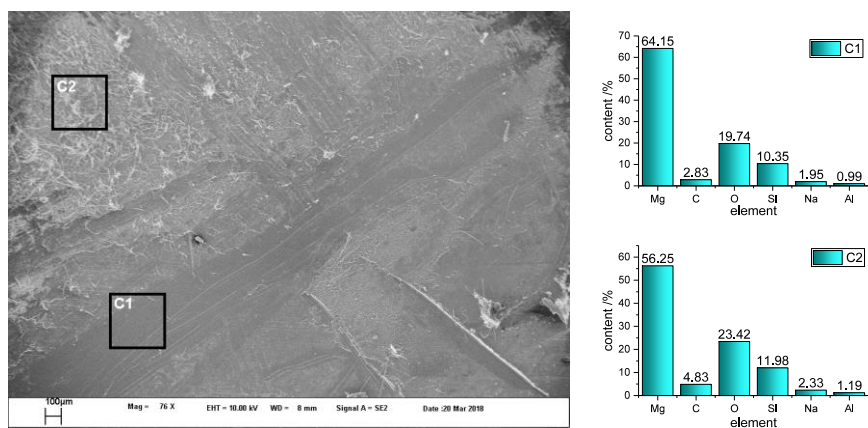


Figure 60: Working electrode used in galvanostatic cycling of E-B in a symmetric cell (Mg-WE vs. Mg-CE; at 1 mAcm^{-2}). Left: SEM micrograph. Black rectangles indicate the areas of EDX-measurement. Right: Results of EDX-measurements, corresponding to the marked areas.

the symmetric cell shows the longest cycling stability for over 450 cycles at an efficiency $>95\%$ and was finally stopped due to scheduled maintenance of the potentiostat before the cell broke down or any irregular cycling behavior became apparent (cf. Figure A - 32, p. 121).

Next to the cycling stability and efficiency, the shape of the individual cycles is noteworthy. On both the deposition and the dissolution period two steps are visible. This behavior is more prominent on the dissolution step but can be seen on both the dissolution and the deposition period. This can be observed on all cycling attempts, with the most prominent example visible in the case of 1.5 mAcm^{-2} . This may indicate that deposition and dissolution is occurring as two consecutive one electron steps.

In order to produce samples for electron microscopy, galvanostatic deposition was attempted

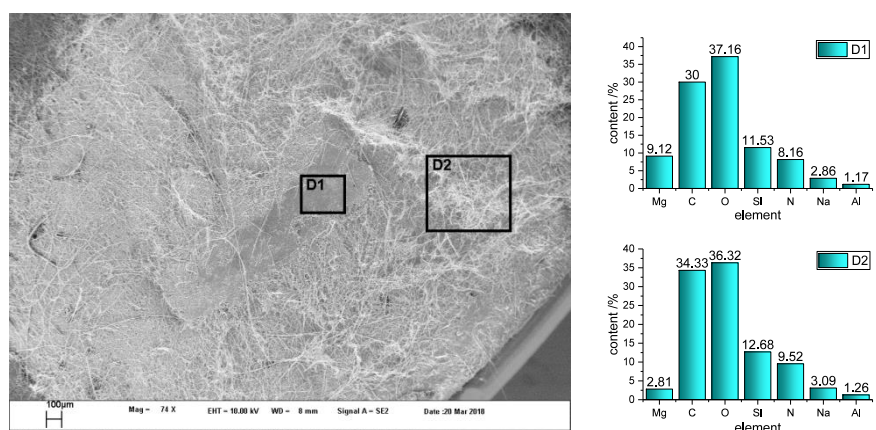


Figure 61: Separator used in galvanostatic cycling of E-B in a symmetric cell (Mg-WE vs. Mg-CE; at 1 mAcm^{-2}). Left: SEM micrograph. Black rectangles indicate the areas of EDX-measurement. Right: Results of EDX-measurements, corresponding to the marked areas.

from both E-H and E-B. In the case of the TFSI-based electrolyte system, no noteworthy deposition was achieved. In the case of E-B, deposition was successful using a Swagelok™-type cell equipped with a SS working electrode and a Mg counter electrode. The so obtained deposit was subjected to scanning electron microscopy (SEM) and energy dispersive X-ray (EDX) analysis. Measurements conducted on the galvanostatic deposit (only one deposition step, no cycling; Figure 58) reveal that magnesium is indeed deposited. However, also relevant amounts of carbon and oxygen are detected which indicates the formation of a blocking layer on the surface. It must be noted at this point that while deconstruction of the Swagelok®-type cells and sample preparation was carried out in the glovebox, transfer of the samples to the electron microscope had to happen under ambient atmosphere.³¹ This is not optimal, since during this time the sample will be contaminated with at least a thin passivation layer due to the exposure to air and ambient moisture.

This is true for all samples and must be kept in mind. Nevertheless spectra A1 and A2 (cf. Figure 58) show that magnesium is easily deposited using galvanostatic methods. In addition to the deposit obtained from galvanostatic deposition, samples were also collected from galvanostatic cycling of E-B using the same cell setup. The EDX-spectra obtained from them (cf. Figure 59) also show that magnesium is deposited during cycling. Comparing spectra B1 and B2 to A1 and A2 reveals that the amount of carbon and oxygen deposited is much smaller in the sample obtained from galvanostatic cycling (cf. Figure 59). This may be the result of a conditioning effect after prolonged cycling. It is also possible that minor impurities decompose in the first cycles and are deposited. In the following cycles this layer would be covered by magnesium, resulting in the difference described above. In any case there does not seem to be a notable negative effect on magnesium deposition. Most interestingly, the

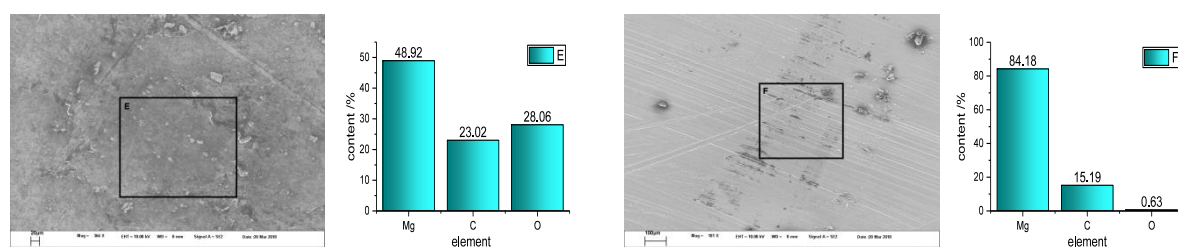


Figure 62: Left side: scanning electron micrograph and EDX spectrum of magnesium metal with a native blocking layer from exposure to ambient atmosphere (scaling bar corresponds to 20 µm). Right side: micrograph and spectrum obtained from magnesium metal thoroughly scraped with a doctor blade (scaling bar corresponds to 100 µm).

³¹ cf. chapter 6.1.

magnesium layer grows into the glass fiber based separator and can be easily peeled off from the SS-WE, to which the metal does not strongly adhere. Consequently the separator was submitted to SEM/EDX testing (the side facing the WE in the battery facing up for scanning). The detected signals corresponding to oxygen and silicon might also derive from the glass fiber filter. While the side facing the WE in the battery was covered by a bare metallic layer, the side facing the CE was simply grey and dull. It should be noted that no corrosion of the SS-WE was observed during the whole testing process.

In samples obtained from the cycling between two magnesium metal electrodes (Mg-WE: Figure 60, separator: Figure 61) the deposited magnesium formed a dense compound with the working electrode that extended into the separator and made simple removal by peel-off impossible. Instead, the filter was removed by cutting/scratching it off the electrode which was only partially successful, as visible in Figure 61. As a result, EDX-analysis detects increased levels of oxygen and silicon in addition to traces of sodium, which originate from parts of the glass fiber filter fixed to the working electrode. The presence of aluminum is probably also a result of the glass fibers present in the measurement area. Figure 61 shows part of the separator that could be peeled off the working electrode. The magnesium content

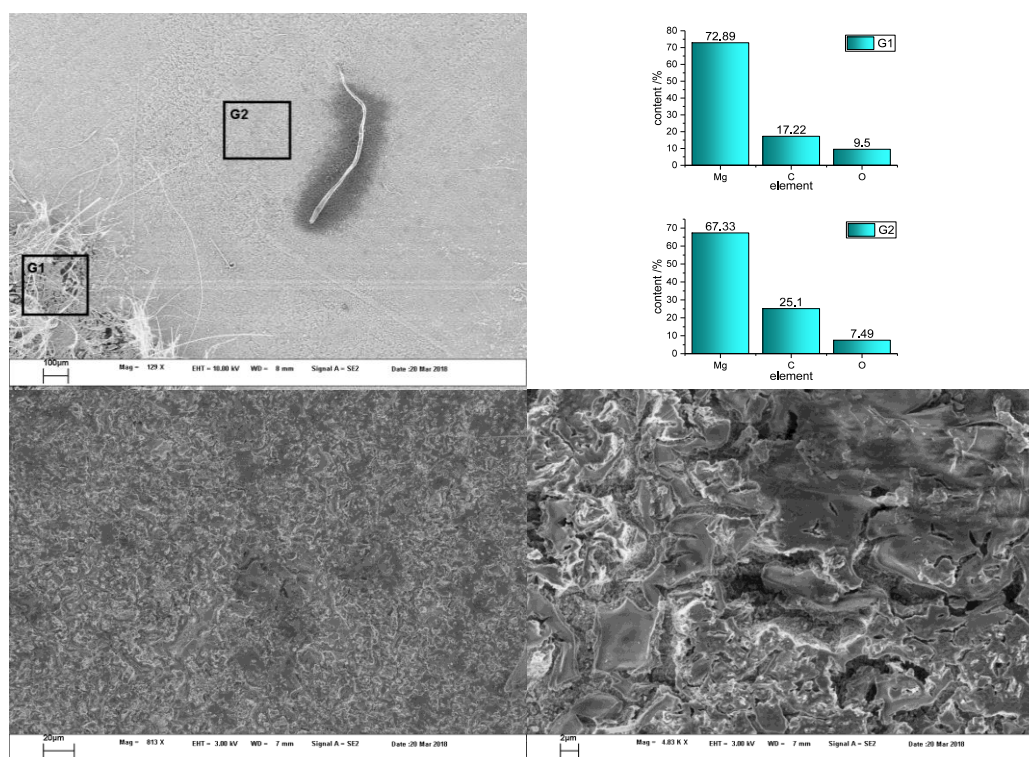


Figure 63: Scanning electron micrograph and EDX-spectra of the counter electrodes used in galvanostatic cycling experiment (SS-WE vs. Mg-CE).

as obtained from EDX-analysis is significantly lower than on the other samples. This is expected, since the magnesium grows from the working electrode to the CE through the separator, and the filter is removed directly above the dense magnesium layer. The presence of nitrogen may be seen as the result of exposition to ambient atmosphere and adsorption, as may be the presence of increased carbon and oxygen peaks resulting from the adsorption of carbon dioxide. Interestingly, decomposition of the electrolyte salt or especially the solvent, which contains carbon and nitrogen, is improbable, due to the complete absence of boron signals in the EDX spectra.

In order to aid comparison, Figure 62 shows the EDX spectra of a magnesium surface covered by a blocking layer (left) and a freshly prepared magnesium surface (right). The native blocking layer contains significant amounts of carbon and oxygen and, notably, more oxygen than carbon. In contrast, the samples obtained from cycling or deposition usually contain more or at least comparable amounts of carbon than oxygen. The cleaned magnesium surface on the other hand contains almost no oxygen. Curiously a significant amount of carbon was detected. To investigate the influence of that the cycling of E-B has on the counter electrodes, SEM/EDX analysis was carried out on respective electrodes used for cycling the electrolyte

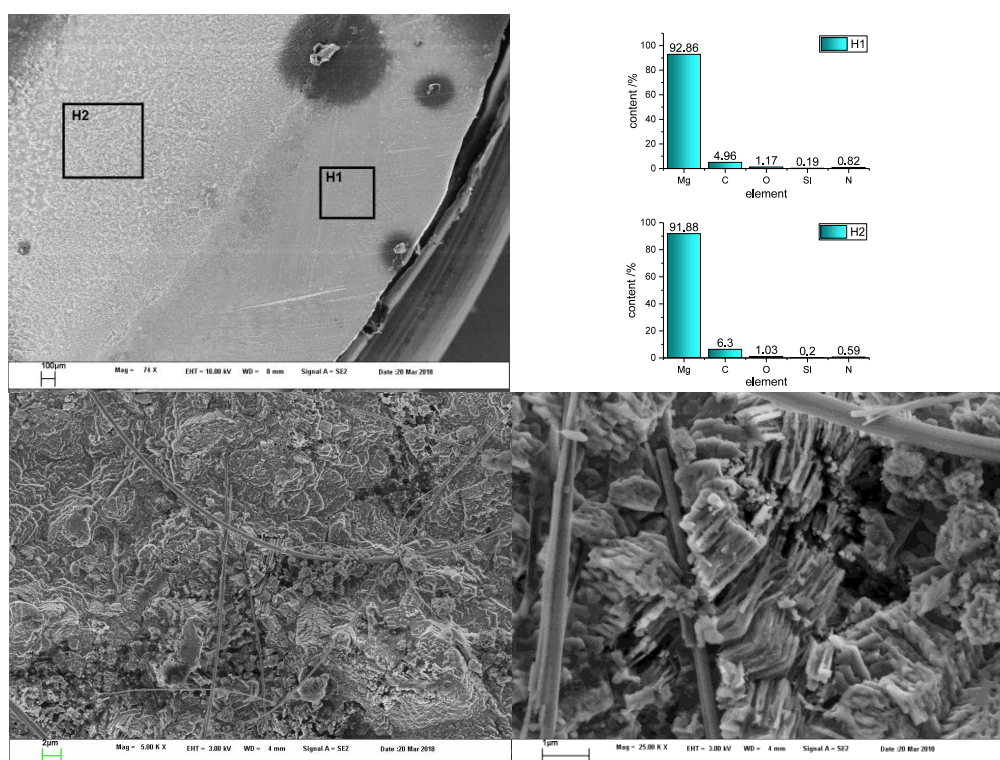


Figure 64: Scanning electron micrograph and EDX-spectra of the counter electrodes used in galvanostatic cycling experiment (Mg-WE vs. Mg-CE)

between SS-WE and Mg-CE, or between Mg-WE and Mg-CE setups. The results are shown in Figure 63 and Figure 64. In both counter electrodes oxygen and carbon are detected by EDX-analysis. Similar to the working electrodes, the counter electrodes demonstrate higher carbon than oxygen content. This is in contrast to the native blocking layer. The amount of carbon and oxygen is lower in the case of cycling between two magnesium electrodes. This may simply be a result of the longer cycling time. Both counter electrodes demonstrate lower carbon and significantly lower oxygen content than the magnesium metal covered by a native passivation layer. The micrographs also reveal that upon cycling, the counter electrode transforms from a plain metal surface (cf. Figure 62 right) to a highly structured state. This indicates that the counter electrode is also subject to frequent dissolution and deposition of magnesium upon cycling.

Overall cycling experiments show the applicability of the electrolyte system based on magnesium borohydride and BBH_3MIm . Electrochemical cycling is possible at high efficiency for several hundred cycles.

4.3 Summary

In this chapter the applicability of an imidazolium based electrolyte system for magnesium electrochemistry was investigated. The common limitation of imidazolium based systems in magnesium electrochemistry can be circumvented by protection of the C2-position with a borohydride group. The resulting *N*-heterocyclic carbene borane is electrochemically stable and allows the reversible cycling of magnesium borohydride on stainless steel and magnesium working electrodes vs. magnesium metal counter electrodes. Even though EDX-analysis reveals the presence of carbon and oxygen in the samples obtained from deposition and cycling of the electrolyte system, no obstructive blocking layer was formed, since cycling at high efficiency (best performance: >96 % efficiency) for a prolonged time was demonstrated. The use of an imidazolium derived electrolyte system for successful magnesium cycling expands the application space of this class of compounds and may allow the transfer of their sustainability to next generation batteries. Using an electrolyte system based on butyl-methyl imidazolium TFSI did not allow successful cycling or deposition of magnesium under similar conditions.

5 Conclusion and outlook

This PhD-thesis has shown how imidazolium based compounds can be synthesized, modified and applied in various ways to bring together their potential for sustainable synthesis with sustainable applications in energy storage.

The first part of this work has shown the great tunability of the modified Debus-Radziszewski reaction (mDRr) to yield ionic liquids with different cation architectures and counterions without the need for multistep or metathesis reactions. Variation of the parameters allows the production of zwitterions and polyelectrolytes. The synthesized products can be obtained using sustainable starting materials with low cost. The used approach is easy to handle and can proceed below, at, or close to room temperature without the use of special conditions such as inert atmosphere. The mDRr is furthermore flow compatible and easily upscalable. Especially the latter simplifies the research of applications on the lab scale.

The second part of this thesis focused on the application of polyelectrolytes synthesized *via* the modified Debus-Radziszewski reaction. The obtained polycations integrate the imidazolium moiety into their backbone. Using chitosan as a crosslinker, polymer electrolyte networks (PENs) were synthesized that show extended swelling behavior in various solvents including water, methanol, and DMSO. The strong cationic charge of the PENs makes them promising candidates for the production of anion conductors. Using cellulose based paper towels as a support, stable membranes were produced that can mitigate the strong swelling of the neat PENs. The obtained membranes demonstrate the ability to conduct anions while almost completely blocking the transition of cations.

The last part of this work explored the application of imidazolium based systems in magnesium batteries. Unfortunately the use of imidazolium compounds as obtained from the mDRr is not possible in magnesium electrochemistry due to the reactivity of the C2-position of the imidazolium ring, which is not stable in the presence of magnesium. However, using a simple reaction it is possible to protect imidazolium compounds at the C2-position with a borohydride group. The obtained zwitterions are remarkable compounds. Especially interesting is the compound butyl-methyl imidazol-2-ylidene borane, which is a zwitterionic liquid. It shows increased reductive stability in systems with lithium or magnesium metal counter electrodes. Reversible magnesium cycling between a stainless steel working electrode and a magnesium metal counter electrode has been achieved (>96 % coulombic efficiency)

using an electrolyte system based on the zwitterionic liquid and magnesium borohydride. This could reopen the door for imidazolium based systems in this next-generation battery technology and make it possible to connect the promising capabilities for sustainable production of imidazolium compounds with the need for more powerful and sustainable batteries.

Without any elaborate synthesis procedure, sustainable imidazolium ionics both in terms of synthesis and in terms of application were described. The simple IL systems are not more complicated than most other ILs investigated today. Research usually focuses either on simple ILs or IL/organic solvent systems, while the use of tertiary and more complex IL systems is still the exception. These more complex systems are attractive due to the possibility of further increased tunability and cost mitigation.³² Such systems are easily available from the mDRr in a one-pot approach by use of amine-mixtures. As such, the approaches described herein are easily extensible to synthesis of more complex systems albeit being made in the same simple and convenient way.

With respect to the PEN based membranes presented in this work, the fabrication process should also be optimized. While chitosan is a cheap and sustainable reagent, its use complicates the fabrication process due to its low solubility. The use of either strongly depolymerized chitosan or a crosslinker of lower molecular weight has the potential to mitigate this. Along with a simplification of the fabrication process, this has the potential to further improve the mechanical characteristics prior to application in energy storage or other fields. Additionally, the system of ion-selective membranes could be expanded to switchable membranes, e.g. by application of lysine which would introduce a carboxylic group to the system. Such a network is expected to change its net charge according to the pH and may allow the fabrication of smart membranes.

Finally, the successful use of an imidazolium derived electrolyte system for magnesium electrochemistry still leads to new questions. The presence of weak interactions between the zwitterionic liquid and magnesium borohydride in the electrolyte systems indicates that the liquid is highly structured. On the one hand, if BBH_3MIm really is highly structured. This suggests that the dissolution of magnesium in BBH_3MIm may be aided by entropic effects,

³² Further reading e.g. Plechkova et al.^[17]

similar to the way that the dissolution of salts in water is aided by the hydrophobic effect. Furthermore, the question of what influence this may have on the magnesium transport within BBH_3MIm is highly relevant. On the other hand, the production of other zwitterions with other substitution patterns or the transfer of this concept to polymeric electrolytes for magnesium batteries could be part of future research in sustainable batteries. In order to produce these battery systems, the compatibility of the zwitterionic species with next generation electrodes based on sustainable materials such as lignin should be evaluated. In any case the curious behavior of the zwitterionic liquid BBH_3MIm is worth further research.

On the small scale this demonstrates that the versatility of imidazolium compounds has not yet reached its limits even though they have received significant attention already. It also illustrates that it is possible to produce ionic liquids in a sustainable way based on reactions that are known for over 130 years.

On the large scale this work aspires to join up with other works in the field of sustainable chemistry that value the importance of a holistic thinking in research and application: Mindful considerations about sustainability must accompany the journey of every chemical from its beginning in synthesis through purification, application, and recycling until the end of its lifecycle and subsequent degradation. This work focusses on the first part of this journey, connecting sustainable synthesis with application in sustainable fields. The assessment of the way ionic liquids influence ecology as they become part of it and begin to degrade is another very important point. In order to design ionic liquids for degradation (as demanded by the 10th principle of green chemistry) more studies about the degradation behavior must be conducted including decomposition in ecology or wastewater treatment. Deploying the strategies developed from the so obtained knowledge will then bring ionic liquids to the next level of sustainability.

6 Appendix

6.1 Methods

Atomic emission spectroscopy

Atomic emission spectroscopy (AES)³³ is based on the fact that for each given element only several energetically excited states are allowed. The transition from one of these states to another is only possible if the change of energy is compensated by absorption or emission, usually observed in the form of radiation. In the case of AES, emission is observed. The specific energies of emission are characteristic for a given element and allow the detection of elements.^[139] Atomic emission spectroscopy is also referred to as optical emission spectroscopy (OES).

Combination of atomic emission spectroscopy with inductively coupled plasma (ICP) creates a very powerful analytic method. The ICP is a gas, usually argon, that is heated by electrical induction to form a plasma (i.e. a hot, partially ionized gas). The plasma operates at temperatures between 6000 and 10,000 K and is an excellent source for thermal excitation. The sample is introduced to the plasma flame as an aerosol and subsequently atomized and excited. At the temperatures present in the plasma, both atomization and excitation are considered quantitative. The resulting atomic emission is detected and allows qualitative and quantitative determination of the analyte, given suitable calibration and instrumentation.

In this work, ICP-OES measurements were carried out using an ICP-OES 8000 (Perkin Elmer). The results of measurements carried out in chapter 3 are given in detail in the following tables.

Additional data

Table A - 1: Silver Chloride test using M-T. Results of ICP-OES: half-cell A initially contained silver nitrate (0.01 M, 1078.9 mg(Ag)l⁻¹ ; half-cell B initially contained sodium chloride (0.01 M, 229.89(Na) mg l⁻¹). Samples taken prior to measurement (1), after 1 h (2) and after 24 h (3). Note: The silver content of the samples used in the silver chloride test are higher than the expected amount as calculated from the concentration of silver nitrate. This is the result of a small inaccuracy during solution preparation.

| sample | silver [mg l ⁻¹] | st. dev. [mg l ⁻¹] | sodium [mg l ⁻¹] | st. dev. [mg l ⁻¹] |
|--------|------------------------------|--------------------------------|------------------------------|--------------------------------|
| A-1 | 1227.0 | 11.5 | 2.16 | 0.09 |
| A-2 | 1230.0 | 0.0 | 4.37 | 0.08 |
| A-3 | 695.0 | 5.0 | 17.1 | 0.25 |
| B-1 | 0.068 | 0.006 | 294 | 5.13 |
| B-2 | 0.087 | 0.001 | 298 | 5.86 |
| B-3 | 0.059 | 0.002 | 299 | 2.08 |

³³ This chapter is based on the text book by Thompson and Walsh.^[138]

Table A - 2: Silver Chloride test using M-C. Results of ICP-OES: half-cell A initially contained silver nitrate (0.01 M, 1078.9 mg(Ag)l⁻¹ ; half-cell B initially contained sodium chloride (0.01 M, 229.89 mg(Na)l⁻¹). Samples taken prior to measurement (1), after 1 h (2) and after 24 h (3). Note: The silver content of the samples used in the silver chloride test are higher than the expected amount as calculated from the concentration of silver nitrate. This is the result of a small inaccuracy during solution preparation.

| sample | silver [mg l ⁻¹] | st. dev. [mg l ⁻¹] | sodium [mg l ⁻¹] | st. dev. [mg l ⁻¹] |
|--------|------------------------------|--------------------------------|------------------------------|--------------------------------|
| A-1 | 1230 | 11.5 | 2.16 | 0.09 |
| A-2 | 1150 | 23.1 | 4.23 | 0.02 |
| A-3 | 388 | 5.9 | 13.5 | 0.15 |
| B-1 | 0.068 | 0.006 | 294 | 2.52 |
| B-2 | 0.041 | 0.001 | 280 | 1.53 |
| B-3 | 0.026 | 0.0001 | 287 | 5.29 |

Table A - 3: Hydroxide test using M-T. Results of ICP-OES: half-cell A initially contained sodium hydroxide (0.01 M, 229.89 mg(Na)l⁻¹ ; half-cell B initially contained potassium chloride (0.01 M, 390.98 mg(K)l⁻¹). Samples taken prior to measurement (1), after 1 h (2) and after 24 h (3).

| sample | sodium [mg l ⁻¹] | st. dev. [mg l ⁻¹] | potassium [mg l ⁻¹] | st. dev. [mg l ⁻¹] |
|--------|------------------------------|--------------------------------|---------------------------------|--------------------------------|
| A-1 | 252 | 3.1 | 2.33 | 0.12 |
| A-2 | 242 | 1.5 | 2.47 | 0.16 |
| A-3 | 257 | 1 | 29.2 | 0.15 |
| B-1 | -3.38 | 0.098 | 413 | 7.0 |
| B-2 | -3.78 | 0.38 | 419 | 3.6 |
| B-3 | 9.2 | 0.58 | 406 | 4.0 |

Table A - 4: Hydroxide test using M-C. Results of ICP-OES: half-cell A initially contained sodium hydroxide (0.01 M, 229.89 mg(Na)l⁻¹ ; half-cell B initially contained potassium chloride (0.01 M, 390.98 mg(K)l⁻¹). Samples taken prior to measurement (1), after 1 h (2) and after 24 h (3).

| sample | sodium [mg l ⁻¹] | st. dev. [mg l ⁻¹] | potassium [mg l ⁻¹] | st. dev. [mg l ⁻¹] |
|--------|------------------------------|--------------------------------|---------------------------------|--------------------------------|
| A-1 | 245 | 7.8 | 2.77 | 0.07 |
| A-2 | 240 | 3.8 | 2.66 | 0.05 |
| A-3 | 248 | 6.7 | 28.2 | 0.67 |
| B-1 | -3.7 | 0.31 | 396 | 4.9 |
| B-2 | -3.4 | 0.10 | 399 | 5.5 |
| B-3 | 8.0 | 0.50 | 410 | 13.7 |

Electron microscopy

Scanning electron microscopy (SEM)

Visual perception is the most important feed of information about the world around us and the desire to *see* is part of our approach to learn and understand³⁴. To see means to distinguish two objects, which are separated by a distance Δx . The ability to do so is dependent on the wavelength λ used to observe an object, as described by the Rayleigh criterion:

Equation A - 1: The Rayleigh criterion. The ability to resolve two points separated by Δx is dependent on the wavelength λ .

$$\Delta x \approx \frac{0.6 * \lambda}{\sin \alpha}$$

where α is the angle of the aperture, a criterion of the used lens. Equation A - 1 applies to the human eye as well as to any other optical instrument. If the measurement setup is assumed to be optimized, λ will be limiting parameter. Since the optical perception of the human eye is limited to ca. 300-700 nm, special instruments are necessary to obtain accurate visual data below the resolution power of optical microscopes. Those instruments use wavelengths smaller than visible light and consequently include the translation of the so obtained data into a perceivable image. The most important technique in the field of materials science in this regard is electron microscopy, which uses electrons to obtain the image. In order to achieve this, an electron beam is produced and focused using suitable electron optics. The focused electron beam is then directed at the sample where the electrons either pass through the sample or are subject to scattering effects. Scanning electron microscopy relies on electrons that do not pass through the specimen but that are either backscattered or released from the sample through other means of interaction, to produce an image of the sample at much higher resolution than possible in classical microscopy.

In this work, a LEO 1550 Gemini microscope and HR-SEM on a JEOL JSM-7001F field emission scanning electron microscope with an Oxford energy dispersive detector is used for SEM. Samples were prepared in a glovebox, washed twice with THF and dried briefly in vacuum. Transfer to the electron microscope was carried out as swift as possible but required exposition of the samples to ambient atmosphere.

Energy dispersive X-ray spectroscopy (EDX)

Interaction of the electron beam with the sample can result in the removal of electrons from the inner orbitals of the atoms constituting the sample³⁵. When the resulting vacancies are filled by electrons from the outer orbitals, X-rays are emitted. The energies of this radiation are element-specific and allow the determination of the elements present in the sample. In order to effect the emission of characteristic X-rays, the acceleration voltage of the electron beam must usually be higher than in standard imaging. In this work EDX is conducted using an

³⁴ This chapter is based on the textbook by Egerton, R.^[140] and the introduction to SEM by JEOL.^[141]

³⁵ This chapter is based on the introduction to SEM by JEOL.^[141]

acceleration voltage of 10kV. The same voltage was usually used for the collection of SEM-micrographs due to the high beam-stability of the samples. Experiments were carried out on the instrument of the previous chapter.

Mass spectrometry (MS)

Mass spectrometry (MS) is a method that detects molecules or fragments of molecules based on their mass to charge ratio (m/z).³⁶ Consequently, at a basic level, mass spectrometry is based on the steps of first generating ions by a suitable method and second detecting the ions in terms of their m/z and abundance. Several things should be noted on this occasion. I) Signals in MS are generally obtained from the physical interaction of actual molecular ions (or fragments) with the detector. One event at the detector thus corresponds to one molecule or fragment. Consequently, MS is a statistical method. II) As a consequence samples are consumed upon measurement. III) The above puts mass *spectrometry* in contrast to methods of *spectroscopy*. A very large variety of MS instrumentations is available from the combination of different ion sources, mass analyzers and detectors. Even though MS is a technique capable of providing much information about the analyzed molecule, this work relies on the ability of MS to detect the masses of molecular ions.

Using an ionization technique that leaves the molecule intact in conjunction with a high accuracy mass analyzer allows the detection of the exact weight of a molecular ion with high precision. This is very useful, since from a molecular mass of sufficient accuracy it is possible to calculate the elemental formula. Corollary, high accuracy MS can be used to verify the successful synthesis of molecular structures. This is especially alluring when substances cannot be completely purified from residual solvents and/or elemental analysis is not suitable, as in the case of ionic liquids.

The ionization method used in this work is the electron spray ionization (ESI), a so called soft ionization method which allows the ionization of intact molecules from the condensed phase (i.e. from solution). In ESI the sample is dissolved in a suitable solvent and subsequently introduced to a spray needle. A high voltage is applied to the needle and effects the formation of *charged* droplets. Further evaporation of the solvent is effected by a suitable method, e.g. the use of a hot inert gas, or a heated capillary. After reaching a threshold size, the charge of the droplet becomes large enough in relation to its surface to effect *coulomb explosion*, i.e. many very small droplets are formed. Two different mechanisms have been proposed for the subsequent ionization. I) Ions eventually leave the surface of the charged droplets due to electrostatic repulsion (ion evaporation theory). II) Eventually all solvents molecules will evaporate, leaving the molecular ion behind (charge residue theory)^[142].

All MS spectra in this work were measured using a Waters QToF Xevo G2-XS mass spectrometer connected to a Waters Acquity H-class HPLC for sampling with two exceptions: The spectrum of BBH₃MIm was recorded on a Bruker MaXis Esi-Q-TOF. The spectrum of E-2 was recorded on a Agilent Technologies Series 1260 Infinity II equipped with an LC/MSCT mass analyzer. All spectra were recorded using acetonitrile as the solvent and formic acid as the ionization agent.

³⁶ This chapter is based on the review of Awad et al.^[142] and the textbook by J. Gross.^[143]

Differential scanning calorimetry (DSC)

Calorimetry is the measurement of heat.³⁷ The use of calorimeters allows the determination of the heat related to many physical and chemical processes such as reactions, phase transitions, solvation and dilution. Consequently various instrumentations are used.

Differential scanning calorimetry measures the difference of heat flow rate between a sample and a reference that are subjected to a temperature program. This means that DSC is always carried out using a setup featuring a reference and a sample. The measurement is carried out by comparing the behavior of both samples subjected to the same treatment. Two modes are generally applied: heat flux DSC and power compensated DSC. In heat flux DSC, the temperature difference between the sample and the reference is measured and expressed as the measurement signal. In power compensated DSC two thermostatically controlled micro-furnaces are used, one to carry the sample, the other to carry the reference. Both furnaces are heated electrically, and the power is monitored while a temperature program is applied. As the temperature program is followed, differences in thermal behavior will result in different amounts of electrical power needed for heating.

DSC in this work was carried out using a Mettler-Toledo DSC1 STARe system. All analysis was carried out using the STARe software V9.30. Measurements were carried out using a heating rate of 10 Kmin⁻¹.

Thermal programs

In chapters 2.2 and 2.3, DSC was conducted under nitrogen atmosphere by first heating the sample from RT to 130 °C, then cooling to -80 °C. The sample was again heated to 130 °C and cooled to -80 °C to erase thermal history. The sample was finally heated to 130 °C to assess thermal behavior and subsequently cooled to RT. Measurements were carried out using a heating rate of 10 Kmin⁻¹ and a holding time of 10 min between the different steps.

In chapter 2.4, DSC was conducted under nitrogen atmosphere by first heating the sample from RT to 160 °C. The sample was held at this temperature for 30 min to allow residual acid and water to evaporate. Then the sample was cooled to -160 °C and held for 10 min (subsequent steps were always followed by a holding time of 10 min). The sample was again heated to 160 °C and cooled to -160 °C to erase thermal history. The sample was finally heated to 160 °C to assess thermal behavior and subsequently cooled to RT. Measurements were carried out using a heating rate of 10 Kmin⁻¹.

In chapter 4.1 (cf. Table 8), DSC of MBH₃MIm, EBH₃MIm, BBH₃MIm was conducted under nitrogen atmosphere by first heating the sample from RT to 100 °C, then cooling to -160 °C. The sample was again heated to 100 °C and cooled to -160 °C to erase thermal history. The sample was finally heated to 100 °C to assess thermal behavior and subsequently cooled to RT. Measurements were carried out using a heating rate of 10 Kmin⁻¹ and a holding time of 10 min between the different steps. DSC of BenzBH₃MIm was carried under similar conditions but was heated to 150 °C instead of 100 °C.

³⁷ This chapter is based on the textbooks by B. Wunderlich^[144] and Höhne et al.^[145]

In chapter 4.2 (cf. Table 9) DSC was conducted under nitrogen atmosphere by first heating the sample from RT to 100 °C, then cooling to -160 °C. The sample was again heated to 100 °C and cooled to -160 °C to erase thermal history. The sample was finally heated to 100 °C to assess thermal behavior and subsequently cooled to RT. Measurements were carried out using a heating rate of 10 Kmin⁻¹ (no holding segments).

Thermogravimetric analysis (TGA)

Thermogravimetry is the measurement of the mass change of a sample against the temperature³⁸. The measurement may be conducted at constant temperatures or using a temperatures program. To conduct the measurement, the sample is placed in a suitable holder (crucible) and attached to a microbalance. The balance is situated in a furnace that allows temperature control. The atmosphere of the measurement setup can be controlled to allow purge, calibration and measurement under specific conditions. Since the measurement relies on a balance, naturally only reactions that effect the evaporation of a species can be observed. Reactions without mass change are not visible with this method, unless it is combined with other methods.^[146] In this work, a linear temperature program was always used and the sample was heated at 10 Kmin⁻¹. TGA was carried out using a thermo microbalance TG 209 F1 Libra (Netzsch, Selb, Germany). Samples were measured using aluminum crucibles under nitrogen atmosphere.

TGA coupled with MS

Coupling the TGA-measurement with a mass spectrometer (TGA-MS) allows the detection of the evaporating species

TGA-MS measurements were performed using a thermos microbalance TG 209 F1 Libra (Netzsch, Selb, Germany) coupled with a Thermostar Mass spectrometer (Pfeiffer Vacuum, Asslar, Germany) with an ionization energy of 75 eV. Measurements were conducted at a heating rate of 2.5 Kmin⁻¹ in aluminum crucibles. m/z data is rounded to the next natural number in this work. TGA-MS was carried out under nitrogen atmosphere with the exception of BBH₃MIm, which was measured under helium atmosphere.

³⁸ This chapter is based on the textbook by B. Wunderlich^[144]

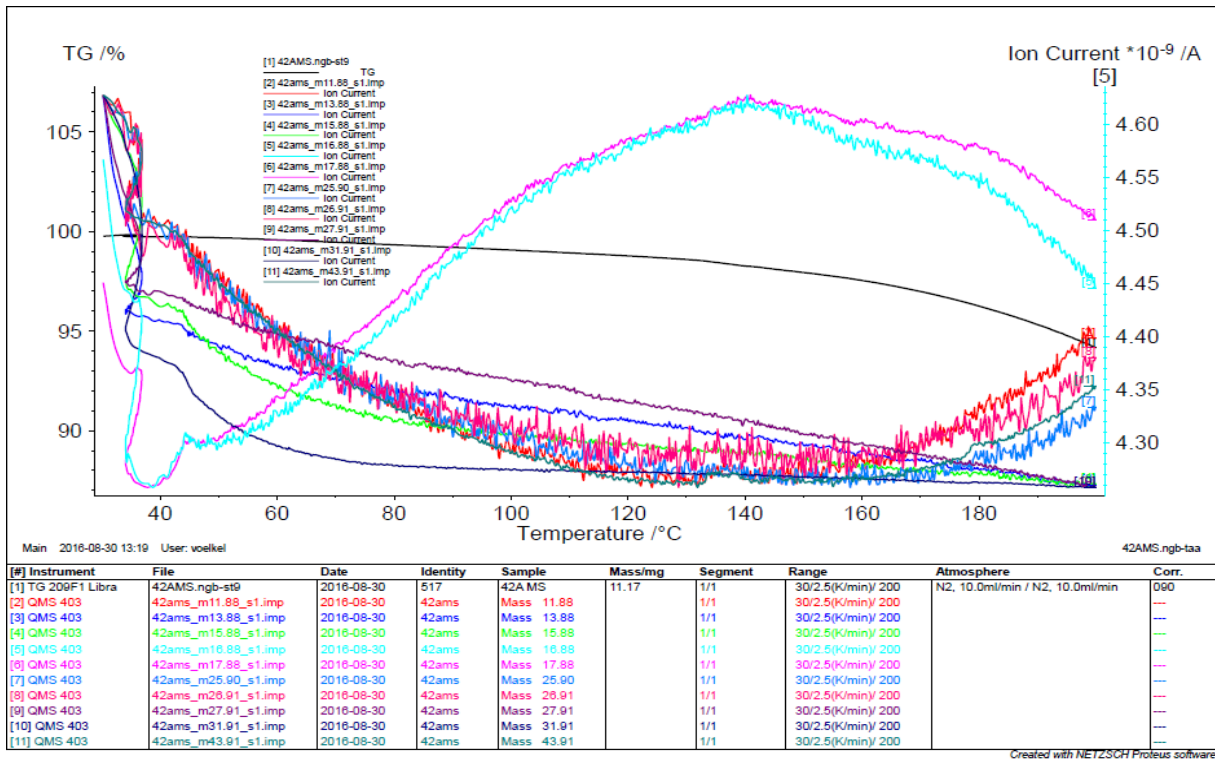


Figure A - 1 TGA-MS graph of THF-2 as exported using the NETZSCH Proteus software. Heating rate 2.5 Kmin⁻¹, ion currents have been normalized. Measured under N₂-atmosphere.

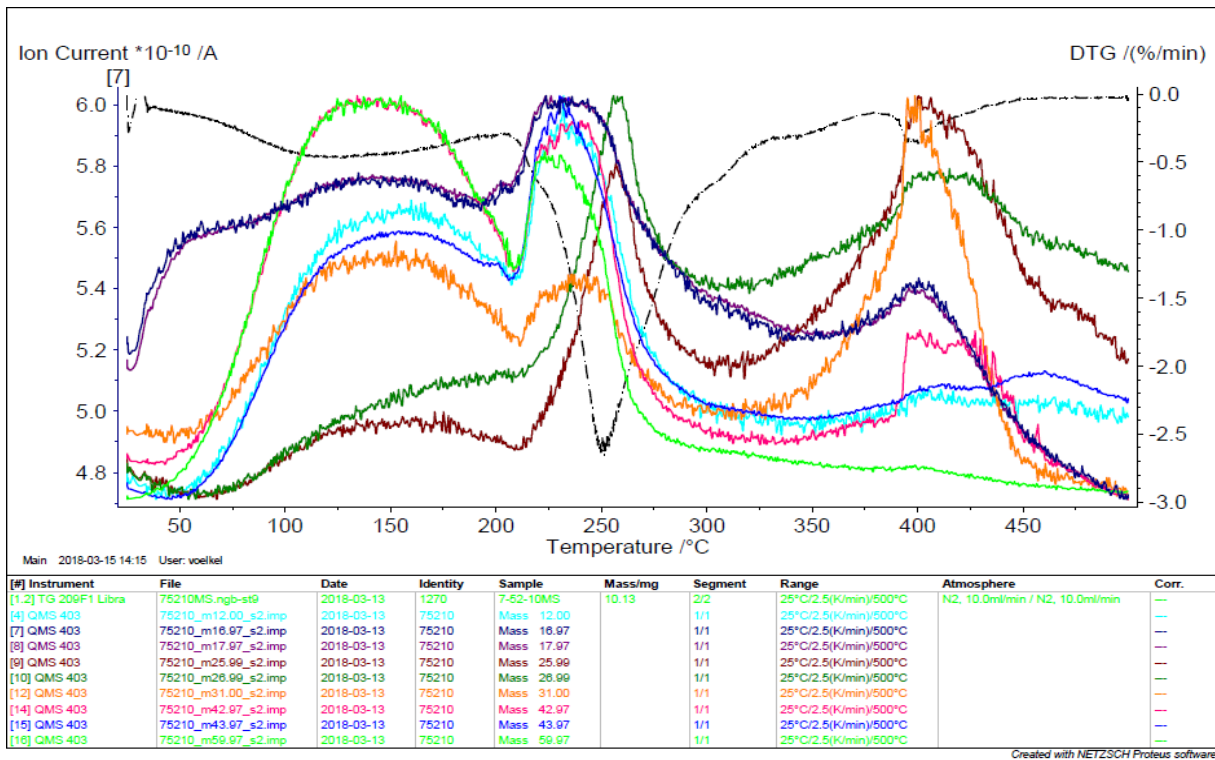


Figure A - 2 TGA-MS graph of T-A-5 as exported using the NETZSCH Proteus software. Heating rate 2.5 Kmin⁻¹, ion currents have been normalized. Measured under N₂-atmosphere.

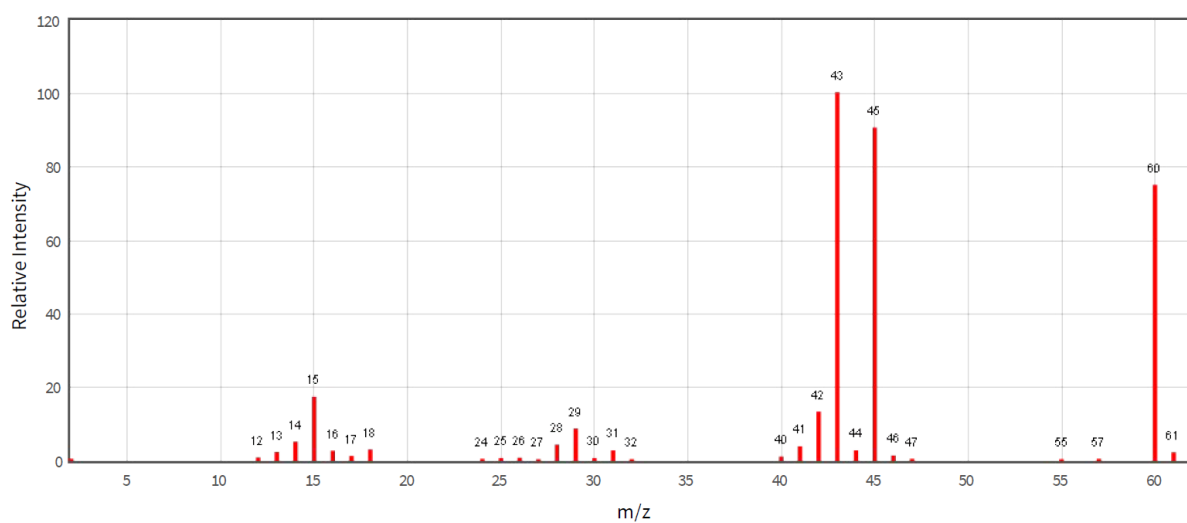


Figure A - 3 Electron Ionization spectrum of acetic acid, obtained from reference^[147]

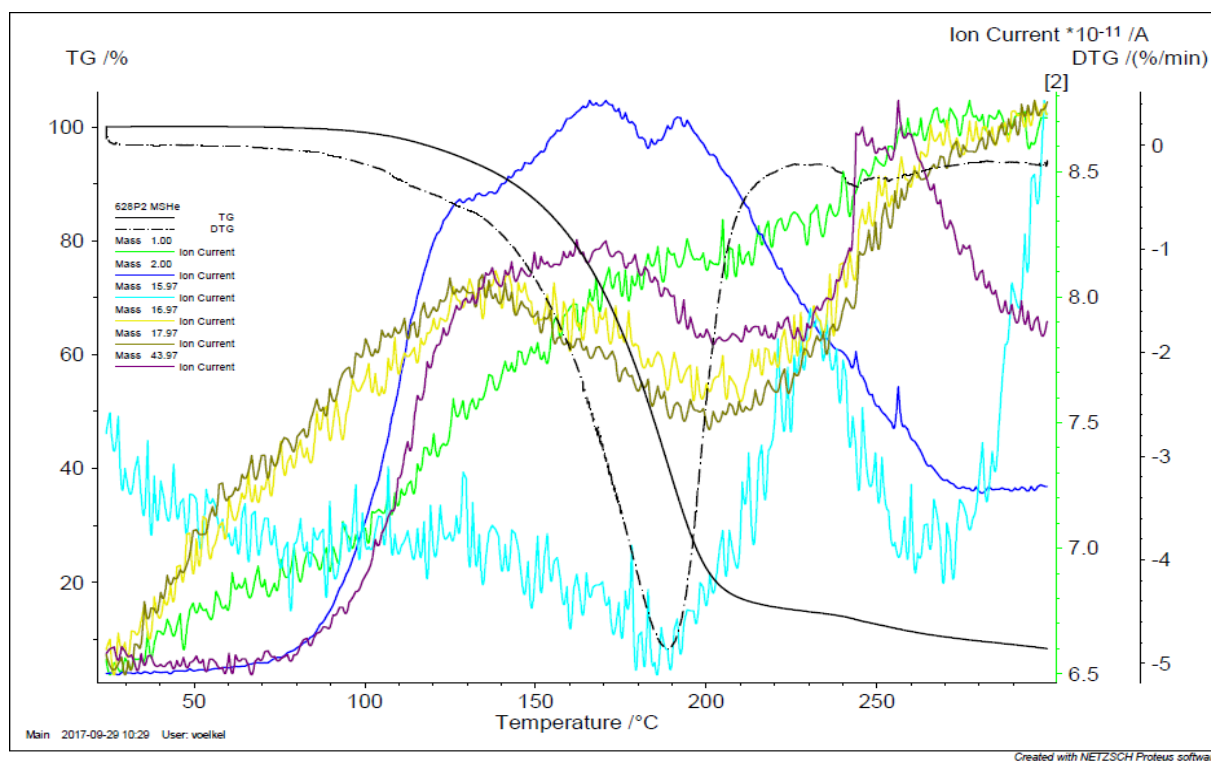


Figure A - 4 TGA-MS graph of BBH₃MIm (m/z 1, 2, 16, 17, 14, 44) as exported using the NETZSCH Proteus software. Heating rate 2.5 Kmin⁻¹, ion currents have been normalized. Measured under He-atmosphere.

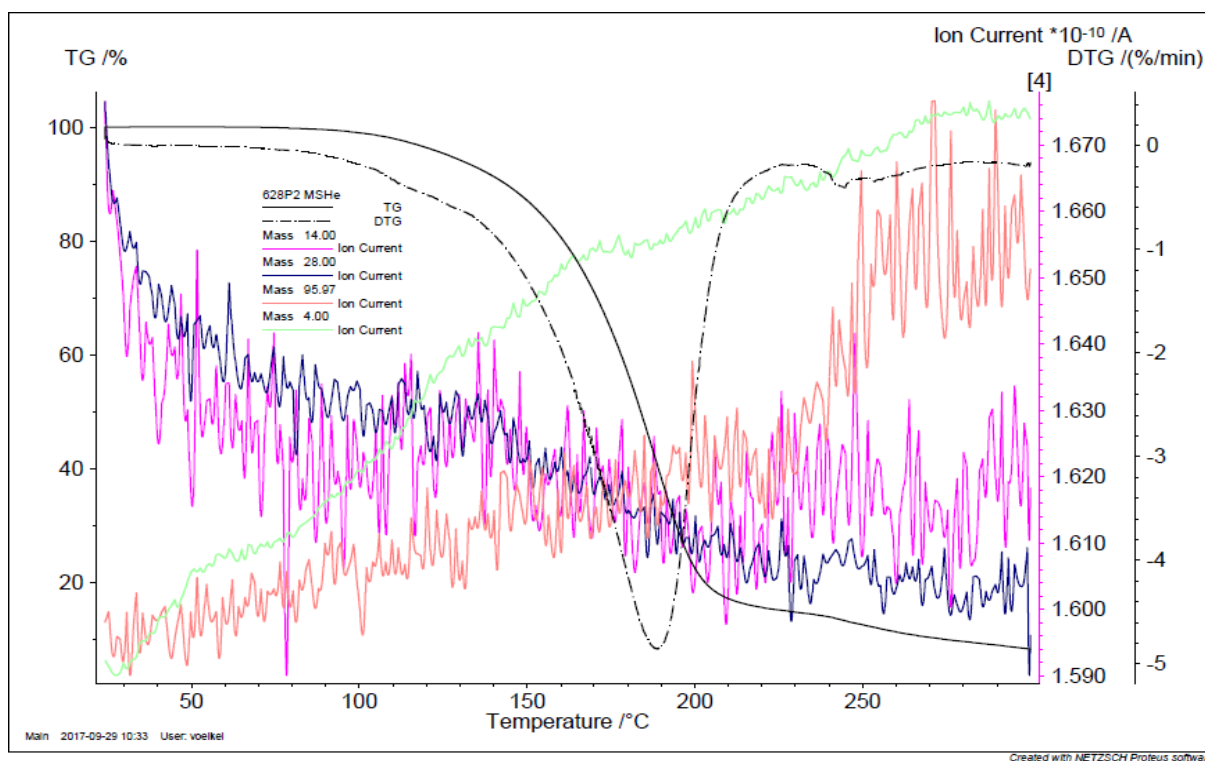


Figure A - 5 TGA-MS graph of BBH₃MIm (m/z 4, 14, 28, 96) as exported using the NETZSCH Proteus software. Heating rate 2.5 Kmin⁻¹, ion currents have been normalized. Measured under He-atmosphere.

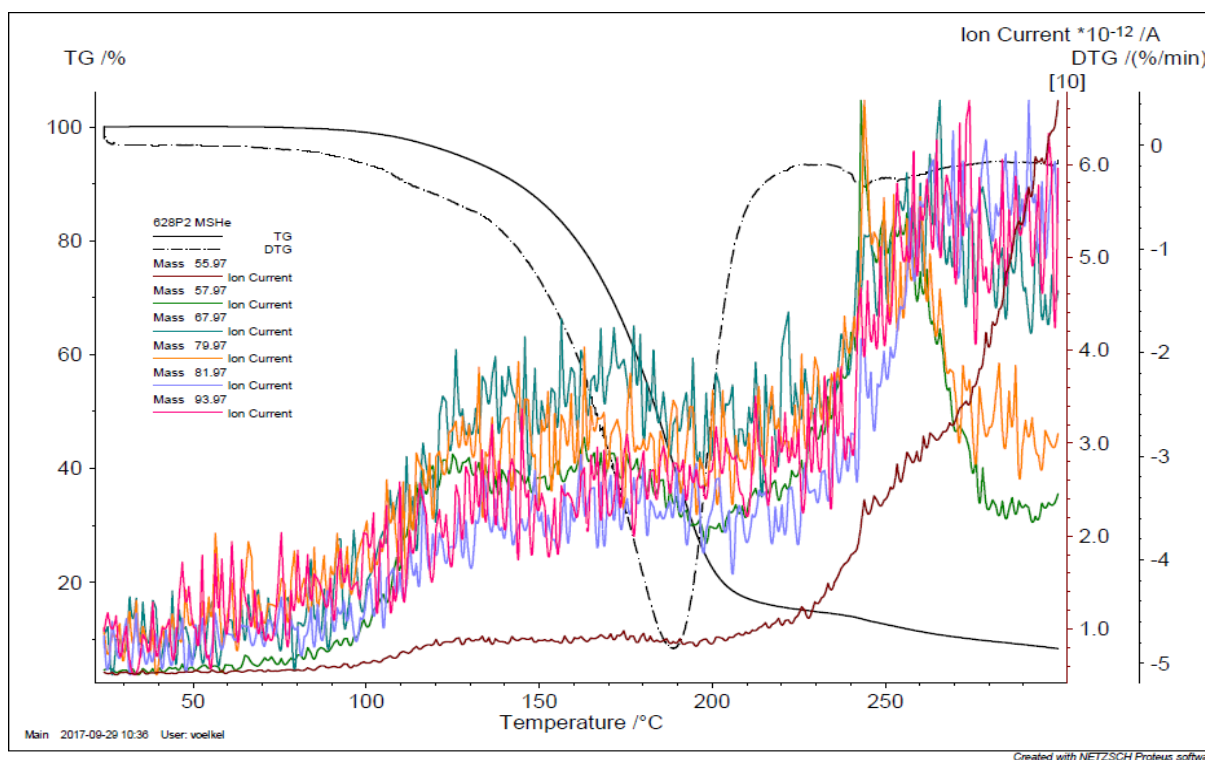


Figure A - 6 TGA-MS graph of BBH₃MIm (m/z 56, 58, 68, 80, 82, 94) as exported using the NETZSCH Proteus software. Heating rate 2.5 Kmin⁻¹, ion currents have been normalized. Measured under He atmosphere.

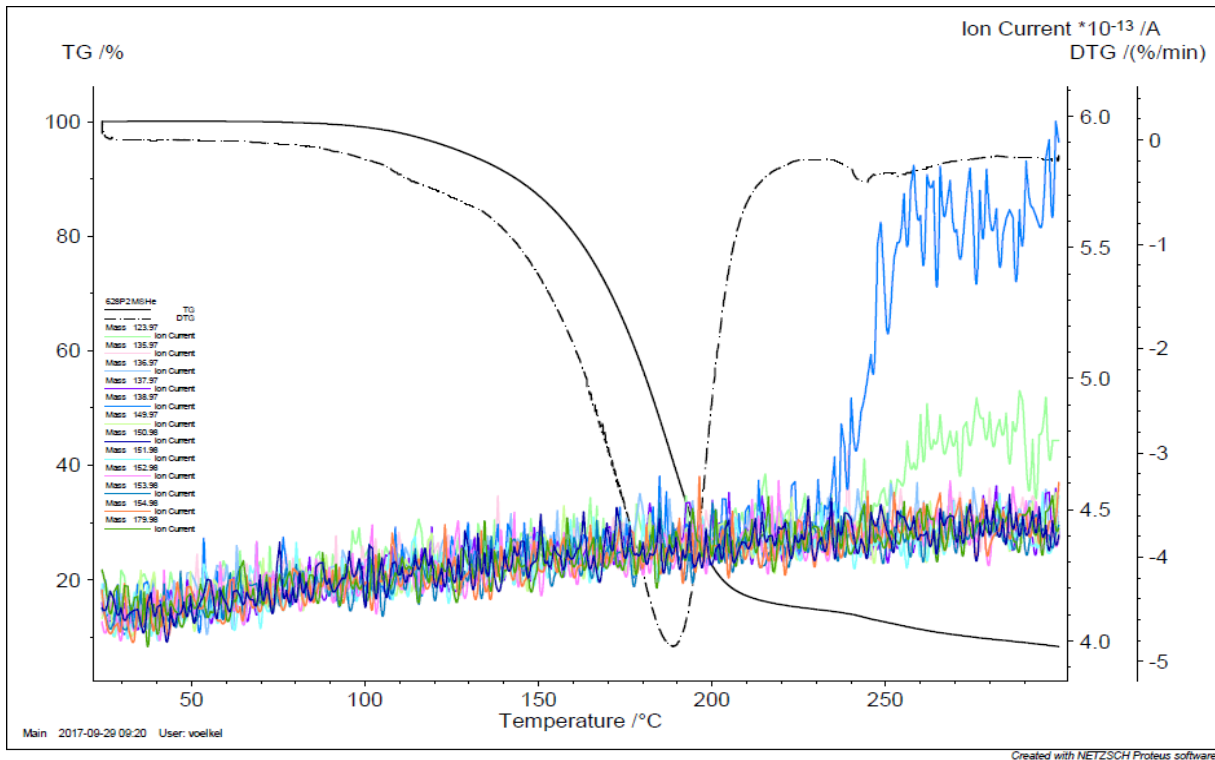


Figure A - 7 TGA-MS graph of BBH₃MIm (m/z 124, 136, 137, 138, 139, 150, 151, 152, 153, 154, 155, 180) as exported using the NETZSCH Proteus software. Heating rate 2.5 Kmin⁻¹, ion currents have been normalized. Measured under He atmosphere.

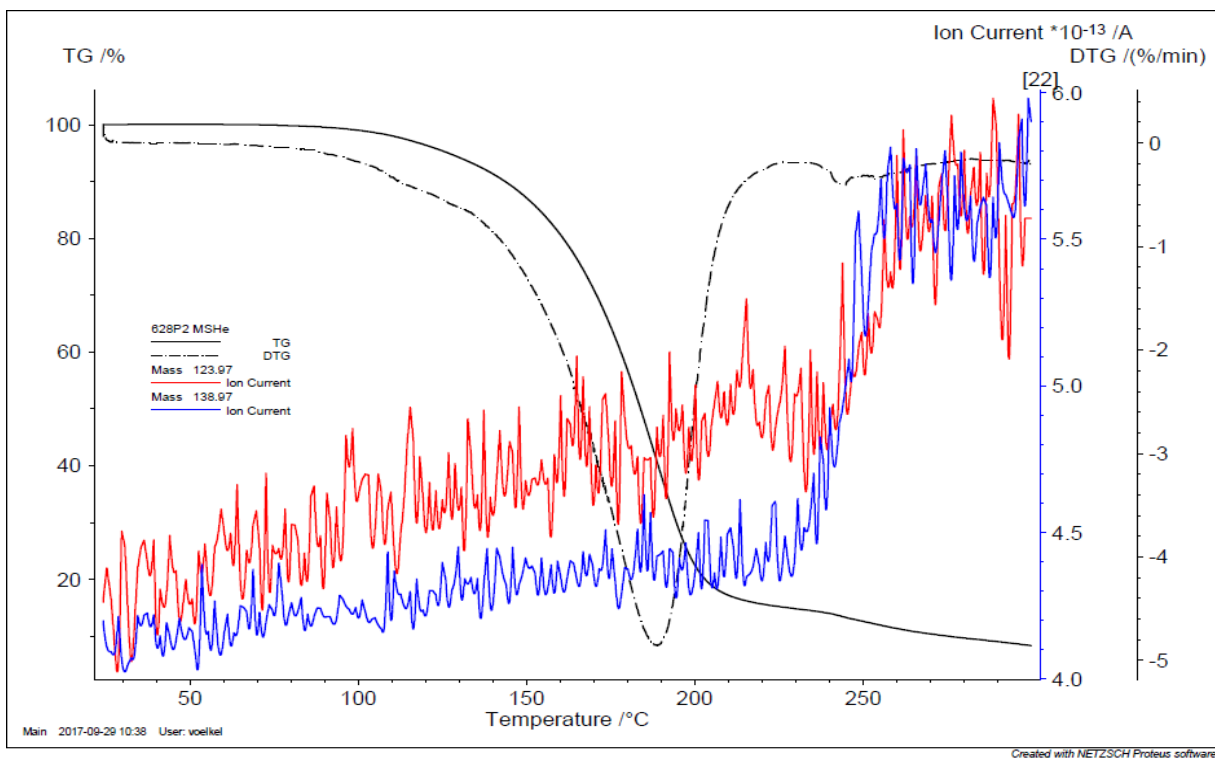


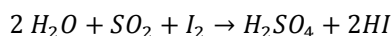
Figure A - 8 TGA-MS graph of BBH₃MIm (m/z 124, 139) as exported using the NETZSCH Proteus software. Heating rate 2.5 Kmin⁻¹, ion currents have been normalized. Measured under He atmosphere.

Karl Fischer Titration

The determination of water content is crucial in many applications. If ionic liquids are used this is especially true due to the usually strong hydrogen bonding behavior and the potentially large influence of the water content on physical characteristics. Also, the high molecular weight of ILs with respect to the low molecular weight of water makes low percentage by weight become a relevant percentage by moles.

The standard method for the determination of water content is the so called Karl-Fischer (KF) titration. The technique was developed on the basis of the Bunsen reaction to consume water and produce acids that can in turn be measured by titration³⁹:

Equation A - 2: The Bunsen reaction.



The Karl Fischer titration is usually conducted in alcoholic solution and in the presence of a suitable base:

Equation A - 3: Reaction of SO₂ in the presence of a suitable base and an alcohol.



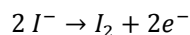
Where ROH is a reactive alcohol and R'N is a suitable base. In the presence of iodine, water is consequently consumed:

Equation A - 4: The Karl-Fischer reaction.



The result of which can be analyzed by titration. In this work coulometric KF titration is used, which means that the reactive agent (iodine in this case) is produced by oxidation from the solution.

Equation A - 5: Oxidation of iodine.



he iodine subsequently reacts according to Equation A - 4. The endpoint is reached when all the water is consumed and excess iodine no longer reacts. The endpoint is detected via voltammetry. The use of a coulometric setup for Karl Fischer titration has the advantage of being very sensitive. Also there is no need for calibration since electrons can be counted in the form of an absolute measurement.

In order allow evaluation whether a measurement is valid, common sources of errors should be discussed. First and foremost the sample handling must be taken into account. The coulometric KF titration is very sensitive and as such contamination of the measurement and transfer equipment is a relevant problem and must be avoided. The working medium chosen for the reaction can also induce relevant deviations from the ideal measurement conditions. Methanol is usually chosen as the alcoholic solvent. The use of other alcohols can substantially influence the result of the measurement. It should further be taken into account that water content is measured in excess of another substance. Solubility of the analyte must be good in the KF solution. Also the quantitative conversion according to Equation A - 3 must be ensured and end point determination must be possible. In

³⁹ This chapter is based on the textbook by E. Scholz.^[148]

coulometric KF titration the latter is less important, however conductivity of the solution becomes relevant. Another relevant factor is the pH value of the solution. KF titration can only be conducted between a pH of 2 and 8. At low pH the reaction rates decrease and the reaction becomes very slow. At alkaline pH, side reactions falsify the measurement. The best range for KF titration is ca. 5.5 to 8. Usually the KF solution is buffered to maintain suitable pH. The mixture of chemicals used for KF titrations is quite complex. Fortunately cases of relevant side reactions are not abundant.

Still some reactions are known to interfere with the measurement, for example:

- reduction of iodine by strong reducing agents
- oxidation of sulfurous compounds by strong oxidizing agents
- esterification of methanol with some carboxylic acids
- formation of acetals and ketals from aldehydes and ketons (such as acetone) due to water release
- addition of iodine to double bonds (rare)

The measurements in this work have been carried out using a Metrohm 756 KF coulometer equipped with a Metrohm 703 Ti Stand using Hydranal–Coulomat AD. Due to the relatively high water content and the high viscosity, ionic liquids were measured in dilution: A portion of IL was transferred into a dried flask using dried glass shards. The flask was equipped with a septum, and a dry solvent was added to completely dissolve the IL. The water content of the IL can be calculated from the mass of IL used, the water content of the dry solvent used (which must be assessed with KF titration, too) and the result of the measurement of IL and solvent.

Rheology

Rheology⁴⁰ is the science of deformation and flow. In this work two types of rheological measurements were conducted. On the one hand the viscosity of ionic liquids was determined, on the other hand the loss and storage moduli of polyelectrolyte networks were determined.

The viscosity of a liquid is a measure of the internal friction forces at work. To calculate viscosity, shear rate – shear stress measurements were carried out. This was done by rotation experiments. In this case shear stress is a measure for the force per area applied to the sample. Shear rate is a measure for the velocity per distance of the deformation. Shear stress, shear rate and viscosity in rotation experiments are related by the following equations:

Equation A - 6: Shear stress τ equals force F per area A of deformation.

$$\tau = \frac{F}{A}$$

Equation A - 7: Shear rate $\dot{\gamma}$ equals velocity v of deformation per layer thickness h of sample.

⁴⁰ This chapter is based on the textbook by T.G. Mezger.^[124]

$$\dot{\gamma} = \frac{v}{h}$$

Equation A - 8: The shear viscosity η is the ratio of shear stress to shear rate.

$$\eta = \frac{\tau}{\dot{\gamma}}$$

As seen in Equation A - 8, the shear viscosity is the ratio of shear stress and shear rate. If the liquid behaves ideally viscous (*Newtonian*), the viscosity is a constant, i.e. independent of shear rate or stress. In this work viscosity was determined by linear regression of the shear stress – shear rate curves according to Equation A - 8⁴¹.

The storage [G'] and loss [G''] moduli give information about the elastic and viscous behavior of the sample, respectively. They were determined using oscillatory tests. In these tests, shear stress and shear strain are used, which obey the following equations:

Equation A - 9: Shear stress τ equals force F per area A of deformation.

$$\pm\tau = \frac{\pm F}{A}$$

Equation A - 10: Shear strain γ equals distance s of deformation per layer height h of sample.

$$\pm\gamma = \frac{\pm s}{h}$$

Due to the oscillating nature of the measurement and the resulting oscillation of the values, Equation A - 9 and Equation A - 10 can be written as sine functions⁴². Shear stress and shear rate in oscillatory tests relate to the complex modulus G^* according to:

Equation A - 11: The complex modulus G^* equals the ratio of the time-dependent shear rate to shear stress.

$$G^* = \frac{\tau(t)}{\dot{\gamma}(t)}$$

The complex modulus G^* contains both the storage and the loss modulus⁴².

Equation A - 12: The complex modulus G^* contains loss and storage modulus.

$$G^* = G' + iG''$$

The determination of both moduli was carried out using amplitude sweeps.

Measurements in this work were carried out using a stress-controlled rotational rheometer (MCR 301, Anton Paar) equipped with either a 12 mm diameter cone-plate geometry with a 1° cone angle and a 20 μm truncation

⁴¹ Solving the equation for the shear stress. The slope of the linear regression represents the viscosity.

⁴² See specialized literature such as reference^[124].

(for viscosity measurements) or a 12 mm diameter plate-plate geometry (stress-strain measurements to determine viscoelastic behavior).

Additional data from viscosity measurements

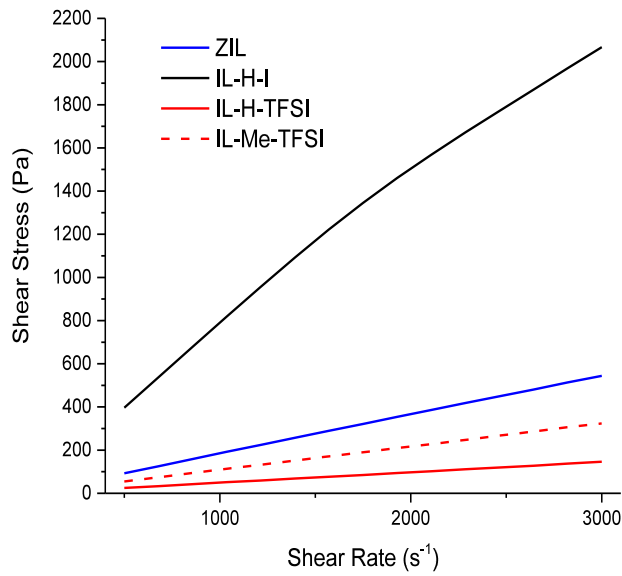


Figure A - 9: Shear rate – shear stress sweeps.

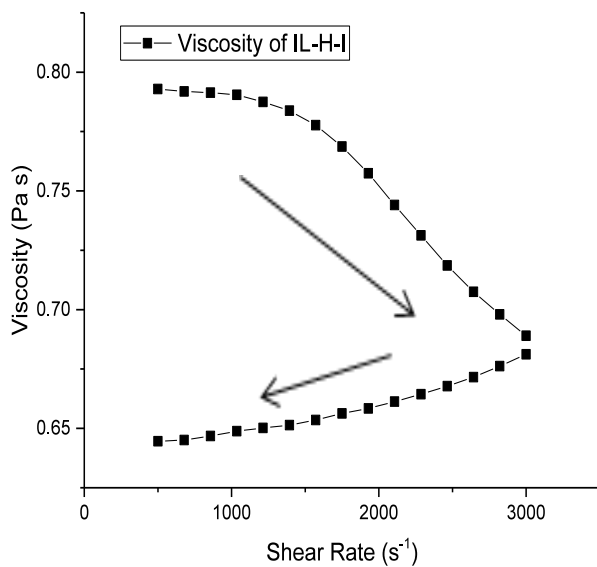


Figure A - 10: Viscosity of H-I over a shear rate sweep. The viscosity is lowered due to the uptake of water from the ambient atmosphere.

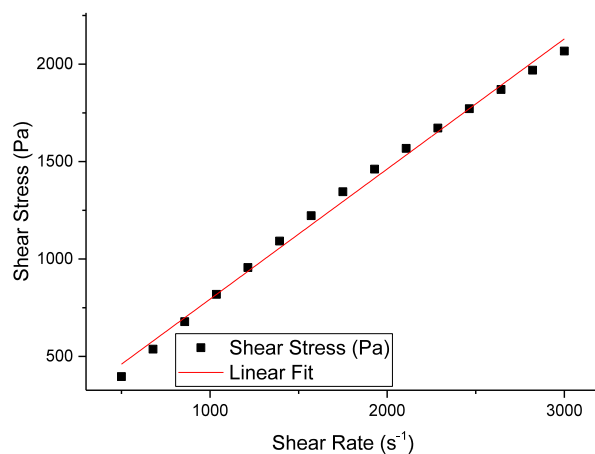


Figure A - 11: Linear regression of the shear stress shear rate curve of H-I.

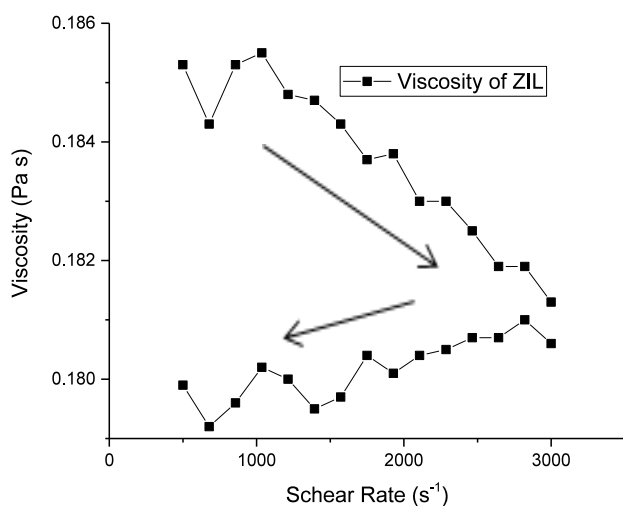


Figure A - 12: Viscosity of BBH_3MIm over a shear rate sweep. The viscosity is lowered due to the uptake of water from the ambient atmosphere.

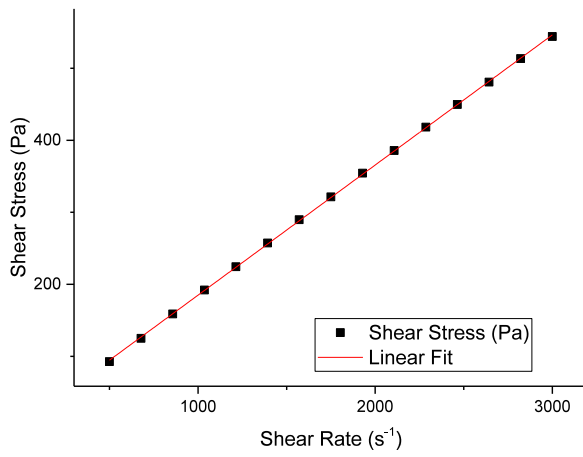


Figure A - 13: Linear regression of the shear stress shear rate curve of BBH_3MIm .

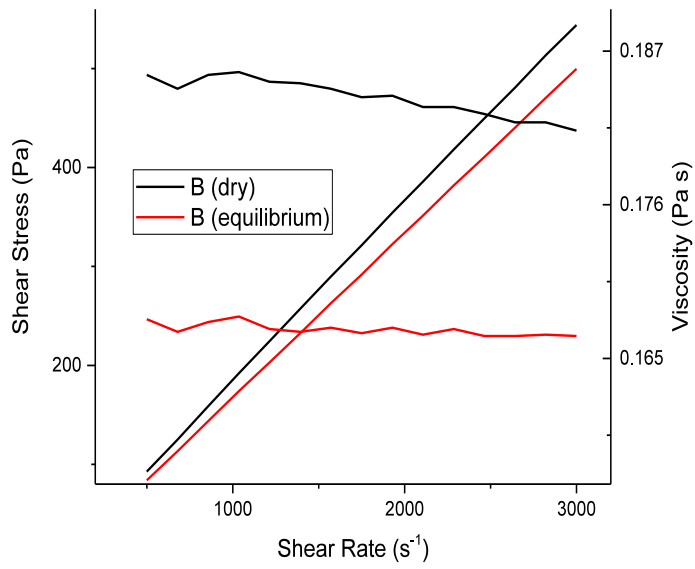


Figure A - 14: Equilibration with the ambient atmosphere effects the reduction of viscosity.

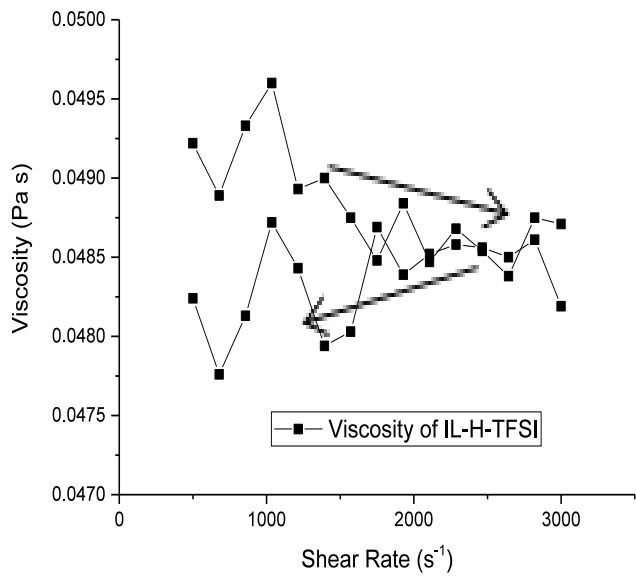


Figure A - 15: Viscosity of H-TFSI over a shear rate sweep. The viscosity is lowered due to the uptake of water from the ambient atmosphere.

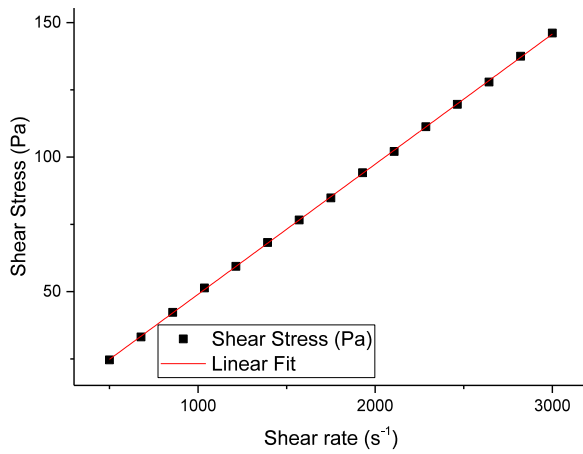


Figure A - 16: Linear regression of the shear stress shear rate curve of the H-TFSI.

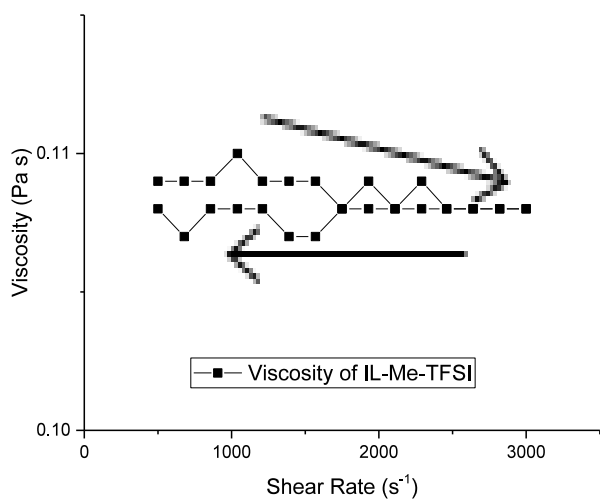


Figure A - 17: Viscosity of M-TFSI over a shear rate sweep. The viscosity is lowered due to the uptake of water from the ambient atmosphere.

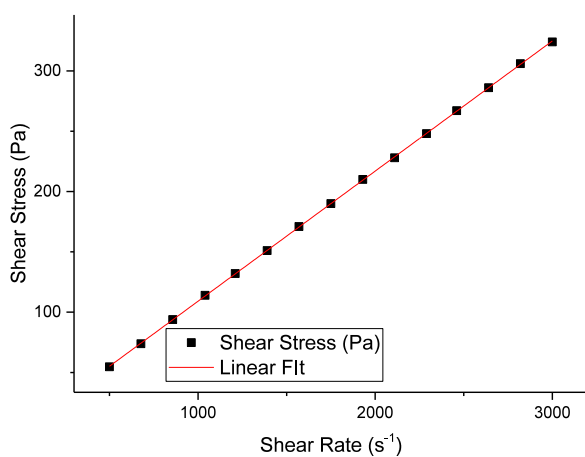


Figure A - 18: Linear regression of the shear stress shear rate curve of the M-TFSI.

Additional data from dynamic modulus measurements

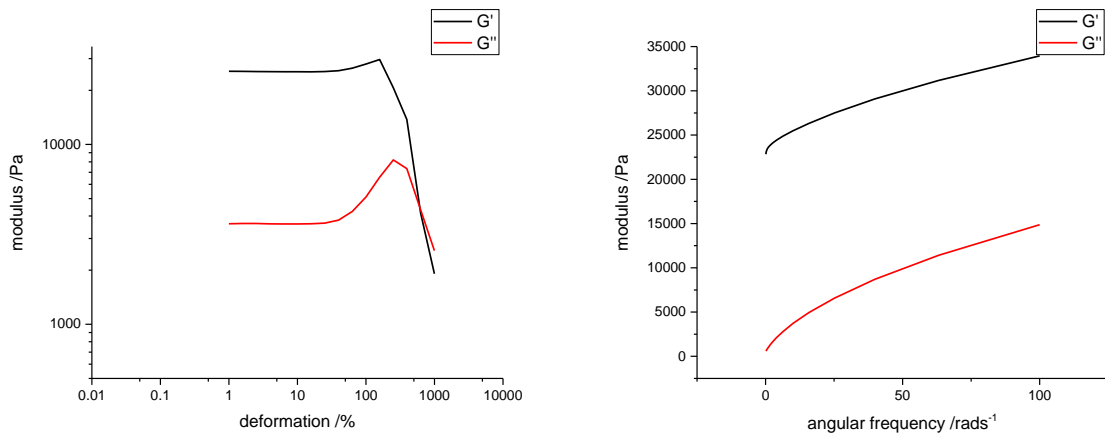


Figure A - 19: T-B-5 – Left: amplitude sweep. Right: frequency sweep.

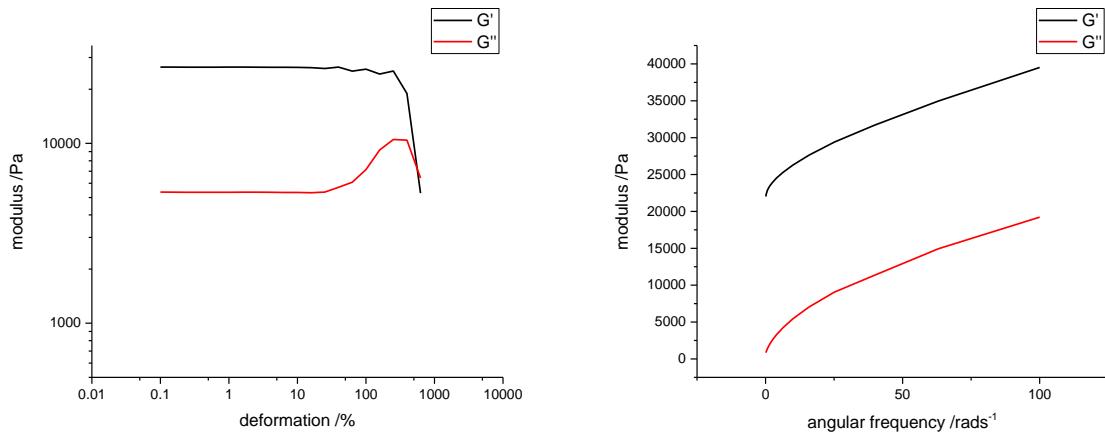


Figure A - 20: T-B-7 – Left: amplitude sweep. Right: frequency sweep.

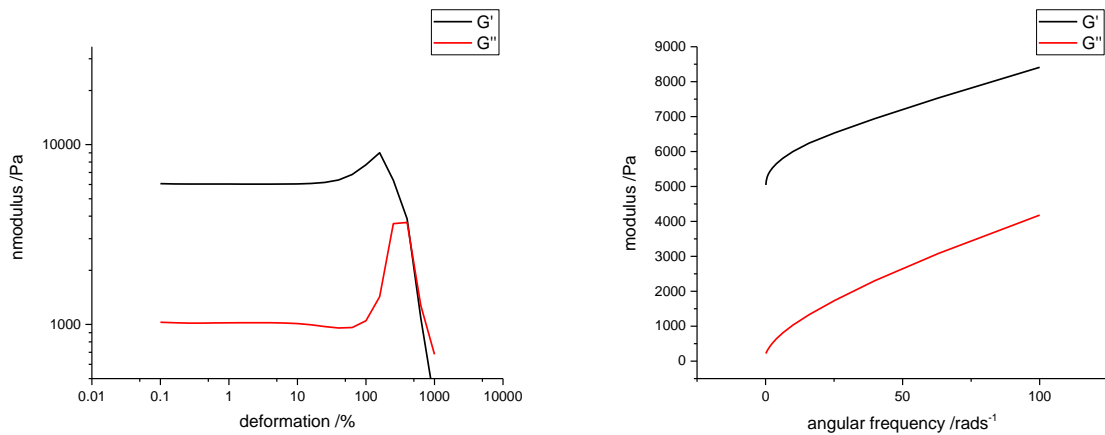


Figure A - 21: T-A-3 – Left: amplitude sweep. Right: frequency sweep.

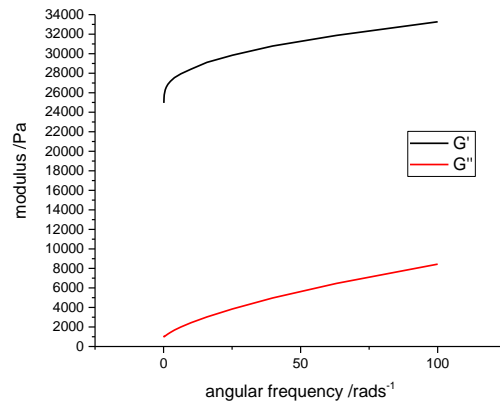
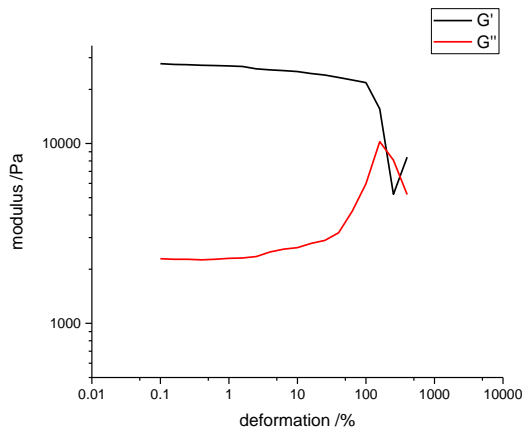


Figure A - 22: T-A-5 – Left: amplitude sweep. Right: frequency sweep.

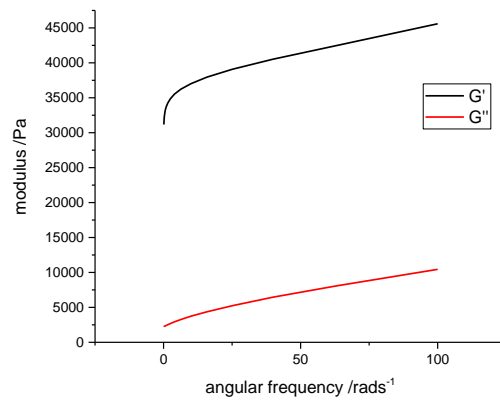
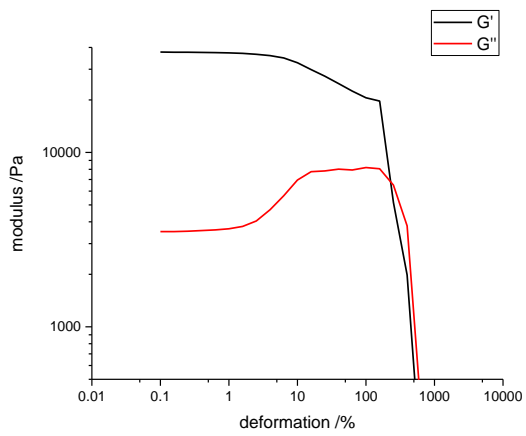


Figure A - 23: T-A-7 – Left: amplitude sweep. Right: frequency sweep.

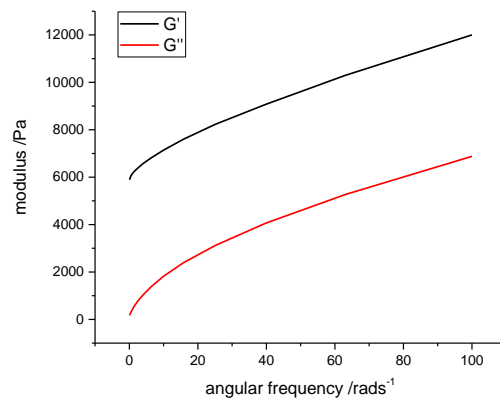
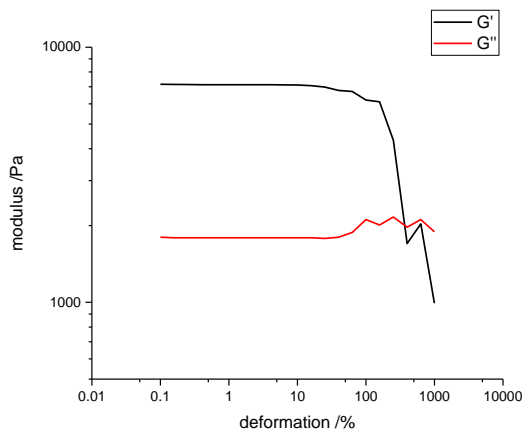


Figure A - 24: C-A-3 – Left: amplitude sweep. Right: frequency sweep.

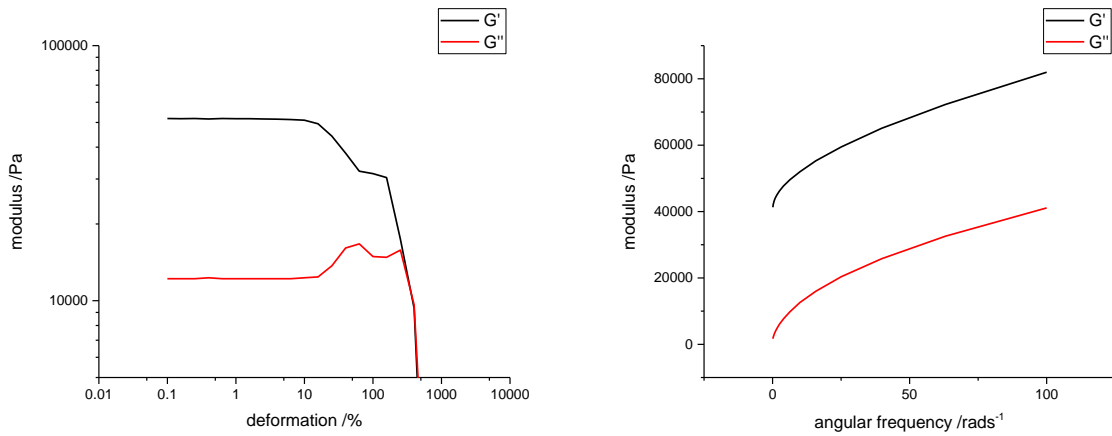


Figure A - 25: C-A-5 – Left: amplitude sweep. Right: frequency sweep.

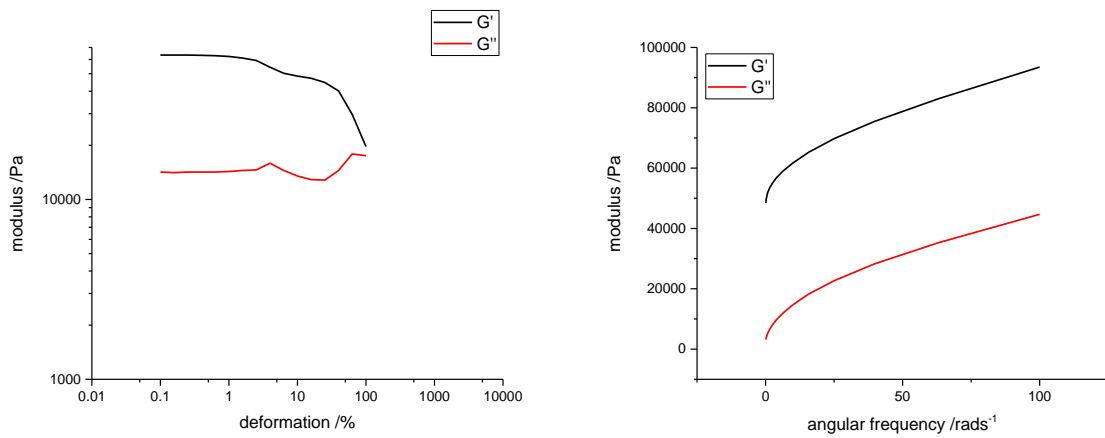


Figure A - 26: C-A-7 – Left: amplitude sweep. Right: frequency sweep.

Nuclear magnetic resonance spectroscopy

Due to its versatility and power, nuclear magnetic resonance (NMR) spectroscopy has become an integral part of chemistry. NMR-spectroscopy is based on the behavior of atoms in an external magnetic field based on their spin. NMR-spectroscopy reveals a multitude of information, the full extent of which is beyond the scope of this work.⁴³ In this work, NMR-spectroscopy is used to observe proton, carbon and boron nuclei. Due to this, it is suitable to briefly introduce the quantum mechanical background of NMR-spectroscopy in order to understand the shape of recorded spectra.

The nuclei of chemical elements generally possess an *angular momentum* \mathbf{P} , also referred to as its *spin*. \mathbf{P} is quantized, meaning it can only take discrete values. The spin quantum number of a nucleus may be zero, which causes it to not have a measurable angular momentum and be unsuitable for NMR-spectroscopy. The spin quantum number of different isotopes of a chemical element can be different. This leads to the situation where only some of the isotopes of a chemical element (if any) can be observed by NMR-spectroscopy. The sensitivity of a nucleus depends on the natural abundance of its isotope and its so called gyromagnetic ratio⁴⁴ γ .

Depending on its spin, the nucleus is able to populate different states, which are also quantized. When subjected to an external magnetic field, these states are separated by energy differences. Consequently, the transition between these states is possible by absorption and emission of energy. The amount of different states is defined by the spin quantum number. For simple nuclei with a spin of $\frac{1}{2}$, like the ^1H and ^{13}C -nucleus, there are two different states. For more complex nuclei (with higher spin), more states are possible. The foundation of NMR-spectroscopy is the observation of transitions between these states.

Doing this in a suitable fashion yields an NMR-spectrum. The primary information content of a spectrum is threefold: The location of signals in the spectrum, their shape and their intensity. The location reveals information about the electronic environment of the nucleus, i.e. the surrounding nuclei and chemical structures. The shape of the signal reveals the number of nuclei interacting with the observed nucleus. Further analysis of the signal shape can reveal information about the interactions with other nuclei. Finally, the intensity, if measured with sufficient accuracy, corresponds to the number of nuclei causing the signal. In this work, the shape of signals – i.e. their multiplicity – is of special interest.

As indicated, the multiplicity reveals information about the number of nuclei interacting with the observed nucleus. In a first-order approximation, the signal shape depends only on number and type of the nuclei in interaction (so called *coupling* nuclei). A general rule for the multiplicity of signals is given in Equation A - 13

Equation A - 13: Multiplicity rule for NMR-spectra (M-multiplicity; J-spin quantum number of the coupling nuclei, n-number of coupling nuclei).

$$M = J * n * 2 + 1$$

The nuclei observed in this work are the ^1H and ^{13}C ($J = 1/2$) and ^{11}B ($J = 3/2$). NMR spectra in this work were measured either on a Bruker ascend400 Avance III with a Prodigy-probe (proton and carbon spectra), a Varian

⁴³ This chapter is based on the textbooks by Hore et al.^[149] and H. Günther.^[150]

⁴⁴ The gyromagnetic ratio is an innate characteristic of any given nucleus.

400MR mit OneNMR-Probe (regular boron spectra), or a Varian 600MR mit OneNMR-Probe (spectra at temperatures other than RT).

Electrochemistry

Voltammetry

In voltammetry⁴⁵, a potential is applied to a system, and the response of the system (i.e. current flow) is measured. The applied potential is varied over time. If a linear increase or decrease of potential is used, the resulting technique is called linear sweep voltammetry (LSV). Using a repeating increase/decrease program is the feature of cyclic voltammetry (CV). The resulting curves list current vs. potential and are called voltammograms. In these curves, peaks or steps translate to a current flow or a change of current flow at a given potential. This corresponds to electrochemical reactions at the working electrode at the observed potential. In this work, LSV voltammograms are used to determine the stability of compounds by observation of their behavior with increasing/decreasing potential until they break down. Using CV, scanning forward and backward over a potential range allows observation of the back reactions of reactions that occur on the first scan. This allows the determination of reversibility, potentials, overpotential and kinetics of electrochemical reactions. In this work, cyclic voltammetry is used to determine the deposition and dissolution behavior of magnesium. All measurements are carried out at 5 mVs^{-1} .

The measurement setup usually features at least a working electrode and a counter electrode (two electrode setup). Using a third electrode with constant potential as a reference is also common (three electrode setup) to improve the accuracy of measurement but not always feasible. In this work, electrochemical measurements were conducted either in a three electrode setup or in Swagelok™ -type cells. Measurements in chapter 2.2 were

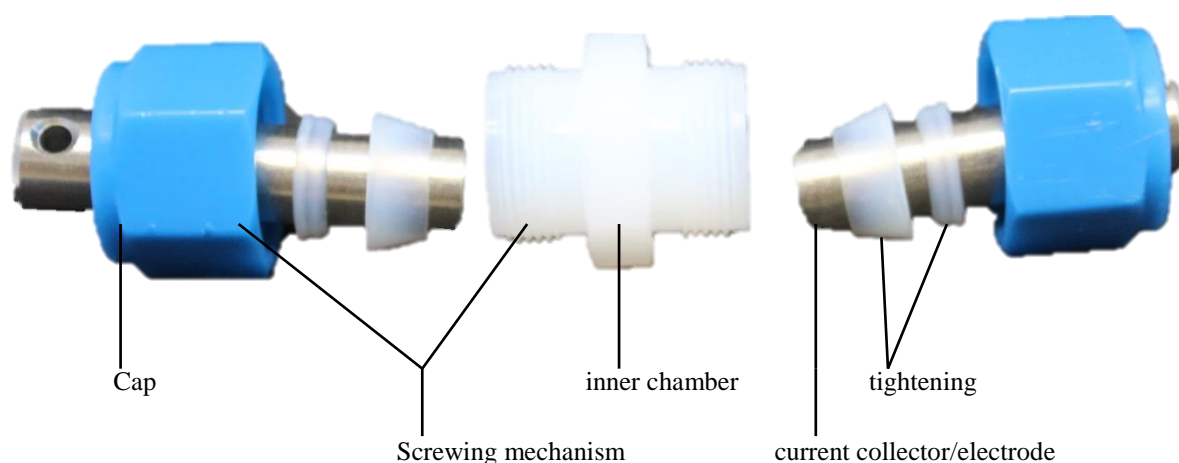


Figure A - 27: Two electrode Swagelok™-type cell. The inner chamber is equipped with a separator and the electrolyte. Electrodes are inserted in front of the current collectors, or the current collectors are used as electrodes.

⁴⁵ This chapter is based on the review article by Elgrishi et al.^[151] and the descriptions included in the EC-Lab® software (V10.40) by Bio-Logic – Science Instruments.

carried out using a three electrode setup with glassy carbon working electrode (1.6 mm diameter), a platinum coil counter electrode and a reference electrode for organic media (silver wire in 0.01 M AgNO₃ and 0.1 M tetrabutylammonium phosphate solution in ACN). All other measurements were carried out using Swagelok™-type cells. These cells used are built as two electrode cells and feature a working electrode and a counter electrode as shown in Figure A - 27. Magnesium and stainless steel⁴⁶ have been used as working electrodes lithium and magnesium have been used as counter electrodes. Measurements were carried out using a BioLogic MPG2 potentiostat. Cells were filled with 84 µl of electrolyte system, and a glass fiber filter separator was used, unless denoted otherwise.

Galvanostatic analysis

Galvanostatic charge/discharge analysis is used in this work to simulate the charge and discharge cycles that the electrolyte system would pass through in a battery.⁴⁷ In galvanostatic cycling, a current is applied to the cell. This current is periodically varied, which results in alternating oxidation and reduction of the electroactive species. The response of the system consequently results in potential vs. current or potential vs. time curves that feature cyclic oxidation and reduction. The measured data allows determination of capacity, efficiency and other important parameters of the system and aids in evaluation of the electrochemistry.

Measurements in this work have been carried out in Swagelok™-type cells (cf. Figure A - 27) using a BioLogic MPG2 potentiostat. Cells were filled with 84 µl of electrolyte system, and a glass fiber filter separator was used unless denoted otherwise.

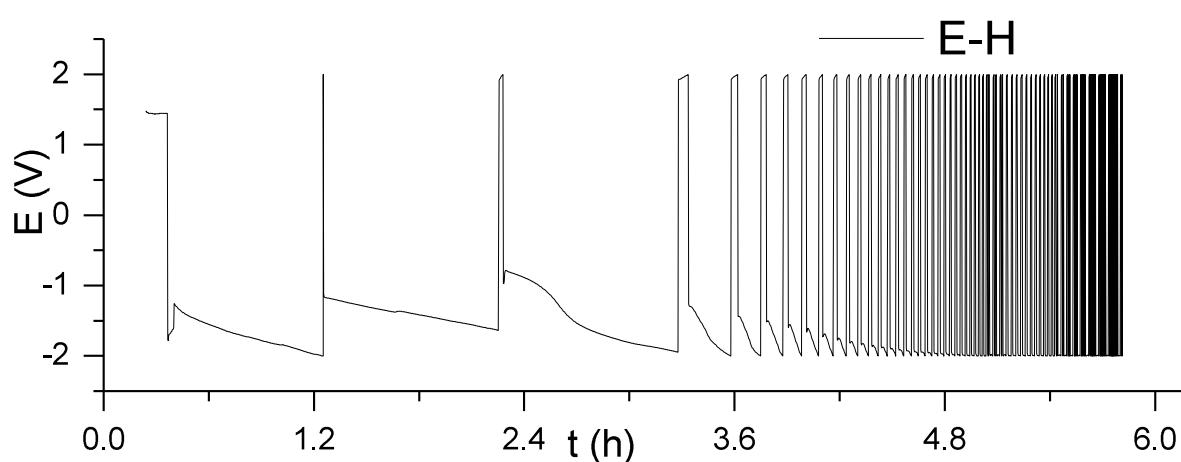


Figure A - 28: Results of galvanostatic cycling of E-H. No reversible activity was achieved (SS-WE, Mg-CE current density: 1 mAcm⁻²).

⁴⁶ All stainless steel electrodes used in this work are built from AISL 316.

⁴⁷ This chapter is based on the descriptions included in the EC-Lab® software (V10.40) by Bio-Logic – Science Instruments.

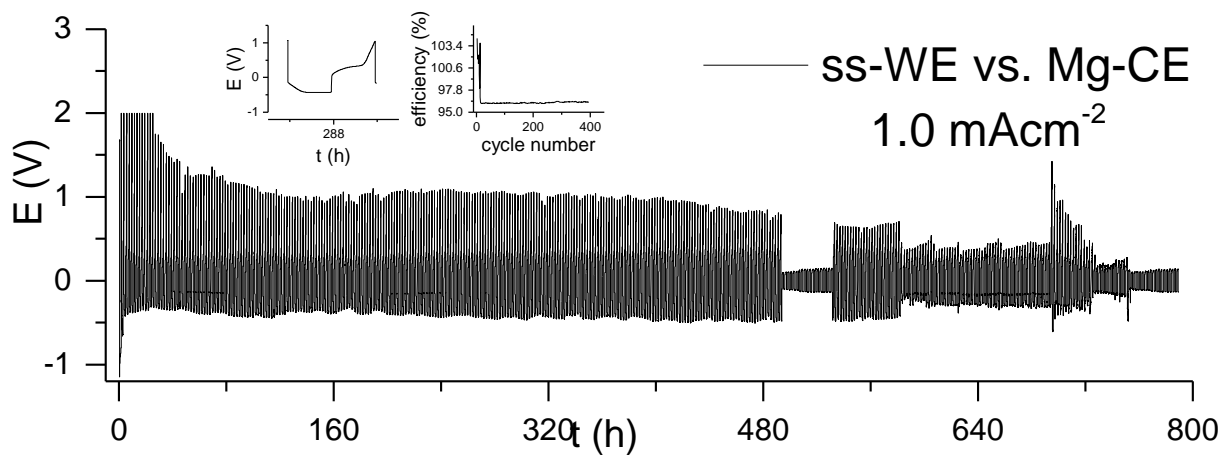


Figure A - 29: Results of galvanostatic cycling of E-B. The inset show a typical cycle and the efficiency vs. cycle number. (SS-WE, Mg-CE; current density: 1 mAcm⁻²).

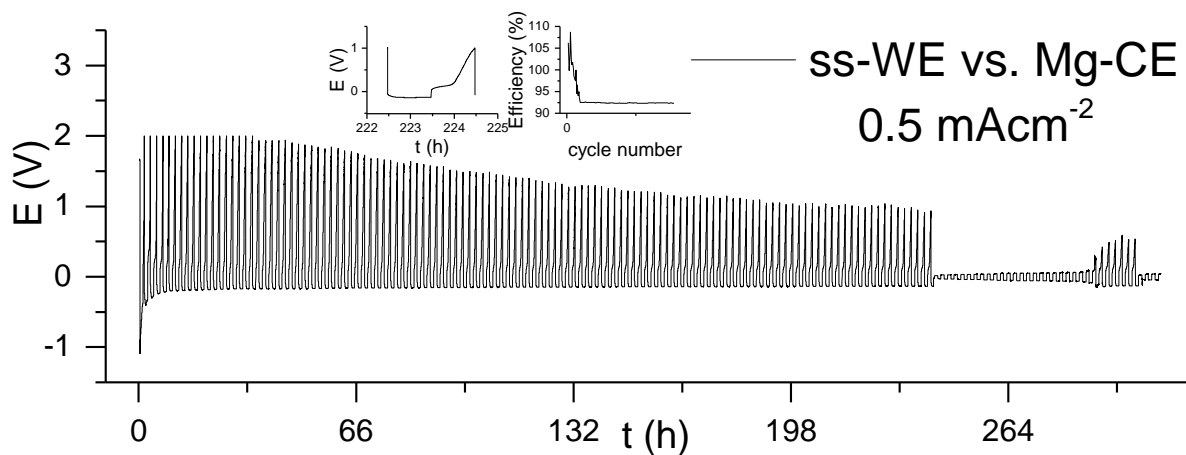


Figure A - 30: Results of galvanostatic cycling of E-B. The inset show a typical cycle and the efficiency vs. cycle number. (SS-WE, Mg-CE; current density: 0.5 mAcm⁻²).

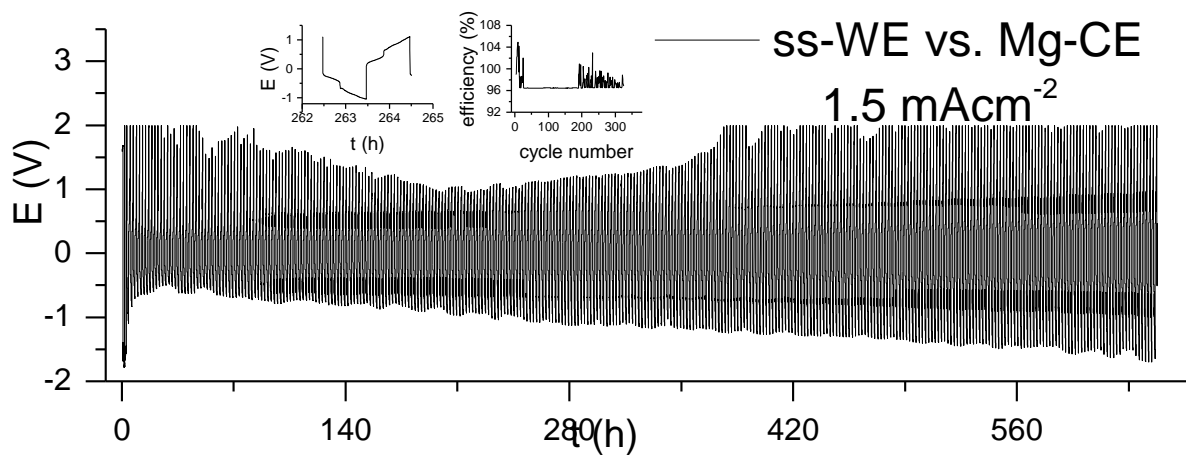


Figure A - 31: Results of galvanostatic cycling of E-B. The inset show a typical cycle and the efficiency vs. cycle number. (SS-WE, Mg-CE; current density: 1.5 mAcm^{-2}).

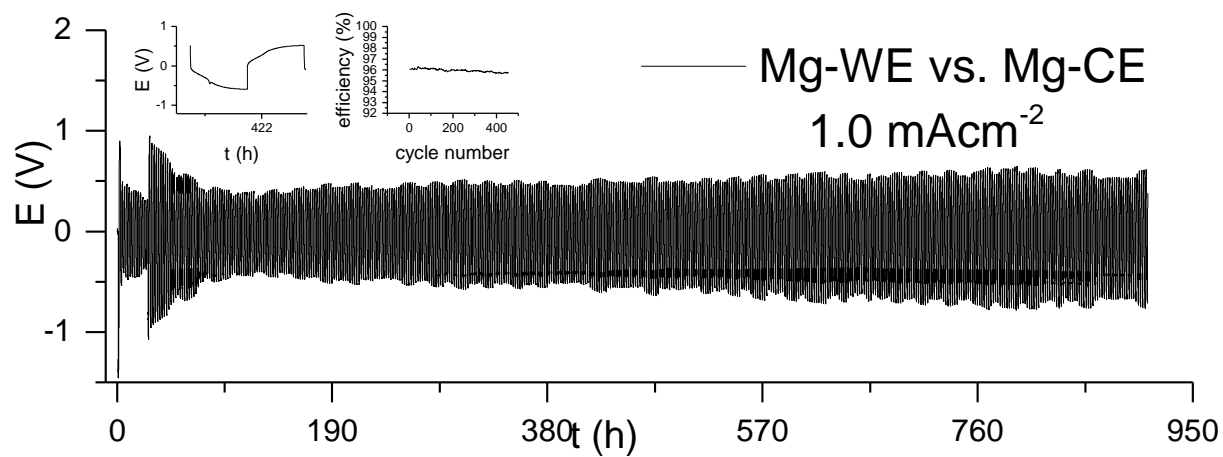


Figure A - 32: Results of galvanostatic cycling of E-B. The inset show a typical cycle and the efficiency vs. cycle number. (Mg-WE, Mg-CE; current density: 1.0 mAcm^{-2}).

6.2 Synthesis of compounds by chapter of occurrence

Compounds from 2.2 Direct anion tuning

Procedure A: General procedure for mDRr based synthesis of imidazolium ionic liquids

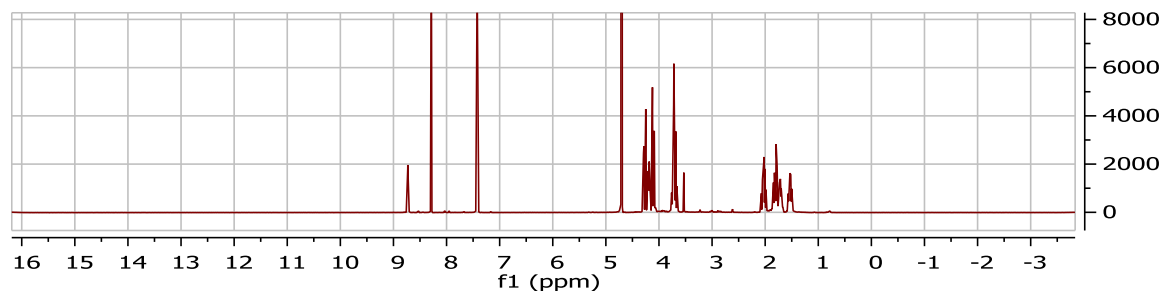
Procedure was adapted from literature^[26]: 2 equivalents of the amine were cooled in an ice-bath. A mixture of the aldehyde (1 equivalent) and the respective acid (1.5 equivalents) is added. The mixture is stirred for 30 minutes and allowed to warm to room temperature. Glyoxal is added and the mixture is stirred overnight. The crude product is extracted thrice with ether and volatiles are removed *en vacuo*.

THF-1: 1,3-bis((tetrahydrofuran-2-yl)methyl)-imidazolium formate

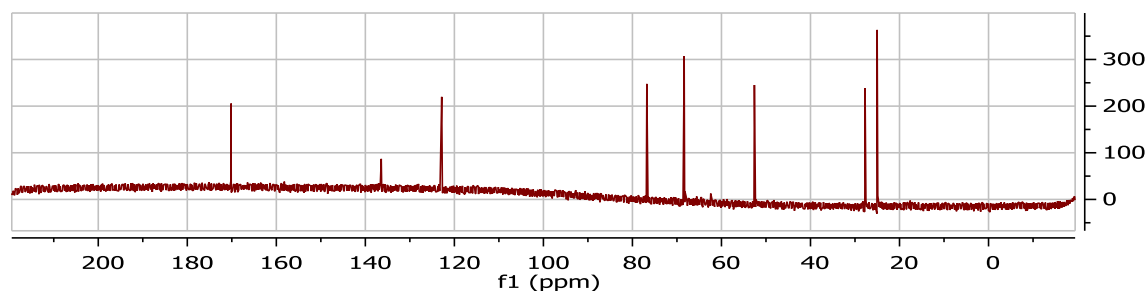
2.07 ml (0.02 mol) tetrahydrofurfurylamine, 0.75 ml formaldehyde mixed with 0.57 ml formic acid (0.01 mol and 0.015 mol, respectively; addition over 40 min), 1.15 ml (0.01 mol) glyoxal. The crude product was extracted with ether (3x20 ml). The product was obtained after removal of volatiles *en vacuo* (86.0 % yield by NMR; 0.00863 mol).

MS (water/FA): $m/z = 237.16$ (calculated for $[M]^+ C_{13}H_{21}N_2O_2^+$ in positive ion mode); found: $m/z = 237.1591$

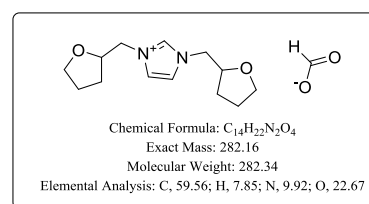
NMR:



Spectrum 1: THF-1 – ¹H-NMR (measured in D₂O).

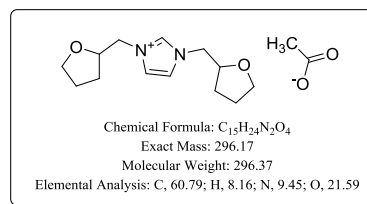


Spectrum 2: THF-1 – ¹³C-NMR (measured in D₂O).



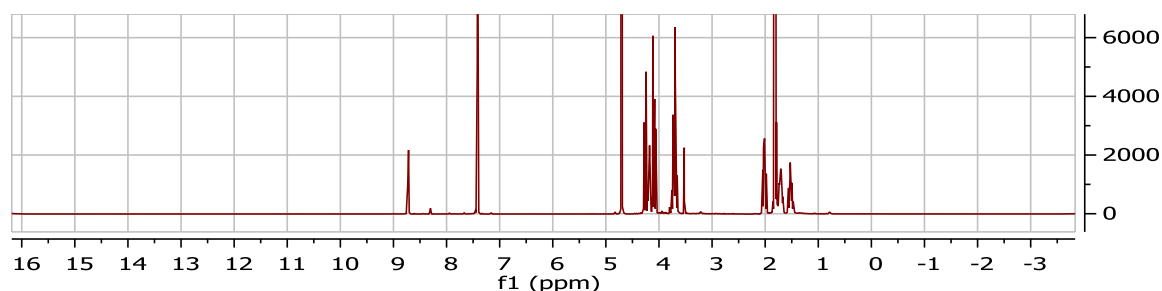
THF-2: 1,3-bis((tetrahydrofuran-2-yl)methyl)-imidazolium acetate

Synthesis carried out under light exclusion (flasks and funnels wrapped in aluminum foil). 2.07 ml (0.02 mol) tetrahydrofurfurylamine, 0.75 ml formaldehyde mixed with 0.86 ml acetic acid (0.01 mol and 0.015 mol, respectively; temperature kept below 15 °C while addition), 1.15 ml (0.01 mol) glyoxal. The crude product was extracted with ether until the organic layer was colorless. The product was freeze-dried and dried under high vacuum conditions (10^{-3} mbar, 1d at RT, 1d at 50 °C) to obtain the pure product (97.0 % yield by NMR; 0.00967 mol).

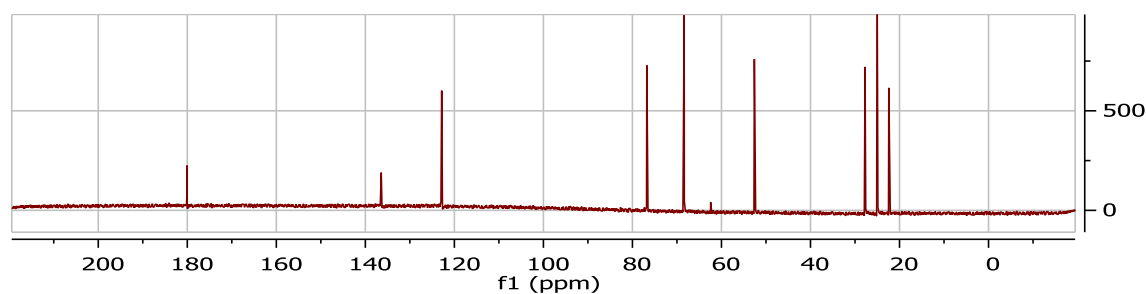


MS (ACN/FA): $m/z = 237.16$ (calculated for $[M]^+ C_{13}H_{21}N_2O_2^+$ in positive ion mode); found: $m/z = 237.1599$

NMR:



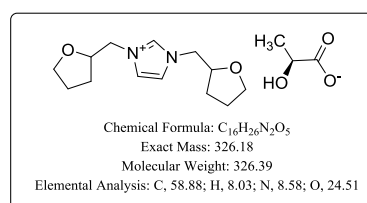
Spectrum 3: THF-2 – 1H -NMR (measured in D_2O).



Spectrum 4: THF-2 – ^{13}C -NMR (measured in D_2O).

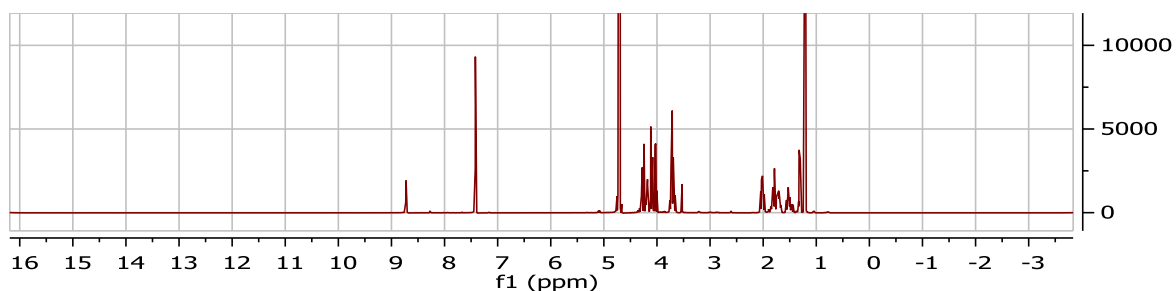
THF-3: 1,3-bis((tetrahydrofuran-2-yl)methyl)-imidazolium L-lactate

2.07 ml (1 mol) tetrahydrofurfurylamine, 0.75 ml formaldehyde mixed with 1.32 ml L-lactic acid (0.01 mol and 0.015 mol, respectively; addition over 40 min), 1.15 ml (1 mol) glyoxal. The crude product was extracted with ether (3x20 ml). The product was obtained after removal of volatiles *en vacuo* (94.0 % yield by NMR; 0.00936 mol).

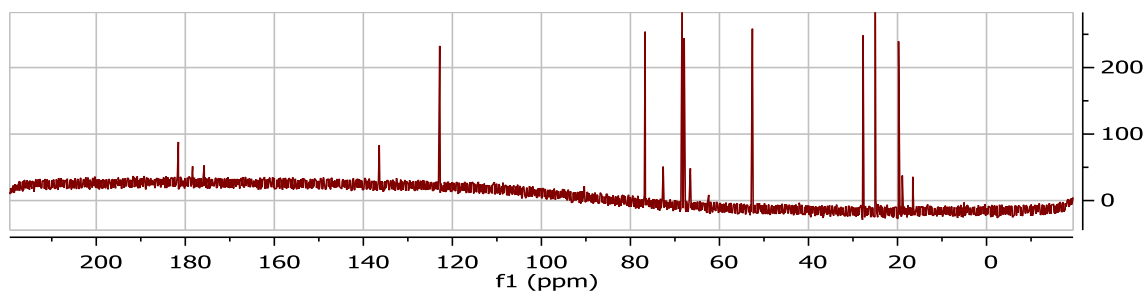


MS (water/FA) $m/z = 237.16$ (calculated for $[M]^+ C_{13}H_{21}N_2O_2^+$ in positive ion mode); found: $m/z = 237.1590$

NMR:



Spectrum 5: THF-3 – ^1H -NMR (measured in D_2O).



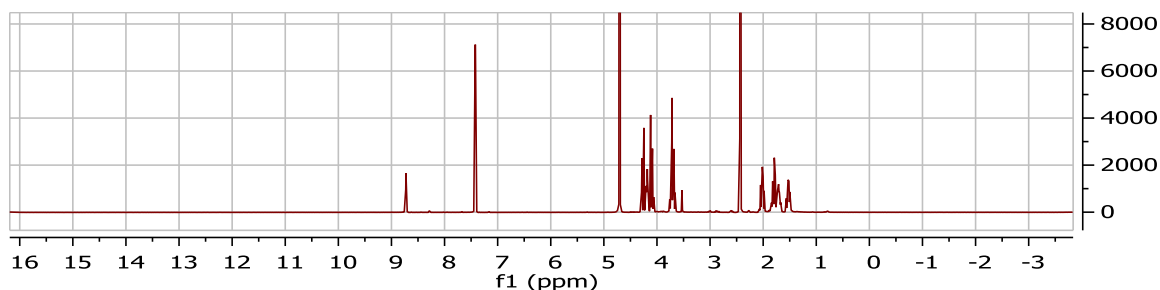
Spectrum 6: THF-3 – ^{13}C -NMR (measured in D_2O).

THF-4: 1,3-bis((tetrahydrofuran-2-yl)methyl)-imidazolium succinate

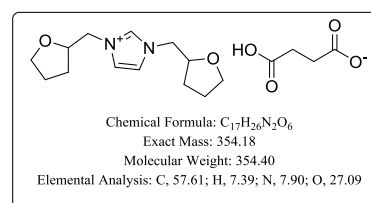
2.07 ml (0.02 mol) tetrahydrofurfurylamine, 0.75 ml formaldehyde mixed with 11.78 g succinic acid dispersed in 15 ml water (0.01 mol and 0.015 mol, respectively), 1.15 ml (0.01 mol) glyoxal. The crude product was extracted with ether (3x20 ml). The product was obtained after removal of volatiles *en vacuo* (88.0 % yield by NMR; 0.00877 mol).

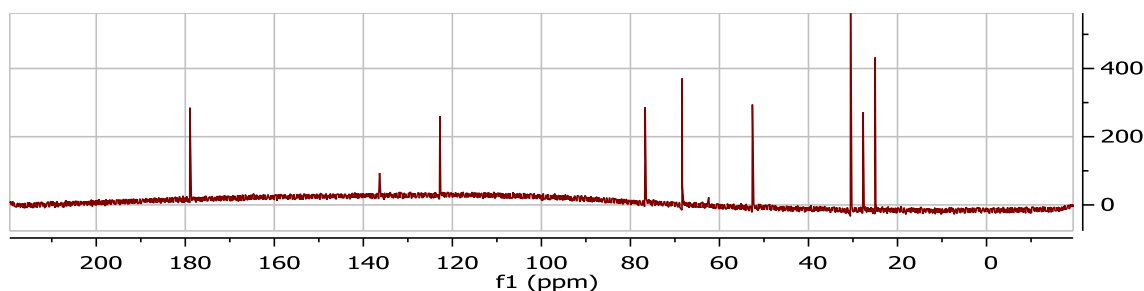
MS: $m/z = 237.16$ (calculated for $[\text{M}]^+ \text{C}_{13}\text{H}_{21}\text{N}_2\text{O}_2^+$ in positive ion mode); found: $m/z = 237.1589$

NMR:



Spectrum 7: THF-4 – ^1H -NMR (measured in D_2O).

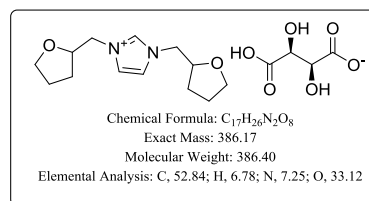




Spectrum 8: THF-4 – ^{13}C -NMR (measured in D_2O).

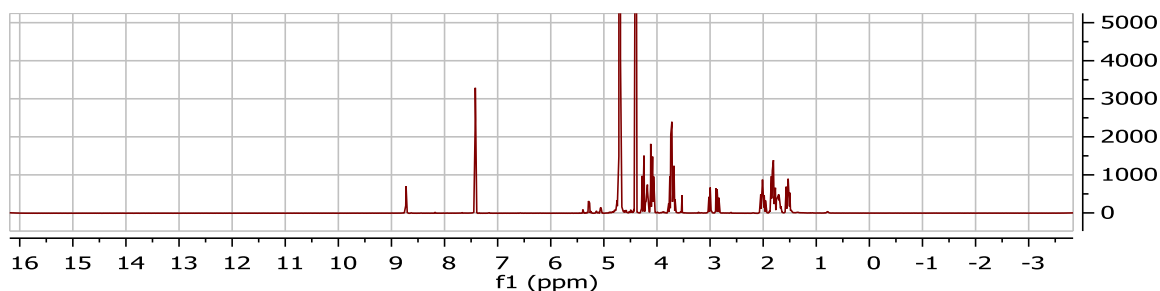
**THF-5: 1,3-bis((tetrahydrofuran-2-yl)methyl)-imidazolium
DL-tartrate**

2.07 ml (0.02 mol) tetrahydrofurfurylamine, 0.75 ml formaldehyde mixed with 2.25 ml DL-tartaric acid dispersed in 15 ml water (0.01 mol and 0.015 mol, respectively), 1.15 ml (0.01 mol) glyoxal. The crude product was extracted with ether (3x20 ml). The product was obtained after removal of volatiles *en vacuo* (81.0 % yield by NMR; 0.00807 mol).

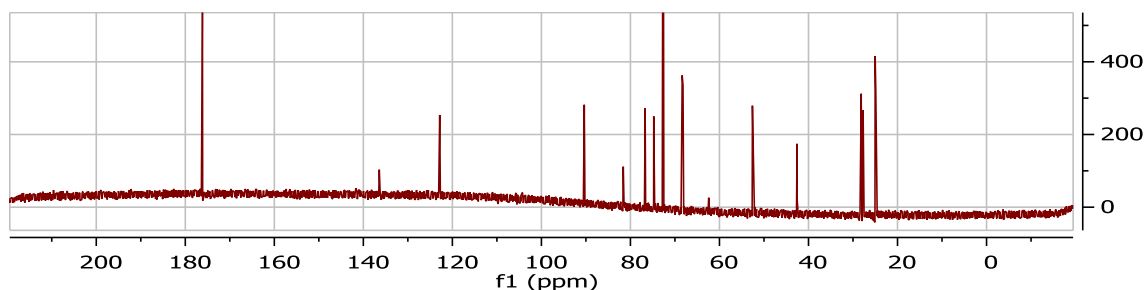


MS (water/FA): $m/z = 237.16$ (calculated for $[\text{M}]^+ \text{C}_{13}\text{H}_{21}\text{N}_2\text{O}_2^+$ in positive ion mode); found: $m/z = 237.1590$

NMR:



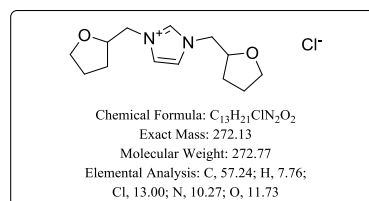
Spectrum 9: THF-5 – ^1H -NMR (measured in D_2O).



Spectrum 10: THF-5 – ^{13}C -NMR (measured in D_2O).

**THF-6: 1,3-bis((tetrahydrofuran-2-yl)methyl)-imidazolium
chloride**

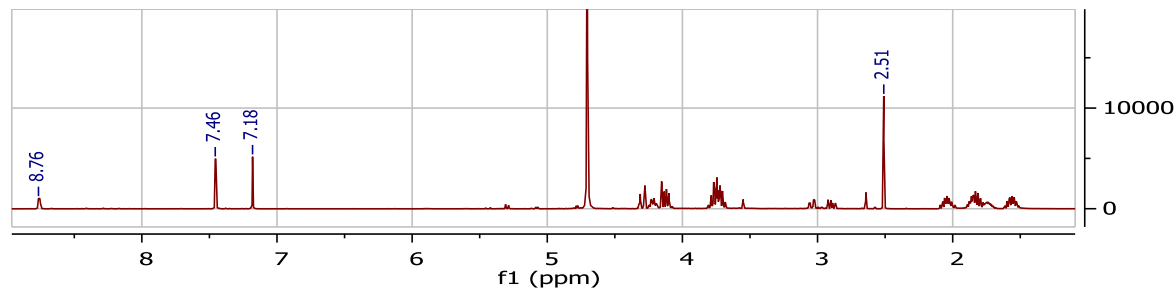
2.07 ml (0.02 mol) tetrahydrofurfurylamine, 0.75 ml formaldehyde mixed with 15 ml 1M hydrochloric acid (0.01 mol and 0.015 mol, respectively), addition over 40 min, 1.15 ml (0.01 mol) glyoxal. The crude product was



extracted with ether until the organic layer was colorless. No pure product could be isolated. The crude product was obtained after removal of volatiles *en vacuo* 3.35 g, 0.002198 molg⁻¹ by NMR (74.0 % yield by NMR; 0.00736 mol).

MS (ACN): m/z = 237.16 (calculated for [M]⁺ C₁₃H₂₁N₂O₂⁺ in positive ion mode); found: m/z = 237.27

NMR:



Spectrum 11: THF-6 – ¹H-NMR (measured in D₂O). Peaks at 7.18 and 2.51 correspond to 2-methyl imidazole used as an internal standard.

THF-7: 1,3-bis((tetrahydrofuran-2-yl)methyl)-imidazolium borate

2.07 ml (0.02 mol) tetrahydrofurfurylamine, 0.75 ml formaldehyde mixed with 0.93 g boric acid (0.01 mol and 0.015 mol, respectively), addition over 40 min, 1.15 ml (0.01 mol) glyoxal. The crude product was extracted with ether until the organic layer was colorless. No product was obtained.

Procedure B: General procedure for metathesis (compounds THF-8 – THF-10)

1 equivalent of THF-2 was dissolved in water, and the respective acid was added. The mixture was stirred. Water and acetic acid were removed *en vacuo* to obtain the product.

THF-8: 1,3-bis((tetrahydrofuran-2-yl)methyl)-imidazolium chloride

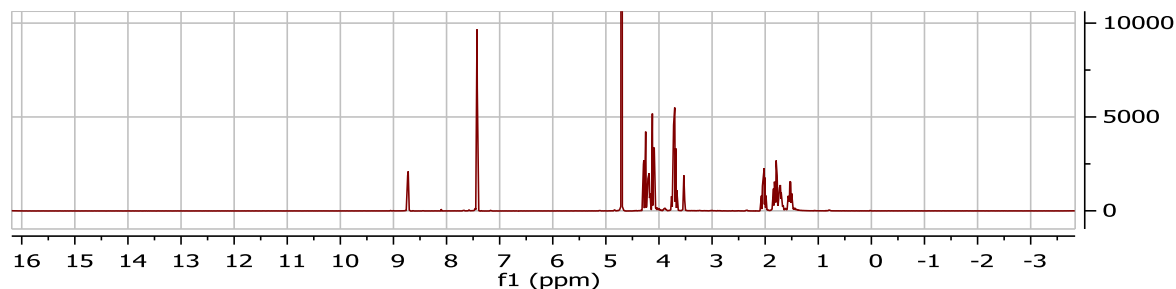
2.98 g THF-2 in 50 ml water, addition of 1 ml conc. HCl in 20 ml water.

Stirred at RT for 2h, freeze-dried overnight and dried at high vacuum. NMR

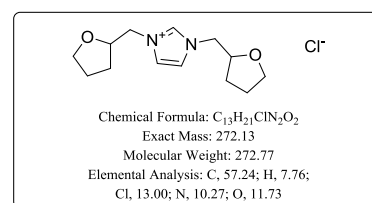
analysis revealed the presence of acetate, so the process was repeated using 0.16 ml conc. HCl in 10 ml water this time to yield the pure product (quant. yield, as determined by NMR).

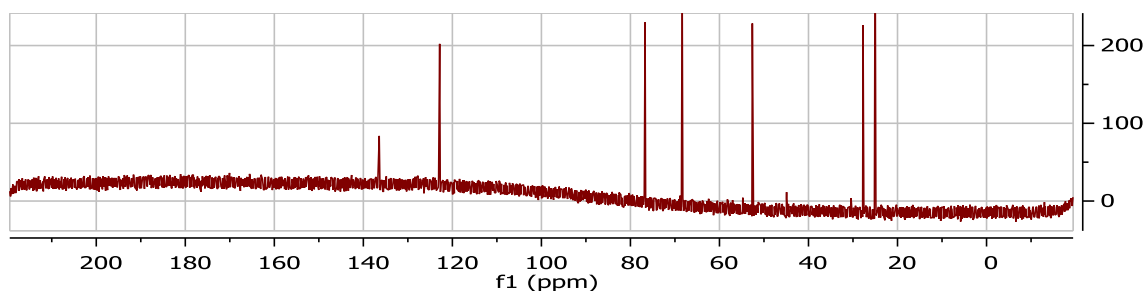
MS (ACN/FA): m/z = 237.16 (calculated for [M]⁺ C₁₃H₂₁N₂O₂⁺ in positive ion mode); found: m/z = 237.1599

NMR:



Spectrum 12: THF-8 – ¹H-NMR (measured in D₂O).

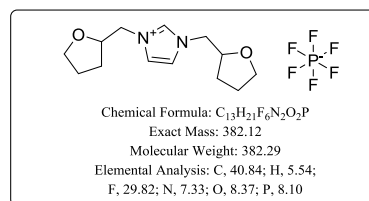




Spectrum 13: THF-8 – ^{13}C -NMR (measured in D_2O).

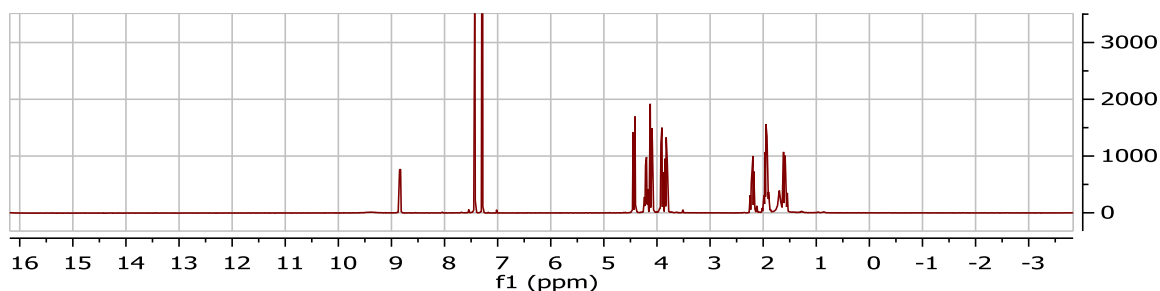
THF-9: 1,3-bis((tetrahydrofuran-2-yl)methyl)-imidazolium hexafluorophosphate

5.90 g THF-2 in 100 ml water, addition of 3.32 ml conc. hexafluorophosphoric acid. Stirred overnight at RT. The product was freeze-dried overnight and dried at high vacuum overnight to yield the pure product (65.0 % yield by NMR, 0.0128 mol).

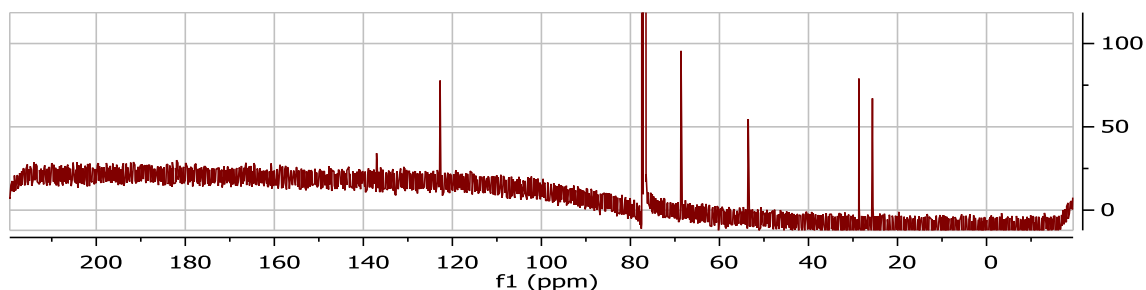


MS (water/FA): $m/z = 237.16$ (calculated for $[\text{M}]^+ \text{C}_{13}\text{H}_{21}\text{N}_2\text{O}_2^+$ in positive ion mode); found: $m/z = 237.1599$
 negative ion mode: $m/z = 144.96$ (calculated for $[\text{M}]^- \text{PF}_6^-$); found: $m/z = 144.9632$

NMR:



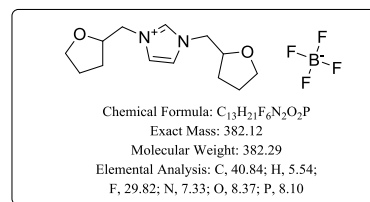
Spectrum 14: THF-9 – ^1H -NMR (measured in CDCl_3).



Spectrum 15: THF-9 – ^{13}C -NMR (measured in CDCl_3).

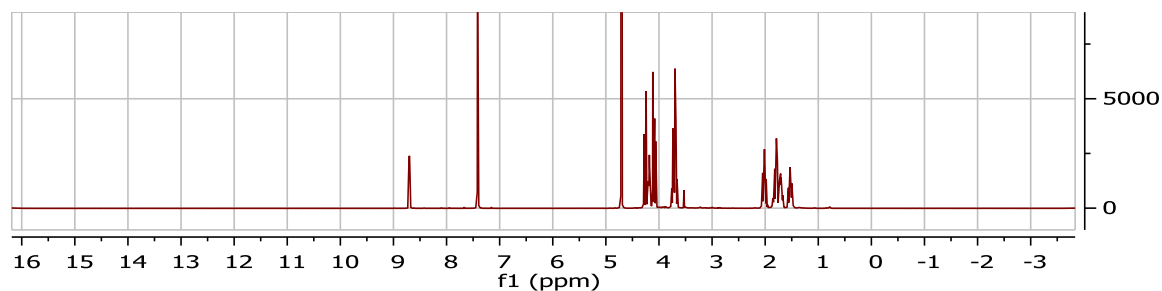
THF-10: 1,3-bis((tetrahydrofuran-2-yl)methyl)-imidazolium tetrafluoroborate

5.94 g THF-2 in 100 ml water, addition of 4.21 ml conc. tetrafluoroboric acid. Stirred overnight at RT. The product was freeze-dried overnight and dried at high vacuum overnight to yield the pure product (quant. yield by NMR)

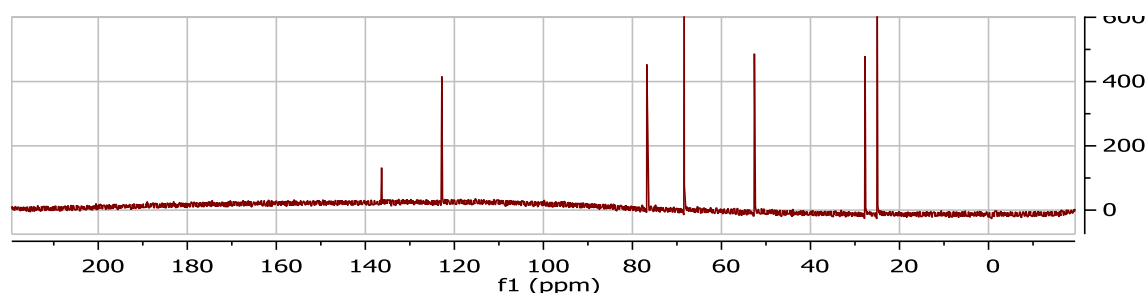


MS (water/FA): $m/z = 237.16$ (calculated for $[M]^+ C_{13}H_{21}N_2O_2^+$ in positive ion mode); found: $m/z = 237.1599$
negative ion mode: $m/z = 87.00$ (calculated for $[M]^- Cl^-$); found: $m/z = 87.0024$

NMR:



Spectrum 16: THF-10 – ¹H-NMR (measured in D₂O).



Spectrum 17: THF-10 – ¹³C-NMR (measured in D₂O).

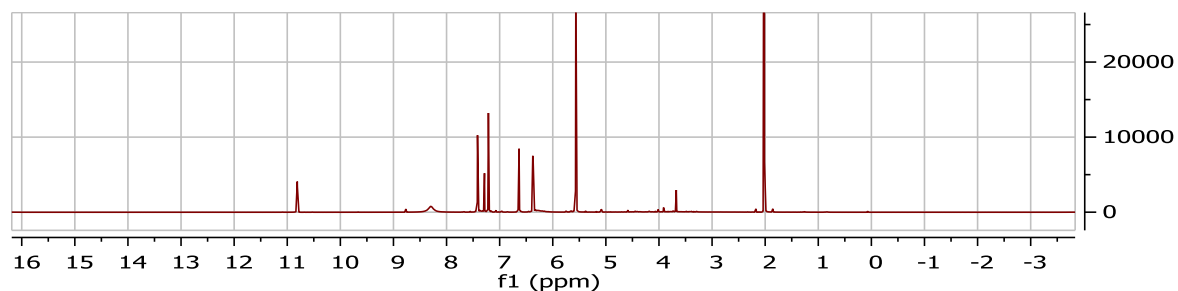
Compounds from 2.3 Cation design

F-2: 1,3-bis((furan-2-yl)methyl)-imidazolium acetate

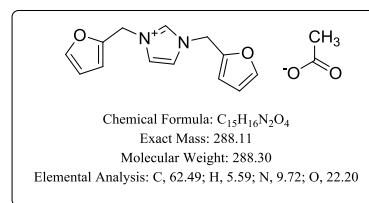
Synthesis carried out according to the procedure A. Synthesis was carried out under light exclusion (flasks and funnels wrapped in aluminum foil). 1.77 ml (0.02 mol) furfurylamine, 0.75 ml formaldehyde mixed with 0.86 ml acetic acid (0.01 mol and 0.015 mol, respectively; temperature kept below 10 °C while addition), 1.15 ml (0.01 mol) glyoxal. The mixture became very viscous. The crude product was extracted with ether until the organic layer was colorless. The product was freeze-dried and dried under high vacuum conditions (10⁻³ mbar, 1d at RT, 1d at 50 °C) to obtain the pure product (54.0 % yield by NMR; 0.00538 mol).

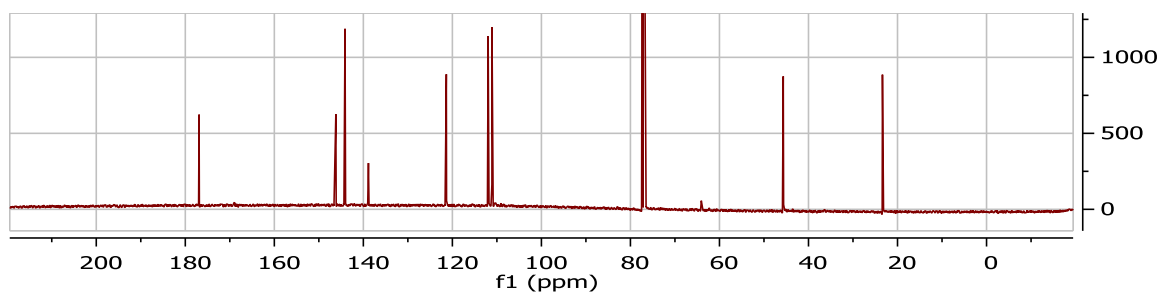
MS (ACN/FA): $m/z = 229.10$ (calculated for $[M]^+ C_{13}H_{21}N_2O_2^+$ in positive ion mode); found: $m/z = 229.0969$

NMR:



Spectrum 18: F-2 – ¹H-NMR (measured in CDCl₃).

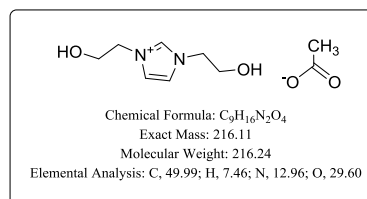




Spectrum 19: F-2 – ^{13}C -NMR (measured in CDCl_3).

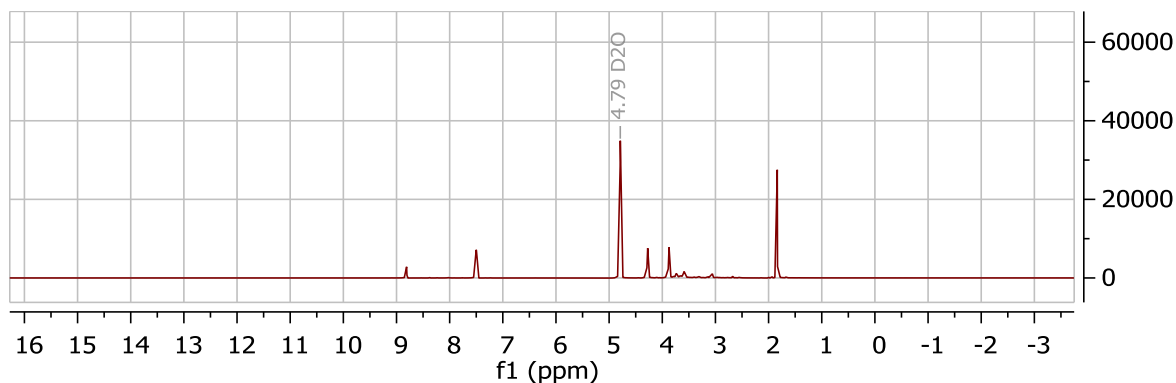
E-2: 1,3-bis((2-hydroxyethyl)-imidazolium acetate

Synthesis carried out according to procedure A. 2.99 ml ethanolamine (0.05 mol), 1.86 ml formaldehyde (0.025 mol) mixed with 2.15 ml acetic acid (0.0375 mol; temperature kept below 10°C while addition), 2.87 ml glyoxal (0.025 mol). The crude product was extracted with ether until the organic layer was colorless. The product was concentrated *en vacuo* to obtain 4.41 g of the pure product (88 % yield, corrected by water content as assessed with TGA).

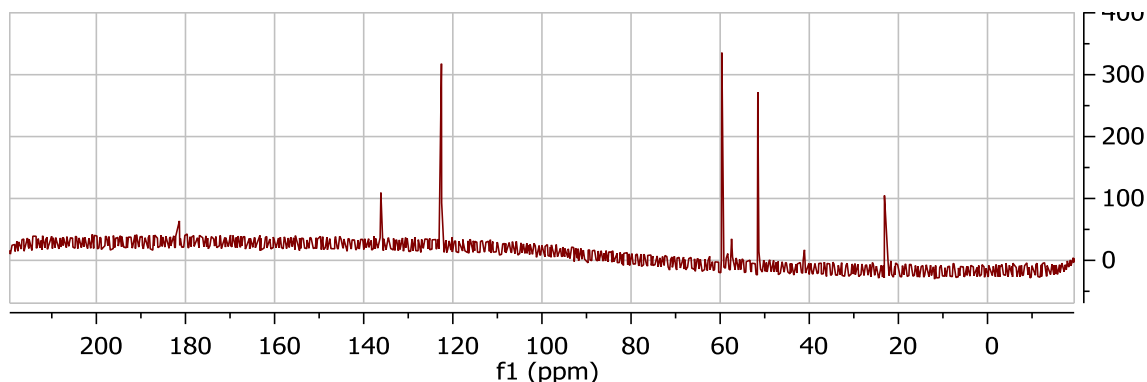


MS (ACN/FA): $m/z = 157.10$ (calculated for $[\text{M}]^+ \text{C}_7\text{H}_{13}\text{N}_2\text{O}_2^+$ in positive ion mode); found: $m/z = 157.10$

NMR:



Spectrum 20: E-2 – ^1H -NMR (measured in D_2O).



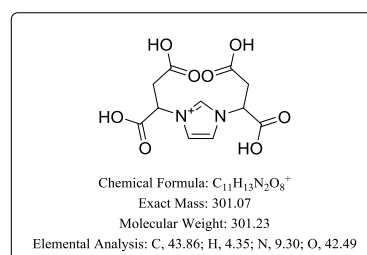
Spectrum 21: E-2 – ^{13}C -NMR (measured in D_2O).

Procedure for the synthesis of zwitterions

Synthesis was developed from literature procedures^[26,45]: 2 equivalents of the amino acid (AS) were dissolved in sodium hydroxide solution. Water was removed and the resulting monosodium salt of the AS was dissolved in water. 1 equivalent of formaldehyde and glyoxal was added and the mixture was stirred overnight. The crude mixture was extracted with ether three times. Residual ether was removed by concentration *en vacuo* for 10 min at 300 mbar and 60 °C. Concentrated hydrochloric acid was slowly added to the so obtained liquid while cooling in an ice-bath until precipitation of the product was observed. The pure product is obtained after filtration.

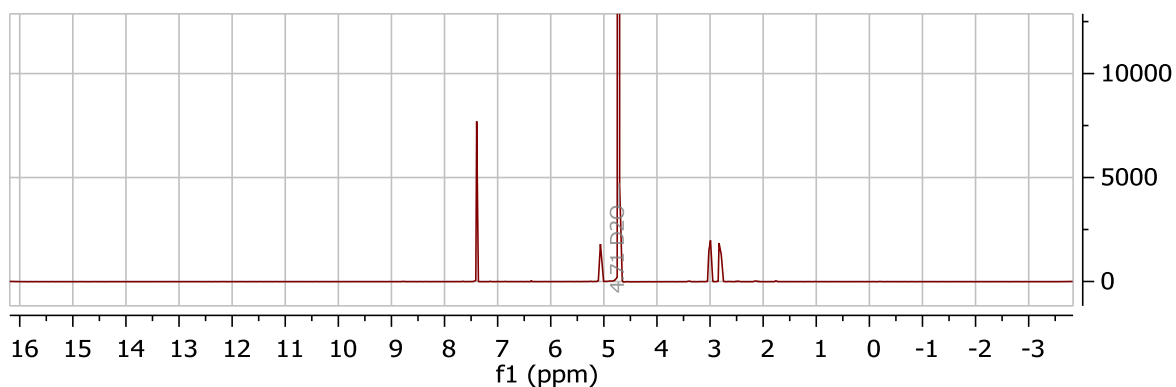
Asp: 3-carboxy-3-(3-(1,2-dicarboxyethyl)-imidazolium) propanoate

26.6 g (0.2 mol) aspartic acid in 200 ml 1 M aqueous NaOH. 7.5 ml (0.1 mol) formaldehyde, 11.4 ml (0.1 mol) glyoxal, stirred at 65 °C. Extracted with ether (3x50 ml). Yield: 6.74 g (0.0225 mol; 11.3 %).

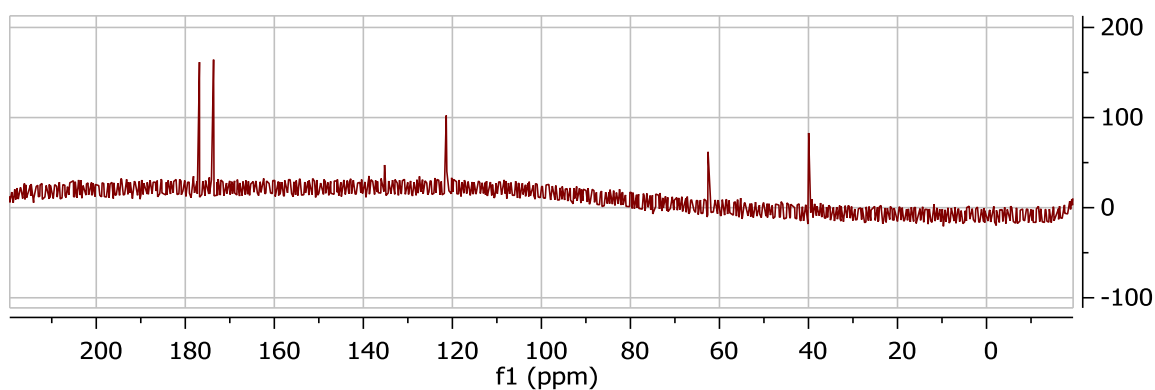


MS (H_2O): $m/z = 301.23$ (calculated for $[M]^+ C_{11}H_{13}N_2O_8^+$ in positive ion mode); found: $m/z = 301.13$

NMR:



Spectrum 22: Asp – 1H -NMR (measured in basic D_2O to aid solubility. Consequently the C2-proton is masked).

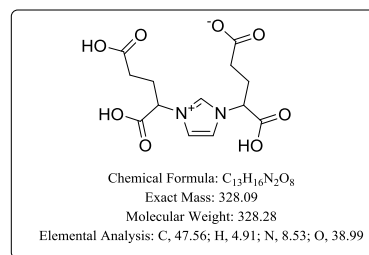


Spectrum 23: Asp – ^{13}C -NMR (measured in basic D_2O to aid solubility).

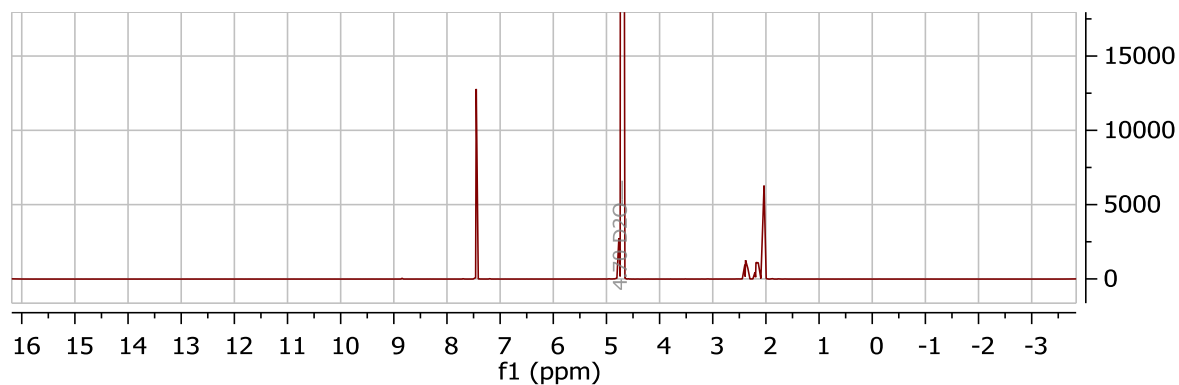
Glu: 4-carboxy-4-(3-(1,3-dicarboxypropyl)-imidazolium butanoate

29.4 g (0.2 mol) glutamic acid in 200 ml 1 M aqueous NaOH. 7.5 ml (0.1 mol) formaldehyde, 11.4 ml (0.1 mol) glyoxal, stirred at 60 °C. Extracted with ether (3x50 ml). Yield: 9.82 g (0.0299 mol; 15.0 %).

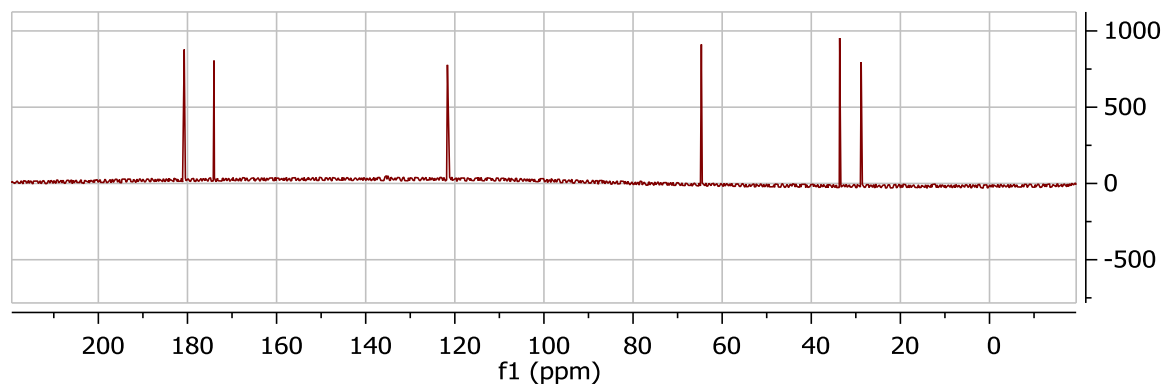
MS (H₂O): m/z = 329.10 (calculated for [M]⁺ C₁₃H₁₇N₂O₈⁺ in positive ion mode); found: m/z = 329.03



NMR:



Spectrum 24: Glu – ¹H-NMR(measured in basic D₂O to aid solubility. Consequently the C2-proton is masked).



Spectrum 25: Glu – ¹³C-NMR (measured in basic D₂O to aid solubility).

PENs from 2.4 Polymer synthesis *via* modified Debus-Radziszewski reaction

In a typical synthesis, chitosan and the diamine were dissolved in a mixture of water and acetic acid and stirred for an hour at room temperature. A mixture of glyoxal and formaldehyde was added and the solution was stirred for 10 minutes. After this the solution was cast into a PTFE petri dish and dried in an air oven over night at 60 °C.

Lysine based PENs

Lysine (diamine) and low-molecular weight chitosan (crosslinker) were used. 0.82 ml formaldehyde (0.011 mol) and 1.26 ml glyoxal (0.011 mol) were added.

Table A - 5: Synthesis of lysine based PENs.

| code | diamine | crosslinker | acetic acid | water |
|-------|----------------------|----------------------|-------------|-------|
| L-A-3 | 1.431 g (0.0094 mol) | 0.120 g (0.0006 mol) | 35 ml | 10 ml |
| L-A-5 | 1.370 g (0.009 mol) | 0.201 g (0.001 mol) | 35 ml | 10 ml |
| L-A-7 | 1.283 g (0.0086 mol) | 0.282 g (0.0014 mol) | 35 ml | 10 ml |

Cadaverine based PENs

Cadaverine (diamine) and low-molecular weight chitosan (crosslinker) were used. 0.82 ml formaldehyde (0.011 mol) and 1.26 ml glyoxal (0.011 mol) were added.

Table A - 6: Synthesis of cadaverine based PENs.

| code | amine | crosslinker | acetic acid | water |
|-------|----------------------|----------------------|-------------|-------|
| C-A-3 | 0.980 g (0.0094 mol) | 0.120 g (0.0006 mol) | 35 ml | 9 ml |
| C-A-5 | 0.938 g (0.009 mol) | 0.201 g (0.001 mol) | 35 ml | 9 ml |
| C-A-7 | 0.897 g (0.0086 mol) | 0.282 g (0.0014 mol) | 35 ml | 9 ml |

4,7,10-Trioxa-1,13-tridecanediamine based PENs

4,7,10-Trioxa-1,13-tridecanediamine (diamine) and low-molecular weight chitosan (crosslinker) were used. 0.82 ml formaldehyde (0.011 mol) and 1.26 ml glyoxal (0.011 mol) were added.

Table A - 7: Synthesis of 4,7,10-trioxa-1,13-tridecanediamine based PENs using crosslinker A.

| code | amine | crosslinker | acetic acid | water |
|-------|---------------------|----------------------|-------------|-------|
| T-A-3 | 2.16 g (0.0094 mol) | 0.120 g (0.0006 mol) | 23 ml | 5 ml |
| T-A-5 | 2.07 g (0.009 mol) | 0.201 g (0.001 mol) | 28 ml | 7 ml |
| T-A-7 | 1.98 g (0.0086 mol) | 0.282 g (0.0014 mol) | 35 ml | 9 ml |

4,7,10-Trioxa-1,13-tridecanediamine (diamine) and chitosan oligosaccharide lactate (crosslinker) were used. 0.82 ml formaldehyde (0.011 mol) and 1.26 ml glyoxal (0.011 mol) were added.

Table A - 8 Synthesis of 4,7,10-trioxa-1,13-tridecanediamine based PENs using crosslinker B.

| code | amine | crosslinker | acetic acid | water |
|-------|---------------------|----------------------|-------------|-------|
| T-B-3 | 2.16 g (0.0094 mol) | 0.120 g (0.0006 mol) | 23 ml | 5 ml |
| T-B-5 | 2.07 g (0.009 mol) | 0.201 g (0.001 mol) | 28 ml | 7 ml |
| T-B-7 | 1.98 g (0.0086 mol) | 0.282 g (0.0014 mol) | 35 ml | 9 ml |

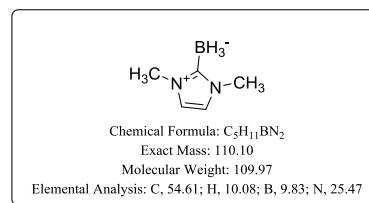
PENbranes from 3.3 Membranes from PENs

A cellulose sheet (ca. 67 mm diameter) is placed on the bottom of a petri dish. A solution of 2.07 g of the trioxatridecane, 0.1612 g chitosan oligosaccharide lactate (crosslinker B) in 23 ml glacial acetic acid 7 ml water is prepared and stirred for 30 min. To this solution, a mixture of 1.26 ml glyoxal and 0.82 ml formaldehyde is added and the resulting activated reaction mixture is stirred another 10 min. 7 ml of this activated reaction mixture are filled into the petri dish so that it rests on top of the cellulose sheet. The petri dish is then placed in an oven at 60 °C overnight. Cadaverine based membranes were fabricated accordingly using 0.94 g cadaverine instead of the trioxatridecane.

Compounds from 4.1 Protection of the C2-position

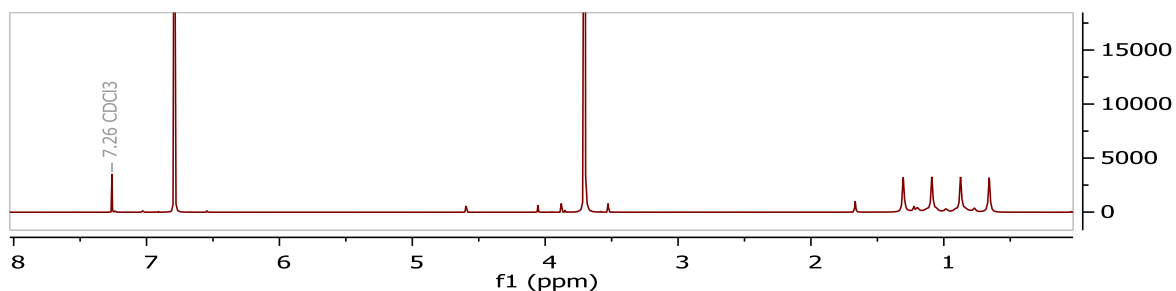
MBH₃MIm: 1,3-dimethylimidazol-2-ylidene borane

Synthesis was carried out from methylimidazole using the procedure described by Gardner et al.^[131] using 4 ml 1-methylimidazole, 3.8 ml 1-iodomethane in 10 ml DCM for the synthesis of 1,3-dimethylimidazolium iodide. The intermediate was not worked up. The round bottom flask (RBF) containing the iodide was set under argon atmosphere and 2.3 g of sodium borohydride and 50 ml toluene were added to the RBF. The mixture was heated to 125 °C overnight. Two phases formed, and the hot toluene was decanted from the sticky lower phase. The residue was extracted three times with 25 ml toluene. Toluene was removed *en vacuo* and the crude product was recrystallized from water to yield 1.6 g of the product in the form of white needles (0.015 mol, 30 % yield over both steps)

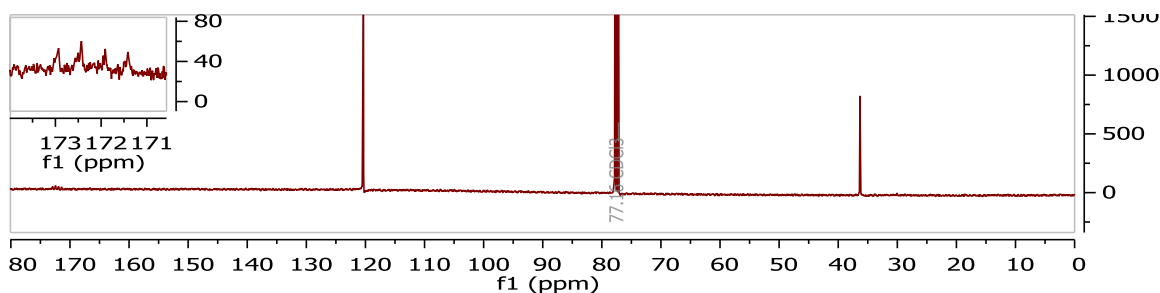


MS (ACN): m/z = 109.0932 (calculated for [M-H] C₅H₁₀BN₂⁺ in positive ion mode); found: m/z = 109.0935

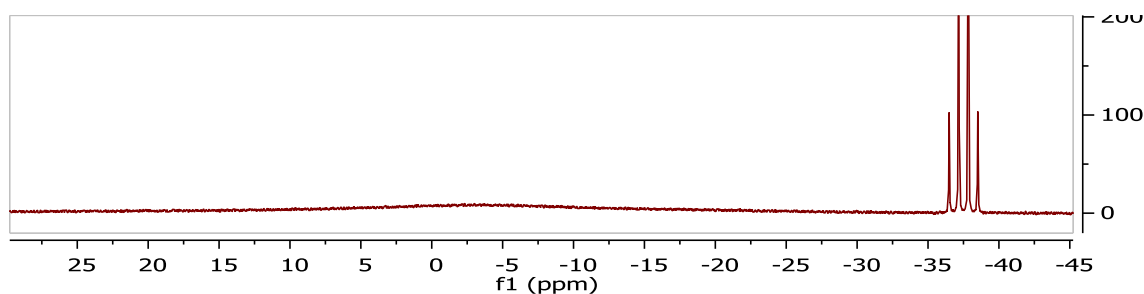
NMR:



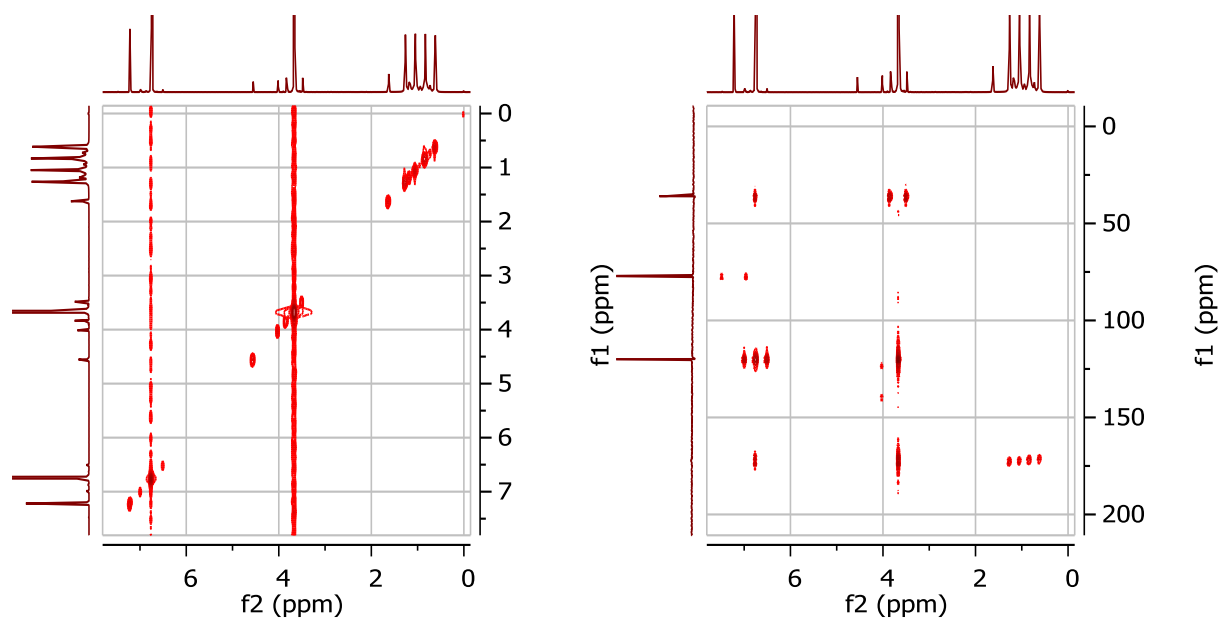
Spectrum 26: MBH₃MIm – ¹H-NMR (measured in CDCl₃).



Spectrum 27: MBH₃MIm – ¹³C-NMR (measured in CDCl₃)



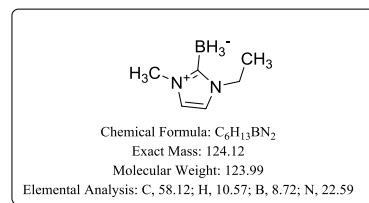
Spectrum 28: MBH₃MIm – ¹¹B-NMR (measured in CDCl₃).



Spectrum 29: MBH₃MIm; Left: COSY Right: HMBC (both measured in CDCl₃).

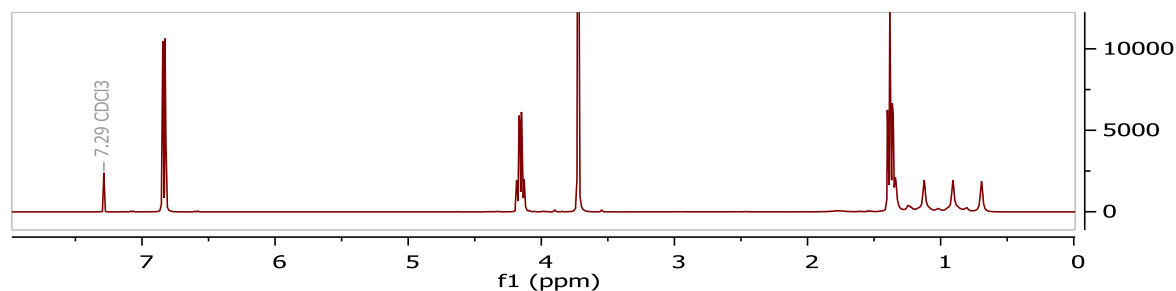
EBH₃MIm: 1-ethyl-3-methylimidazol-2-ylidene borane

Synthesis of 1-ethyl-3-methyl imidazolium iodide was carried out in a RBF by slowly adding 9.68 ml of ethyliodide to a solution of 8 ml 1-methylimidazole in 30 ml DCM. The mixture was stirred at 50 °C overnight. After removal of the solvent *en vacuo* and drying at 40 °C under vacuum conditions overnight, 23.14 g (M = 238.07; 0.097 mol; 97 % yield) of the product was obtained. Synthesis of 1-ethyl-3-methylimidazol-2-ylidene borane was carried out adapting the procedure described by Gardner et al.^[131] 22.82 g 1-ethyl-3-methyl imidazolium iodide and 100 ml toluene were filled into a RBF. After addition of 4.34 g sodium borohydride the mixture was heated to 125 °C overnight. The hot toluene was decanted, and the residue was extracted three times with 50 ml hot toluene. The solvent was removed *en vacuo* and the crude product was dissolved in ethylacetate. The organic phase was extracted three times with water, reduced *en vacuo*, washed with n-hexane and dried to yield 3.68 g of the product (0.030 mol; 30 % yield over both steps)

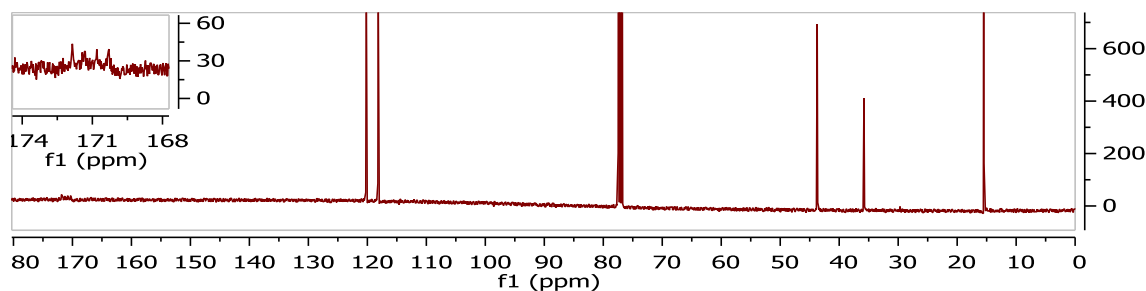


MS (ACN): m/z = 121.0932 (calculated for [M-3H] C₆H₁₀BN₂⁺ in positive ion mode); found: m/z = 121.0935

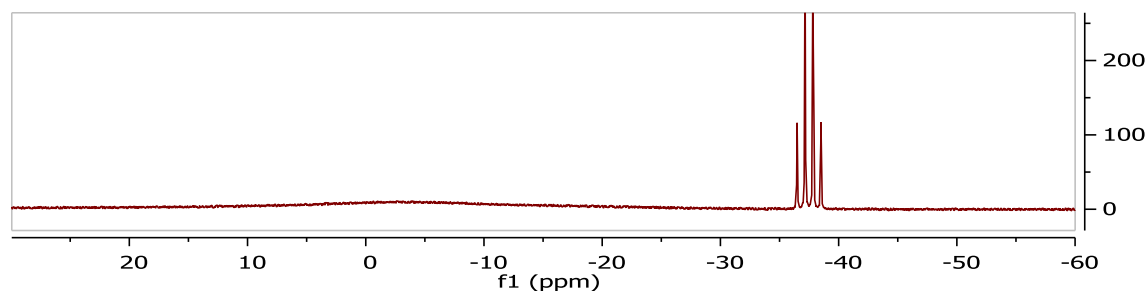
NMR:



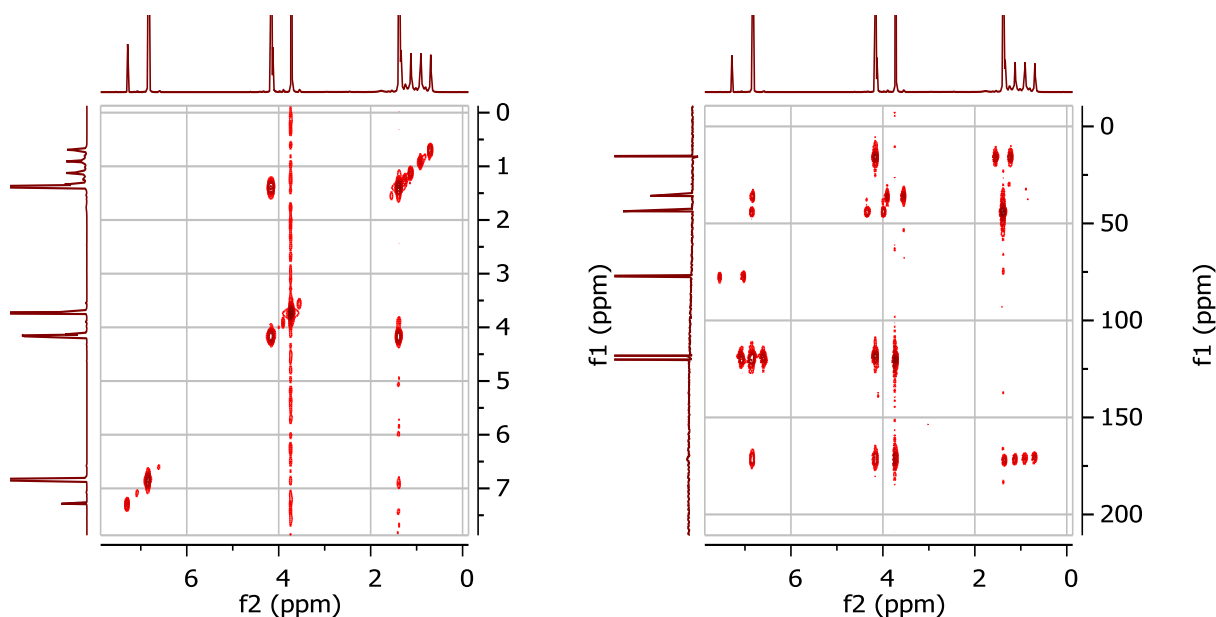
Spectrum 30: EBH₃MIm – ¹H-NMR (measured in CDCl₃).



Spectrum 31: EBH₃MIm – ¹³C-NMR (measured in CDCl₃).



Spectrum 32: EBH₃MIm – ¹¹B-NMR (measured in CDCl₃).



Spectrum 33: EBH_3MIm ; Left: COSY Right: HMBC (measured in $CDCl_3$).

BBH_3MIm : 1-butyl-3-methylimidazol-2-ylidene borane^[125]

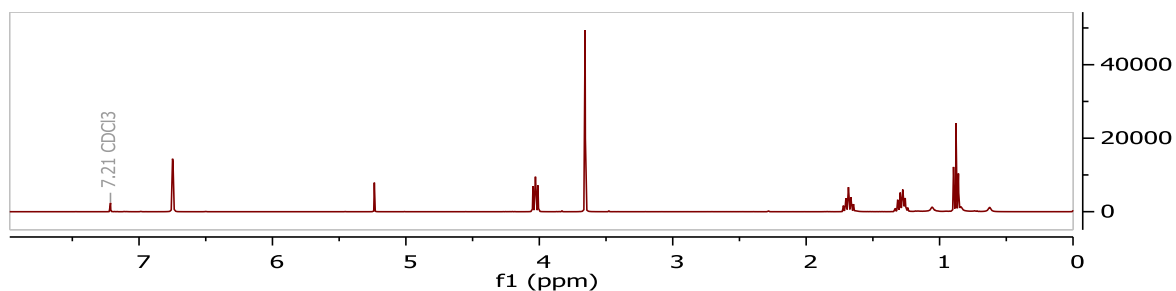
Synthesis of 1-butyl-3-methyl imidazolium iodide is described below (H-I; quant.) Synthesis of 1-butyl-3-methylimidazol-2-ylidene borane was carried out adapting the procedure described by Gardner et al.^[131]

13.32 g 1-butyl-3-methyl imidazolium iodide and 50 ml toluene were

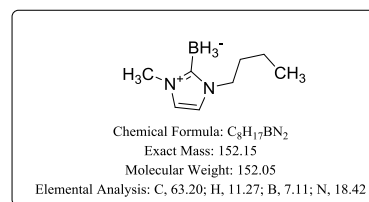
filled into a RBF. After addition of 2.27 g sodium borohydride the mixture was heated to 105 °C overnight. The reaction mixture forms two phases. The hot toluene (upper phase) was decanted from the viscous lower phase into an Erlenmeyer flask. Bubbles, formed from the lower phase, floated up during this process and were transferred to the Erlenmeyer flask, where they adhered to the glass. The still hot toluene was decanted into a RBF. This was repeated twice with 25 ml toluene which was always heated to 105 °C prior to decantation. The united toluene phases were left to settle overnight to allow the precipitation of residual salts and decanted. After removing the toluene *en vacuo*, the crude product was dissolved in DCM and decanted from the insoluble residue. Removal of the solvent yielded 2.54 g (0.017 mol, 34.0 % yield over both steps).

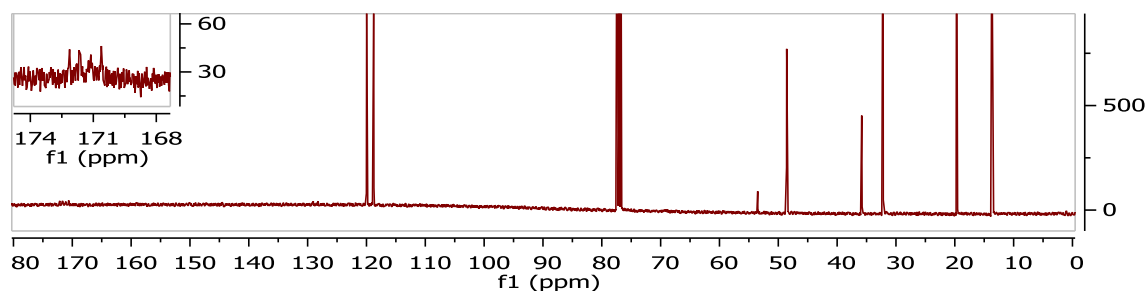
MS (ACN): $m/z = 175.1377$ (calculated for $[M+Na] C_8H_{17}BN_2Na^+$ in positive ion mode); found: $m/z = 175.1376$

NMR:

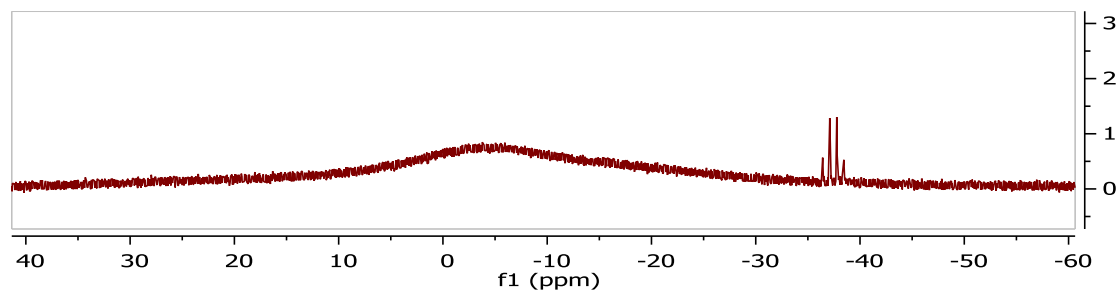


Spectrum 34: BBH_3MIm – 1H -NMR (measured in $CDCl_3$).

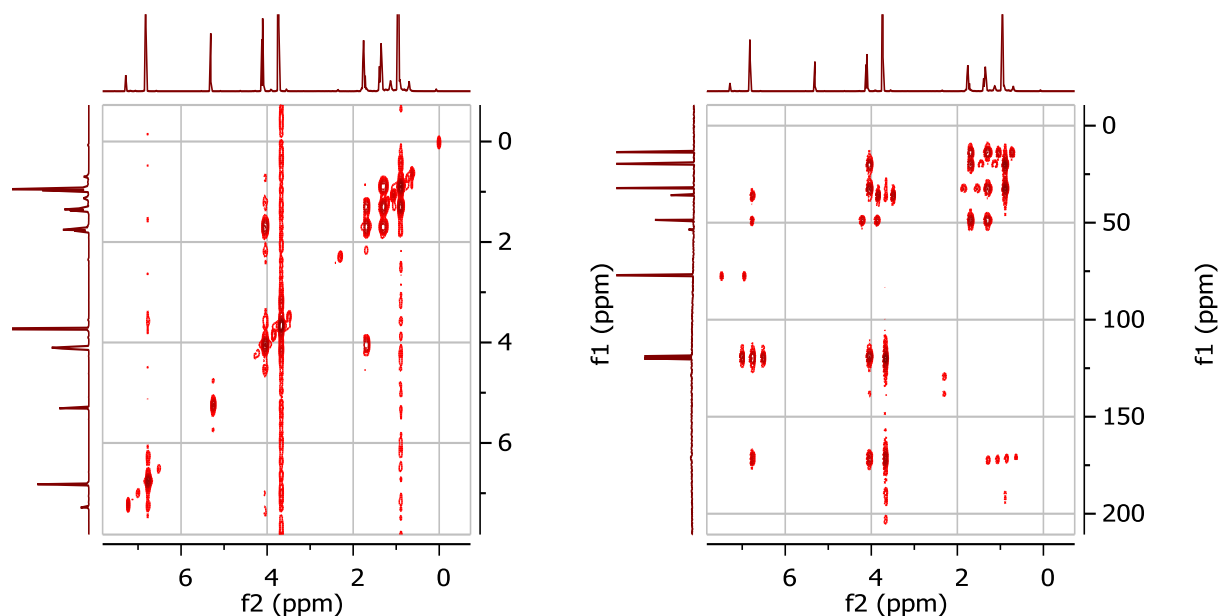




Spectrum 35: $BBH_3MIm - ^{13}C-NMR$ (measured in $CDCl_3$).



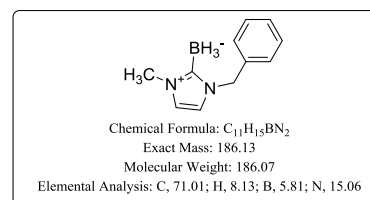
Spectrum 36: $BBH_3MIm - ^{11}B-NMR$ (measured in $CDCl_3$).



Spectrum 37: BBH_3MIm ; Left: COSY Right: HMBC (both measured in $CDCl_3$).

Benz BH_3MIm : 1-benzyl-3-methylimidazol-2-ylidene borane

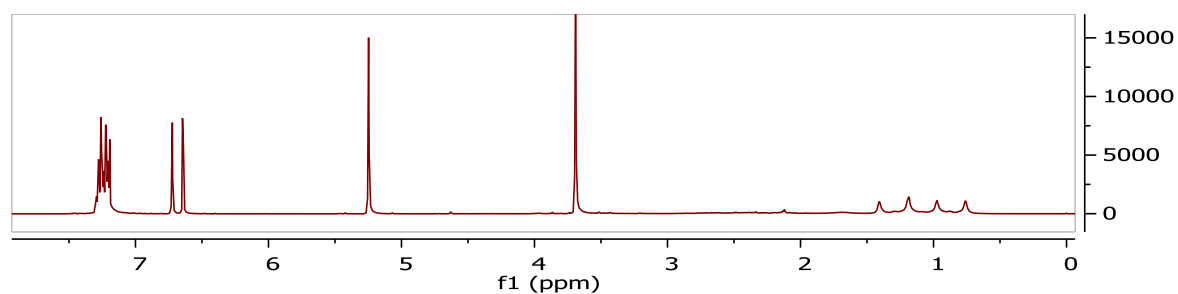
Synthesis of 1-benzyl-3-methyl imidazolium iodide was carried out in a RBF by slowly adding 7.47 ml of methyl iodide to a solution of 15.82 g 1-benzylimidazole in 50 ml DCM. The mixture was stirred at 50 °C for 2h. After removal of the solvent *en vacuo* the crude product was washed with ethylacetate which triggered precipitation of the product. After drying at 60 °C under vacuum conditions overnight, 27.81 g ($M = 300.01$; 0.093 mol; 93 % yield) of the product was obtained. Synthesis of 1-benzyl-3-methylimidazol-2-ylidene borane was carried out adapting the procedure described by Gardner et al.^[131] 6.0 g



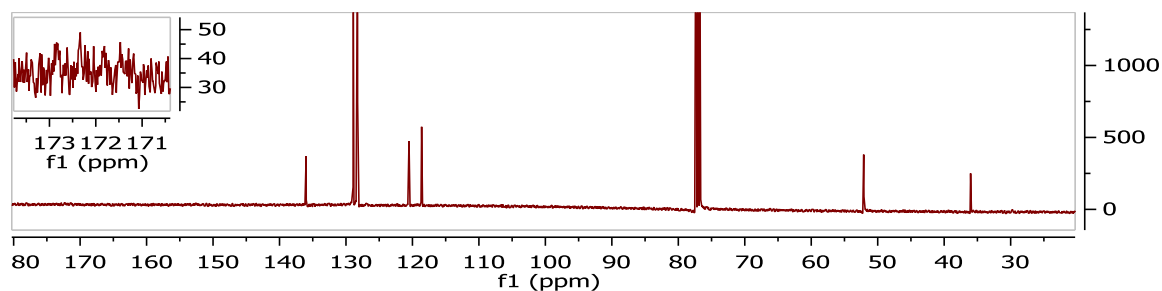
1-benzyl-3-methyl imidazolium iodide and 20 ml toluene were filled into a RBF. After addition of 0.92 g sodium borohydride the mixture was heated to 125 °C overnight. The hot toluene was decanted, and the residue was extracted three times with 20 ml hot toluene. The solvent was removed *en vacuo* and the crude product was dissolved in DCM and filtered to remove insoluble solids. The organic phase was removed *en vacuo*, to yield 0.31 g of the product (0.0017 mol; 7.9 % yield over both steps)

MS (ACN): m/z = 183.1088 (calculated for [M-2H] C₁₁H₁₂BN₂⁺ in positive ion mode); found: m/z = 183.1063)

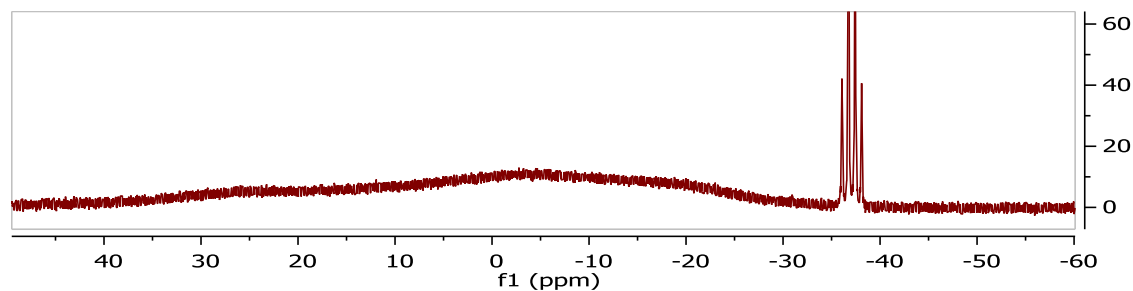
NMR:



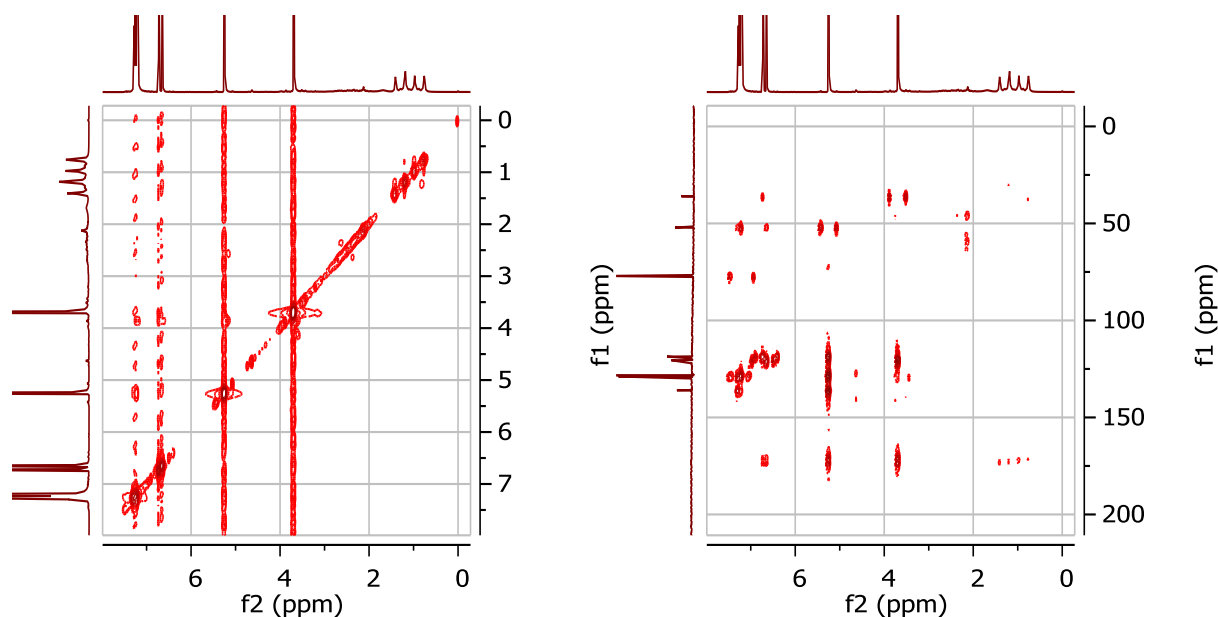
Spectrum 38: BenzBH₃MIm – ¹H-NMR (measured in CDCl₃).



Spectrum 39: BenzBH₃MIm – ¹³C-NMR (measured in CDCl₃).



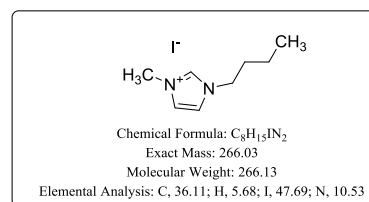
Spectrum 40: BenzBH₃MIm – ¹¹B-NMR (measured in CDCl₃).



Spectrum 41: BenzBH₃MIm; Left: COSY Right: HMBC (both measured in CDCl₃).

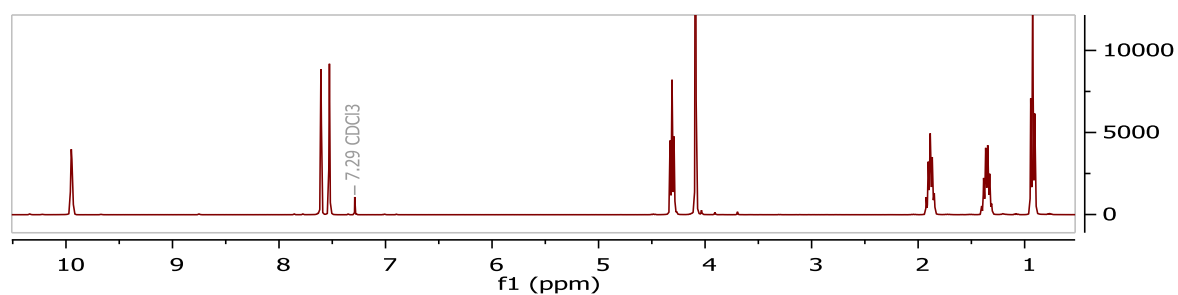
H-I: 1-butyl-2-methylimidazolium iodide^[125]

Synthesis was adapted from literature^[132,133]. 13.7 ml iodobutane were added to 8 ml 1-methylimidazole in 30 ml DCM. Reaction was heated to reflux and stirred overnight. After NMR-spectroscopy revealed the absence of 1-methylimidazole based peaks the solvent was removed *en vacuo*. The so obtained product (28.34 g, quant. yield) was used without further purification

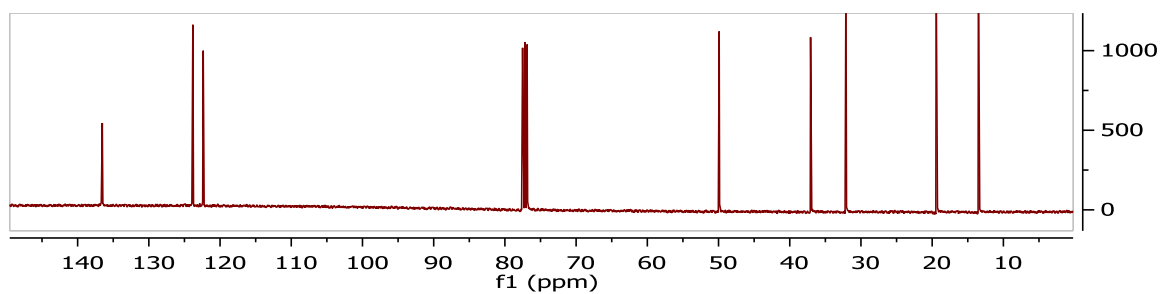


MS: positive ion mode: m/z = 139.12 (calculated for [M]⁺ C₈H₁₅BN₂⁺); found: m/z = 139.108; negative ion mode: m/z = 126.19 (calculated for [M]⁻ I⁻); found: m/z = 126.907

NMR:



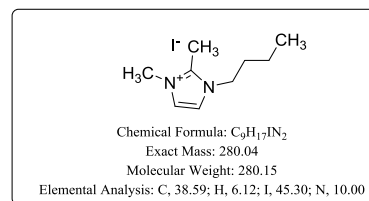
Spectrum 42: H-I – ¹H-NMR (measured in CDCl₃).



Spectrum 43: $H-I-^{13}C$ -NMR (measured in $CDCl_3$).

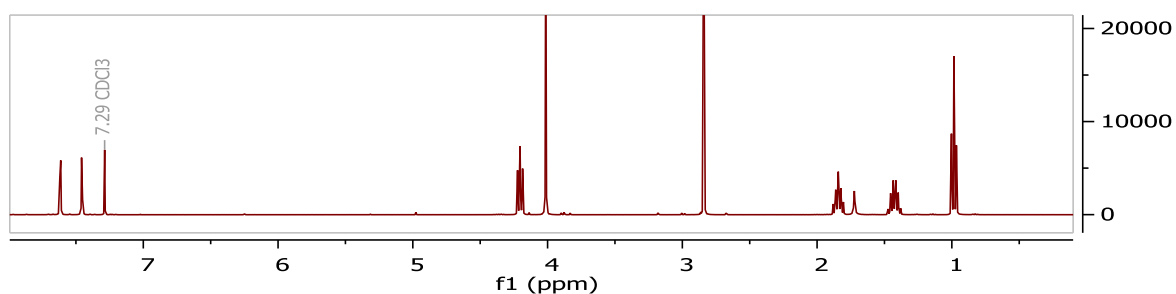
Me-I: 1-butyl-2,3-dimethylimidazolium iodide^[125]

13.7 ml iodobutane were added to 8.87 ml 1,2-dimethylimidazole in 30 ml DCM. Reaction was heated to reflux and stirred overnight. On the next day the solvent was removed *en vacuo*. The so obtained solid product (26.45.34 g, 0.094 mol, 94.0 % yield) was used without further purification

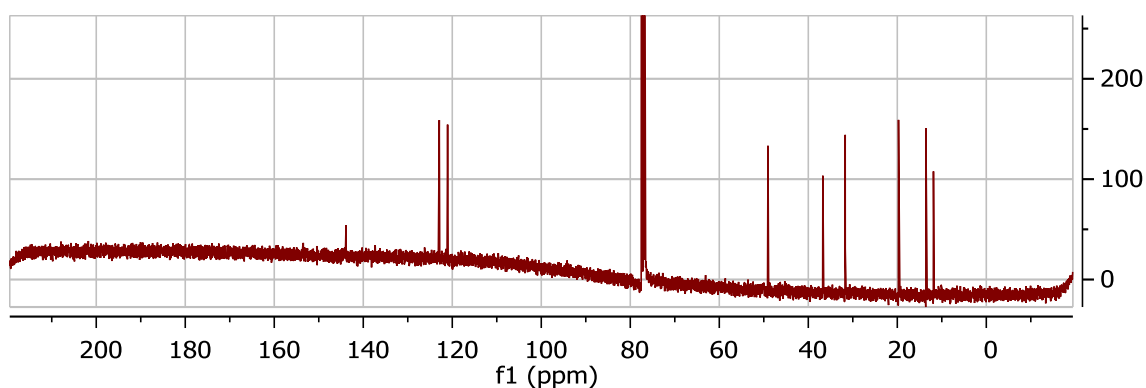


MS: positive ion mode: $m/z = 153.14$ (calculated for $[M]^+ C_9H_{17}BN_2^+$); found: $m/z = 153.138$; negative ion mode: $m/z = 126.19$ (calculated for $[M]^- I^-$); found: $m/z = 126.903$

NMR:

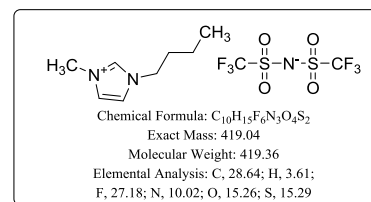


Spectrum 44: $M-I-^1H$ -NMR (measured in $CDCl_3$).



Spectrum 45: $M-I-^{13}C$ -NMR (measured in $CDCl_3$).

H-TFSI: 1-butyl-2-methylimidazolium bis(trifluoromethanesulfonyl) imide

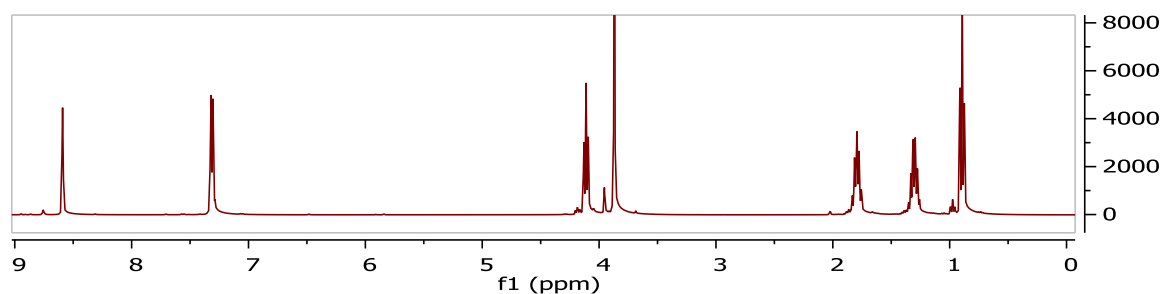


18.3 g lithium bis(trifluoromethylsulfonyl)imide in 30 ml dest. water were added to 14.13 g H-I in 20 ml dest. water. The mixture was stirred overnight

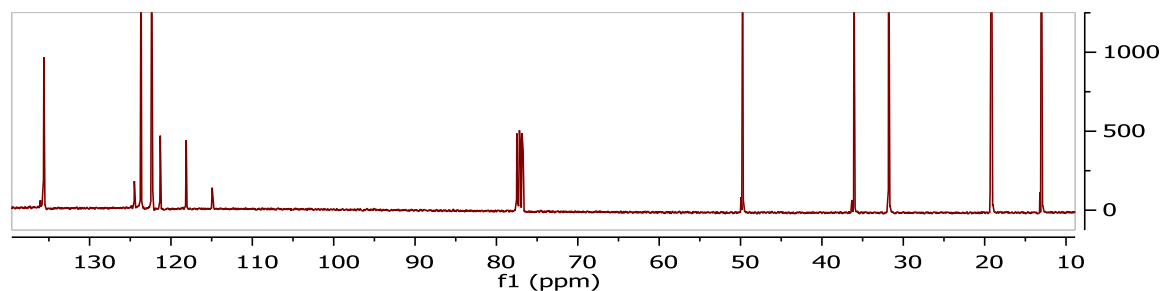
at RT. The resulting phases were separated, and the hydrophobic phase was washed with water until testing with silver nitrate solution did not form a visible precipitate and one more time after that. After drying the hydrophobic phase *en vacuo* 16.74 g (0.040 mol, 75.5 % yield) of the ionic liquid were obtained.

MS: positive ion mode: $m/z = 139.12$ (calculated for $[M]^+ C_8H_{15}BN_2^+$); found: $m/z = 139.118$; negative ion mode: $m/z = 279.92$ (calculated for $[M]^- C_2O_4S_2F_6N^-$); found: $m/z = 279.924$

NMR:

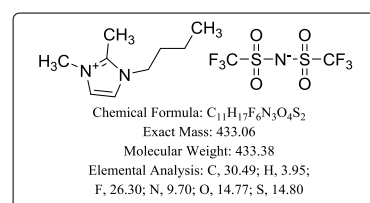


Spectrum 46: H-TFSI $-^1H$ -NMR (measured in $CDCl_3$).



Spectrum 47: H-TFSI $-^{13}C$ -NMR (measured in $CDCl_3$).

M-TFSI: 1-butyl-2,3-dimethylimidazolium bis(trifluoromethanesulfonyl)imide

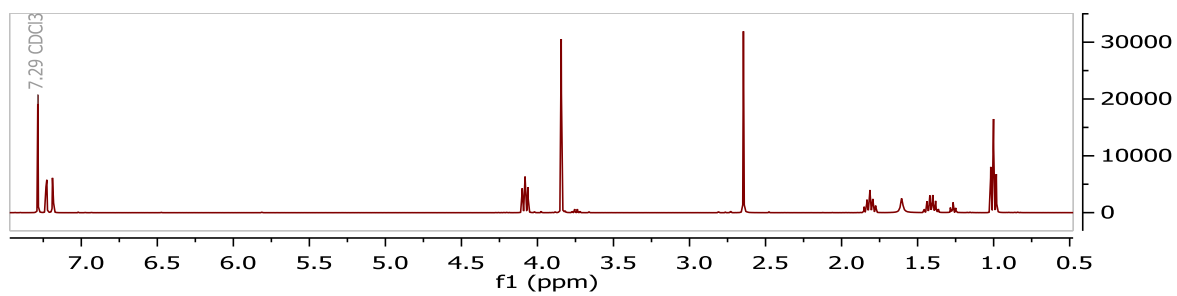


6.86 g lithium bis(trifluoromethylsulfonyl)imide in 20 ml dest. water were added to 5.35 g H-I in 40 ml dest. water. The mixture was stirred overnight

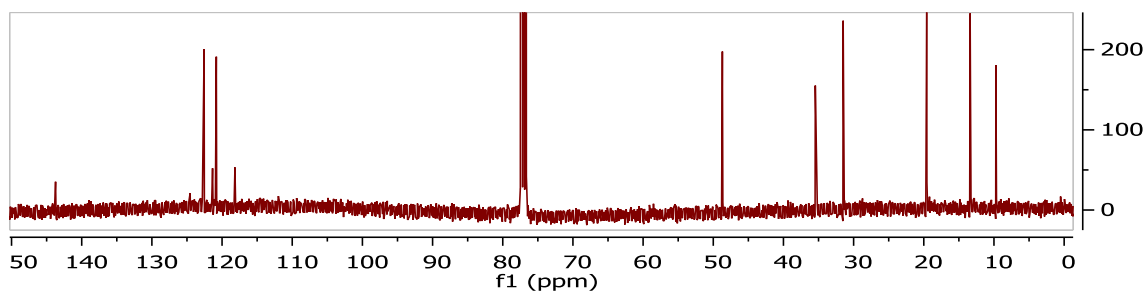
at RT. The resulting phases were separated, and the hydrophobic phase was washed with water until testing with silver nitrate solution did not form a visible precipitate and one more time after that. After drying the hydrophobic phase in high vacuum at 60 °C overnight, 6.64 g (0.015 mol, 79.0 % yield) of the ionic liquid was obtained.

MS: positive ion mode: $m/z = 153.14$ (calculated for $[M]^+ C_9H_{17}BN_2^+$); found: $m/z = 153.137$; negative ion mode: $m/z = 279.92$ (calculated for $[M]^- C_2O_4S_2F_6N^-$); found: $m/z = 279.917$

NMR:



Spectrum 48: *M*-TFSI – ^1H -NMR (measured in CDCl_3).



Spectrum 49: *M*-TFSI – ^{13}C -NMR (measured in CDCl_3).

6.3 Abbreviations and units used

| | |
|--------------------------------------------------|-----------------------------------------------------------------------------------------|
| % _m | mass percent |
| ACN | acetonitrile |
| CIB | chloride ion battery |
| CL | crosslinker |
| e.g. | exempli gratia (for example) |
| <i>en vacuo</i> | using rotary evaporation (60 °C water bath, max. 40 mBar, unless denoted otherwise) |
| DCM | dichloromethane |
| EI | electron ionization |
| ESI | electrospray ionization |
| FA | formic acid |
| FSI | bis(fluorosulfonyl)imide anion |
| HOAc | acetic acid |
| HCl | hydrochloric acid |
| i.e. | id est (that is) |
| IL | ionic liquid |
| ImIL | imidazolium ionic liquid |
| l.t.r. | from left to right |
| M | molar (mol ⁻¹) |
| mDRr | modified Debus-Radziszewski reaction |
| NHC | <i>N</i> -heterocyclic carbene |
| NHE | normal hydrogen electrode |
| pDRr | poly Debus-Radziszewski reaction |
| PIL | poly(ionic liquid) |
| RBF | round bottom flask |
| RT | room temperature (20 °C) |
| SHE | standard hydrogen electrode |
| T _G , T _M , T _C | temperature of a glass transition, melting point, (cold) crystallization (respectively) |
| TFSI | bis(trifluoromethylsulfonyl)imide anion |
| trioxatridecane | 4,7,10-trioxa-1,13-tridecanediamine |
| TSIL | task-specific ionic liquid |
| v.s. | vide supra (see above) |
| v.i. | vide infra (see below) |

6.4 Materials

List of chemicals:

| chemical (name in text) | synonym | CAS-number | purity/grade | supplier |
|----------------------------------|-------------------------------|-------------|---------------------------------------------------------------|-------------------|
| acetic acid | glacial acetic acid | 64-19-7 | analytical reagent grade | fisher Scientific |
| acetone | dimethyl ketone, propanone | 67-64-1 | ≥99.8% ACS Reag. Ph. Eur. Zur Analyse | VWR chemicals |
| L-aspartic acid | (S)-(+) Aminosuccinic acid | 56-84-8 | 98+% | Acros Organics |
| cadaverine | 1,5-Diaminopentane | 462-94-2 | 98% | Acros Organics |
| chitosan (low molecular weight) | deacetylated chitin | 9012-76-4 | low molecular weight | Aldrich |
| chitosan oligosachharide lactate | - | 148411-57-8 | average M _n 5,000 | Aldrich |
| choroform | trichloromethane | 67-66-3 | 99.0-99.4% stabilisiert. ACS, Reag. Ph. Eur zur Analyse | VWR chemicals |
| chloroform-d | deuteriochloroform | 865-49-6 | 99.8 %D | Aldrich |
| diethylether | DEE, ether | 60-29-7 | contains BHT as inhibitor, puriss. p.a., ACS reagent., ≥99.8% | Sigma-Aldrich |
| dimethylsulfoxide | DMSO | 67-68-5 | puriss. p.a., dried, ≤0.02% water | Sigma-Aldrich |
| ethanol | ethyl alcohol | 64-17-5 | absolut | Sigma-Aldrich |
| ethanolamine | 2-aminoethanol | 141-43-5 | ACS reagent, ≥99.0% | Sigma-Aldrich |
| formaldehyde | Formalin | 50-00-0 | 37-38% w/w, stab with methanol | Applicem Panreac |
| formic acid | methanoic acid | 64-18-6 | 98-100%, certified AR for Analysis | fisher scientific |
| furfurylamine | 2-Aminoethylfuran | 617-89-0 | 99% | Alfa Aesar |
| dichloromethane | methylene dichloride | 75-09-2 | 99.9 % by GC | Sigma-Aldrich |
| glyoxal | ethanedial, oxalaldehyde | 107-22-2 | 40% _m solution in water | Roth |
| glutamic acid | (S)-2-aminopentanedioic acid | 56-89-0 | reagent plus | Sigma |
| hexafluorophosphoric acid | hydrogen hexafluoro-phosphate | 16940-81-1 | 60 wt.% solution in water (PF6) | Acros Organics |
| hydrochloric acid | - | 7647-01-0 | rauchend, ROTIPURAN® | Roth |

| | | | | |
|---------------------------------------------|------------------------------------------------|------------|----------------------------------------|-------------------|
| | | | 37%, p.a. | |
| iodobutane | 1-iodobutane butyl iodide | 542-69-8 | 99 % | Aldrich |
| L-lactic acid | Sarcosine acid, (S)-2-hydroxypropionic acid | 79-33-4 | >85% _m solution in water | Aldrich |
| L-lysine | (2)-2,6-Diaminocaproic acid | 56-87-1 | ≥98% (TLC) | Sigma |
| lithium bis (trifluoromethanesulfonyl)imide | bis(trifluoromethanesulfonyl)lithium salt | 90076-65-6 | 99 % | io-li-tec |
| magnesium borohydride | - | 16903-37-0 | 95% | Sigma -Aldrich |
| methanol | methyl alcohol | 67-56-1 | certified AR for Analysis | fisher scientific |
| methylimidazole | 1-methylimidazole | 616-47-7 | ReagentPlus®, 99% | Aldrich |
| methylimidazole | 1-methylimidazole | 616-47-7 | ≥99 % purified by redistillation | Sigma-Aldrich |
| pyridine | - | 110-86-1 | 99+% | Alfa Aesar |
| sodium borohydride | sodium tetrahydridoborate | 16940-66-2 | 99 % | Acros |
| sodium hydroxide | caustic soda | 1310-73-2 | Certified AR for Analysis | fisher scientific |
| succinic acid | butanedioic acid | 110-15-6 | ≥99.0% | Sigma-Aldrich |
| DL-tartaric acid | DL-2,3-dihydroxybutanedioic acid | 133-37-9 | 99% reagent plus | Aldrich |
| tetrafluoroboric acid | - | 16872-11-0 | 50% w/w aq. soln. | Alfa Aesar |
| tetrahydrofuran | 2-(amionethyl) tetrahydrofuran | 4795-29-3 | 97% | Acros Organics |
| 4,7,10-trioxa-1,13 tridecanediamine | oxolane, tetramethylene oxide | 109-99-9 | ≥ 99.5 stabilisiert, AnalaR NORMAPUR ® | VWR chemicals |
| toluene | - | 108-88-3 | 99.7 % by GC | Honeywell |

6.5 Declaration

Die Vorliegende Arbeit entstand im Zeitraum zwischen Dezember 2015 und Mai 2018 unter der Betreuung von Prof. Dr. Dr. h.c. Markus Antonietti am Max-Planck-Institut für Kolloid- und Grenzflächenforschung.

Hiermit erkläre ich, dass die vorliegende Arbeit an keiner anderen Hochschule eingereicht sowie selbstständig von mir angefertigt wurde und nur hier angegebenen Hilfsmittel und Literatur verwendet wurden.

The present work was carried out and written during December 2015 and May 2018 at the Max Planck Institute of Colloids and Interfaces under the supervision of Prof. Markus Antonietti.

I declare that I have produced this work using only literature and other aids as described and listed here.

STEFFEN TRÖGER-MÜLLER,

POTSDAM, 2018

7 Acknowledgements

It would have been impossible to conduct the experiments and measurements, do the research and collect the data used to write this thesis without the support of a lot of people. In science we may stand on the figurative shoulders of giants when we can rely on the work of those that came before us, but it is the people that are here with us now that enable our work in every way.

First I would like to thank my family, the tiny and the big one, for support, motivation, kindness and a kick every now and then. The same gratitude extends to my friends. I would like to thank everybody in the MPIKG and this expressively includes the administration, store, workshop, library and IT-department. Research would not be possible without them even though most of the time we do not even see them doing their work. I would like to specially thank Marco Bott, Jan von Szada-Borrryszkowski, Annette Pape, Silke Niehaus-Weingärtner, Klaus Bienert, Robert Gaebel, Henry Liebner, Cliff Janiszewski, Judith Hoyer, Jasmin Müller, Heike Kienert, Ralf Ditsch, Paul Meißner, Fridtjof Neuber, René Genz, and of course everybody else.

I would like to thank my colleagues for creating the unique working atmosphere of the MPIKG. Thank You Valerio, Jessica, Ivan, Lucky, Jinyeon, Elliot, Chris, Noah, Caro, Jochen, Marlies, Baris, Victoria, Thomas and Thomas, Max, Antje, Silvia, Tabea, Majd, Ines, Katharina, Jeannette, Olaf, Irina, Sasha, Heike, Eva, Runyu, Bernhard and so many more. I want to expressively thank the technicians that are a part of the list above for conducting any measurements (You know what You did!) and I want to include another special *thank You* to Jessica.

Needless to say I want to thank Prof. Markus Antonietti for support, constructive discussions and a nudge in the right direction at the right moment. The same gratitude extends to Prof. Andreas Taubert for many a constructive discussion.

I also want to thank Prof Andrea Balducci for making himself available as my third reviewer.

Finally, I want to thank Dr. Clemens Liedel for being an amazing boss, for always having an open door and time to discuss relevant and less relevant matters and for giving me enough space to tinker without allowing me to float away.

8 References

- [1] W. Steffen, P. J. Crutzen, J. R. McNeill, *Ambio* **2007**, *36*(8), 614–621.
- [2] P. J. Crutzen, *Nature* **2002**, *415*(6867), 23.
- [3] NASA, "GLOBAL CLIMATE CHANGE . Vital Signs of the Planet", The consequences of climate change, to be found under <https://climate.nasa.gov/effects/>. Accessed: 07.02.2018; 20:15
- [4] L. Caesar, S. Rahmstorf, A. Robinson, G. Feulner, V. Saba, *Nature* **2018**, *556*(7700), 191–196.
- [5] a) S. Zhao, B. Lü, R. Li, A. Zhu, C. Wu, *Sci. China Earth Sci.* **2016**, *59*(2), 223–235; b) A. H. Arthington, N. K. Dulvy, W. Gladstone, I. J. Winfield, *Aquatic Conserv: Mar. Freshw. Ecosyst.* **2016**, *26*(5), 838–857;
- [6] a) M. Winter, R. J. Brodd, *Chem. Rev.* **2004**, *104*(10), 4245–4270; b) G. L. Soloveichik, *Chem. Rev.* **2015**, *115*(20), 11533–11558;
- [7] U. Bardi, *The Limits to Growth Revisited*; Springer New York, New York, NY, **2011**.
- [8] OECD, "A Definition of Sustainable Chemistry", to be found under <http://www.oecd.org/chemicalsafety/risk-management/sustainablechemistry.htm>. Accessed: 07.01.2018; 20:17
- [9] P. T. Anastas, J. C. Warner, *Green chemistry: Theory and practice*; Oxford Univ. Press, Oxford, **2000**.
- [10] ACS Green Chemistry Institute, "Green Chemistry Pocket Guide", to be found under <https://www.acs.org/content/acs/en/greenchemistry/what-is-green-chemistry/principles/12-principles-of-green-chemistry.html>, **2014**. Accessed: 18.01.2018; 14:33
- [11] a) K. R. Seddon, *J. Chem. Technol. Biotechnol.* **1997**, *68*(4), 351; b) J. S. Wilkes in *Ionic Liq., Vol. 818*; (Eds. R. D. Rogers, K. R. Seddon), American Chemical Society, Washington, DC, **2002**, pp. 214–229;
- [12] P. Walden, *Bull. Acad. Imp. Sci. Saint-Pétersbourg*, *1914*(8), 405.
- [13] S. Gabriel, *Ber. Dtsch. Chem. Ges.* **1888**, *21*(2), 2664–2669.

- [14] S. Mallakpour, M. Dinari in *Green Solvents II, Chemistry*; (Eds. A. Mohammad, D. Inamuddin), Springer Netherlands, Dordrecht, **2012**, pp. 1–32.
- [15] A. A. C. Toledo Hijo, G. J. Maximo, M. C. Costa, E. A. C. Batista, A. J. A. Meirelles, *ACS Sustainable Chem. Eng.* **2016**, *4*(10), 5347–5369.
- [16] J. Ranke, S. Stolte, R. Störmann, J. Arning, B. Jastorff, *Chem. Rev.* **2007**, *107*(6), 2183–2206.
- [17] N. V. Plechkova, K. R. Seddon, *Chem. Soc. Rev.* **2008**, *37*(1), 123.
- [18] A. Stark, K. R. Seddon in *Kirk-Othmer Encyclopaedia of Chemical Technology*; (Ed. A. Seidel), John Wiley & Sons, Inc, Hoboken, New Jersey, **2007**, pp. 836–920.
- [19] S. Kirchhecker, S. Tröger-Müller, S. Bake, M. Antonietti, A. Taubert, D. Esposito, *Green Chem.* **2015**, *17*(8), 4151.
- [20] K. C. Badgajar, B. M. Bhanage, *Bioresour. Technol.* **2015**, *178*, 2–18.
- [21] T. Kakibe, N. Yoshimoto, M. Egashira, M. Morita, *Electrochem. Commun.* **2010**, *12*(11), 1630.
- [22] G. B. Appetecchi, M. Montanino, D. Zane, M. Carewska, F. Alessandrini, S. Passerini, *Electrochim. Acta* **2009**, *54*(4), 1325.
- [23] T. Watkins, A. Kumar, D. A. Buttry, *J. Am. Chem. Soc.* **2016**, *138*(2), 641.
- [24] B. Gelinas, J. C. Forgie, D. Rochefort, *J. Electrochem. Soc.* **2014**, *161*(4), H161.
- [25] J. Yuan, D. Mecerreyes, M. Antonietti, *Prog. Polym. Sci.* **2013**, *38*(7), 1009.
- [26] D. Depuydt, A. van den Bossche, W. Dehaen, K. Binnemans, *RSC Adv.* **2016**, *6*(11), 8848.
- [27] M. Francisco, S. Lago, A. Soto, A. Arce, *Fluid Phase Equilib.* **2010**, *296*(2), 149–153.
- [28] R. Klein, O. Zech, E. Maurer, M. Kellermeier, W. Kunz, *The journal of physical chemistry. B* **2011**, *115*(29), 8961–8969.
- [29] S. Kirchhecker, D. Esposito, *Current Opinion in Green and Sustainable Chemistry* **2016**, *2*, 28–33.
- [30] T. Welton, *Chem. Rev.* **1999**, *99*(8), 2071.
- [31] C. Dai, J. Zhang, C. Huang, Z. Lei, *Chem. Rev.* **2017**, *117*(10), 6929–6983.

- [32] P. Wasserscheid, W. Keim, *Angew. Chem, Int. Ed.* **2000**, 39(21), 3772.
- [33] Z. Zhang, J. Song, B. Han, *Chem. Rev.* **2017**, 117(10), 6834–6880.
- [34] a) M. Watanabe, M. L. Thomas, S. Zhang, K. Ueno, T. Yasuda, K. Dokko, *Chem. Rev.* **2017**, 117(10), 7190–7239; b) M. Galiński, A. Lewandowski, I. Stępnia, *Electrochim. Acta* **2006**, 51(26), 5567;
- [35] M. Maase, K. Massonne, U. Vagt, "BASIL™—BASF's Processes Based on Ionic Liquids", to be found under <https://www.sigmaaldrich.com/technical-documents/articles/chemfiles/basil-basf-s-processes.html>. Accessed: 09.01.2018; 15:17
- [36] V. Fábos, D. Lantos, A. Bodor, A.-M. Bálint, L. T. Mika, O. E. Sielcken, A. Cuiper, I. T. Horváth, *ChemSusChem* **2008**, 1(3), 189–192.
- [37] V. Calò, *J. Mol. Catal. A: Chem.* **2004**, 214(1), 45–56.
- [38] S. Tang, G. A. Baker, H. Zhao, *Chem. Soc. Rev.* **2012**, 41(10), 4030.
- [39] a) X. Tang, R. Muchakayala, S. Song, Z. Zhang, A. R. Polu, *J. Ind. Eng. Chem.* **2016**, 37, 67; b) H. S. Schrekker, D. O. Silva, M. A. Gelesky, M. P. Stracke, C. M. L. Schrekker, R. S. Gonçalves, J. Dupont, *J. Braz. Chem. Soc.* **2008**, 19(3), 426;
- [40] M. Döbbelin, I. Azcune, M. Bedu, A. Ruiz de Luzuriaga, A. Genua, V. Jovanovski, G. Cabañero, I. Odriozola, *Chem. Mater.* **2012**, 24(9), 1583.
- [41] M. Dilip, *Nanomater. Energy* **2012**, 1(4), 193–206.
- [42] B. Kirchner, Ed, *Ionic liquids*; Springer, Heidelberg, New York, **2009**.
- [43] a) Y. Fukaya, Y. Iizuka, K. Sekikawa, H. Ohno, *Green Chem.* **2007**, 9(11), 1155–1157; b) M. Petkovic, J. L. Ferguson, H. Q. N. Gunaratne, R. Ferreira, M. C. Leitão, K. R. Seddon, L. P. N. Rebelo, C. S. Pereira, *Green Chem.* **2010**, 12(4), 643–649;
- [44] a) G. Singh, R. Kamboj, V. Singh Mithu, V. Chauhan, T. Kaur, G. Kaur, S. Singh, T. Singh Kang, *J. Colloid Interface Sci.* **2017**, 496, 278–289; b) A. R. Hajipour, Y. Heidari, G. Kozehgary, *RSC Adv.* **2015**, 5(75), 61179–61183;
- [45] D. Esposito, S. Kirchhecker, M. Antonietti, *Chem. - Eur. J.* **2013**, 19(45), 15097.
- [46] J.-P. Lindner, *Macromolecules* **2016**, 49(6), 2046–2053.

- [47] A. Dani, V. Crocellà, C. Magistris, V. Santoro, J. Yuan, S. Bordiga, *J. Mater. Chem. A* **2017**, 5(1), 372–383.
- [48] K. Ebel, H. Koehler, A. O. Gamer, R. Jäckh, *Imidazole and Derivatives, Ullmann's Encyclopedia of Industrial Chemistry*, **2000**.
- [49] Z. Wang, *Comprehensive Organic Name Reactions and Reagents*; John Wiley & Sons, Inc, Hoboken, NJ, USA, **2010**.
- [50] H. Debus, *Ann. Chem. Pharm.* **1858**, 107(2), 199–208.
- [51] a) B. Radziszewski, *Ber. Dtsch. Chem. Ges.* **1883**, 16(1), 487–494; b) B. Radziszewski, *Ber. Dtsch. Chem. Ges.* **1882**, 15(2), 1493–1496; c) B. Radziszewski, *Ber. Dtsch. Chem. Ges.* **1883**, 16(1), 747–749;
- [52] a) K. H. Bleicher, F. Gerber, Y. Wüthrich, A. Alanine, A. Capretta, *Tetrahedron Lett.* **2002**, 43(43), 7687; b) D. V. Paone, A. W. Shaw, *Tetrahedron Lett.* **2008**, 49(42), 6155; c) C. Maton, N. de Vos, B. I. Roman, E. Vanecht, N. R. Brooks, K. Binnemans, S. Schaltin, J. Fransaer, C. V. Stevens, *ChemPhysChem* **2012**, 13(13), 3146;
- [53] S. Kirchhecker, M. Antonietti, D. Esposito, *Green Chem.* **2014**, 16(8), 3705.
- [54] J. Zimmermann, B. Ondruschka, A. Stark, *Org. Process Res. Dev.* **2010**, 14(5), 1102–1109.
- [55] K.-S. Krannig, D. Esposito, M. Antonietti, *Macromolecules* **2014**, 47(7), 2350–2353.
- [56] P. G. Jessop, *Green Chem.* **2011**, 13(6), 1391.
- [57] H. Cheung, R. S. Tanke, P. G. Torrence, *Acetic Acid, Ullmann's Encyclopedia of Industrial Chemistry*, **2011**.
- [58] J. Andersson, J. Lundgren, E. Furusjö, I. Landälv, *Fuel* **2015**, 158, 451.
- [59] G. Iaquaniello, G. Centi, A. Salladini, E. Palo, S. Perathoner, L. Spadaccini, *Bioresour. Technol.* **2017**, 243, 611–619.
- [60] Jörg Ott, Veronika Gronemann, Florian Pontzen, Eckhard Fiedler, Georg Grossmann, D. Burkhard Kersebohm, Günther Weiss, Claus Witte, *Methanol, Ullmann's Encyclopedia of Industrial Chemistry*, **2012**.
- [61] G. Mattioda, A. Blanc, *Glyoxal, Ullmann's Encyclopedia of Industrial Chemistry*, **2011**.

- [62] Marc Eckert, Gerald Fleischmann, Reinhard Jira, Hermann M. Bolt, Klaus Golka, *Acetaldehyde, Ullmann's Encyclopedia of Industrial Chemistry*, **2006**.
- [63] G. M. Lari, R. García-Muelas, C. Mondelli, N. López, J. Pérez-Ramírez, *Green Chem.* **2016**, *18*(17), 4682–4692.
- [64] a) D. Esposito, M. Antonietti, *ChemSusChem* **2013**, *6*(6), 989–992; b) Z. Srokol, A.-G. Bouche, A. van Estrik, R. C. J. Strik, T. Maschmeyer, J. A. Peters, *Carbohydr. Res.* **2004**, *339*(10), 1717–1726;
- [65] K. Eller, E. Henker, R. Rossbacher, H. Höke, *Amines, Aliphatic, Ullmann's Encyclopedia of Industrial Chemistry*, **2000**.
- [66] B. Dong, X. Guo, B. Zhang, X. Chen, J. Guan, Y. Qi, S. Han, X. Mu, *Catalysts* **2015**, *5*(4), 2258.
- [67] S. Hegde, J. S. Lodge, T. A. Trabold, *Renewable Sustainable Energy Rev.* **2018**, *81*, 510–523.
- [68] J. B. Goodenough, K.-S. Park, *J. Am. Chem. Soc.* **2013**, *135*(4), 1167–1176.
- [69] K. Zaghbi, M. Dontigny, A. Guerfi, P. Charest, I. Rodrigues, A. Mauger, C. M. Julien, *J. Power Sources* **2011**, *196*(8), 3949–3954.
- [70] Ulrich Wietelmann, Martin Steinbild, *Lithium and Lithium Compounds, Ullmann's Encyclopedia of Industrial Chemistry*, **2014**.
- [71] R. Mohtadi, F. Mizuno, *Beilstein J. Nanotechnol.* **2014**, *5*, 1291–1311.
- [72] Q. Chen, K. Geng, K. Sieradzki, *J. Electrochem. Soc.* **2015**, *162*(10), A2004-A2007.
- [73] A. Mauger, C. M. Julien, *Ionics* **2017**, *23*(8), 1933–1947.
- [74] E. A. Olivetti, G. Ceder, G. G. Gaustad, X. Fu, *Joule* **2017**, *1*(2), 229–243.
- [75] a) Amnesty International, "Time To Recharge. Corporate action and inaction to tackle abuses in the cobalt supply chain", to be found under <https://cloud.amnesty.de/index.php/s/afgC1C6mupigGmw#pdfviewer>, **2017**; Accessed: 16.01.2018; 10:33 b) Amnesty International, "Exposed: Child labour behind smart phone and electric car batteries", to be found under <https://www.amnesty.org/en/latest/news/2016/01/child-labour-behind-smart-phone-and-electric-car-batteries/>, **2016**; Accessed: 16.01.2018; 10:27

- [76] Ketil Amundsen, Terje Kr. Aune, Per Bakke, Hans R. Eklund, Johanna Ö. Haagensen, Carlos Nicolas, Christian Rosenkilde, Sia Van den Brecht, Oddmund Wallevik, *Magnesium, Ullmann's Encyclopedia of Industrial Chemistry*, 1, **2003**.
- [77] P. Saha, M. K. Datta, O. I. Velikokhatnyi, A. Manivannan, D. Alman, P. N. Kumta, *Prog. Mater. Sci.* **2014**, 66, 1.
- [78] D. Aurbach, I. Weissman, Y. Gofer, E. Levi, *Chem. Rec.* **2003**, 3(1), 61.
- [79] I. Shterenberg, M. Salama, Y. Gofer, E. Levi, D. Aurbach, *MRS Bull.* **2014**, 39(05), 453.
- [80] M.-S. Park, J.-G. Kim, Y.-J. Kim, N.-S. Choi, J.-S. Kim, *Isr. J. Chem.* **2015**, 55(5), 570–585.
- [81] L. W. Gaddum, H. E. French, *J. Am. Chem. Soc.* **1927**, 49(5), 1295–1299.
- [82] T. D. Gregory, *J. Electrochem. Soc.* **1990**, 137(3), 775.
- [83] D. Aurbach, Z. Lu, A. Schechter, Y. Gofer, H. Gizbar, R. Turgeman, Y. Cohen, M. Moshkovich, E. Levi, *Nature* **2000**, 407(6805), 724–727.
- [84] F. Bertasi, C. Hettige, F. Seppehr, X. Bogle, G. Pagot, K. Vezzù, E. Negro, S. J. Paddison, S. G. Greenbaum, M. Vittadello, V. Di Noto, *ChemSusChem* **2015**, 8(18), 3069.
- [85] Z. Ma, M. Kar, C. Xiao, M. Forsyth, D. R. MacFarlane, *Electrochem. Commun.* **2017**, 78, 29–32.
- [86] C. Liao, N. Sa, B. Key, A. K. Burrell, L. Cheng, L. A. Curtiss, J. T. Vaughey, J.-J. Woo, L. Hu, B. Pan, Z. Zhang, *J. Mater. Chem. A* **2015**, 3(11), 6082–6087.
- [87] R. Mohtadi, M. Matsui, T. S. Arthur, S.-J. Hwang, *Angew. Chem., Int. Ed. Eng.* **2012**, 51(39), 9780–9783.
- [88] O. Tutusaus, R. Mohtadi, *ChemElectroChem* **2015**, 2(1), 51–57.
- [89] O. Tutusaus, R. Mohtadi, T. S. Arthur, F. Mizuno, E. G. Nelson, Y. V. Sevryugina, *Angew. Chem., Int. Ed. Eng.* **2015**, 54(27), 7900–7904.
- [90] J. Muldoon, C. B. Bucur, T. Gregory, *Angew. Chem., Int. Ed. Eng.* **2017**, 56(40), 12064–12084.

- [91] O. Shimamura, N. Yoshimoto, M. Matsumoto, M. Egashia, M. Morita, *J. Power Sources* **2011**, *196*(3), 1586.
- [92] M. Kar, Z. Ma, L. M. Azofra, K. Chen, M. Forsyth, D. R. MacFarlane, *Chem. Commun.* **2016**, *52*(21), 4033.
- [93] Z. Feng, Y. NuLi, J. Wang, J. Yang, *J. Electrochem. Soc.* **2006**, *153*(10), C689.
- [94] P. Wang, Y. NuLi, J. Yang, Z. Feng, *Surf. Coat. Technol.* **2006**, *201*(6), 3783–3787.
- [95] G. T. Cheek, W. E. O’Grady, S. Z. El Abedin, E. M. Moustafa, F. Endres, *J. Electrochem. Soc.* **2008**, *155*(1), D91.
- [96] G. H. Lane, *Electrochim. Acta* **2012**, *83*, 513–528.
- [97] E. I. Izgorodina, R. Maganti, V. Armel, P. M. Dean, J. M. Pringle, K. R. Seddon, D. R. MacFarlane, *J. Phys. Chem. B* **2011**, *115*(49), 14688–14697.
- [98] C. Schreiner, S. Zugmann, R. Hartl, H. J. Gores, *J. Chem. Eng. Data* **2010**, *55*(5), 1784–1788.
- [99] P. Walden, *Z. Phys. Chem.* **1906**, *55U*(1).
- [100] S. Tröger-Müller, J. Brandt, M. Antonietti, C. Liedel, *Chem. - Eur. J.* **2017**, *23*(49), 11810–11817.
- [101] a) H. E. Hoydonckx, W. M. Van Rhijn, W. Van Rhijn, D. E. De Vos, P. A. Jacobs, *Furfural and Derivatives, Ullmann's Encyclopedia of Industrial Chemistry, 1*, **2007**; b) A. Deng, Q. Lin, Y. Yan, H. Li, J. Ren, C. Liu, R. Sun, *Bioresour. Technol.* **2016**, *216*, 754;
- [102] a) T. Liu, J. T. Cox, D. Hu, X. Deng, J. Hu, M. Y. Hu, J. Xiao, Y. Shao, K. Tang, J. Liu, *Chem. Commun.* **2015**, *51*(12), 2312–2315; b) Y. Shao, T. Liu, G. Li, M. Gu, Z. Nie, M. Engelhard, J. Xiao, D. Lv, C. Wang, J.-G. Zhang, J. Liu, *Sci. Rep.* **2013**, *3*, 3130;
- [103] R. P. Pohanish, S. A. Greene, *Wiley Guide to Chemical Incompatibilities*; John Wiley & Sons, Inc, Hoboken, NJ, USA, **2009**.
- [104] D. R. Lide, Ed, *CRC handbook of chemistry and physics: A ready-reference book of chemical and physical data*; CRC Taylor & Francis, Boca Raton, Fla, **2008**.

- [105] E. Raamat, K. Kaupmees, G. Ovsjannikov, A. Trummal, A. Kütt, J. Saame, I. Koppel, I. Kaljurand, L. Lipping, T. Rodima, V. Pihl, I. A. Koppel, I. Leito, *J. Phys. Org. Chem.* **2013**, 26(2), 162–170.
- [106] A. Elaiwi, P. B. Hitchcock, K. R. Seddon, N. Srinivasan, Y.-M. Tan, T. Welton, J. A. Zora, *J. Chem. Soc., Dalton Trans.* **1995**(21), 3467–3472.
- [107] H. OHTANI, S. ISHIMURA, M. KUMAI, *Anal. Sci.* **2008**, 24(10), 1335–1340.
- [108] Institut für Arbeitsschutz der Deutschen Gesetzlichen Unfallversicherung (IFA), "Natriumformiat", to be found under [http://gestis.itrust.de/nxt/gateway.dll/gestis_de/002560.xml?f=templates\\$fn=document-frameset.htm\\$3.0](http://gestis.itrust.de/nxt/gateway.dll/gestis_de/002560.xml?f=templates$fn=document-frameset.htm$3.0). Accessed: 26.02.2018; 22:05
- [109] Institut für Arbeitsschutz der Deutschen Gesetzlichen Unfallversicherung (IFA), "Natriumacetate", to be found under [http://gestis.itrust.de/nxt/gateway.dll/gestis_de/010760.xml?f=templates\\$fn=document-frameset.htm\\$3.0](http://gestis.itrust.de/nxt/gateway.dll/gestis_de/010760.xml?f=templates$fn=document-frameset.htm$3.0). Accessed: 26.02.2018; 22:05
- [110] C. J. Caires, L. S. Lima, C. T. Carvalho, M. Ionashiro, *Eclat. Quím.* **2010**, 35(4), 73–80.
- [111] Institut für Arbeitsschutz der Deutschen Gesetzlichen Unfallversicherung (IFA), "Kaliumnatriumtartrat", to be found under [http://gestis.itrust.de/nxt/gateway.dll/gestis_de/491070.xml?f=templates\\$fn=document-frameset.htm\\$3.0](http://gestis.itrust.de/nxt/gateway.dll/gestis_de/491070.xml?f=templates$fn=document-frameset.htm$3.0). Accessed: 26.02.2018; 22:02
- [112] M. Smith, Ed, *March's advanced organic chemistry: Reactions, mechanisms, and structure*; Wiley, Hoboken, **2013**.
- [113] J. Clayden, N. Greeves, S. G. Warren, *Organic chemistry*; Oxford University Press, Oxford, New York, **2012**.
- [114] a) D. Esposito, M. Antonietti, *Chemical Society reviews* **2015**, 44(16), 5821–5835; b) E. D. Jong, A. Higson, P. Walsh, M. Wellisch, "IEA Bioenergy - Task 42 Biorefinery. Biobased Chemicals - Value Added Products From Biorefineries", to be found under <http://www.nnfcc.co.uk/publications/biorefinery-biobased-chemicals>, **2012**; Accessed: 19.02.2018; 20:20 c) A. Kokel, B. Török, *Toxicol. Sci.* **2018**, 161(2), 214–224;
- [115] J. Chocholoušová, J. Vacek, P. Hobza, *J. Phys. Chem. A* **2003**, 107(17), 3086–3092.

- [116] J. A. Sirviö, M. Visanko, H. Liimatainen, *RSC Adv.* **2016**, 6(61), 56544–56548.
- [117] a) J. Gong, H. Lin, K. Grygiel, J. Yuan, *Applied Materials Today* **2017**, 7, 159–168; b) K. Grygiel, S. Kirchhecker, J. Gong, M. Antonietti, D. Esposito, J. Yuan, *Macromol. Chem. Phys.* **2017**, 218(18), 1600586;
- [118] S. Tröger-Müller, J. Brandt, M. Antonietti, C. Liedel **2018**.
- [119] F. Gschwind, H. Euchner, G. Rodriguez-Garcia, *Eur. J. Inorg. Chem.* **2017**, 2017(21), 2784–2799.
- [120] F. Gschwind, D. Steinle, D. Sandbeck, C. Schmidt, E. von Hauff, *ChemistryOpen* **2016**, 5(6), 525–530.
- [121] A. Kirubakaran, S. Jain, R. K. Nema, *Renewable Sustainable Energy Rev.* **2009**, 13(9), 2430–2440.
- [122] G. Merle, M. Wessling, K. Nijmeijer, *J. Membr. Sci.* **2011**, 377(1-2), 1–35.
- [123] B. Lin, L. Qiu, J. Lu, F. Yan, *Chem. Mater.* **2010**, 22(24), 6718–6725.
- [124] T. G. Mezger, *The Rheology Handbook: 4th Edition*; Vincentz Network, Hannover, **2014**.
- [125] S. Tröger-Müller, M. Antonietti, C. Liedel, *Phys. Chem. Chem. Phys.* **2018**, 20(16), 11437–11443.
- [126] N. de Vos, C. Maton, C. V. Stevens, *ChemElectroChem* **2014**, 1(8), 1258–1270.
- [127] Y. Chu, H. Deng, J.-P. Cheng, *J. Org. Chem.* **2007**, 72(20), 7790–7793.
- [128] A. J. Arduengo, R. L. Harlow, M. Kline, *J. Am. Chem. Soc.* **1991**, 113(1), 361–363.
- [129] N. Marion, S. Díez-González, S. P. Nolan, *Angew. Chem, Int. Ed. Engl.* **2007**, 46(17), 2988–3000.
- [130] D. P. Curran, A. Solovyev, M. Makhlouf Brahmī, L. Fensterbank, M. Malacria, E. Lacôte, *Angew. Chem, Int. Ed. Engl.* **2011**, 50(44), 10294–10317.
- [131] S. Gardner, T. Kawamoto, D. P. Curran, *Org. Synth.* **2015**, 92, 342–355.
- [132] S. Gardner, T. Kawamoto, D. P. Curran, *J. Org. Chem.* **2015**, 80(19), 9794–9797.
- [133] S. Huang, X. Qi, T. Liu, K. Wang, W. Zhang, J. Li, Q. Zhang, *Chem. - Eur. J.* **2016**, 22(29), 10187.

- [134] A. R. Choudhury, N. Winterton, A. Steiner, A. I. Cooper, K. A. Johnson, *J. Am. Chem. Soc.* **2005**, *127*(48), 16792–16793.
- [135] B. Wrackmeyer, *Prog. Nucl. Magn. Reson. Spectrosc.* **1979**, *12*(4), 227–259.
- [136] E. Gómez, N. Calvar, Á. Domínguez, E. A. Macedo, *Ind. Eng. Chem. Res.* **2013**, *52*(5), 2103–2110.
- [137] S. Tröger-Müller, M. Antonietti, C. Liedel **2018**.
- [138] M. Thompson, J. N. Walsh, *Handbook of Inductively Coupled Plasma Spectrometry*; Springer US, Boston, MA, **1989**.
- [139] L. Lajunen, *Spectrochemical Analysis by Atomic Absorption and Emission*; Royal Society of Chemistry, Cambridge, **2007**.
- [140] R. F. Egerton, *Physical principles of electron microscopy: An introduction to TEM, SEM, and AEM*; Springer, New York, NY, **2008**.
- [141] JEOL, "Scanning Electron Microscope A To Z", to be found under <https://www.jeol.co.jp/en/applications/detail/891.html>. Accessed: 03.05.2018; 23:41
- [142] H. Awad, M. M. Khamis, A. El-Aneed, *Appl. Spectrosc. Rev.* **2014**, *50*(2), 158–175.
- [143] J. H. Gross, *Mass Spectrometry: A Textbook*; Springer International Publishing, Cham, s.l, **2017**.
- [144] B. Wunderlich, *Thermal Analysis of Polymeric Materials*; Springer-Verlag Berlin Heidelberg, Berlin, Heidelberg, **2005**.
- [145] G. W. H. Höhne, W. F. Hemminger, H.-J. Flammersheim, *Differential Scanning Calorimetry*; Springer, Berlin, Heidelberg, **2003**.
- [146] G. R. Heal in *Principles of Thermal Analysis and Calorimetry*; (Ed. P. Haines), Royal Society of Chemistry, Cambridge, **2002**, pp. 10–54.
- [147] National Institute of Standards and Technology, *Acetic Acid*, to be found under <https://webbook.nist.gov/cgi/cbook.cgi?ID=C64197&Units=SI&Mask=200#Mass-Spec>. Accessed: 24.04.2018; 22:19
- [148] E. Scholz, *Karl Fischer Titration*; Springer Berlin Heidelberg, Berlin, Heidelberg, **1984**.

- [149] P. J. Hore, J. A. Jones, S. Wimperis, *NMR: the toolkit: How pulse sequences work*; Oxford University Press, Oxford, **2015**.
- [150] H. Günther, *NMR spectroscopy: Basic principles, concepts and applications in chemistry*; Wiley-VCH Verlag GmbH & Co. KGaA, Weinheim, **2013**.
- [151] N. Elgrishi, K. J. Rountree, B. D. McCarthy, E. S. Rountree, T. T. Eisenhart, J. L. Dempsey, *J. Chem. Educ.* **2017**, 95(2), 197–206.